The Atomic Structure of Diamond Surfaces and Interfaces

Michael Sternberg

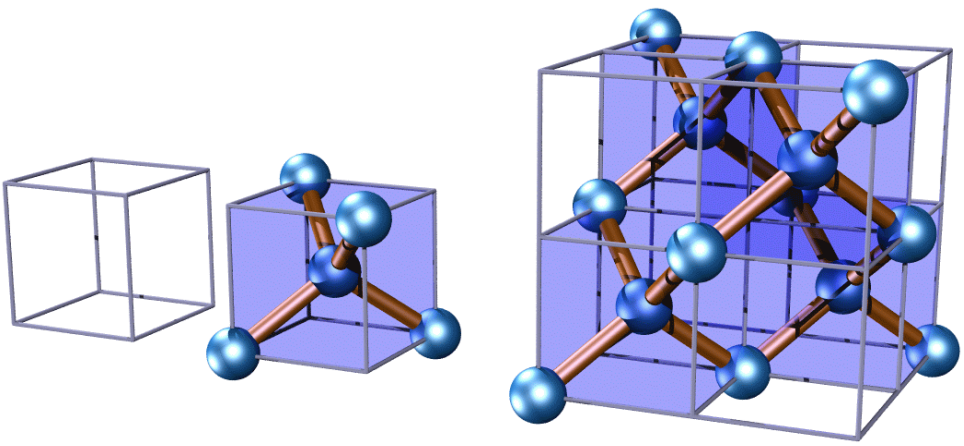

The Atomic Structure of Diamond Surfaces and Interfaces

Dissertation
zur Erlangung des akademischen Grades
Doktor der Naturwissenschaften (Dr. rer. nat.)
vorgelegt dem
Fachbereich Physik der Universität Paderborn

Michael Sternberg

Paderborn, 2001

Vom Fachbereich Physik der Universität Paderborn als Dissertation genehmigt.

Tag der Einreichung:	27. September 2001
Tag der mündlichen Prüfung:	14. November 2001

Promotionskommission

Vorsitzender	Prof. Dr. rer. nat. Gerhard Wortmann
Erstgutachter	Prof. Dr. rer. nat. Thomas Frauenheim
Mitgutachter	Dr. habil. Hans-Gerd Busmann
Beisitzer	PD Dr. Siegmund Greulich-Weber

Archiv

Elektronische Dissertationen und Habilitationen der Universität Paderborn
http://www.ub.upb.de/volltext/ediss

Version: 14. November 2001

Michael Sternberg, *The Atomic Structure of Diamond Surfaces and Interfaces*.
PhD Thesis (in english), Department of Physics, University of Paderborn, Germany (2001).
137 pages, 41 figures, 24 tables.

Abstract

This thesis investigates several theoretical issues on the growth and structure of diamond films produced by chemical vapour deposition. The work is divided into two major parts, the first being methodological in character, and the second devoted to applications.

After an overview on electronic structure theory certain aspects of the density-functional-based tight-binding method (DFTB) are examined, primarily its connection to the underlying density functionals. A review of the approximations taken in various implementations of this scheme over the years is given as well. In the present work this method is extended to a linear scaling ($\mathcal{O}(N)$) formulation. The first part concludes with test results and a general assessment.

In part two, the standard DFTB method is applied to several problems of interest in the context of diamond materials. First, an overview of the properties of diamond bulk and surfaces is given. Energy and geometry data set the stage for the subsequent calculations and serve as performance benchmarks. The remaining chapters address questions related to the relatively new class of ultrananocrystalline diamond (UNCD) thin films grown primarily from C_2 species. A complete mechanism for the growth of a diamond (110) monolayer is established by investigating total energies and adsorption barriers on an initially clean surface, followed by chain growth and coalescence, and finishing with the filling of surface vacancies. The mechanism is qualitatively different from conventional methyl-based diamond growth. A stabilisation of the diamond phase over graphite due to C_2 was observed in the absence of hydrogen.

The internal structure of UNCD films is investigated by considering high-angle high-energy (100) twist grain boundaries. They differ significantly from those in microcrystalline diamond, where low-angle and tilt grain boundaries, as well as stacking faults and twins prevail. First, the structure of pure grain boundaries is established, followed by an investigation of the effects of impurities. The grain boundaries are confirmed to be very narrow, essentially spanning only two atomic monolayers. The atomic structure is characterised by threefold coordinated atoms which amount to about 50% of all interface atoms and introduce electronic levels into the diamond band gap. The electrical conductivity observed in the films is attributed to carbon π-states in the grain boundary regions. It is found that nitrogen impurities are energetically easier to incorporate into the grain boundaries than into the grain bulk and that nitrogen promotes threefold coordination of carbon atoms in the grain boundary. A shift in the Fermi energy towards the conduction band at larger nitrogen concentrations was noticed. These mechanisms support experimental evidence on enhanced electrical conductivity due to nitrogen. In contrast, hydrogen saturates dangling bonds and so lowers the film conductivity.

Keywords

diamond, surfaces, grain boundaries, growth, conductivity, density functional theory, tight-binding, linear scaling, O(N)

PACS

`71.15.Dx` Computational methodology
`61.43.Bn` Structural modeling: serial-addition models, computer simulation
`61.72.Mm` Grain and twin boundaries
`68.35.-p` Solid surfaces and solid-solid interfaces: Structure and energetics
`81.15.Aa` Theory and models of film growth

Michael Sternberg, *Die Atomare Struktur von Diamantoberflächen und Grenzflächen*.
Dissertation (in englischer Sprache), Fachbereich Physik, Universität Paderborn (2001).
137 Seiten, 41 Abbildungen, 24 Tabellen.

Kurzfassung

Diese Dissertation untersucht verschiedene theoretische Fragen zu Wachstum und Struktur von Diamantschichten, welche mittels chemischer Dampfphasenabscheidung hergestellt werden. Die Arbeit ist in zwei Hauptteile gegliedert, von denen der erste methodischen Charakter hat und der zweite Anwendungen gewidmet ist.

Nach einem Überblick zur Theorie der Elektronenstruktur werden einige Aspekte der Dichtefunktional-basierten Tight-Binding Methode (DFTB) beleuchtet, insbesondere deren Beziehung zu den zugrundeliegenden Dichtefunktionalen. Ferner wird ein Rückblick zu den angewandten Näherungen in den verschiedenen Implementierungen des Verfahrens im Verlauf der letzten Jahre gegeben. In der vorliegenden Arbeit wird die Methode um eine linear skalierende ($\mathcal{O}(N)$) Formulierung erweitert. Der Teil schließt mit Testergebnissen und einer allgemeinen Einschätzung ab.

Im zweiten Teil wird die Standard-DFTB-Variante auf verschiedene Probleme im Umfeld von Diamantmaterialien angewandt. Zunächst wird ein Überblick zu Eigenschaften des Diamantfestkörpers und seinen Oberflächen gegeben. Daten zu Energie and Geometrie ebnen den Weg zu den anschließenden Rechnungen und dienen zur Abschätzung ihrer Zuverlässigkeit. Die verbleibenden Kapitel behandeln Fragen zur relativ neuen Klasse von ultrananokristallinen Diamantschichten (UNCD), welche hauptsächlich mittels C_2-Spezies gewachsen werden. Anhand von Berechnungen zu Gesamtenergien und Barrieren an einer ursprünglich reinen Oberfläche, gefolgt von Kettenwachstum und -verschmelzung sowie abgeschlossen durch die Auffüllung von Oberflächenleerstellen wird ein vollständiger Mechanismus zum Wachstum einer (110) Monolage aufgestellt. Der Mechanismus unterscheidet sich qualitativ von konventionellem, methylbasiertem Wachstum. Eine Stabilisierung der Diamantphase gegenüber Graphit unter Einfluß von C_2 und ohne Wasserstoff wurde beobachtet.

Schließlich wird die innere Struktur der UNCD-Schichten anhand von vergleichsweise hochenergetischen (100) Großwinkeldrehkorngrenzen untersucht. Die Korngrenzen unterscheiden sich von jenen in mikrokristallinem Diamant, wo Kleinwinkelkorngrenzen, Kippkorngrenzen sowie Zwillingsbildung vorherrschen. Zunächst wird die Struktur von reinen Korngrenzen aufgestellt, gefolgt von Betrachtungen zum Einfluß von Defekten. Die Korngrenzen werden als extrem dünn bestätigt, da sie lediglich zwei atomare Monolagen umfassen. Die atomare Struktur ist gekennzeichnet durch dreifach koordinierte Atome, welche etwa 50% aller Grenzflächenatome ausmachen und elektronische Zustände in der Bandlücke hervorrufen. Die an den Schichten beobachtete elektrische Leitfähigkeit wird Kohlenstoff-π-Zuständen innerhalb der Korngrenzen zugeschrieben. Es wird festgestellt, daß Stickstoffverunreinigungen in die Korngrenzen energetisch günstiger als in das Innere der Kristalle einzufügen sind sowie außerdem die Dreifachkoordinierung von Kohlenstoffatomen fördern. Eine Verschiebung des Ferminiveaus zum Leitungsband hin wurde bei höheren Stickstoffkonzentrationen konstatiert. Diese Mechanismen stützen experimentelle Befunde einer erhöhten elektrischen Leitfähigkeit infolge von Stickstoff. Im Gegensatz dazu sättigt Wasserstoff freie Bindungen ab und senkt daher die Leitfähigkeit.

Schlagwörter

Diamant, Oberflächen, Korngrenzen, Wachstum, Leitfähigkeit, Dichtefunktional-Theorie, Tight-Binding, Lineare Skalierung, O(N)

Contents

Contents **v**

List of Figures viii

List of Tables x

Symbols and abbreviations xi

Introduction **1**

1 Theoretical Foundations **5**

1.1 Wave mechanics and density functional theory 5

1.2 The density as basic variable 7

1.3 The Hohenberg-Kohn variational principle 7

1.4 The Kohn-Sham equations 9

1.5 Solutions to the Kohn-Sham equation 11

1.5.1 The Kohn-Sham total energy 12

1.5.2 Charges and forces 13

2 The DFTB Method **15**

2.1 Historical sketch 15

2.2 Variational approach and stationary principle 18

2.3 Approximations in DFTB 20

2.3.1 Pseudo-atomic starting density 21

2.3.2 Tight-Binding integrals and the two-centre approximation . . 22

2.3.3 Repulsive potential 23

2.3.4 Second-order corrections 25

2.4 The DFTB secular equation 28

3 Order-N Method and Implementation **31**

3.1 Introduction 31

3.2 Energy functional and charges 32

3.2.1 Energy functional . . . 32
3.2.2 Localisation of support functions . . . 34
3.2.3 Hamilton and overlap matrices . . . 35
3.2.4 Atomic charges and SCC energy contributions . . . 38
3.3 Electronic minimisation . . . 39
3.3.1 The Lagrange multiplier η . . . 41
3.3.2 The adaptive secant method . . . 42
3.4 The calculation of forces . . . 45
3.5 Accuracy and performance . . . 46
3.5.1 Energy and charges . . . 47
3.5.2 Forces . . . 48
3.5.3 Scaling . . . 49
3.5.4 Assessment . . . 50

4 Properties of Diamond 51
4.1 History and economics . . . 51
4.2 Bulk structure and properties . . . 52
4.3 Diamond surface structure . . . 55
4.3.1 General properties . . . 55
4.3.2 The individual surfaces . . . 58
4.4 Reference calculations on diamond bulk and surfaces . . . 60
4.4.1 Atomic and diatomic energies . . . 60
4.4.2 Bulk systems . . . 61
4.4.3 Surfaces . . . 63
4.4.4 Summary . . . 68

5 Growth of (110) Diamond Using Pure Dicarbon 71
5.1 Introduction . . . 71
5.2 Simulation setup . . . 73
5.3 Adsorption and energetics of small carbon clusters . . . 73
5.3.1 Initial C_2 deposition . . . 73
5.3.2 Addition of C_2 . . . 76
5.3.3 C_4 clusters . . . 77
5.3.4 C_6 and C_8 clusters . . . 78
5.3.5 Adsorption barriers . . . 79
5.3.6 Surface defect formation . . . 79
5.3.7 Surface vacancy filling . . . 80

5.3.8 Graphitisation and rebonding 80
5.4 Surface diffusion of C_2 83
5.5 Molecular dynamics depositions 84

6 Structure and Impurities in UNCD Grain Boundaries 85
6.1 Introduction 85
6.1.1 Grain boundary primer 87
6.1.2 Grain boundary supercell setup 90
6.2 Twist (100) grain boundaries without impurities 91
6.2.1 Structure and bonding 91
6.2.2 Energetics 96
6.2.3 Energy levels 97
6.3 Nitrogen substitutional impurities 99
6.3.1 Structure and bonding 99
6.3.2 Energetics 102
6.3.3 Energy levels 102
6.4 Silicon substitutional impurities 106
6.5 Hydrogen addition 106
6.6 Summary 109

7 Summary and Conclusions 111

A Atomic Units Reference 115

B Approximations for Exchange and Correlation Energies 118

Bibliography 121

Acknowledgements 135

Colophon 137

List of Figures

2.1 Example for generating the repulsive potential 25
2.2 Interpolation functions for the γ_{ab} term in SCC-DFTB 27

3.1 Spatial relations between localisation regions 36
3.2 Line minimisation update step $\lambda_{\min}$ vs. iteration 41
3.3 Flowchart for the $\mathcal{O}(N)$ minimisation of the total energy 42
3.4 Calculated energy, charges, and η-parameter during iteration 43
3.5 Examples for the application of the adaptive secant method 45
3.6 Accuracy of $\mathcal{O}(N)$ force calculation 48
3.7 Scaling behaviour for CPU time and memory requirements 50

4.1 The crystal structure of diamond and lonsdaleite 53
4.2 Geometry of diamond surfaces 56
4.3 $\{111\} - (1 \times 1)$ surface net (hexagonal) 58
4.4 $\{111\} - (2 \times 1)$ surface net 58
4.5 $\{110\} - (1 \times 1)$ surface net (rectangular) 59
4.6 $\{100\} - (1 \times 1)$ surface net (square) 59
4.7 $\{100\} - (2 \times 1)$ surface net 59

5.1 Cross-section SEM images of as-grown UNCD films 72
5.2 Overview of relaxed structures from subsequent C_2 depositions . . . 74
5.3 Initial steps for deposition of a C_2 molecule 74
5.4 Continued deposition of C_2 next to an existing adsorbate 77
5.5 Continued deposition of C_2 on top of an existing adsorbate 78
5.6 Continued deposition of C_2 with high insertion energy 79
5.7 Final stages of chain growth and coalescence 81
5.8 Graphitisation and induced rebonding after additional deposition . . 82

6.1 Crystallographic relation for twist grain boundaries 88
6.2 Setup of a grain boundary simulation cell 89
6.3 Side view of the periodic cell for a $\Sigma 13$ grain boundary 91
6.4 Comparison of $\Sigma 13$, $\Sigma 5(2 \times 2)$, and $\Sigma 29$ grain boundaries 92
6.5 Radial distribution function $J(r)$ for $\Sigma 13$ 94
6.6 Overview of individual interface planes 95
6.7 Electronic density of states for diamond and twist grain boundaries . 97

6.8 Local density of states for a diamond twist grain boundary 98
6.9 Schematic band structure for a diamond Σ13 grain boundary 98
6.10 Substitution sites selected in a Σ13 grain boundary 100
6.11 Relaxed local structure around a substitutional nitrogen atom 101
6.12 Localisation of states near substitutional N in diamond (P1 centre) . . 103
6.13 Density of states for a Σ13 grain boundary with nitrogen impurities . 105
6.14 Side and top view of a grain boundary with a silicon impurity 107
6.15 Relaxed local structure around a substitutional silicon atom 107
6.16 Relaxed structure of a Σ13 grain boundary with hydrogen 108
6.17 Molecular dynamics path of hydrogen atoms in a grain boundary . . 109

List of Tables

2.1 Schemes for pseudo-atom calculation in DFTB 22
2.2 Integral types in the DFTB Hamiltonian 23
2.3 Chemical hardness for some elements 27

3.1 Comparison of $\mathcal{O}(N)$ total energies and charges 47
3.2 Scaling of $\mathcal{O}(N)$ CPU time and memory requirements 49

4.1 Elementary properties of low-index diamond surfaces 55
4.2 Pseudo-atom parameters for SCC-DFTB 60
4.3 SCC-DFTB reference calculations for diatomic molecules 61
4.4 Reference energies of bulk diamond 62
4.5 Reference energies of graphite 62
4.6 Reference energies of diamond surfaces 64
4.7 Calculated geometry of diamond $\{111\}$ surfaces 65
4.8 Calculated geometry of diamond $\{110\}$ surfaces 67
4.9 Calculated geometry of diamond $\{100\}$ surfaces 68
4.10 Summary of stable reconstructions on diamond surfaces 69

5.1 Energy barriers and adsorption energies of C_2 during growth stages 75
5.2 Diffusion barriers and change in total energy along diffusion path . . 83

6.1 Structure and energetics of twist grain boundaries 90
6.2 Coordination and bondlengths for atoms in grain boundary planes . 93
6.3 Coordination for nitrogen and carbon atoms in grain boundary planes 100

A.1 List of the CODATA recommended values of fundamental constants 116
A.2 Values in SI units of some atomic units 116
A.3 Conversion between units of energy and values of energy equivalents 117
A.4 Energy equivalents for electromagnetic radiation 117

Symbols and abbreviations

This list is limited to the most important symbols. Others are explained in the text when first used. Appendix A contains symbols and reference data for fundamental constants and atomic units (which are used throughout).

DFT	density functional theory
KS	Kohn-Sham
LCAO	linear combination of atomic orbitals
TB	tight binding
DFTB	density functional based tight binding
SCC	self-consistent charge
$\mathcal{O}(N)$	Order-N (scaling linearly with system size N)
LR	localisation region (range) for one-electron wave functions $\Phi(\boldsymbol{r})$ (*q.v.*)
LRSK	localisation region for Slater-Koster integrals
OV	overlap region for $\Phi_i(\boldsymbol{r})$ with other $\Phi_j(\boldsymbol{r})$
CVD	chemical vapour deposition
UNCD	ultrananocrystalline diamond
GB	grain boundary
$\widehat{H}$	Hamilton operator
$n(\boldsymbol{r})$	electron density
occ	number of occupied one-electron states (in summation bounds)
$\Psi(\{x_i\})$	many-particle wave function of spatial and spin variables x_i
$\Phi(\boldsymbol{r})$, $\|\Phi\rangle$	one-electron wave function (molecular orbital)
$\varphi(\boldsymbol{r})$, $\|\varphi\rangle$	basis function (usually atomic)
i, j	label for molecular orbitals
$\mu, \nu, \ldots$	label for basis functions, regardless of atomic site
$a, b, \ldots$	label for atoms
$\boldsymbol{R}_a$	positions of atoms
$\boldsymbol{r}_a$, r_a	spatial vector relative to an atomic position $\boldsymbol{r}_a = \boldsymbol{r} - \boldsymbol{R}_a$, and its length $r_a = \|\boldsymbol{r}_a\|$
$\mu[a]$	(set of) basis functions located on specified atom a
$a[\mu]$	atom corresponding to a specified basis function or set thereof.
$\mathbf{H}$, H_{ij}	Hamilton matrix (element) for *molecular orbitals* ($\equiv \varepsilon_i$ for eigenstates)
$\mathbf{S}$, S_{ij}	overlap matrix (element) for *molecular orbitals* ($\equiv \delta_{ij}$ for eigenstates)
$\mathbf{h}$, $h_{\mu\nu}$	Hamiltonian matrix (element) between *basis functions*
$\mathbf{s}$, $s_{\mu\nu}$	overlap matrix (element) between *basis functions*

Crystallographic notation

The following are the standard recommended symbols to describe crystallographic planes and directions (Miller indices), emphasising the distinction between a generic notation for a *family* of planes or directions, and a specific notation for *individual* ones, to be used where the distinction is important. A frequent exception, however, employed here as well, is the generic use of (hkl) for planes to improve readability in text.

(hkl)	plane, specific. $(100) \neq (010)$
$\{hkl\}$	plane, generic. $(100), (010), (\bar{1}00), \ldots$
$[hkl]$	direction, specific. $[100] \neq [010]$
$\langle hkl \rangle$	direction, generic. $[100], [010], \ldots$

Introduction

> *On two occasions I have been asked [by members of parliament] 'Pray, Mr Babbage, if you put into the machine wrong figures, will the right answers come out?' [...] I am not able rightly to apprehend the kind of confusion of ideas that could provoke such a question.*
>
> *– Charles Babbage (1792-1871)*

This thesis investigates several theoretical aspects of the growth and structure of diamond films produced by chemical vapour deposition.

Diamond as material

Gemstone-quality diamond is found only in nature, in strongboxes, and occasionally in ballrooms, where it sparkles at its best. Materials scientists have a farther reaching interest in diamond as material of choice for current and future applications. Diamond has an attractive combination of physical properties like extreme hardness, high refractive index, high heat conductivity, high IR-transmissivity and interesting electronic properties like a wide bandgap and negative electron affinity. Natural diamond is the paragon for many of these parameters.

The majority of mined diamonds is of industrial grade and is consumed largely as grinding material. Research efforts in the 1950s led to the development of several technologies to produce synthetic diamond. By far the largest share of production derives from a high-pressure high-temperature (HPHT) process developed for industrial scales contemporaneously by the General Electric Company (GE) in the US and Allmanna Svenska Elektriska Aktiebolaget (ASEA) in Sweden, see [1, "Matter"]. This type of material is used mostly in the form of grit or sintered powder in coatings for cutting and grinding tools to improve their hardness and wear resistance. However, efforts to produce high quality diamond encounter significant problems, since classical techniques for growing large single crystals, e.g. the Czochralski method, fail, because the melting point of diamond under reasonable pressure is so high that it is not known, see [1, "Structure of carbon allotropes"].

A completely different strategy suitable for modern applications is the actual growth of diamond by chemical vapour deposition (CVD). It was developed independently by Eversole and subsequently Angus in the USA and by Spitsyn and Deryagin in the USSR [2]. This method allows the direct deposition of diamond polycrystalline

films on substrates of possibly complicated shapes. By growing films to a thickness in the millimetre range and subsequently etching away the substrate, one may even fabricate free platelets, or wafers. Devices based on diamond thin films are being developed e.g. for cold electron emitters and high-temperature applications, while platelets find application as heat spreaders or as mechanically robust infrared-transmissive windows.

The CVD growth process must be delicately controlled since the formation of diamond competes thermodynamically with that of graphite. At room temperature (298 K) and atmospheric pressure, the free energy for graphite is lower than that of diamond by 30 meV/atom [3]. Conventionally, methane (CH_4) is used as feed gas in a low-pressure chamber. To stabilise diamond over graphite, the methyl content in the gas has to be kept in the 1% range, with hydrogen constituting the rest, acting as catalyst. The resulting growth rate and film morphology of CVD films depend on the growth conditions; typical rates are nowadays of the order of a few micrometres per hour, resulting in polycrystalline films with a typical grain size of 1 micrometre.

It was a long-standing assertion that hydrogen in its role of etching graphitic deposits is essential for the growth of diamond. In the 1990s research at Argonne National Laboratory led to a new type of diamond film grown from fullerene-fragmented C_2 precursors in hydrogen-poor, argon-rich plasmas [4]. The resulting films differ markedly in their morphology from conventional microcrystalline films. They consist of ultrananocrystalline diamond with crystallite sizes in the range of 3–10 nanometres. This is at least an order of magnitude smaller than occasionally observed submicron grain sizes in traditional films, and so justifies a separate classification for the new films.

The role of theory

Theoretical studies help to understand and overcome some of the problems involved in the production of CVD diamond. While a great deal is known experimentally about bulk properties and crystal defects, detailed information about the atomic surface structure is derived largely from quantum-mechanical models involving the calculation of total energies, atomic forces, and electronic properties. The spectrum of theoretical methods for atomic structure calculations ranges from high-accuracy techniques based on configuration interactions, over the large realm of Hartree-Fock and density-functional based methods, and into empirical force-fields. Each class of methods has its particular domain of applicability, characterised roughly by the system size, i.e., the number of atoms which can comfortably be handled at a desired accuracy level.

Surfaces and interfaces are in general more complex than highly symmetric bulk systems, and therefore have larger periodic cell sizes. This fact curtails the applicability of high-accuracy wave-function- and density-functional methods alike. Classical potentials, on the other hand, allow to investigate mesoscopic phenomena like crack propagation or surface roughening but cannot provide a description of the electronic properties of the material. It is the tight-binding methods of the medium-accuracy level, such as the one employed here, which provide a quantum mechanical description of chemical bonding sufficient to describe the electronic and

atomic structure of large scale bulk, surface and interface systems. They may also yield insight into system evolution, e.g. during growth and phase transitions.

Outline

The subject of the present work is the application of a particular density-functional based tight-binding method (DFTB) to diamond and related systems. The work is divided into two major parts, the first being methodological in character, and the second devoted to applications.

The goal of part one is to consider a linear-scaling development of the tight binding formalism in the context of density functional theory. The standard implementation of tight-binding involves the solution of an eigenvalue problem which scales as N^3 in terms of the size of the system, N representing the number of basis functions. In line with several attempts during the last decade to find alternative solutions which scale linearly with the system size, one goal of this thesis is to extend our tight-binding method to such an Order-N formulation. To this end, the background of the density-functional theory is given in Chapter 1 and that on a tight-binding formulation derived directly from it in Chapter 2. The extension of this tight-binding method into an $\mathcal{O}(N)$ formulation is then presented in Chapter 3, which concludes the first part.

In part two, the standard DFTB method is applied to several problems of interest in the context of diamond materials. The first chapter in the second part (4) gives an overview of the properties of bulk diamond and especially diamond surfaces—including hydrogenated surfaces and various reconstructions. The data on energies and geometries not only provide the basis for the subsequent calculations but also serve as a benchmark for the performance of the method.

The next two Chapters (5 and 6) address questions related to the new class of ultrananocrystalline diamond (UNCD). While the conventional methyl-based growth process is believed to be largely understood, the predominant growth species for UNCD films is C_2 produced in great abundance from the fragmentation of C_{60} fullerenes. To shed light on this process, Chapter 5 addresses the question of growth due to C_2 on the (110)-face which is the fastest growing face. In this chapter, a complete mechanism for the growth of a diamond (110) monolayer is established by investigating total energies and adsorption barriers for clusters on an initially clean surface, followed by chain growth and coalescence, and finishing with a mechanism for filling surface vacancies. In this context, a stabilisation effect of the diamond phase over graphite was observed without hydrogen participation.

In Chapter 6 the structural properties of UNCD films are investigated in a study of high-angle high-energy (100) twist grain boundaries. Such grain boundaries occur in the films as a result of the more or less random orientation of the small grains. Again, they differ significantly from those in microcrystalline diamond, where low-angle and twist grain boundaries, as well as stacking faults and twins prevail, all of which have been extensively studied. In this work, the structure of pure grain boundaries is established, followed by an investigation of the effects of impurities.

Appendix A contains reference material on relevant atomic units which the reader and author alike will find convenient to be included. Some notes on the widely used local density approximation (LDA) and generalised gradient approximations (GGA) to the density functional theory have found a place in Appendix B.

Chapter 1

Theoretical Foundations

In this chapter, we will briefly review the density functional theory, to the extent appropriate for the scope of the present work. The background, precise mathematical formulation, and extensions are reviewed regularly and at length in the literature [5, 6, 7, 8]. The most recent treatise *from the horse's mouth* [9] discusses the connection between density functional theory and venerable wave mechanics, an approach most appealing to take as a starting point.

1.1 Wave mechanics and density functional theory

The basic problem posed in electronic structure calculations is to determine the time-independent many-electron wave function [10]

$$\Psi = \Psi(\{x_i\}), \quad i = 1 \dots N \tag{1.1}$$

for N interacting electrons moving in a static potential, usually the potential of the atomic nuclei of a solid or molecule. The parameters x_i in general contain the spatial and spin coordinates, i.e., $x_i \equiv (\boldsymbol{r}_i, s_i)$, but the spin variables will not play a role in most of the present work. The wave function for stationary states is the solution of the Schrödinger equation [11]:

$$\widehat{H}\Psi^{(n)}(\{x_i\}) = E^{(n)}\Psi^{(n)}(\{x_i\}). \tag{1.2}$$

It has solutions for a number of different states, labelled n. The state with the lowest energy is the ground state. The non-relativistic and stationary Hamiltonian in the Schrödinger equation is given by:[1]

$$\widehat{H} = \sum_{i=1}^{N} \left[-\frac{\Delta_i}{2} + \sum_{j>i}^{N} \frac{1}{|\boldsymbol{r}_i - \boldsymbol{r}_j|} + V_{\text{ext}}(\boldsymbol{r}_i) \right]. \tag{1.3}$$

[1] Atomic units are used; cf. Appendix A.

In atomic systems, the external potential $V_{\text{ext}}(\boldsymbol{r})$ is the potential of nuclei with atomic numbers Z_a and positions $\boldsymbol{R}_a$:

$$V_{\text{ext}}(\boldsymbol{r}) = -\sum_{a=1}^{N_{\text{at}}} \frac{Z_a}{|\boldsymbol{r} - \boldsymbol{R}_a|} \tag{1.4}$$

This Hamiltonian embodies the *adiabatic* or Born-Oppenheimer approximation, which describes the system of electrons in the static field of the nuclei, an approximation justified by the large difference in mass, and therefore, length and time scales for the motion of nuclei and electrons. Consequently, all physical properties of the system depend parametrically on the positions of the nuclei, i.e.,

$$\Psi = \Psi(\{x_i\}, \{\boldsymbol{R}_a\}) \tag{1.5}$$
$$E = E(\{\boldsymbol{R}_a\})\,. \tag{1.6}$$

For the purpose of electronic structure calculations, this dependency will be put aside. It will be revisited in the calculation of forces on atoms for the purpose of a quasi-classical integration of motion.

The many-particle Schrödinger equation (1.2), a second-order partial differential equation of many variables, cannot in principle be solved exactly because of its complexity due to electron-electron interaction. Straightforward approximate solutions are sought within the Hartree- and Hartree-Fock theory [12, 13, 14] and their extensions, developed steadily since the early days of wave mechanics in the 1920s. The Hartree theory expresses the many-particle wave function Ψ in terms of a simple product of one-electron orbitals, while on the Hartree-Fock level this is generalised to a Slater determinant of spin orbitals. The determinant form ensures that the solution be antisymmetric with respect to particle exchange, as dictated by the Fermi statistics. The Hartree-Fock theory thus treats particle exchange interactions correctly while it does not, however, describe *correlation effects*, i.e., further many-particle effects. Extensions to the single-determinant HF theory invoke a linear combination of many different Slater determinants to describe *configuration interaction* between different states. The highest accuracy solutions of this type achievable nowadays involve up to 10^9 determinants. As a result of the mutual interaction of all electrons across the whole configuration space of spatial and spin variables, the computational complexity is exponential in the number of electrons. Therefore, the excellent accuracy of wave function methods comes at an insurmountably steep price tag when the number of atoms exceeds about 10–20.

Density functional theory (DFT) provides a radically different approach by recasting the basic problem in terms of the electron density [15]. The spin-free density in terms of the wave function can be formally defined as follows:

$$n(\boldsymbol{r}) = \sum_{s_1 \ldots s_N} \int \Psi^*(\boldsymbol{r}s_1, \boldsymbol{r}_2 s_2, \ldots \boldsymbol{r}_N s_N) \Psi(\boldsymbol{r}s_1, \boldsymbol{r}_2 s_2, \ldots \boldsymbol{r}_N s_N)\, \mathrm{d}\boldsymbol{r}_2 \ldots \mathrm{d}\boldsymbol{r}_N\,. \tag{1.7}$$

The concept of employing the electron density in an energy functional dates back to the Thomas-Fermi theory [16, 17], which has been reviewed by Lieb [19] and Jones and Gunnarsson [5].

With the appropriate approximations devised since its inception in 1964, DFT has paved the way for the successful modelling of ever larger systems. Walter Kohn, as one of the fathers of DFT, has been honoured "for his development of the density-functional theory", by the award of the 1998 Nobel Prize in Chemistry [20], jointly with John Pople "for his development of computational methods in quantum chemistry".

1.2 The density as basic variable

At the heart of DFT stand two rigorous mathematical statements. The first is a lemma linking the density and the potential of a Hamiltonian, and the second is a theorem about the existence of a universal functional of the electron density describing the ground state energy of a system of N electrons within an external potential. The theorem will be discussed in a moment. First, here is the lemma:

Lemma 1 (Basic Lemma of Hohenberg-Kohn) *The ground state density $n(\boldsymbol{r})$ of a bound system of a fixed number of interacting electrons in an external potential $V_{\text{ext}}(\boldsymbol{r})$ determines this potential uniquely (to within an additive constant).*

The proof (for non-degenerate ground states) is rather simple and need not be repeated here. Suffice to say that it represents the density in terms of wave functions, invokes the Rayleigh-Ritz principle[2] and proceeds by *reductio ad absurdum*. The lemma is mathematically exact and holds for any density, including any one of degenerate states, as shown later by Kohn [22] and others [6].

Since the density determines the potential, it establishes the full Hamiltonian of the system, and hence, determines *all* physical quantities derived through $\widehat{H}$, including the many-particle eigenstates $\Psi^{(n)}(\{x_i\})$ of the Schrödinger equation.

One issue remains to be resolved in a satisfactory manner, namely, that not all well-behaved positive functions $n(\boldsymbol{r})$ are indeed the ground state density corresponding to *some* external potential $V_{\text{ext}}(\boldsymbol{r})$, as has been demonstrated by example independently by Levy and Lieb [23, 24]. This so-called *v-representability problem* is mostly a formal one, with little impact on the applicability of DFT for real systems.

It should be noted that the basic lemma does *not* hold in its generalisation to spin-dependent density functional-theory, as was pointed out early on by von Barth and Hedin [25] and clarified recently by Eschrig [26]. The Levy/Lieb formulation, as shown below, does away with the requirement of a unique mapping of density to potential.

1.3 The Hohenberg-Kohn variational principle

For the study of molecules and solids our primary interest is the total energy of a given arrangement of atoms; ultimately, we want to find, within suitable boundary conditions, the *atomic* arrangement that is lowest in total energy and hence the most

[2] An introductory discussion of the Rayleigh-Ritz minimal principle is given, e.g., in Ref.[21].

stable. Besides contributions from the internuclear interactions, this task requires knowledge of the energy of the electronic system.

The Schrödinger equation is essentially an eigenvalue problem in the space of normalised wave functions. The lowest eigenvalue, representing the ground state energy, may be found from the Rayleigh-Ritz principle (cf. footnote 2 on the preceding page). In the original work by Hohenberg and Kohn [15] this principle was reformulated in terms of trial densities. A refined description, known as the *constrained search method*, was given later by Levy and Lieb [23, 24] as follows.

For a physical system, a given density determines, by Lemma 1, its external potential, and therefore, the Hamiltonian and thus, in turn, by the Schrödinger equation (1.2), the many-particle wave function $\Psi(\{\boldsymbol{r}_i\})$. Hence, the latter is strictly a functional of $n(\boldsymbol{r})$, albeit not a trivial one. Accordingly, Levy and Lieb define $\Psi(\{\boldsymbol{r}_i\})$ as minimum of a universal functional of a trial density as

$$F[\tilde{n}(\boldsymbol{r})] = \min_{\widetilde{\Psi}\to\tilde{n}} \langle \widetilde{\Psi} | \widehat{T} + \widehat{U} | \widetilde{\Psi} \rangle \,, \tag{1.8}$$

where $\widehat{T}$ and $\widehat{U}$ are the operators of the kinetic energy and the Coulomb repulsion of the interacting many-electron system, respectively. $\widetilde{\Psi}$ extends over the class of wave functions yielding the argument density $\tilde{n}$. The functional $F[\tilde{n}]$ is universal in the sense that it does not refer to an external potential. By Lemma 1, V_{ext} is fixed for a given density. Therefore, $F[\tilde{n}]$ also minimises, within the space of trial wave functions reproducing the particular argument density $\tilde{n}(\boldsymbol{r})$, the total energy functional

$$E[\tilde{n}(\boldsymbol{r})] = \int V_{\text{ext}}(\boldsymbol{r})\tilde{n}(\boldsymbol{r}) \, \mathrm{d}\boldsymbol{r} + F[\tilde{n}(\boldsymbol{r})] \,. \tag{1.9}$$

The key difference between this definition and the original formulation [15] is, that $F[\tilde{n}]$ is defined for all "N-representable" densities $\tilde{n}(\boldsymbol{r})$, whether "$V$-representable" or not.

A second minimisation step, now in the space of all densities for which the functional $F[\tilde{n}]$ is defined, finally minimises (1.9) for *all* normalised densities $\tilde{n}$ by the following theorem:

Theorem 1 (Hohenberg-Kohn variational principle) *For all N-representable densities the functional (1.9) has a minimum, which it assumes at the ground state density n_{GS}.*

$$E[\tilde{n}(\boldsymbol{r})] \geq E_{\text{GS}} \,, \qquad E_{\text{GS}} = \min_{\tilde{n}(\boldsymbol{r})\to N} E[\tilde{n}(\boldsymbol{r})] = E[n_{\text{GS}}(\boldsymbol{r})] \,. \tag{1.10}$$

As for Lemma 1, the theorem also holds for any one of a number of possibly degenerate ground state densities.

The electronic ground state energy of a system of interacting electrons is thus rigorously expressed in terms of their spatial charge density instead of the many-particle wave function.

1.4 The Kohn-Sham equations

The difficulties in finding the energy and ground state density of a system of interacting electrons according to (1.10) are formidable. Most prominently, the functional $F[\tilde{n}(\boldsymbol{r})]$ is not explicitly known.

Kohn and Sham (KS) suggested in 1965 [27] a separation of $F[\tilde{n}(\boldsymbol{r})]$ into appropriate major components:

$$F[n(\boldsymbol{r})] = T_0[n(\boldsymbol{r})] + E_H[n(\boldsymbol{r})] + E_{xc}[n(\boldsymbol{r})]\,. \tag{1.11}$$

The components are:

- $T_0[n(\boldsymbol{r})]$ is the kinetic energy functional for a fictitious system of *non-interacting* electrons producing the same density as $n(\boldsymbol{r})$.
- $E_H[n(\boldsymbol{r})]$ is the so-called Hartree energy, arising classically from the mutual Coulomb repulsion of all electrons,

$$E_H[n(\boldsymbol{r})] = \frac{1}{2}\iint \frac{n(\boldsymbol{r})n(\boldsymbol{r}')}{|\boldsymbol{r}-\boldsymbol{r}'|}\,\mathrm{d}\boldsymbol{r}\,\mathrm{d}\boldsymbol{r}'\,. \tag{1.12}$$

- The last term, $E_{xc}[n(\boldsymbol{r})]$, called the *exchange-correlation functional*, is a correction term, which accounts for all many-body effects in $F[n(\boldsymbol{r})]$. The treatment of this term decides upon the viability of any DFT implementation. Equation (1.11) is the *definition* of $E_{xc}[n(\boldsymbol{r})]$.

The Hohenberg-Kohn functional (1.9) now takes the form:

$$E_{\mathrm{KS}}[n(\boldsymbol{r})] = T_0[n(\boldsymbol{r})] + \int V_{\mathrm{ext}}(\boldsymbol{r})n(\boldsymbol{r})\,\mathrm{d}\boldsymbol{r} + \frac{1}{2}\iint \frac{n(\boldsymbol{r})n(\boldsymbol{r}')}{|\boldsymbol{r}-\boldsymbol{r}'|}\,\mathrm{d}\boldsymbol{r}\,\mathrm{d}\boldsymbol{r}' + \\ + E_{xc}[n(\boldsymbol{r})]\,. \tag{1.13}$$

All terms but the last of the preceding equation are known analytically. As inheritance from the Hohenberg-Kohn functional, the functional form of the correction term $E_{xc}[n(\boldsymbol{r})]$ is still unknown and must be approximated. Practical applications of the DFT are classified according to the approximations taken for the exchange-correlation functional E_{xc}. Details are discussed in Appendix B.

In order to describe the kinetic energy functional $T_0[n(\boldsymbol{r})]$, KS instituted single-particle orbitals $\Phi_i(\boldsymbol{r})$ representing the density. The orbitals are normalised as

$$\langle\Phi_i|\Phi_i\rangle = \int |\Phi_i(\boldsymbol{r})|^2\,\mathrm{d}\boldsymbol{r} = 1\,. \tag{1.14}$$

Janak [28] introduced normalised occupation numbers n_i as follows:

$$n(\boldsymbol{r}) = \sum_{i=1}^{occ} n_i|\Phi_i(\boldsymbol{r})|^2\,; \qquad N = \sum_{i=1}^{occ} n_i\,. \tag{1.15}$$

In the general, spin-unrestricted case, the label i spans spin variables, and the occupation numbers are 0 or 1. However, in a spin-restricted formalism, the occupation numbers represent orbitals occupied by two electrons of equal and opposite spin and are then integers between 0 and 2. By extension, small thermal excitations may be modelled through fractional occupation numbers subject to a Fermi-Dirac distribution, $n_i = f(\varepsilon_i)$. Janak notes that the energy functional (1.13) is represented correctly only for these limited cases, and not for arbitrary sets of n_i.

The kinetic energy in the KS formulation is now written in terms of an expectation value over the single-particle orbitals, $T_0[n(\boldsymbol{r})] \approx T[\{\Phi_i\}]$, with

$$T[\{\Phi_i\}] = \sum_{i=1}^{occ} n_i \left\langle \Phi_i \left| -\frac{\Delta}{2} \right| \Phi_i \right\rangle = \sum_{i=1}^{occ} n_i \int \Phi_i^*(\boldsymbol{r}) \left[-\frac{\Delta}{2} \right] \Phi_i(\boldsymbol{r}) \, \mathrm{d}\boldsymbol{r} \,. \tag{1.16}$$

With the preceding substitution, the ground state energy of the functional (1.13), subject to the normalisation constraint (1.14), is found through the Euler-Lagrange formalism. With the Lagrange parameters designated ε_i, the variation at the ground state energy must vanish:

$$\frac{\delta}{\delta \Phi_i^*(\boldsymbol{r})} \left\{ E[n(\boldsymbol{r})] + \sum_{i=1}^{occ} n_i \varepsilon_i \left[1 - \int |\Phi_i(\boldsymbol{r})|^2 \, \mathrm{d}\boldsymbol{r} \right] \right\} = 0 \,; \quad \forall i \,. \tag{1.17}$$

Noting that $\dfrac{\delta n(\boldsymbol{r})}{\delta \Phi_i^*(\boldsymbol{r})} = 2\Phi(\boldsymbol{r})$ one can carry out the variation straightforwardly and obtains:

$$\left[-\frac{\Delta}{2} + V_{\mathrm{ext}}(\boldsymbol{r}) + V_H([n(\boldsymbol{r})], \boldsymbol{r}) + V_{xc}([n(\boldsymbol{r})], \boldsymbol{r}) \right] \Phi_i(\boldsymbol{r}) = \varepsilon_i \Phi_i(\boldsymbol{r}) \,; \quad \forall i \,. \tag{1.18}$$

This set of equations, supplemented by the density definition (1.15), is called the *Kohn-Sham equations.*

Equation (1.18) is an eigenvalue equation for the ε_i and their eigenfunctions $\Phi_i(\boldsymbol{r})$. It has the form of a single-particle Hartree equation,

$$\left[-\frac{\Delta}{2} + V_{\mathrm{eff}}([n(\boldsymbol{r})], \boldsymbol{r}) \right] \Phi_i(\boldsymbol{r}) = \varepsilon_i \Phi_i(\boldsymbol{r}) \,, \tag{1.19}$$

with an effective potential

$$V_{\mathrm{eff}}([n(\boldsymbol{r})], \boldsymbol{r}) = V_{\mathrm{ext}}(\boldsymbol{r}) + V_H([n(\boldsymbol{r})], \boldsymbol{r}) + V_{xc}([n(\boldsymbol{r})], \boldsymbol{r}) \,, \tag{1.20}$$

yet it describes, through V_{xc}, in a formally exact manner the interacting electron system including many-body effects.

The classical contribution to $V_{\mathrm{eff}}(\boldsymbol{r})$ due to the Coulomb interaction is called the Hartree potential:

$$V_H([n(\boldsymbol{r})], \boldsymbol{r}) = \frac{\delta E_H[n(\boldsymbol{r})]}{\delta n(\boldsymbol{r})} = \int \frac{n(\boldsymbol{r}')}{|\boldsymbol{r} - \boldsymbol{r}'|} \, \mathrm{d}\boldsymbol{r}' \,, \tag{1.21}$$

and contributions due to the Pauli repulsion, correlation, and the interaction contribution in the kinetic energy are expressed by the exchange-correlation potential

$$V_{xc}([n(\boldsymbol{r})],\boldsymbol{r}) = \frac{\delta E_{xc}[n(\boldsymbol{r})]}{\delta n(\boldsymbol{r})}\,. \tag{1.22}$$

Both contributions are local potentials, though they depend functionally on the entire density distribution.

1.5 Solutions to the Kohn-Sham equation

An analytic solution of the Kohn-Sham equation (1.18) is quite unattainable. Instead, the unknown functions $\Phi_i(\boldsymbol{r})$ are sought numerically employing routine tools from the arsenal of mathematical physics. Two classes of approaches will yield a solution: (a) real-space grid methods and (b) basis function expansions. Either approach will transform the differential equation for the unknown functions into a set of algebraic ones for unknown grid values or expansion coefficients.

Grid methods have not really been successful so far because the amplitude of the solution typically varies over several orders of magnitude in space and thus presents a great deal of numerical difficulty. Though this initial obstacle was overcome through the use of adaptive curvilinear coordinates [29, 30, 31], much room for improvement remains. Currently, the field experiences a renaissance spurred by the growth in computing power and a drive towards parallelisation because of the inherent real-space separability of grid-based algorithms [32, 33].

Still, the more established tools are basis function methods. The general expansion of the one-electron wave functions reads:

$$|\Phi_i\rangle = \sum_{\nu=1}^{N} C_{i\nu}|\varphi_\nu\rangle\,; \quad \forall i\,. \tag{1.23}$$

The unknown functions Φ_i are thus represented by their expansion- or Fourier-coefficients $C_{i\nu}$. In principle, the basis set $\{|\varphi_\nu\rangle\}$ ought to be complete within the configuration space. In practice, one strives to use a basis as small as possible in order to reduce the computational effort in determining its Fourier coefficients.

Which basis set to use depends on the type of problem investigated. For periodic structures of solids, one often employs plane waves. Plane wave functions are easy to handle mathematically, because they are tightly knit to the Bloch paradigm. For non-periodic structures, i.e., molecules and clusters, a great number of plane waves is required to represent the strictly localised density distributions. Thus, for finite systems, atomiclike basis sets are more popular.

Once a basis has been chosen, the Hamilton operator must be expressed within such basis as a matrix. Applying the expansion (1.23), the Kohn-Sham equation (1.18) reads:

$$\widehat{H}|\Phi_i\rangle = \sum_{\nu=1}^{N} \widehat{H}C_{i\nu}|\varphi_\nu\rangle = \sum_{\nu=1}^{N} \varepsilon_i C_{i\nu}|\varphi_\nu\rangle = \varepsilon_i|\Phi_i\rangle\,; \quad \forall i\,. \tag{1.24}$$

Through multiplication on the left with any one $\langle\varphi_\mu|$ and utilising the linearity of the matrix operator one obtains a generalised hermitian eigenvalue problem:

$$\sum_{\nu=1}^{N} C_{i\nu}\left(h_{\mu\nu} - \varepsilon_i s_{\mu\nu}\right) = 0\,; \quad \forall i,\mu\,, \tag{1.25}$$

with the matrix elements

$$\begin{array}{rcccl} h_{\mu\nu} & = & \langle\varphi_\mu|\widehat{H}|\varphi_\nu\rangle & = & \int \varphi_\mu^*(\boldsymbol{r})\left[-\frac{\Delta}{2} + V_{\text{eff}}([n(\boldsymbol{r})],\boldsymbol{r})\right]\varphi_\nu(\boldsymbol{r})\;\mathrm{d}\boldsymbol{r} \\ s_{\mu\nu} & = & \langle\varphi_\mu|\varphi_\nu\rangle & = & \int \varphi_\mu^*(\boldsymbol{r})\varphi_\nu(\boldsymbol{r})\;\mathrm{d}\boldsymbol{r}\,. \end{array} \tag{1.26}$$

The matrices **h** and **s** are termed Hamilton- and overlap-matrix, respectively. They depend on the atomic positions and on a well-guessed density $n(\boldsymbol{r})$. After the matrices have been established, eq. (1.25) may be solved using standard mathematical methods. The solutions comprise the eigenvalues ε_i and eigenvectors $C_{i\nu}$.

Since the orbital solution depends on the density, and in turn, by eq. (1.15), on the orbitals themselves, equation (1.25) needs to be solved *self-consistently*. One starts with a suitable input density $n^0_{\text{in}}(\boldsymbol{r})$, constructs the effective potential $V_{\text{eff}}[n(\boldsymbol{r})]$ through proper approximations, solves eq. (1.25) for the orbitals $\Phi_i(\boldsymbol{r})$, and obtains a density $n^0_{\text{out}}(\boldsymbol{r})$, which is used as new input density $n^1_{\text{in}}(\boldsymbol{r})$. Refined procedures construct $n^j_{\text{in}}(\boldsymbol{r})$ from a weighted mixture of one or more previous densities. This procedure must be iterated until the input and output densities agree to within a certain precision.

Upon convergence related physical observables like atomic charges, dielectric functions or vibrational properties may be extracted, although some of these only at considerable additional effort. The basic electronic structure problem, however, is thus solved.

1.5.1 The Kohn-Sham total energy

It is instructive to write the total energy in terms of the Lagrange parameters ε_i. To this end, it follows from their eigenvalue equation (1.19) after multiplication with $\Phi_i^*(\boldsymbol{r})$ and integration,

$$\int \Phi_i^*(\boldsymbol{r})\left[-\frac{\Delta}{2} + V_{\text{eff}}(\boldsymbol{r})\right]\Phi_i(\boldsymbol{r})\;\mathrm{d}\boldsymbol{r} = \varepsilon_i\,\langle\Phi_i|\Phi_i\rangle = \varepsilon_i\,, \tag{1.27}$$

where the orbital normalisation constraints (1.14) were used. Multiplication with n_i and summation yields

$$\sum_{i}^{occ} n_i \int \Phi_i^*(\boldsymbol{r})\left[-\frac{\Delta}{2} + V_{\text{ext}}(\boldsymbol{r}) + V_H(\boldsymbol{r}) + V_{xc}(\boldsymbol{r})\right]\Phi_i(\boldsymbol{r})\;\mathrm{d}\boldsymbol{r} = \sum_{i}^{occ} n_i\varepsilon_i\,. \tag{1.28}$$

Considering the expressions for the total density, eq. (1.15) and the kinetic energy, eq. (1.16), the preceeding equation already looks very similar to the Kohn-Sham energy functional (1.13), except for some unbalanced potential contributions. To restore $E_{\text{KS}}[n(\boldsymbol{r})]$, the following additive corrections are required:

$-\frac{1}{2}\int V_H(\boldsymbol{r})n(\boldsymbol{r})\,\mathrm{d}\boldsymbol{r} + E_{xc} - \int V_{xc}(\boldsymbol{r})n(\boldsymbol{r})\,\mathrm{d}\boldsymbol{r}$. Thus, the Kohn-Sham ground state energy in terms of the eigenvalues is given by

$$E_{\mathrm{KS}}[n(\boldsymbol{r})] = \sum_{i=1}^{occ} n_i\varepsilon_i - \frac{1}{2}\int V_H(\boldsymbol{r})n(\boldsymbol{r})\,\mathrm{d}\boldsymbol{r} + E_{xc}[n(\boldsymbol{r})] - \int V_{xc}(\boldsymbol{r})n(\boldsymbol{r})\,\mathrm{d}\boldsymbol{r}\,. \tag{1.29}$$

The first term on the right-hand-side includes most of the electronic shell structure effects that arise from the exact treatment of the kinetic energy within the KS formulation.[3] The additive terms are collectively known as *double-counting corrections*.

One might wish to assign a physical meaning to the Lagrange parameters ε_i. A straightforward interpretation, known as Janak's Theorem [28], is derived from equation (1.29) for the minimising density:

$$\frac{\partial E}{\partial n_i} = \varepsilon_i\,. \tag{1.30}$$

For the highest occupied electronic levels this relation is often interpreted as an approximation to true ionisation energies. However, it must be recalled that the relation stems from a fictitious one-electron system. Almbladh and von Barth [35] however, have given a proof that the highest occupied eigenvalue for isolated systems does indeed equal the exact ionisation potential.

1.5.2 Charges and forces

In the chosen basis, the density matrix operator $\widehat{n}(\boldsymbol{r},\boldsymbol{r}')$ takes the following form:

$$\widehat{n} = \sum_{i}^{occ} n_i|\Phi_i\rangle\langle\Phi_i| = \sum_{\mu,\nu}\sum_{i}^{occ} n_i C^*_{i\mu}C_{i\nu}|\varphi_\mu\rangle\langle\varphi_\nu|\,, \tag{1.31}$$

with

$$P_{\mu\nu} = \sum_{i}^{occ} P^i_{\mu\nu} = \sum_{i}^{occ} n_i C^*_{i\mu}C_{i\nu} \tag{1.32}$$

being the elements of the density matrix, which may be further subdivided into their contributions $P^i_{\mu\nu}$ from individual eigenstates i, as shown.

The spatial charge density is given by (cf. eq. (1.15)):

$$n(\boldsymbol{r}) = \langle\boldsymbol{r}|\widehat{n}|\boldsymbol{r}\rangle = \sum_{\mu}\sum_{\nu} P_{\mu\nu}\varphi^*_\mu(\boldsymbol{r})\varphi_\nu(\boldsymbol{r})\,. \tag{1.33}$$

Energy-resolved charge densities $n(\boldsymbol{r},\varepsilon_i)$ are obtained by using the density matrix of the individual eigenstates, $P^i_{\mu\nu}$.

[3] Only for this purpose were the single-particle orbitals introduced [34].

To obtain the total energy within the Born-Oppenheimer approximation, the internuclear Coulomb repulsion and the classical kinetic energy for the nuclei must be added to the KS energy considered so far:

$$\begin{aligned} E_{\mathrm{tot}} &= E_{\mathrm{KS}} + E_{\mathrm{nuc}} + E_{\mathrm{K}} \\ &= E_{\mathrm{KS}}[n(\boldsymbol{r}); \{\boldsymbol{R}_a\}] + \frac{1}{2} \sum_{a}^{N_{\mathrm{at}}} \sum_{b \neq a}^{N_{\mathrm{at}}} \frac{Z_a Z_b}{|\boldsymbol{R}_a - \boldsymbol{R}_b|} + \sum_{a}^{N_{\mathrm{at}}} \frac{m_a}{2} \dot{\boldsymbol{R}}_a^2 \,. \end{aligned} \tag{1.34}$$

Since the KS energy depends parametrically on the positions of the atoms, cf. (1.6), the nuclei can be seen as moving in a potential $V = E_{\mathrm{KS}} + E_{\mathrm{nuc}}$. The dependence of the total energy on atomic coordinates has the meaning of forces. This leads to a classical equation of motion according to Newton's law:

$$\boldsymbol{F}_a = -\frac{\partial}{\partial \boldsymbol{R}_a} \left(E_{\mathrm{KS}} + E_{\mathrm{nuc}} \right) = m_a \ddot{\boldsymbol{R}}_a \,, \quad a = 1 \ldots N_{\mathrm{at}} \tag{1.35}$$

In general, the forces may be obtained analytically from the eigenstates $\{C_{i\mu}\}$ at modest computational cost; however, for complicated Hamiltonians, numerical derivatives must be resorted to. The forces may either be used for molecular dynamics runs integrating Newton's equation of motion or for quasistatic minimisations of the total energy as function of atomic positions. This matter has been broadly reviewed by Payne [36]. Because the kinetic energy is irrelevant for minimisation procedures, the term *total energy* is occasionally used in this context to cover just the sum of the KS energy and the internuclear repulsion.

Chapter 2

The DFTB Method

The preceding chapter attempted to give an overview on the background and formalism of the density-functional theory. Evidently, a full-potential self-consistent solution of the Kohn-Sham equations demands considerable computational resources. This demand may be satisfied up to certain practical limits from the as yet uninhibited growth in capacity of computational hardware characterising our era [37]. In the 1980s, using the machines *en vogue*, the complete and precise electronic structure of molecules or crystals with at most a handful of unique atoms could be calculated. Today, at the beginning of the new century, that number has risen to around 100, encompassing such exciting systems as biological molecules, fullerene cages, new superconductors or zeolites.

A great many problems exist beyond the reach of full *ab initio* DFT. This includes, for instance, structural simulations of amorphous materials, or surfaces and interfaces of crystals and their interaction with ad-species–which forms a major part of this work. Also, the study of smaller systems on long timescales necessitates approximations. These methods retain part of the quantum mechanical description, and they are therefore referred to as *semi-empirical* methods.

Even larger systems and timescales call for the use of empirical potentials [38]. These are simplified mathematical expressions fitted to represent the complex quantum mechanical interactions between atoms. Of course, the price to pay for the use of approximative methods is their limited transferability to systems beyond their fitting database. Nonetheless, appropriate questions may be answered for problems like the structure of enzymes in biology, statistical growth simulations in physical chemistry, and multiple-phase systems or the study of crack propagation for materials science.

2.1 Historical sketch

The method employed in this thesis is called density-functional based tight-binding (DFTB) and belongs to the semi-empirical category. It is similar to empirical tight-binding [39] but replaces, as its main characteristic, the empirical fitting procedure for matrix elements by a well-defined integration process.

Before the method is presented mathematically, a brief historical outline is called for, given that its origins date back more than 15 years by now. The definitive review of the method, its background, and applications can be found in Ref. [40], which is much more accessible today than are the original sources.

DFTB emerged from a fully self-consistent linear combination of atomic orbitals (LCAO) model by Eschrig et al. [41, 42]. This approach is characterised as follows:

- Expansion of (a) basis functions, (b) molecular density, and (c) molecular potential into Slater-Type functions (STF).
- Split of the molecular problem into formally independent *atomic* Kohn-Sham problems and their self-consistent solution.
- Calculation of *molecular* orbitals within a valence-basis which is *implicitly* orthogonalised to all core functions. Formally, this may be represented by a pseudo-potential approach. The valence basis itself is non-orthogonal.

Seifert et al. [43] retained the essential points but suggested several approximations to simplify and greatly speed up the calculation as follows:

- *non*-self-consistent treatment of the molecular problem.
- Superposition of the (fixed) potential of neutral atoms as molecular potential.
- Neglection of certain integrals for the calculation of Hamiltonian matrix elements.

In the early 1990s, the method was applied with great success to relatively large atomic systems, notably, amorphous carbon [44]. To describe the total and cohesive energy of such systems and to facilitate molecular dynamics, the following modification was necessary:

- Introduction of an atomic short-range repulsive potential to include (screened) core-core interactions.

In the mid-1990s, Porezag et al. [45, 46] put the basis set generation under intense scrutiny and refined the procedure as follows:

- Improvement of the initial molecular density guess by employing a *confinement potential* in the self-consistent pseudo-atom calculation. A similar auxiliary potential had been proposed early on by Eschrig, but it was applied to wave functions only, and was more geared toward solids rather than molecules.

Finally, Porezag and Elstner worked out a *self-consistent charge* (SCC) extension to the DFTB method as derived from of a second-order expansion of the Kohn-Sham energy w.r.t. atomic charge fluctuations. This extension is characterised as follows:

- Calculation of atomic Mulliken charges

- *ab initio* derivation of Hubbard-like parameters.
- Superposition of atomiclike *densities* instead of potentials for the calculation of exchange-correlation contributions to the two-centre Hamiltonian matrix elements.

The work on the theoretical foundations has not stood isolated, but was largely prompted by demands and shortcomings that became evident in the course of implementation and application of the method to real systems. Work in this class includes:

- Calculation of vibrational properties by Th. Köhler et al. [47].
- The calculation of infrared- and Raman-intensities by Porezag et al. [46, 48].
- The calculation of spatial charge densities to provide links to scanning tunnelling microscopy (STM) results on crystalline surfaces, by the author [49, 50].
- Linear-scaling formulation of the secular problem, by Stephan et al. [51, 52, 53] and the author [54]. The latter implementation is reviewed in Chapter 3 within the present work.

The work on the methodological improvement continues. The current and near-future developments involve the time-dependent description of excited states by Niehaus et al. [55, 56], and a spin-dependent formulation by Ch. Köhler et al. [57].

The introduction of new methodological aspects is but one part of the development of materials modelling. Another part concerns the actual implementation of the new methods in computer code and its documentation for users and developers. Original work in this respect goes back to H. Eschrig and G. Seifert. P. Blaudeck improved upon earlier programs and assembled a program version called `dylcao` around 1990, supplemented by analysis tools and viewers.

This program has been extended 1995–1997 by Haugk and Elstner to implement the self-consistent charge extensions. Significant changes to the file formats were introduced at this stage. This program version was called `dftb` and has since evolved into several branches with capabilities like the treatment of van der Waals interactions and time-dependent effects in DFT.

Since about 1992, G. Jungnickel maintained a separate development line pursuing a more monolithic design strategy, out of which arose the menu-driven programs `dylax` for the DFTB modelling and `statix` for structure file modifications, analysis and viewing. The main contribution was the capability for a full $\boldsymbol{k}$-point sampling of the Brillouin zone rather than a Γ-point only sampling.

This concludes the historical perspective. DFTB is now capable of modelling with sufficient accuracy the structure and properties of e.g. the bulk, surfaces and defects of crystalline semiconductors, as well as organic and inorganic molecules of medium complexity with absolute accuracies in the 1 eV range and relative accuracies down to 30 meV.

2.2 Variational approach and stationary principle

The previous section recounted a historical aspect of how DFTB was developed from a simplified description of the electronic structure of molecules to a full-fledged materials modelling method. The present section will now attempt to give a review of the mathematical derivation of the underlying formalism up to the self-consistent charge level, as seen from a modern perspective.

In DFT, the total energy of an atomic system is the energy of its electron distribution plus the ion-ion repulsion:

$$E_{\text{tot}} = E_{\text{KS}}[n(\boldsymbol{r})] + E_{\text{nuc}}(\{\boldsymbol{R}_a\})\,, \tag{2.1}$$

The latter is trivial to obtain:

$$E_{\text{nuc}}(\{\boldsymbol{R}_a\}) = \frac{1}{2}\sum_{a,b\neq a}^{M} \frac{Z_a Z_b}{|\boldsymbol{R}_a - \boldsymbol{R}_b|}\,. \tag{2.2}$$

The first term is the Kohn-Sham energy of an ideally self-consistent density distribution $n(\boldsymbol{r})$ as given by (1.29) in section 1.4. This density is obtained from an iterative solution of the Kohn-Sham equation (1.18). During the iteration, the potentials within the equation are calculated from a non-converged input density. The solutions of the Kohn-Sham equation are the orbitals $\Phi_i(\boldsymbol{r})$ which, together with an appropriate set of occupation numbers n_i, yield a new output density. As a last step for an iteration, the Kohn-Sham energy is evaluated. Usually, this involves both the input and output densities. For instance, the potentials of the double counting terms are functionals of the input density, but they are multiplied with the output density, as in the double-counting term $\int V_{xc}([n_{\text{in}}],\boldsymbol{r})n_{\text{out}}(\boldsymbol{r})\,\mathrm{d}\boldsymbol{r}$. It is quite possible to circumvent this heterogeneity. Brought to its conclusion, this eventually helps to formulate a non-self-consistent energy functional, cutting short the iteration cycle entirely. Harris [58] was one of the first authors to do this. He introduced a functional $\mathcal{E}[n_{\text{in}}]$ which solely uses the input density to evaluate the total-energy expression (1.29). This functional is not strictly *variational*, i.e., yielding energies above the ground state for non-converged densities, but at the ground state it is (a) equivalent to the Kohn-Sham functional and (b) *stationary*, which means deviations of the input density from the ground state density lead to energy deviations of second and higher order only. However, the sign of the quadratic term cannot be deduced *a priori*, as Harris points out. Later, Foulkes and Haydock [59, Sec. III] analysed the second-order term in more detail.

Foulkes and Haydock [59], wrote the Kohn-Sham functional (1.13) as:

$$E_{\text{KS}}[n(\boldsymbol{r})] = T_0[n(\boldsymbol{r})] + \mathcal{V}[n(\boldsymbol{r})] \tag{2.3}$$

with the potentials compounded in[1]

$$\mathcal{V}[n(\boldsymbol{r})] = \int V_{\text{ext}}(\boldsymbol{r})n(\boldsymbol{r})\,\mathrm{d}\boldsymbol{r} + \frac{1}{2}\int V_H([n],\boldsymbol{r})n(\boldsymbol{r})\,\mathrm{d}\boldsymbol{r} + E_{xc}[n(\boldsymbol{r})]\,. \tag{2.4}$$

[1] In Ref. [59], this term is denoted $F[n]$, in regrettable overlap with the universal functional $F[n]$ in the Hohenberg-Kohn formulation, eqs. (1.8) and (1.11). The latter encompasses $\widehat{T}$, but not V_{ext}.

The effective potential in the KS equations is just the functional derivative of $\mathcal{V}[n]$,

$$V_{\text{eff}}([n],\boldsymbol{r}) = \frac{\delta \mathcal{V}[n]}{\delta n} = V_{\text{ext}}(\boldsymbol{r}) + V_H([n],\boldsymbol{r}) + V_{xc}([n],\boldsymbol{r})\,. \tag{2.5}$$

With the kinetic energy operator denoted $\widehat{T} = -\frac{1}{2}\Delta$ for short, the *non*-self-consistent Kohn-Sham equations (1.19) for a given input density $n_{\text{in}}(\boldsymbol{r})$ read

$$\left(\widehat{T} + V_{\text{eff}}([n_{\text{in}}],\boldsymbol{r})\right)\Phi_i(\boldsymbol{r}) = \varepsilon_i \Phi_i(\boldsymbol{r})\,; \quad \forall i\,. \tag{2.6}$$

As solution, one obtains the one-electron eigenvalues ε_i and orbitals Φ_i, from which the output density is easily obtained using eq. (1.15) (with appropriate occupation numbers n_i):

$$n_{\text{out}}(\boldsymbol{r}) = \sum_i^{occ} n_i \int |\Phi_i(\boldsymbol{r})|^2 \;\mathrm{d}\boldsymbol{r}\,. \tag{2.7}$$

In the non-scf Harris functional, the output density itself does not enter. Employing just the eigenvalues of Eq. (2.6) the functional is defined as follows:

$$\mathcal{E}[n_{\text{in}}] = \sum_i^{occ} n_i\varepsilon_i - E_H[n_{\text{in}}] + E_{xc}[n_{\text{in}}] - \int V_{xc}([n_{\text{in}}],\boldsymbol{r}) n_{\text{in}}\;\mathrm{d}\boldsymbol{r}\,. \tag{2.8}$$

The form is similar to the Kohn-Sham total energy (1.29) functional for the ground state. Naturally, the question arises: *What is the deviation of $\mathcal{E}[n_{\text{in}}]$ from $E_{\text{KS}}[n_{\text{scf}}]$?* Foulkes and Haydock [59] concluded from a Taylor-expansion of $\mathcal{V}[n]$ that this deviation is of second order in the charge differences, $\Delta n(\boldsymbol{r}) = n_{\text{out}}(\boldsymbol{r}) - n_{\text{in}}(\boldsymbol{r})$, namely,[2]

$$\begin{aligned} E_{\text{KS}}[n_{\text{out}}] &= \mathcal{E}[n_{\text{in}}] + \mathcal{E}^{(2)}[n_{\text{in}},\Delta n] \\ &= \mathcal{E}[n_{\text{in}}] + \frac{1}{2}\iint \left.\frac{\delta^2\mathcal{V}[n]}{\delta n^2}\right|_{n_{\text{in}}} \Delta n(\boldsymbol{r})\Delta n(\boldsymbol{r}')\;\mathrm{d}\boldsymbol{r}\;\mathrm{d}\boldsymbol{r}'\,. \end{aligned} \tag{2.9}$$

For the kernel in the second-order term $\mathcal{E}^{(2)}[n_{\text{in}},\Delta n]$ one derives from eq. (2.5):

$$\frac{\delta^2\mathcal{V}[n]}{\delta n^2} = \frac{\delta V_{\text{eff}}([n(\boldsymbol{r}')],\boldsymbol{r})}{\delta n(\boldsymbol{r}')} = \frac{1}{|\boldsymbol{r}-\boldsymbol{r}'|} + \frac{\delta V_{xc}([n(\boldsymbol{r}')],\boldsymbol{r})}{\delta n(\boldsymbol{r}')} \tag{2.10}$$

The functional $\mathcal{E}[n_{\text{in}}]$ of eq. (2.8) forms the basis for the DFTB method. The method is implemented on two levels, called the "non-self-consistent" and "self-consistent charge" (SCC) versions. Both approaches start from a guess of the input density, $n_{\text{in}}(\boldsymbol{r}) \equiv n_0(\boldsymbol{r})$. In the non-scc approach, the Kohn-Sham equation is solved by a single iteration to obtain the eigenvalues and an improved density $n_{\text{out}}(\boldsymbol{r})$, which adapts the input density to the given arrangement of atoms. The SCC extension retains the second-order corrections $\mathcal{E}^{(2)}[n_0,\Delta n]$ by iteratively improving the charge fluctuations Δn, with $\Delta n(\boldsymbol{r}) \equiv n_{\text{out}}(\boldsymbol{r}) - n_0(\boldsymbol{r})$. Obviously, a good guess of the initial density is essential for the success of either approach. Both methods are efficient only due to a sequence of approximations, which is outlined in the next section.

[2] Note that this is not a Taylor-expansion of the Kohn-Sham energy itself because the functionals on the left and right side of the equation are different.

2.3 Approximations in DFTB

The DFTB method applies the stationary principle introduced above while making a number of approximations. These mostly take the form of separations into atomic contributions of global quantities like potentials, densities, and wave functions. This separation principle allows the effective treatment of compound atomic systems by building as much as possible upon preparatory work, which is performed beforehand on isolated subsystems of atoms and atom pairs. The preparatory calculations capsule the computationally demanding tasks of establishing the Hamiltonian matrix elements and double-counting terms into convenient functions and tables. The method itself has recently been reviewed in detail in Ref. [40]. The background, justification and tests of major developments were discussed at length by the respective authors [43, 45, 46, 60, 61].

Traditionally, the method is being presented in two separate stages, i.e., in its non-self-consistent formulation and the SCC extension. The present treatment attempts to give a unified view instead.

The main approximations to obtain the DFTB method from the stationary principle of DFT are in turn:

- superposition of pseudo-atomic densities as starting density
- minimal-basis, valence-only LCAO wave functions
- two-centre Hamiltonian (neglect of crystal-field and three-centre terms)
- repulsive pair potential for the double-counting and inter-nuclear energies
- for the second-order corrections:
  - monopole approximation and extrapolation of $\delta V_{xc}[n]/\delta n$
  - Mulliken charges

The total-energy expression of the DFTB approach is gathered from Eqs. (2.8) and (2.9) and written as follows:

$$\begin{aligned} E_{\mathrm{tot}}[n_0+\Delta n] &= \sum_i^{occ} n_i \langle \Phi_i | \widehat{H}^0 | \Phi_i \rangle + E_{\mathrm{rep}}[n_0] + \mathcal{E}^{(2)}[n_0, \Delta n] \\ &= E_{\mathrm{BS}} + E_{\mathrm{rep}} + E_{\mathrm{G}}\,, \end{aligned} \tag{2.11}$$

where

$$\widehat{H}^0 = \widehat{T} + V_{\mathrm{eff}}([n_0], \boldsymbol{r})\,. \tag{2.12}$$

The first energy term, the so-called band-structure energy E_{BS}, is the trace of a reference Hamiltonian $\widehat{H}^0$ over the one-electron eigenstates Φ_i of the system. The second term in Eq. (2.11), E_{rep}, constitutes a repulsion energy similar to standard tight-binding theory, which subsumes the double counting terms of the reference Hamiltonian, as well as the nuclear repulsion. Finally, the last term, E_{G}, describes atomic charge fluctuations and is subject to a self-consistency treatment.

2.3.1 Pseudo-atomic starting density

In DFTB, the starting density is chosen as superposition of slightly compressed densities of neutral atoms,

$$n_0(\boldsymbol{r}) = \sum_a n_0^a(\boldsymbol{r}_a)\,; \quad \boldsymbol{r}_a = \boldsymbol{r} - \boldsymbol{R}_a\,. \tag{2.13}$$

The densities of free atoms are too diffuse to be a good initial guess in compound systems. Compressed densities anticipate the density modification of free atoms when surrounded by other atoms in a solid or molecule. Furthermore, the limited range of the atomic density works better with a number of integral approximations discussed later. The densities are the result of a self-consistent LDA or GGA calculation[3] of *pseudo-atoms*, i.e., atoms placed within a weak parabolic constriction potential as expressed in a modified Kohn-Sham equation:

$$\left\{\widehat{T} + V_{\text{eff}}^{\text{at}}[n_0^a] + \left(\frac{r}{r_0}\right)^m\right\} \varphi_\nu^{\text{psat}}(\boldsymbol{r}) = \varepsilon_\nu^{\text{psat}} \varphi_\nu^{\text{psat}}(\boldsymbol{r})\,. \tag{2.14}$$

The constriction potential is characterised by its exponent m and range r_0. The exponent was shown to have rather small influence on the final results [46], so that $m = 2$ is usually used. For the range parameter, a number of calculations has lead to results with optimal transferability in covalent systems (barring $3d$ transition metals [62]) using $r_0 \approx 1.85\, r_{\text{cov}}$, where r_{cov} is the covalent radius of the given element.

Owing to the slightly empirical nature of using confined orbitals, there is some degree of arbitrariness as to which density and potential to choose for the calculation of the atomic orbitals and ultimately, the Hamiltonian matrix elements. Originally, in the approximate scheme by Seifert [43], the scf-potential of the *free* atom was used. Later, Porezag [46] modified the scheme to use the scf-potential of the *confined* atom, making the pseudo-atom calculation self-consistent. Finally, Elstner [60] suggested an intermediate approach using a *weakly confined* density resulting from an scf-potential with a density specific compression radius r_0^ϱ. This radius introduces, besides r_0, another parameter into the model, which is debatable on formal grounds. It does, however, provide an opportunity to improve upon covalent energies and geometries.

Table 2.1 on the next page summarises the calculation steps for the three schemes. All schemes obtain atomic orbital *energies* from an scf-calculation of the free atom, in the absence of any additional potential. Overall, the first and second scheme each require two stages of the pseudo-atom calculation, while the third one relegates the generation of wave functions to a third stage. Thus, the atomic orbitals in the latter scheme can be considered as one iteration step ahead of the atomic density, which is justifiable within the Foulkes-Haydock picture discussed in section 2.2.

In all schemes, the pseudo-atomic wave functions themselves are represented by Slater-type orbitals (STO) characterised by coefficients a_{ij} and exponents α_j:

$$\varphi_\nu(\boldsymbol{r}) \equiv \varphi_{nlm}(\boldsymbol{r}) = \sum_{i=1}^{5}\sum_{j=0}^{3} a_{ij} r^{l+j} e^{-\alpha_i r} Y_{lm}\left(\frac{\boldsymbol{r}}{r}\right)\,. \tag{2.15}$$

[3] cf. Appendix B.

Table 2.1: Summary of schemes for the DFTB pseudo-atom calculation of orbital energies ε_ν, effective (pseudo-)atomic potentials V_{eff}, atomic densities n_0^a, and basis functions φ_ν.

	Seifert [43]		Porezag [46]		Elstner [60]	
step	r_0/r_{cov}	*result*	r_0/r_{cov}	*result*	r_0/r_{cov}	*result*
	$(m=4)$		$(m=2)$		$(m=2)$	
1.	∞	$V_{\text{eff}}^{\text{at}}$, n_0^a, ε_ν	∞	ε_ν	∞	ε_ν
2.	≈ 1.85	φ_ν	≈ 1.85	$V_{\text{eff}}^{\text{psat}}$, n_0^a, φ_ν	$5\ldots14$	$V_{\text{eff}}^{\text{psat}}$, n_0^a
3.					≈ 1.85	φ_ν

The optimisation of the basis sets for the first- and second-row elements was discussed in depth in Ref. [46]. In the cited work the STO representation is used only externally. Internal to the pseudo-atom calculation, the STO-basis is in fact projected onto a set of contracted Gaussians (i.e., linear combinations of primitive Gaussians).

2.3.2 Tight-Binding integrals and the two-centre approximation

The pseudo-atomic basis set finds its application in the LCAO expansion of the eigenfunctions:

$$\Phi_i(\boldsymbol{r}) = \sum_a \sum_{\nu[a]} C_{i\nu}\varphi_\nu(\boldsymbol{r}_a)\,. \tag{2.16}$$

The reference Hamiltonian expressed in this basis gives matrix elements denoted $h^0_{\mu\nu}$ and non-orthogonal overlap elements $s_{\mu\nu}$:

$$\begin{aligned} h^0_{\mu\nu} &= \langle\varphi_\mu|\widehat{H}^0|\varphi_\nu\rangle &&= \int \varphi^*_\mu(\boldsymbol{r})\widehat{H}^0\varphi_\nu(\boldsymbol{r})\,\mathrm{d}\boldsymbol{r} \\ s_{\mu\nu} &= \langle\varphi_\mu|\varphi_\nu\rangle &&= \int \varphi^*_\mu(\boldsymbol{r})\varphi_\nu(\boldsymbol{r})\,\mathrm{d}\boldsymbol{r}\,. \end{aligned} \tag{2.17}$$

These integrals are calculated immediately following the pseudo-atom calculations and are tabulated as function of distance between the two centres. The integrals at general difference vectors as needed in the system, $\Delta\boldsymbol{R}_{ab} = \boldsymbol{R}_a - \boldsymbol{R}_b$, are transformed using well-known projection relations [39, 63]. Due to symmetry, only 10 integrals between basis functions remain nonzero for angular momenta up to $l = 2$. Their sequence as tabulated is, in standard molecular orbital notation:

$$\mathrm{dd}\sigma,\ \mathrm{dd}\pi,\ \mathrm{dd}\delta,\ \mathrm{pd}\sigma,\ \mathrm{pd}\pi,\ \mathrm{pp}\sigma,\ \mathrm{pp}\pi,\ \mathrm{sd}\sigma,\ \mathrm{sp}\sigma,\ \mathrm{ss}\sigma.$$

To achieve the above *two-centre* representation for the Hamiltonian matrix elements, the effective Kohn-Sham potential is formally decomposed into atomiclike contributions. Because the exchange-correlation potential is non-linear, there are two ways to do this in practice, either to sum atomic *potentials* or atomic *charges*:

$$V_{\text{eff}}([n_0],\boldsymbol{r}) \approx \begin{cases} \sum_c V_c^0([n_c^0(\boldsymbol{r}_c],\boldsymbol{r}_c) & \text{“potential superposition”} \\ V_{\text{eff}}\left(\sum_c n_c^0(\boldsymbol{r}_c)\right) & \text{“density superposition”} \end{cases} \tag{2.18}$$

Table 2.2: Integral types in the DFTB Hamiltonian $h^0_{\mu\nu}$ according to eq. (2.17). Centres a and b denote orbital centres, with basis functions $\mu \in a$, $\nu \in b$, and c is the potential centre.

Type	Classification	Centres	Status
(A)	onsite-terms	$a = b = c$	retained
(B)	crystal-field terms	$a = b \neq c$	neglected
(C)	two-centre terms	$a \neq b$, $c = a$ or $c = b$	retained
(D)	three-centre terms	$c \neq a \neq b \neq c$	neglected

The potential superposition was applied in the original schemes by Seifert and Porezag, while the density superposition was later introduced by Elstner.

Depending on the centres involved for the basis functions and the potential, the Hamiltonian matrix elements fall into a number of categories, which are summarised in Table 2.2. As indicated, a number of these integrals are neglected in either approach. Besides, a *valence-only* basis is used, which implies a core-valence orthogonalisation between different centres. The neglect of three-centre terms provides the largest formal and practical simplification because on the one hand the handling for three centres is more involved than for two centres and on the other hand there are many more combinations. Conversely, the crystal-field integrals are relatively simple and appear to provide leverage for improvement. However, the integral neglections work only in concert because there is error-cancellation of a considerable degree. The justification of this process as a whole is complex and was discussed originally by Seifert et al. [43] and later reviewed in Ref. [40].

Among the retained integrals, type (A) represents onsite energies ε_ν of single atoms,

$$h^0_{\nu\nu} = \varepsilon_\nu \,, \tag{2.19}$$

which are obtained in the first step of the atom calculation discussed in the preceeding section. In the other remaining integral type (C), the potentials and densities of two distinct atoms are to be combined:

$$h^0_{\mu\nu} = \langle \varphi_\mu | \widehat{T} + \left\{ \begin{array}{l} V^0_a(\boldsymbol{r}_a) + V^0_b(\boldsymbol{r}_b) \\ V_{\text{eff}}([n^0_a + n^0_b], \boldsymbol{r}) \end{array} \right\} | \varphi_\nu \rangle \,; \quad a[\mu],\, b[\nu] \,. \tag{2.20}$$

The density superposition mode is coupled to a weaker density compression for pseudo atoms. A strong density compression, as implicit in the previous pseudo-atom scheme, would unsuitably limit the range of the effective potential in this case.

The use of weakly compressed densities in concert with the density superposition for the Hamiltonian matrix elements has lead to improved energies, vibrational frequencies and reaction barriers mainly for organic molecules [60]. There is evidence, however, that the band structures of crystalline systems are less well represented [62, 64] than in the potential superposition previously employed.

2.3.3 Repulsive potential

In the above description, the double-counting terms of the Kohn-Sham energy, evaluated at the input density, and the inter-nuclear repulsion are approximated as a

sum of short-ranged repulsive pair potentials:

$$E_{\mathrm{rep}}(n_0, \{\boldsymbol{R}_a\}) \approx \frac{1}{2} \sum_a \sum_{b \neq a} V_{\mathrm{rep}}^{ab} \left(|\boldsymbol{R}_a - \boldsymbol{R}_b| \right) \tag{2.21}$$

This approximation is justified by the following observations:

- With n_0 represented by neutral atomic fragments, there are no long-range Coulomb interactions in the combined electrostatic Hartree and nuclear contributions to the double counting energy, $E_H[\sum_a n_0^a] + E_{\mathrm{nuc}}(\{\boldsymbol{R}_a\})$, due to mutual screening. Furthermore, since the atomic starting densities are spherically symmetric, the Hartree integrals for atom pairs (1.12) depend on internuclear distance only. The same is trivially the case for the nuclear repulsion. Therefore, these contributions together are representable by short-range pair potentials without loss of accuracy.

- Contributions due to exchange and correlation are not separable into pair potential form *per se* because of the non-linearity of the *xc*-functional. However, a cluster expansion [40, 59] allows to extract two-body components. Its higher-order terms involve the overlap of the densities of three centres, which is negligible for the compressed starting densities used here. The remaining two-body terms may again be represented by pair-potentials.

All monomer contributions are contained within the atomic orbital energies ε_ν. This ensures that the repulsive potential actually goes to zero in the dissociation limit.

The repulsive potential is obtained from self-contained *ab initio* calculations of the energy of a set of reference molecules for a range of a typical bond length. Most conveniently, the reference molecules are dimers, but also methanelike structures. For solid state calculations, as in diamond, which is the subject of this study, crystal reference structures may be used. For each reference structure j, the energy difference

$$\widetilde{E}_{\mathrm{rep}}^j(r) = E_{\mathrm{scf}}^j(r) - E_{\mathrm{BS}}^j(r) \tag{2.22}$$

is calculated as function of distance r.

As a consequence of the concepts and approximations taken thus far, the set of repulsive energies has the following important properties:

- $\widetilde{E}_{\mathrm{rep}} > 0$. For small distances, i.e., close atoms, E_{rep} has a steep repulsive slope indicative of strong Pauli repulsion of the electron shells.

- It decays rapidly to zero between typical first- and second-neighbour distances. This is another indication that the pair-potential representation of the double-counting terms embodied within E_{rep}, is valid.

- Most importantly, $\widetilde{E}_{\mathrm{rep}}^j(r)$ for different molecules are close to each other. This property is indicative of the degree of *transferability* of the method, i.e., its applicability to a wide range of atomic structures, extending beyond the set of

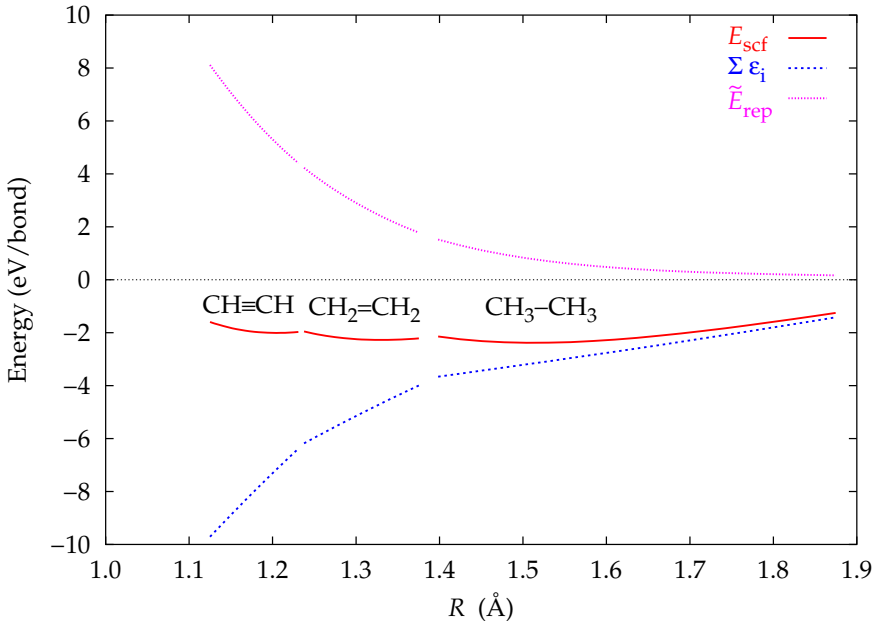

Figure 2.1: Example for generating the repulsive potential by eq. (2.22). The C–C bond for three different coordination numbers is scaled while the C–H bond lengths and -angles were kept fixed at their equilibrium values. SCF-data were produced using the Gaussian program. Data courtesy of M. Elstner [60]

reference molecules. It was found that $\widetilde{E}_{\mathrm{rep}}(r)$ for high-coordinated crystal phases such as fcc and bcc often does *not* coincide with the curve of other structures. Such phases cannot be treated with the present method.

For practical calculations, the set of repulsive energies are represented numerically by a polynomial or spline for each atom type combination. The polynomial has the form

$$V_{\mathrm{rep}}(r) = \sum_n a_n (R_c - r)^n\,, \quad r < R_c\,. \tag{2.23}$$

The cutoff radius R_c represents the distance beyond which the repulsive potential has subsided. R_c is typically chosen between 1.5—2 equilibrium bond lengths, and the polynomial coefficients a_n are fitted to $\widetilde{E}^j_{\mathrm{rep}}(r)$. As an alternative, a spline representation allows greater flexibility in this respect, at the price of a somewhat more complicated handling.

2.3.4 Second-order corrections

It remains to discuss the last term in the DFTB total-energy expression, the second-order correction $\mathcal{E}^{(2)}[n_0, \Delta n]$, or E_{G} (where "G" stands for γ, which is properly introduced below). This term becomes important in the simulation of heteroatomic molecules and polar semiconductors where chemical bonding is influenced considerably by charge transfer effects and long-range Coulomb interactions.

In line with previous procedures, the charge fluctuations Δn are decomposed into atomic contributions which are expected to decay rapidly with increasing distance from their centre. The second-order term then reads, using (2.9) and (2.10):

$$\mathcal{E}^{(2)}[n,\Delta n] = \frac{1}{2}\sum_{a,b}\iint\left[\frac{1}{|\boldsymbol{r}-\boldsymbol{r}'|}+\frac{\delta V_{xc}([n(\boldsymbol{r}')],\boldsymbol{r})}{\delta n(\boldsymbol{r}')}\right]_{n_0}\Delta n_a(\boldsymbol{r})\Delta n_b(\boldsymbol{r}')\;\mathrm{d}\boldsymbol{r}\;\mathrm{d}\boldsymbol{r}'\,. \quad (2.24)$$

The term is expected to contribute only a small part of the total energy, so that elaborate integrations can be forgone, in favour of quite crude approximations. First, one expresses Δn_a as a mere monopole contribution:

$$\Delta n_a(\boldsymbol{r}) = \sum_{lm} c^a_{lm}F^a_{lm}(r_a)Y_{lm}\left(\frac{\boldsymbol{r}_a}{r_a}\right) \approx \Delta q_a F^a_{00}(r_a)Y_{00}\,; \quad \boldsymbol{r}_a = \boldsymbol{r}-\boldsymbol{R}_a\,. \quad (2.25)$$

Thus, eq. (2.24) takes a rather simple matrix form, which shall be denoted E_G:

$$E_{\mathrm{G}} = \frac{1}{2}\sum_{a,b}^{M}\gamma_{ab}\Delta q_a\Delta q_b\,, \quad \text{with} \quad (2.26)$$

$$\gamma_{ab} = \iint\left[\frac{1}{|\boldsymbol{r}-\boldsymbol{r}'|}+\frac{\delta V_{xc}[n]}{\delta n(\boldsymbol{r}')}\right]_{n_0}F^a_{00}(r_a)F^b_{00}(r'_b)\frac{1}{4\pi}\;\mathrm{d}\boldsymbol{r}\;\mathrm{d}\boldsymbol{r}'\,. \quad (2.27)$$

The latter, so-called $\boldsymbol{\gamma}$ matrix, encapsulates the dependency of $\mathcal{E}^{(2)}$ on ionic positions. This matrix, except for the V_{xc} part, is well-known from the CNDO-formalism by Pople, Santry and Segal [65]. Density data enter in the form of known pseudo-atomic starting densities and orbital relaxation functions $F_{00}(r)$. If the latter are assumed to be fixed radial functions to be weighted by Δq_a, the only geometry parameter in γ_{ab} will be the interatomic distance $R = |\boldsymbol{R}_a - \boldsymbol{R}_b|$.

The limit $R \to 0$ represents coinciding atomic centres a and b. In this case, γ_{aa} equals a Hubbard-like parameter U_a for the atom. In chemical terminology, the Hubbard parameter is related to the chemical hardness $\eta_a \approx U_a/2$, which is a measure of the ionisation potential and electron affinity of the atom. Neglecting the influence of the environment and employing Janak's theorem [28], U_a is obtained non-empirically at the DFT level during the pseudo-atom calculation as the derivative of the HOMO of the free atom with respect to its occupation number:

$$\gamma_{aa} = U_a = \left.\frac{\partial^2 E_{\mathrm{at}}}{\partial q^2_{\mathrm{at}}}\right|_{q=q_0} = \frac{\partial\varepsilon^a_{\mathrm{HOMO}}}{\partial n_{\mathrm{HOMO}}}\,. \quad (2.28)$$

For convenience, Table 2.3 gives the values of γ_{aa} for frequently used elements.

In the limit of large interatomic distances, γ_{ab} reduces to a $1/R$ dependency, since xc interactions vanish in this case. To obtain a continuous transition between the limits of small and large interatomic distances, various interpolation formulae were used [66]. E.g., the one suggested by Ohno/Klopman [67, 68] reads:

$$\gamma_{ab}(U_a,U_b,R) = 1\Big/\sqrt{R^2+\frac{1}{4}\left(\frac{1}{U_a}+\frac{1}{U_b}\right)^2}\,. \quad (2.29)$$

H	Li	B	C	N	O	F	Si
11.06	4.69	8.05	9.91	11.71	13.46	15.18	6.74

Table 2.3: Chemical hardness U in V/e as defined by eq. (2.28) for free spin-unpolarised atoms as calculated within LSDA. Source: Porezag [46].

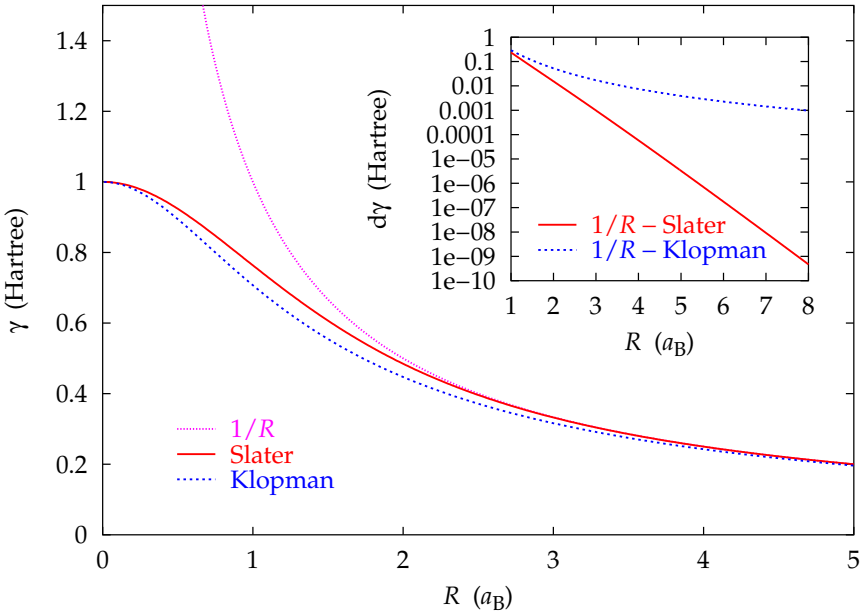

Figure 2.2: Comparison of the Klopman and Slater interpolation functions for the scc γ interaction, eqs. (2.29) and (2.31). The Hubbard parameter was $U_a = U_b = 1\,\mathrm{H}$. The inset shows the deviation of the interpolation formulae from the Coulomb behaviour on a logarithmic scale.

While illustrative and obvious in its behaviour for $R \to 0$ and $R \to \infty$, eq. (2.29) proved numerically unsuitable for periodic systems, since the asymptotic Coulomb-behaviour is reached only for distances much larger than common supercell sizes, see Fig. 2.2. A more stable behaviour is achieved by an integration of eq. (2.27) for known charge fluctuations, neglecting the V_{xc} term for the moment. Assuming a normalised Slater-type function with a range parameter τ_a,

$$n_a(r) = \frac{\tau_a^3}{8\pi} \mathrm{e}^{-\tau_a |\boldsymbol{r} - \boldsymbol{R}_a|} \,, \tag{2.30}$$

the Coulomb integral (1.12) of two such charge densities reads, after quite lengthy manipulations (for integrals of this type, see Pople and Beveridge [69, App. B]):

$$\gamma_{ab}(\tau_a, \tau_b, R) = \frac{1}{R} - \mathcal{S}(\tau_a, \tau_b, R) \,, \quad \text{with} \tag{2.31}$$

$$\begin{aligned} \mathcal{S}(\tau_a, \tau_b, R) &= \mathrm{e}^{-\tau_a R} \left(\frac{\tau_b^4 \tau_a}{2(\tau_a^2 - \tau_b^2)^2} - \frac{\tau_b^6 - 3\tau_b^4 \tau_a^2}{R(\tau_a^2 - \tau_b^2)^3} \right) + \\ &+ \mathrm{e}^{-\tau_b R} \left(\frac{\tau_a^4 \tau_b}{2(\tau_b^2 - \tau_a^2)^2} - \frac{\tau_a^6 - 3\tau_a^4 \tau_b^2}{R(\tau_b^2 - \tau_a^2)^3} \right) ; \quad \tau_a \neq \tau_b \end{aligned} \tag{2.32}$$

$$\mathcal{S}(\tau,R) \;=\; \mathrm{e}^{-\tau R}\left(\frac{48+33\tau R+9(\tau R)^2+(\tau R)^3}{48R}\right);\quad \tau_a=\tau_b\equiv\tau\,. \tag{2.33}$$

As before, in the limit of small distances γ_{ab} should equal the Hubbard parameter for an isolated atom. This being a known quantity, one obtains, noting eq. (2.28), a one-to-one relation between the hitherto unspecified charge fluctuation range τ_a of an atom and its Hubbard parameter:

$$\gamma_{aa}=U_a=\lim_{R\to 0}\left(\frac{1}{R}-\mathcal{S}(\tau_a,R)\right)=\frac{1}{R}-\left(\frac{1}{R}-\frac{5}{16}\tau_a\right)=\frac{5}{16}\tau_a \tag{2.34}$$

Since (2.31) was derived from pure Coulomb interactions, yet the Hubbard parameter incorporates *xc* contributions, this step may seem inconsistent. To reconcile the approaches, the following should be considered: Appreciable deviations from the point charge behaviour of $1/R$ occur only close to atoms, namely, within radii of typical bond lengths, as Fig. 2.2 attests. Adjusting the inner limit to include *xc* interactions by way of equating it to the *ab initio* DFT value, one corrects mainly the onsite terms of γ_{ab}. The remaining influence on first-neighbour interactions is, although not quite negligible, still acceptable within the monopole approximation and the somewhat arbitrary choice of the interpolation function.

For periodic systems, the Ewald technique [36, 70, 71] is used to take care of the long-range Madelung-like contributions to the $\boldsymbol{\gamma}$ matrix. The short-range deviation terms from the $1/R$ behaviour, i.e., $\mathcal{S}(\tau_a,\tau_b,R)$, are calculated by an explicit sum over all neighbours within a reasonable distance of a given atom.

To finally evaluate the second-order energy contributions, one needs the atomic charge deviations Δq_a. These are obtained from Mulliken charges, which are not undisputed (see, e.g., Ref. [66]) but widely popular because they are easy to obtain from the eigenstates without the need for elaborate spatial partitioning schemes which have their own share of problems. Given real-valued eigenvectors $C_{i\mu}$ in an atomic basis with overlap matrix $\mathbf{s}$, the Mulliken charges q_a and charge deviations Δq_a on atoms are, using eq. (1.32) on page 13:

$$\begin{aligned} q_a &= \sum_i^{occ} n_i q_a^i = \sum_i^{occ} n_i \sum_{\mu[a]}\sum_{\nu} C_{i\mu}C_{i\nu}s_{\mu\nu} = \sum_{\mu[a]}\sum_{\nu} q_{\mu\nu} \\ \Delta q_a &= q_a - q_a^0\,, \end{aligned} \tag{2.35}$$

where q_a^0 are the charges of the respective neutral atoms.

2.4 The DFTB secular equation

With the approximations discussed above the DFTB total-energy expression derived from eq. (2.11) reads:

$$E_{\mathrm{tot}} \;=\; \sum_i^{occ} n_i \sum_{\mu}\sum_{\nu} C_{i\mu}C_{i\nu}h^0_{\mu\nu} + \frac{1}{2}\sum_{ab}^{M}\gamma_{ab}\Delta q_a\Delta q_b + E_{\mathrm{rep}}(\{\boldsymbol{R}_a\}) \tag{2.36}$$

Given a set of atomic coordinates $\boldsymbol{R}_a$ and the resulting matrices $\mathbf{h}$, $\mathbf{s}$, and $\boldsymbol{\gamma}$, the LCAO coefficients which minimise the DFTB total energy (2.36) are found by the variation principle subject to orbital normalisation, eq. (1.14):

$$\frac{\partial}{\partial C_{i\mu}}\left[E_{\mathrm{tot}}+\sum_{i}^{occ} n_i\tilde{\varepsilon}_i\left(1-\sum_{\mu}\sum_{\nu}C_{i\mu}C_{i\nu}s_{\mu\nu}\right)\right]=0\,. \tag{2.37}$$

The procedure is quite similar to the standard tight binding case and was given in detail in [46]. The resulting secular equation reads:

$$\sum_{\nu=1}^{N} C_{i\nu}\left(h_{\mu\nu}-\tilde{\varepsilon}_i s_{\mu\nu}\right)=0\,;\quad \forall i,\mu\,, \tag{2.38}$$

where, as a consequence of the minimisation of E_{G} alongside E_{BS} the original Hamiltonian matrix elements are augmented as follows:

$$h_{\mu\nu}=h^0_{\mu\nu}+\frac{1}{2}s_{\mu\nu}\sum_{c}^{M}(\gamma_{ac}+\gamma_{bc})(q_c-q^0_c)\,;\quad a[\mu],\,b[\nu]\,. \tag{2.39}$$

As for the generic Kohn-Sham system (1.25), eq. (2.38) is a generalised eigenvalue problem which is solved using standard libraries. Since the charges in the augmented Hamiltonian depend upon the coefficients of the solution, the equation has to be solved self-consistently. The iteration is driven by Broyden mixing [72] for the charges $\{q_a\}$. Typically, between 5–20 iterations are required. Upon convergence, one obtains the eigenvectors $C_{i\mu}$, the one-electron energy levels $\tilde{\varepsilon}_i$ and derived quantities, like the density of states, or charge distributions.

The total energy can be conveniently expressed in terms of the eigenvalues $\tilde{\varepsilon}_i$ to avoid an explicit calculation of the matrix products in eq. (2.36). The joint minimisation of E_{BS} and E_{G} leads to a double-counting-like expression for E_{G}. A discussion and derivation of this term has been omitted from the relevant publications on DFTB so far [40, 46, 60, 61]. For completeness, it is given here:

$$\begin{aligned}
\sum_{i}^{occ} n_i\tilde{\varepsilon}_i &= \sum_{i}^{occ} n_i\langle\Phi_i|\widehat{H}|\Phi_i\rangle = \sum_{i}^{occ} n_i\sum_{\mu}\sum_{\nu}C_{i\mu}C_{i\nu}h^0_{\mu\nu}+\\
&\quad+\sum_{i}^{occ} n_i\sum_{\mu}\sum_{\nu}C_{i\mu}C_{i\nu}\frac{s_{\mu\nu}}{2}\sum_{c}(\gamma_{ac}+\gamma_{bc})\Delta q_c\,;\quad a[\mu],\,b[\nu]\\
\sum_{i}^{occ} n_i\tilde{\varepsilon}_i &= E_{\mathrm{BS}}+\frac{1}{2}\sum_{c}\Delta q_c\left(\sum_{a}q_a\gamma_{ac}+\sum_{b}q_b\gamma_{bc}\right) \qquad (2.40)\\
&= E_{\mathrm{BS}}+\frac{1}{2}\sum_{c}\Delta q_c\sum_{b}2q_b\gamma_{bc}\,. \qquad (2.41)
\end{aligned}$$

Use has been made of the definition of Mulliken charges (2.35) to arrive at eq. (2.40). Since the summations over a and b are independent in eq. (2.40), the last sums are

in fact equal. Observing the triviality $2q_b = (q_b - q_b^0) + (q_b + q_b^0)$ one obtains from eq. (2.41):

$$\sum_i^{occ} n_i \tilde{\varepsilon}_i - \frac{1}{2} \sum_{bc} \gamma_{bc} \Delta q_c (q_b + q_b^0) = E_{\mathrm{BS}} + E_{\mathrm{G}} \tag{2.42}$$

Renaming $c \to a$, the total energy is given finally by the following *decidedly asymmetric* expression:

$$E_{\mathrm{tot}} = \sum_i^{occ} n_i \tilde{\varepsilon}_i - \frac{1}{2} \sum_{ab}^{M} \gamma_{ab} (q_a - q_a^0)(q_b + q_b^0) + E_{\mathrm{rep}}(\{\boldsymbol{R}_a\}) \,. \tag{2.43}$$

Forces on atoms can be obtained analytically [46] without resorting to repeated energy calculations for finite displacements. They are derived directly from the total energy expression subject to the normalisation condition for orbitals:

$$\boldsymbol{F}_k = -\frac{\partial}{\partial \boldsymbol{R}_k} \left[E_{\mathrm{tot}} + \sum_i^{occ} n_i \tilde{\varepsilon}_i \left(1 - \sum_\mu \sum_\nu C_{i\mu} C_{i\nu} s_{\mu\nu} \right) \right] \tag{2.44}$$

At the variational minimum (2.37) of the electronic degrees of freedom all contributions due to the eigenvectors $C_{i\mu}$ vanish. Only the matrices $\mathbf{h}$, $\mathbf{s}$, and $\boldsymbol{\gamma}$ depend explicitly on the atomic positions. Using (2.36) one obtains:

$$\begin{aligned} \boldsymbol{F}_k \;=\; & -\sum_i^{occ} n_i \sum_\mu \sum_\nu C_{i\mu} C_{i\nu} \left[\frac{\partial h^0_{\mu\nu}}{\partial \boldsymbol{R}_k} - \left(\tilde{\varepsilon}_i - \frac{1}{2} \sum_c (\gamma_{ac} + \gamma_{bc})(q_c - q_c^0) \right) \frac{\partial s_{\mu\nu}}{\partial \boldsymbol{R}_k} \right] \\ & - (q_k - q_k^0) \sum_c \frac{\partial \gamma_{kc}}{\partial \boldsymbol{R}_k} (q_c - q_c^0) - \sum_{c \neq k} \frac{\partial V_{\mathrm{rep}}(|\boldsymbol{R}_k - \boldsymbol{R}_c|)}{\partial \boldsymbol{R}_k} \,; \quad a[\mu],\, b[\nu] \,. \end{aligned}$$

This concludes the review of the DFTB formalism. The essential result of the DFTB calculation is available in form of the total energy and the electronic eigenvectors. Other physical observables like charge distributions or vibrational properties may be extracted, the latter not without considerable numerical effort.

Chapter 3

Order-N Method and Implementation

3.1 Introduction

Customary approaches to the solution of the Schrödinger equation or the Kohn-Sham equations such as those outlined in the preceding chapters require a workload proportional to the third power of the number of atoms involved in the simulation — Doubling the size of the system amounts to multiplying by eight the computing time [73, 74]. This applies to both first-principle and tight-binding Hamiltonians. The reason is mathematical in nature because at the heart of either approach lies an eigenvalue problem where typically about half of all eigenvectors must be found. Speaking somewhat simplistically, ensuring the mutual orthogonality of the eigenvectors spatially interweaves all parts of the solution and so requires multiple passes.

Current implementations of first principles density-functional calculations using the local density approximation (LDA) and standard approaches can handle up to about 1200 electrons using supercomputers and parallelised algorithms. On workstation hardware, about 400 . . . 500 electrons appear to be a practical limit. First principles LDA calculations using linear scaling algorithms have appeared in the literature [75, 76], although algorithms as robust, transferable, and efficient as those used in standard approaches have yet to be implemented. There are also algorithms which implement self-consistent LDA directly and employ, as in the present work, non-orthogonal basis sets and non-orthogonal orbitals [77, 78]. Their applicability has been demonstrated for systems of moderate size built of repetitive or characteristic building blocks.

So far, linear scaling algorithms have mainly been used within a tight-binding framework and have provided several valuable results in the last decade [73, 74, 79, 80]. Such methods can help tackle a number of materials science and condensed matter physics issues requiring a qualitative quantum mechanical description for fairly large systems, containing, e.g., 5 000 . . . 10 000 electrons. Examples include the study of extended defects and large scale growth simulations.

All linear scaling approaches which have appeared in the literature avoid diago-

nalisation of the Hamiltonian matrix, and compute an approximate value of the ground state energy and forces without ever calculating the Hamiltonian eigenvalues and eigenvectors. The main classification of a method can be made whether the approach is based on an orbital formulation, or uses a density matrix picture.

The two key points involved in orbital based methods are the following: (i) the full physical system is divided into subsystems, and orbitals *localised* in the subsystems are defined as electronic degrees of freedom [81]; these orbitals are used during an energy functional minimisation, instead of the Hamiltonian extended eigenstates. The subsystems are overlapping portions of the full system, called *localisation regions* or *support regions*. The extent of a localisation region depends on the physical and chemical properties of the system but not on the entire volume of the system. (ii) Electronic orbitals are never explicitly orthonormalised; this is accomplished by defining an appropriate energy functional whose minimisation requires neither explicit orthonormalisation of electronic orbitals, nor the inversion of an overlap matrix ($\mathbf{S}$) between single particle wave functions. Such a functional is in general different from the functional minimised by the Hamiltonian eigenstates but it has the same absolute minimum.

One of the major drawbacks of most TB formulations is the lack of self-consistency between the charge density and the mean-field potential of the system. This is a particularly severe problem for polar systems involving charge transfer, such as SiC, GaAS and GaN and for any organic compound.

In this chapter we describe the implementation of the DFTB approach in the charge self-consistency (SCC) version. The approach is characterised by both the non-orthogonal basis set inherent to DFTB and non-orthogonal localised orbitals, within the linear scaling algorithm.

The linear-scaling formulation is based on the formalism outlined by Kim et al. [82]. The present work extends this formalism in three respects:

- to make use of a non-orthogonal basis,
- to treat multiple species, and
- to include charge-self-consistency effects.

The implementation of the algorithm was carried out on a serial computer. Parallelisation with load balancing might be performed later along the principles laid out by Canning et al. [83].

3.2 Energy functional and charges

3.2.1 Energy functional

The DFTB energy expression for a system containing N_{el} electrons and N_{at} ions is (cf. 2.11):

$$E_{\mathrm{tot}} = E_{\mathrm{BS}} + E_{\mathrm{G}} + E_{\mathrm{rep}}. \tag{3.1}$$

The $\mathcal{O}(N)$ functional describing the band structure energy E_{BS} in a tight-binding formulation has been discussed in detail by Kim et al. [82] and Mauri and Galli [84]. It expresses the energy in terms of the TB Hamiltonian $\widehat{H}$, a set of M overlapping and non-normalised orbitals $|\Phi_i\rangle$ (instead of molecular or extended eigenstates) and a Lagrangian multiplier η ensuring the correct filling of the localised orbitals:

$$\begin{aligned} E_{\mathrm{BS}}(\{\Phi_i\}, \eta, M) &= 2\sum_{ij=1}^{M} \left(\langle \Phi_j | \widehat{H} - \eta | \Phi_i \rangle \, Q_{ij} \right) + \eta N_{\mathrm{el}} \\ &= 2\mathrm{Tr}(\mathbf{H}'\mathbf{Q}) + \eta N_{\mathrm{el}}. \end{aligned} \tag{3.2}$$

The factor 2 accounts for spin degeneracy. In general, the number M of electronic orbitals is larger than the number of occupied states $N_{\mathrm{el}}/2$, as discussed, e.g., in Ref. [82].

Both $\mathbf{H}'$ and $\mathbf{Q}$ are $(M \times M)$ matrices where $\mathbf{H}'$ is the Hamilton matrix between the localised support orbitals (or generalised Wannier functions), augmented by the η Lagrange parameter; $\mathbf{Q}$ is a truncated Taylor expansion around the identity matrix $\mathbf{I}$ of the inverse of the overlap matrix $S_{ij} = \langle \Phi_i | \Phi_j \rangle$.

$$\mathbf{Q} = 2\mathbf{I} - \mathbf{S}. \tag{3.3}$$

To include charge self consistency effects within the tight-binding framework we add to the band structure contribution the term E_{G} from 2.26. The calculation of the E_{G} term is known as the electronic quantum Coulomb problem. Classical algorithms for its solution involve the calculation of the Madelung matrix via the Ewald technique and exhibit $\mathcal{O}(N^2)$ scaling. However, in recent years a number of algorithms exhibiting linear scaling have been proposed in the literature, in particular generalisations of the fast multipole method (FMM) [85]. These algorithms could in principle be applied to make the calculation of E_{G} show the same scaling with system size as the evaluation of E_{BS}. In this work, as in most other $\mathcal{O}(N)$ approaches [75, 86], this problem was put aside. We note that the $\mathcal{O}(N^2)$ evaluation of E_{G} becomes a limiting factor when the time for *one* calculation of the Madelung matrix is comparable to the time for the *total* number of iterations required to minimise the electronic energy functional, at each MD step. In our current implementation this is the case for about 8000 electrons. The bulk of our calculations consists of repeated minimisations of the electronic energy.

In the $\mathcal{O}(N)$ functional, the regular DFTB basis functions $\{\varphi_\mu\}$ will be used, and the TB hopping and overlap terms $h_{\mu\nu} = \langle \varphi_\mu | \widehat{H} | \varphi_\nu \rangle$ and $s_{\mu\nu} = \langle \varphi_\mu | \varphi_\nu \rangle$ are calculated as usual from the directional cosines of the ionic positions and tabulated Slater-Koster integrals. However, in order to achieve linear scaling, the range of these interactions is limited by an imposed cutoff radius R_{SK}. Currently, the LCAO basis is not optimised for short-ranged interactions. The cutoff radius is chosen typically such that all second and most third neighbours are taken into account. Under these conditions, the energy deviations of the $\mathcal{O}(N)$ scheme from exact diagonalisation results are largely due to the chosen size of localisation regions. In order to investigate the effect of the basis cutoff, we have compared the total energies as obtained from exact diagonalisations with full and reduced range. The results are

given in Table 3.1 on page 47. For carbon the cutoff increases the total energy per atom by about 30 meV, while in the mixed system of SiC the effect is a mere 5 meV per atom. These energy deviations are all of smaller magnitude than the energy deviations of the localised solutions discussed further. We notice that the effect of the basis cutoff is most pronounced in the homogeneous carbon systems. To reduce this contribution to the total energy deviation of the localised solution, the process of basis function generation and fitting of the repulsive potential will have to be repeated.

3.2.2 Localisation of support functions

Within the real-space basis of the LCAO approach (1.23), a localisation constraint on orbitals can easily be imposed by restricting the expansion coefficients $C_{i\mu}$ to be nonzero only for a set of basis functions $\{\mu\}$ localised within a *Localisation Region* (LR). Here, a localisation region is defined by a topological criterion as a set of atoms including N_h nearest neighbour shells, or *hops*, around a central atom [83]. The neighbour shells are identified once per ionic step from a bond map constructed using species dependent nearest neighbour cutoff radii. In principle this step can be performed in $(N_{\mathrm{at}} \log N_{\mathrm{at}})$ operations [87]. Furthermore, if atomic relaxations or molecular dynamics simulations are performed but no significant atomic migrations take place, the topological information built in the initial ionic step can be upheld throughout the simulation. In these cases, the calculation of distances is required only for atoms which are linked within these topologies.

The localisation regions are described by a pair of topology arrays. A two-dimensional array of fixed size lists for each central atom i the corresponding atom numbers of its neighbours up to the N_hth shell. Typically, we choose $N_h = 2$ or $N_h = 3$. This requires for diamondlike interfacial and bulk models about 20 and 50 entries per atomic localisation region, respectively. The number of atoms actually present in each LR_i is stored in an associated one-dimensional vector.

A given localisation region carries a number ns of localised orbitals. While we typically choose $ns = 3$, for an LR centred on a Hydrogen atom ns can be reduced to 1.

The localised orbitals are stored in terms of their LCAO coefficients. Each atom contributes to a localised orbital with a number nb of basis functions or, equivalently, LCAO coefficients. Since each LR carries ns orbitals and each atom within the LR carries nb basis functions, the LCAO coefficients are stored in a matrix of size $(ns \times nb)$ for each atom. These matrices are mapped in a one-to-one fashion to the atomic lists of the LR topology description. The dimensions of the atomic matrices may vary by species.

This storage scheme for the wave function is generally referred to as “sparse” or “packed” storage. Essentially, all nonzero elements of a sparsely occupied matrix (here, the LCAO coefficients $C_{i\mu}$), are identified and shifted to the leftmost column of the matrix, keeping track of the original column positions in a separate list (here, the LR array).

3.2.3 Hamilton and overlap matrices

The band structure energy term in eq. (3.2) is the trace of the product of two sparse matrices: $\mathbf{H}'$ and $\mathbf{Q} = 2\mathbf{I} - \mathbf{S}$. Their matrix elements are:

$$\begin{aligned} H'_{ij} &= \langle \Phi_i | \widehat{H} - \eta | \Phi_j \rangle = \sum_{\mu\nu} C_{i\mu} C_{j\nu} (h_{\mu\nu} - \eta s_{\mu\nu}) \\ S_{ij} &= \langle \Phi_i | \Phi_j \rangle = \sum_{\mu\nu} C_{i\mu} C_{j\nu} s_{\mu\nu}; \quad \mu \in LR_i, \nu \in LR_j, \end{aligned} \tag{3.4}$$

where Φ_i are localised orbitals. The TB hopping and overlap elements $h_{\mu\nu}$ and $s_{\mu\nu}$ between basis functions need to be calculated once for a given ionic configuration from the directional cosines and atom pair specific Slater-Koster tables. In order to keep the range of the hopping and overlap terms limited in a well-defined manner, we impose a Euclidian cutoff radius R_{SK} around each atom. This defines, for each atom, a *Slater-Koster region*, tagged SK. The cutoff radius is species dependent and typically chosen to be twice the threshold distance used as nearest neighbour criterion. This leads to about 50 neighbours within the Slater-Koster region of a given atom.

The elements $h_{\mu\nu}$ and $s_{\mu\nu}$ are stored similar to the wave functions in atomic submatrices mapped to the Slater-Koster topology lists. The dimension of each submatrix is determined here by the number of basis functions on the central atom of a given Slater-Koster region and the number of basis functions on the subordinate atom.

Given the complications of the sparse storage of both wave functions and Slater-Koster elements, the evaluation of the elements of the $\mathbf{H}'$ and $\mathbf{S}$ matrices naturally proceeds in two steps. One of the summations over atoms in eqs. (3.4) are carried out first:

$$\begin{aligned} \widetilde{C}^H_{j\mu} &= \sum_{\nu} C_{j\nu} (h_{\mu\nu} - \eta s_{\mu\nu}) \\ \widetilde{C}^S_{j\mu} &= \sum_{\nu} C_{j\nu} s_{\mu\nu}; \quad \nu \in LR_j. \end{aligned} \tag{3.5}$$

These summations define so-called *projected orbitals* $|\widetilde{\Phi}^H_j\rangle$ and $|\widetilde{\Phi}^S_j\rangle$. Similar definitions of projected or conjugate orbitals have been used in other orbital based $\mathcal{O}(N)$ approaches [51, 52, 53]. The projection can also be seen as a conversion between co- and contravariant vectors.

The projected orbitals are stored in the same manner as the original localised orbitals using atomic submatrices tied to an appropriate topology description. The projected orbitals differ from the original orbitals by a bigger localisation range. The increase in localisation range is induced by gathering contributions from atoms outside the original LR's through the hopping and overlap integrals. The extended localisation regions of projected orbitals are named $LRSK$. Each $LRSK_j$ is constructed from its LR_j parent by linking to it the neighbours of the Slater-Koster topologies SK_k of each atom k within LR_j:

$$LRSK_j = LR_j \bigcup_{k \in LR_j} SK_k. \tag{3.6}$$

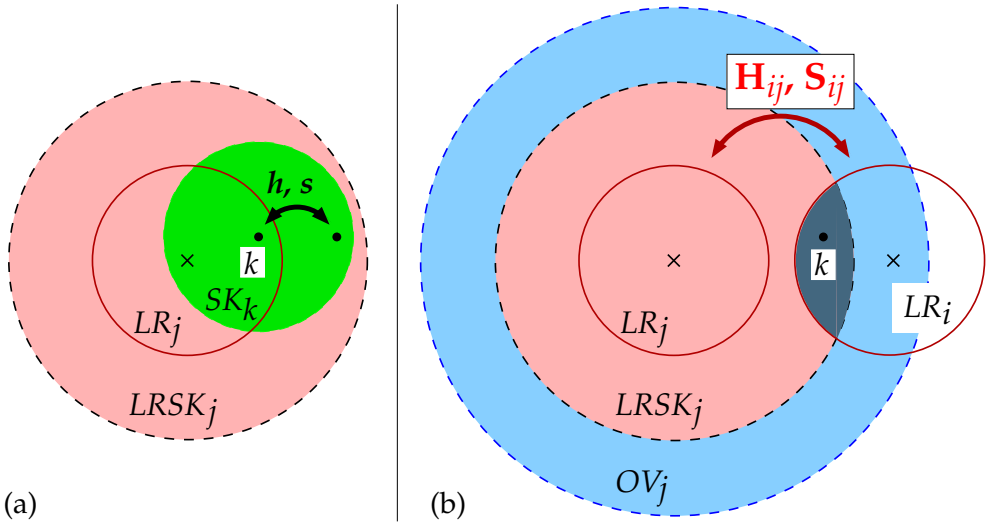

Figure 3.1: (a) Spatial relation between Localisation Regions (LR), the Slater-Koster (SK) topologies of the tight-binding hopping and overlap elements and the resulting extended localisation regions (LRSK). (b) Contribution to matrix elements H_{ij} and S_{ij} between support functions from two localisation regions LR_i and LR_j mediated by atoms k within the extension $LRSK_j$ of one of the localisation regions.

Fig. 3.1 (a) illustrates this operation.

By making use of the projected orbitals the calculation for the matrix elements H'_{ij} and S_{ij} is reduced to contributions from wave function expansion coefficients C and $\widetilde{C}$ located on the *same* atom (an important aspect for parallelisation):

$$\begin{aligned} H'_{ij} &= \sum_{\mu} C_{i\mu}\widetilde{C}^{H}_{j\mu} \\ S_{ij} &= \sum_{\mu} C_{i\mu}\widetilde{C}^{S}_{j\mu}; \quad \mu \in LR_i \cap LRSK_j. \end{aligned} \tag{3.7}$$

Due to the limited range of the orbitals $|\Phi_i\rangle$ and $|\widetilde{\Phi}_j\rangle$, the matrix elements of $\mathbf{H}'$ and $\mathbf{S}$ involve only summations over specific localisation regions. The localisation is again described in terms of a topology list, which is named OV. The construction of this topology uses a topological addition operation similar to (3.6) and is illustrated in Fig. 3.1 (b):

$$OV_j = LRSK_j \bigcup_{k \in LRSK_j} LR_k. \tag{3.8}$$

The number of nonzero elements of the $\mathbf{H}'$ and $\mathbf{S}$ matrices depends on the topological hopping range of the LR's and the Euclidian cutoff for the construction of the SK regions. With the extents of the contributing regions listed above, a row of the overlap matrix contains typically 300 elements. For comparison, with an orthogonal nearest neighbour Hamiltonian, a row of the $\mathbf{H}'$ matrix contains typically about 150 elements. The matrix $\mathbf{S}$ in this case is even smaller because it is constructed using only the intersections between two LR localisation regions due to the vanishing

basis overlap, in contrast to the intersection between an LR and an $LRSK$ used for $\mathbf{H}'$.

The data entity associated with an entry in the OV topology is a submatrix of dimension $(ns_i \times ns_j)$, where ns_i and ns_j are the number of orbitals carried by the contributing regions LR_i and $LRSK_j$.

The matrices $\mathbf{H}'$ and $\mathbf{S}$ are constructed from the same topologies, imposing identical cutoffs for the hopping and overlap terms. This allows to access their matrix elements by the same topology tables. Both matrices are symmetric; taking into account symmetry nearly halves the computational cost of their evaluation.

In order to exploit the symmetry in sparse coded matrices, tailored information must be built explicitly into the topology descriptions. This is a non-trivial step. A sparse topology description contains for each atom i a sequence of indices j addressed by the sparse, or indirect, index j'. In other words, a topology entry at address (j', i) contains the non-sparse column index j for a given matrix element, say S_{ij}. The transposed element S_{ji} is accessed by the topology entry (i', j). The indirect indices i' and j' are unrelated because they are the result of different neighbour gathering steps for the sites i and j, respectively. In order to allow a handshaking between transposed matrix elements, the topology description needs to carry a cross-reference list $i'(j', i)$ besides each regular entry $j(j', i)$.

To actually calculate only one symmetry half of a sparse coded matrix it is necessary to decide whether a desired matrix element must be calculated explicitly or is to be taken from the transposed position within the matrix. Conventionally, the symmetry of a full matrix is employed by limiting the index loops to the upper or lower triangle of the matrix. This is inconvenient here because of implied load imbalances. Instead, we apply a checkerboard type criterion introduced in [83]: Matrix elements characterised by the full indices (i, j) are calculated explicitly, if either they fulfil $(i < j)$ or $(i + j)$ is even (an EXCLUSIVE-OR relation). To simplify the decision for repeated accesses of the matrix, the topology lists are re-arranged such that the data elements which are to be calculated explicitly are listed *first* in the sparse topology list for each row of the matrix. The number of entries matching this criterion is stored next to the total number of entries per row. The remaining elements of a row which do not match the selection criterion are listed *after* the last element that does. In the complete list of indices, the elements at the tail of the list of row i are being pointed at by the cross-reference list from the elements at the head of row j and vice versa. The cross-reference list only needs to extend through the first part of each row which contains the unique matrix elements.

To circumvent storing $\mathbf{Q}$ separately, the Taylor expansion of $\mathbf{Q}$ for the calculation of the band structure energy is applied through the trivial relation

$$E_{\mathrm{BS}} = 2\mathsf{Tr}(H'_{ji}Q_{ij}) = 4\mathsf{Tr}(H'_{ij}) - 2\mathsf{Tr}(H'_{ij}S_{ij}). \tag{3.9}$$

The TB elements $h_{\mu\nu}$ and $s_{\mu\nu}$ are also symmetric. The topology table SK used to describe their symmetry and sparse storage is organised and accessed similar to the OV description.

3.2.4 Atomic charges and SCC energy contributions

The E_G term in the total energy expression (2.11) requires the calculation of atomic charges. For non-orthogonal molecular orbitals, this calculation is a trifle more involved than for orthogonal states.

Using the approximate inverse overlap matrix $\mathbf{Q}$ from eq. (3.3) the charge density for a system of non-orthogonal support functions $\Phi_i(\boldsymbol{r})$ is given by

$$\varrho(\boldsymbol{r}) = 2\sum_{ij} \Phi_i^*(\boldsymbol{r}) Q_{ij} \Phi_j(\boldsymbol{r}). \tag{3.10}$$

Similar to the energy expression, the factor 2 accounts for the spin degeneracy. By spatial integration within the LCAO expansion the contributions due to the non-orthogonal basis functions can be expressed in terms of their overlap integrals and one obtains the total charge as

$$q_{\text{tot}} = 2\sum_{\mu\nu}\sum_{ij} C_{i\mu} C_{j\nu} s_{\mu\nu} Q_{ij}. \tag{3.11}$$

The summation over one orbital index is carried out first:

$$\overline{C}^{Q}_{i\nu} = \sum_j C_{j\nu} Q_{ij}. \tag{3.12}$$

This defines, for a given i, the *conjugate orbital* $|\overline{\Psi}_i\rangle = \sum_j |\Phi_j\rangle Q_{ij}$. Formally, it linearly combines all localised orbitals $|\Phi_j\rangle$ contributing to the row i of the overlap matrix. However, only the atomic components within reach of the Slater-Koster integrals $s_{\mu\nu}$ around atoms from LR_i are needed further and hence, only the components of $|\overline{\Psi}_i\rangle$ within $LRSK_i$ are required and stored for the calculation of the elements of a bond charge matrix $q_{\mu\nu}$:

$$q_{\mu\nu} = 2\sum_i C_{i\mu} \overline{C}^{Q}_{i\nu} s_{\mu\nu}; \quad \nu \in LRSK_i. \tag{3.13}$$

The atomic charges q_k are obtained from this expression by a Mulliken analysis, which places the elements of the full bond charge matrix in halves onto the contributing atoms, cf. eq. (2.35):

$$q_k = \sum_{\mu[k],\nu} \frac{q_{\mu\nu} + q_{\nu\mu}}{2}. \tag{3.14}$$

In this notation, $\mu[k]$ picks the basis functions μ located on atom k. Eq. (3.11) can be written and calculated in the same form as the band structure energy:

$$q_{\text{tot}} = 2\mathsf{Tr}(S_{ij} Q_{ij}). \tag{3.15}$$

In this form, the direct calculation of atomic Mulliken charges is not required.

The energy correction due to the self-consistent charge effects (2.26) is evaluated using an intermediate atomic vector G, which contains the Coulomb potential for each atom:[1]

$$G_k = \sum_{k'} \gamma_{kk'} \Delta q_{k'}. \tag{3.16}$$

If a Hubbard-like energy correction of the form $E_{\mathrm{H}} = \sum_k U_k (\Delta q_k)^2$ is used, with species dependent constants U_k, the vector G takes the form

$$G_k = 2U_k \Delta q_k. \tag{3.17}$$

Both forms of charge-related energy corrections can then be calculated from the same expression:

$$E_{\mathrm{G}} = \sum_k G_k \Delta q_k. \tag{3.18}$$

The atomic vector G_k needs to be stored for the calculation of force components, as described later.

3.3 Electronic minimisation

The electronic contribution to the energy functional, $E_{\mathrm{el}} = E_{\mathrm{BS}} + E_{\mathrm{G}}$, is minimised for a given ionic configuration and a given η parameter with respect to the orbitals by a conjugate gradient technique [72]. The gradient of the band structure energy is:

$$\frac{\partial E_{\mathrm{BS}}}{\partial |\Phi_i\rangle} = |\xi_i^{BS}\rangle = 4 \sum_j \left(\widehat{h'} |\Phi_j\rangle Q_{ij} - \widehat{s} |\Phi_j\rangle \langle \Phi_i | \widehat{h'} |\Phi_j\rangle \right). \tag{3.19}$$

The non-orthogonality of the basis functions appears in the form of the basis overlap operator $\widehat{s}$, mirroring the role of the hopping elements. The gradient components are evaluated by re-using the projected orbitals $|\widetilde{\Phi}^H\rangle$ and $|\widetilde{\Phi}^S\rangle$ defined in eq. (3.5). The gradient components have the same spatial extent as the corresponding wave functions. Therefore, only the LCAO components of $|\xi_i^{BS}\rangle$ within the associated localisation region LR_i are needed.

If SCC corrections are included, the respective energy gradients are, as a result of a cumbersome manipulation:

$$\begin{aligned} \frac{\partial E_{\mathrm{G}}}{\partial |\Phi_i\rangle} &= |\xi_i^G\rangle = 4 \sum_j (\widehat{g} |\Phi_j\rangle Q_{ij} - \widehat{s} |\Phi_j\rangle \langle \Phi_i | \widehat{g} |\Phi_j\rangle), \\ g_{\mu\nu} &= \frac{G_{k[\mu]} + G_{k[\nu]}}{2} s_{\mu\nu}\,; \end{aligned} \tag{3.20}$$

This is the same expression as eq. (3.19), with the operator $\widehat{h'}$ replaced by a modified overlap operator $\widehat{g}$, where each basis function overlap $s_{\mu\nu}$ is weighted with

[1] Throughout this chapter, the indices k and k' are used to signify running indices.

the average components of the Coulomb potential G on both contributing atoms. This allows one to re-use the routines and intermediate results of the band structure gradients for the calculation of the charge-related gradient contributions.

In the conjugate gradient procedure, a line minimisation has to be performed along a search direction determined by the local gradient and an admixture from the previous direction. The band structure energy along the search direction $|\xi_i\rangle$ is a fourth order polynomial in the displacement λ:

$$E_{\mathrm{BS}}(\{\Phi_i + \lambda\xi_i\}) = \sum_{m=0}^{4} a_m \lambda^m. \tag{3.21}$$

The coefficients of the polynomial are evaluated explicitly; this requires the calculation of the matrices $\langle\xi_i|\widehat{h}'|\Phi_j\rangle$, $\langle\xi_i|\widehat{h}'|\xi_j\rangle$, $\langle\xi_i|\Phi_j\rangle$, and $\langle\xi_i|\xi_j\rangle$. These evaluations are similar to the calculation of the total energy itself. The matrices which combine the wave function on one side and the gradients on the other are symmetrised beforehand using $A^s_{ij} = (A_{ij} + A_{ji})/2$. This allows for a symmetry reduced calculation of the trace of the product between any of the matrices above. For the symmetrisation, the index transposition tables of the topology are used.

The SCC energy contributions E_{G} along the search directions form a polynomial of 8th degree. The coefficients of this polynomial are also calculated explicitly. Because of the presence of Mulliken bond charges and their mixing, this is much more difficult than finding the coefficients of the polynomial of the band structure energy. This complexity can be reduced significantly because each atomic charge alone is a fourth order polynomial along the search direction:

$$q_k(\{\Phi_i + \lambda\xi_i\}) = \sum_{m=0}^{4} b_{km} \lambda^m. \tag{3.22}$$

The coefficients b_{km} are calculated with the subroutines used to evaluate the atomic charges, plugging in the set of overlap matrices involving gradients as defined above. In a next step, the polynomials of atoms k' are projected to the atomic G array using eq. (3.16), which thus represents a quartic polynomial for each atom. The full 8th order polynomial for the SCC energy is constructed following (3.18).

Both the band structure and SCC energy polynomials are added and the minimum $\lambda_{\min}$ is calculated directly. Finally, the wave function is updated as $|\Phi_i + \lambda_{\min}\xi_i\rangle$.

We note that in the line minimisation involved in the conjugate gradient procedure, spurious minima along the search direction may be present. Indeed, the polynomial in λ may have several minima. All but one are characterised by an unphysical charge distribution. It would be expensive to discard solutions corresponding to an unphysical charge only after the charge has been calculated. Unphysical solutions are recognisable from other general properties. Firstly, the total energy in the conjugate gradient procedure changes only by small steps. Only a solution with the polynomial value close to the previous energy minimum is acceptable, with the exception of the early stages of an iterative minimisation started, e.g., from random wave functions. Negative values can be discarded as well, since they indicate a discrepancy with the downhill search paradigm. Finally, experience has shown that

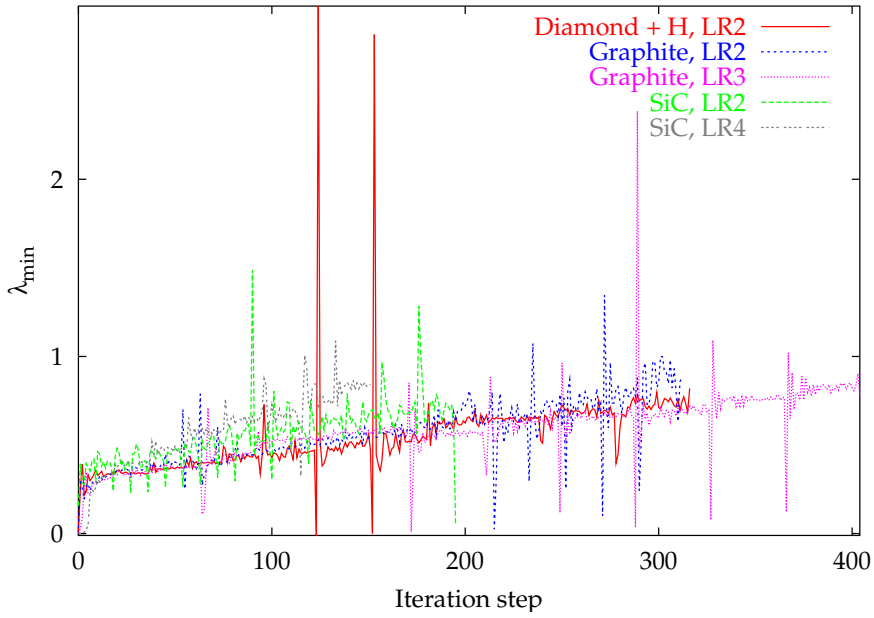

Figure 3.2: Line minimisation step $\lambda_{\min}$ vs. iteration for various test systems. Starting from random wave functions, the energy gradient itself is initially steep (has a high norm), so that sensible wave function updates arise from small $\lambda_{\min}$. After a few steps, the gradient norm gets smaller, and the update step lies typically within 0.5...1.

$\lambda_{\min}$ typically has values between 0.5 and 1.0, see Fig. 3.2. Much larger values are therefore rejected.

3.3.1 The Lagrange multiplier η

During the conjugate gradient minimisation of the energy functional, η is treated as an external parameter. The parameter η has to be adjusted so as to have the correct number of electrons (i.e., the correct orbital filling) at the end of the iterative minimisation. Contrary to the energy functional which depends explicitly on the value of η, the total charge depends only implicitly on η, through the localised wave functions minimising the energy functional at that given η. We note that the location of the energy functional minimum changes as η is varied. Therefore the evaluation of the function

$$\mathcal{Q} = q_{\text{tot}}(\eta) - N_{\text{el}} \tag{3.23}$$

can only be performed approximately: the value of $\mathcal{Q}$ is determined after a certain number of conjugate gradient steps have been performed at a fixed η. If $\mathcal{Q}$ is positive, η needs to be reduced, which corresponds to emptying the upper occupied states. Conversely, for negative $\mathcal{Q}$, i.e., a charge deficiency in the system, η must be increased. A suitable iteration scheme for η needs to be wrapped around the electronic conjugate gradient algorithm. Fig. 3.3 gives an overview of the extended iteration scheme in the form of a flowchart. The η iteration scheme is the subject of the next section.

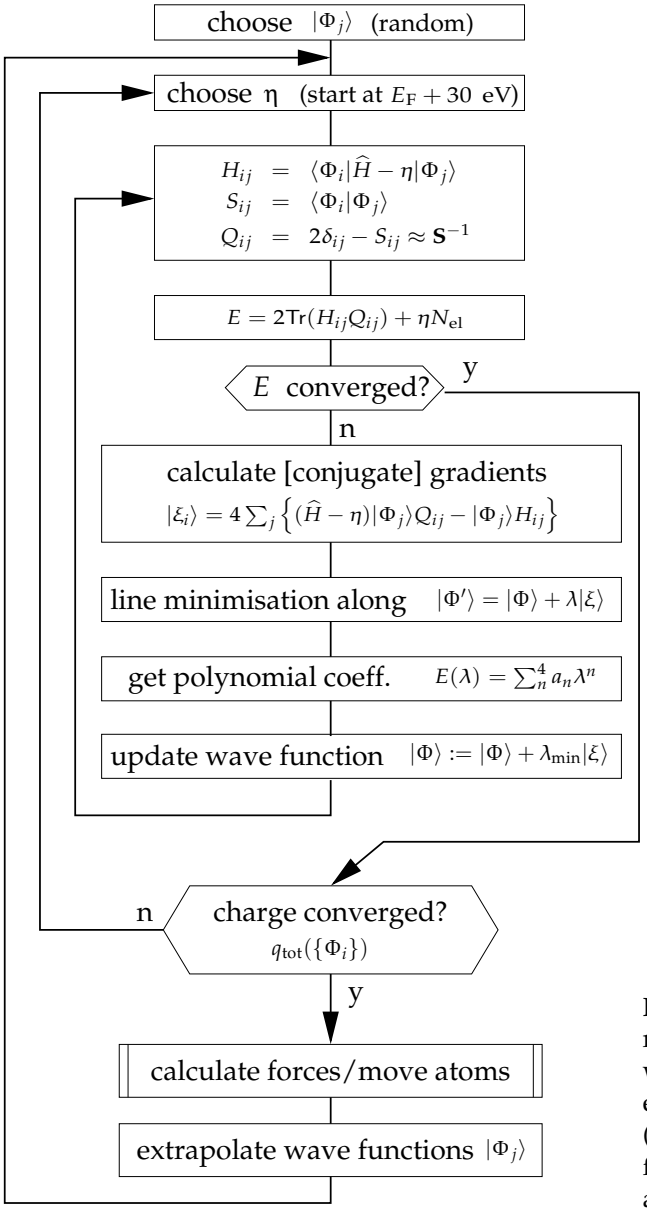

Figure 3.3: Flowchart for the $\mathcal{O}(N)$ minimisation of the total energy w.r.t. atomic positions (outermost iteration), the Lagrange parameter η (medium iteration), and the wave function coefficients $C_{i\mu}$ (inner iteration).

3.3.2 The adaptive secant method

There are two facts which may cause convergence difficulties when optimising the η parameter. Firstly, although monotonous, the relation $q_{\mathrm{tot}}(\eta)$ is non-linear. The slope is lower for undercharged systems than for excess charges. Secondly and more severely, a premature readout of the charge before the wave function is stepped close enough to the energy minimum may be inappropriate for choosing η for the next cycle of conjugate gradient steps. A balance must be found between letting the electronic conjugate gradient algorithm for the energy minimisation run for too many steps, and accepting an approximate value of the charge, at a given η.

Another control parameter which needs to be optimised is the the amplitude $\Delta\eta$ with which η is changed. If $\Delta\eta$ is chosen too small, a change in sign for $\mathcal{Q}$ is not reached for many update steps; if $\Delta\eta$ is chosen too large, then the energy minimum

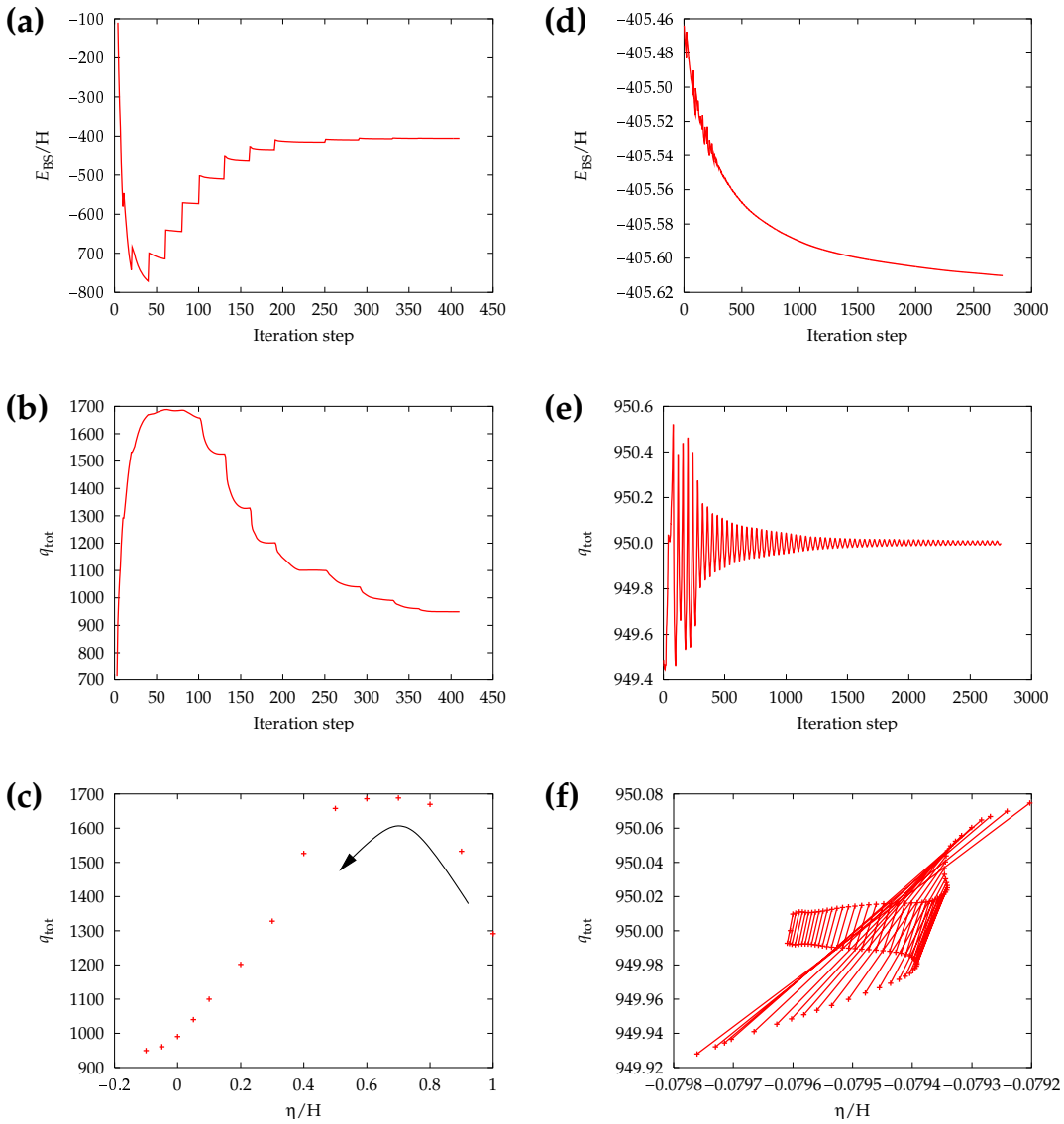

Figure 3.4: Calculated quantities during stepped and feedback wave function iteration phases (see text): (a,d) energy, (b,e) charges, and (c,f) η-parameter. The sample structure is a stable silicon-diamond interface structure (B_0^s in Ref. [88]) with 284 atoms total (174 C, 52 Si, 10 H, 48 H′). (a,b,c) starting from random input wave functions with η stepped; (d,e,f) feedback-controlled iteration phase, with $\Delta\eta$ depending on the charge defect $\mathcal{Q}$. The arrow in (c) indicates the iteration sequence. Lines in (f) connect pairs of subsequent iteration steps.

is shifted far away from the previous location in wave function space, and convergence proximity for the wave function may be lost.

Essentially, the root of the one-dimensional relation $\mathcal{Q}(\eta)$ is searched iteratively starting from a pair η_1 and η_2 yielding $\mathcal{Q}$ values of opposite sign. In principle this search could be performed by a standard root finding technique. However, the properties of the relation $\mathcal{Q}$ disallow a black-box approach. As mentioned above, due to the finite number of electronic iterations n_{CG}, $\mathcal{Q}(\eta)$ is evaluated for a given iteration m in wave function space at a point $\mathcal{P}_m$ which is in general not the energy minimum

location $\mathcal{P}_{\min}(\eta_m)$, giving rise to an error $\Delta\mathcal{Q}_m$. This error tends to systematically drop in subsequent iterations because the repeated underlying electronic conjugate gradient iterations will normally reduce the distance $\|\mathcal{P}_m - \mathcal{P}_{\min}(\eta_m)\|$, even though $\mathcal{P}_{\min}(\eta_m)$ is a "moving target". We note that $\mathcal{Q}(\eta)$ can attain different values, depending on the stage of the minimisation procedure (i.e., the value of the charge density) at which the η value is visited. Therefore, the calculation of the derivative of $\mathcal{Q}(\eta)$ is subject to large errors due to the dynamic behaviour of the charge error $\Delta\mathcal{Q}_m$. Since most black-box root solvers rely on derivative information or expect a "smooth" behaviour of the function, they cannot be used without applying tailored safeguard mechanisms to avoid divergence from a known good search interval for η.

The following scheme has been established to find the value of η corresponding to a minimum of the energy functional at the correct charge, i.e., fulfilling the condition $\mathcal{Q}(\eta) = 0$. A sequence of electronic conjugate gradient iterations are nested within iterations for η.

The scheme starts from a random wave function and a well-guessed η. A fixed number n_{CG} (typically, 20...50) of electronic conjugate gradient iterations is performed where η is held constant. At the end of this set of iterations the charge deviation $\mathcal{Q}$ is evaluated. Subsequently, a fixed correction $\Delta\eta$ is applied and the electronic conjugate gradient cycle is restarted. This procedure is repeated until $\mathcal{Q}$ changes sign. These steps are illustrated in Fig. 3.4(a) through (c). Now an adaptive update scheme is switched on, where $\Delta\eta$ is calculated depending on the value of the charge defect $\mathcal{Q}$. This phase is shown in Fig. 3.4(d) through (f), which illustrates in particular some of the problems related to the update step $\Delta\eta$ mentioned above.

The dynamic charge error $\Delta\mathcal{Q}_m$ has the effect of letting functional values $\mathcal{Q}(\eta)$ "age" during the ongoing electronic minimisation, as can be seen in the example calculation in Fig. 3.4(f). Therefore, the secant method has been chosen and adapted as root finding technique [72]. It limits the influence of the charge error effects by making use of only the latest two iteration results $\mathcal{Q}(\eta_m)$ and $\mathcal{Q}(\eta_{m-1})$. For comparison, the closely related *regula falsi* method may keep one particular iteration result for many cycles and is therefore not suitable. The unknown changes in the charge error $\Delta\mathcal{Q}$ along the iteration for η may send the intersection of the secant with the η axis far away from the latest search interval when $\mathcal{Q}(\eta_m) \approx \mathcal{Q}(\eta_{m-1})$, see Fig. 3.5 (a). As a safeguard mechanism in this case, the update step $\Delta\eta_m$ is chosen to be the same as the previous one, $\Delta\eta_{m-1}$. In other cases, the slope $\partial\mathcal{Q}/\partial\eta$ may appear to be negative and would point to the wrong direction for updating η, as illustrated in Fig. 3.5 (b). Since it is known that the derivative $\partial\mathcal{Q}/\partial\eta$ is positive this case is recognised easily. As a correction, the previous slope is used again. A third mechanism is put in place to avoid making a much smaller step in η than in the previous iteration, i.e., avoiding the case $|\eta_{m+1} - \eta_m| \ll |\eta_m - \eta_{m-1}|$. This is necessary to circumvent being committed to small steps for many iterations.

In summary, the iteration for η is wrapped around the conjugate gradient iterations for the wave functions. In each set of wave function iterations, n_{CG} steps are made. The resulting charge is evaluated and used to control a modified secant algorithm for finding the root of the function $\mathcal{Q}(\eta)$. Safeguard mechanisms are applied in three cases: (1) the secant is nearly parallel to the η axis, (2) the slope is negative and (3) only a small step would have to be made.

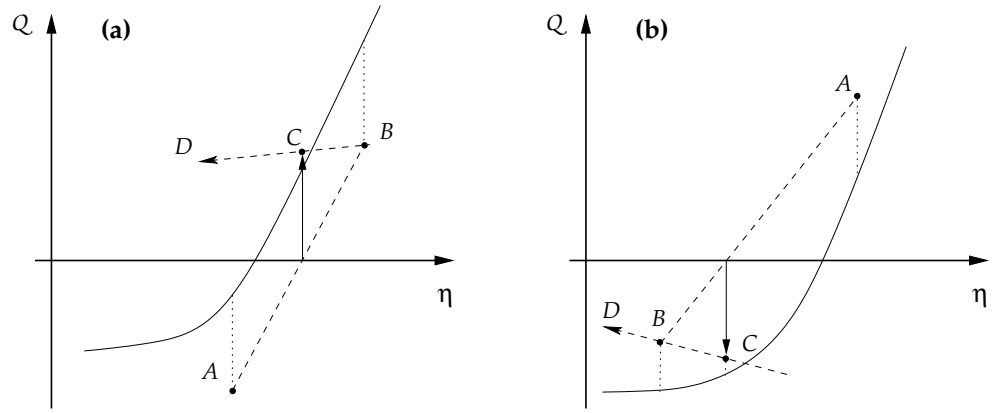

Figure 3.5: Examples for the application of the adaptive secant method to find the root of the function $\mathcal{Q}(\eta)$. The function can be evaluated only approximately. Consecutive function evaluations yield the points A, B and C, each subject to an error $\Delta\mathcal{Q}$. The abscissa of C is obtained from the secant AB. (a) The errors cause the secant BC to point far away from the current search interval $[\eta_A, \eta_B]$. (b) The secant BC has a negative slope, despite the function being known to be monotonously increasing. Safeguard mechanisms are employed to remain near the current search interval.

3.4 The calculation of forces

After convergence is achieved for the wave function and the η parameter, forces on the atoms can be obtained analytically by calculating the derivative of the total energy with respect to the ionic positions. We show here a rigorous derivation of the force expression. We start the calculation by taking into account each independent variable in the total energy expression:

$$\boldsymbol{F}_l = -\frac{\partial}{\partial \boldsymbol{R}_l} E(\{C_{i\mu}, h_{\mu\nu}, s_{\mu\nu}, \gamma_{kk'}\}, \eta, V_{\text{rep}}) \tag{3.24}$$

Thus,

$$\begin{aligned} \boldsymbol{F}_l \;=\; & -\sum_{i\mu}\left(\frac{\partial E}{\partial C_{i\mu}}\frac{\partial C_{i\mu}}{\partial \boldsymbol{R}_l}\right) - \sum_{\mu\nu}\left(\frac{\partial E}{\partial h_{\mu\nu}}\frac{\partial h_{\mu\nu}}{\partial \boldsymbol{R}_l} + \frac{\partial E}{\partial s_{\mu\nu}}\frac{\partial s_{\mu\nu}}{\partial \boldsymbol{R}_l}\right) \\ & -\sum_{kk'}\left(\frac{\partial E}{\partial \gamma_{kk'}}\frac{\partial \gamma_{kk'}}{\partial \boldsymbol{R}_l}\right) - \frac{\partial E}{\partial \eta}\frac{\partial \eta}{\partial \boldsymbol{R}_l} - \frac{\partial V_{\text{rep}}}{\partial \boldsymbol{R}_l} \end{aligned} \tag{3.25}$$

The contributions from the LCAO coefficients $C_{i\mu}$ cancel because the total energy was explicitly minimised in this space and the gradient components $\partial E/\partial C_{i\mu}$ vanish in the ideally converged case. The force contribution due to the repulsive potential V_{rep} is trivial to calculate. The last outright simplification arises from the fact that the total charge is supposed to be well converged; thus the contribution due to the Lagrange parameter η vanishes by virtue of $\partial E/\partial\eta = N_{\text{el}} - q_{\text{tot}} = 0$.

The remaining force components due to the band structure energy are

$$\boldsymbol{F}_l^{BS} \;=\; -\sum_{\mu\nu}\left(\frac{\partial E_{\text{BS}}}{\partial h_{\mu\nu}}\frac{\partial h_{\mu\nu}}{\partial \boldsymbol{R}_l} + \frac{\partial E_{\text{BS}}}{\partial s_{\mu\nu}}\frac{\partial s_{\mu\nu}}{\partial \boldsymbol{R}_l}\right)$$

$$= -2\sum_{\mu\nu}\left\{\widetilde{s}_{\mu\nu}\frac{\partial h_{\mu\nu}}{\partial \boldsymbol{R}_l} - \left(\widetilde{h}'_{\mu\nu} + \eta\widetilde{s}_{\mu\nu}\right)\frac{\partial s_{\mu\nu}}{\partial \boldsymbol{R}_l}\right\}. \tag{3.26}$$

The arrays $\widetilde{h}'_{\mu\nu}$ and $\widetilde{s}_{\mu\nu}$ introduced here are of the same dimension and topology as the Slater-Koster hopping and overlap matrices $h_{\mu\nu}$ and $s_{\mu\nu}$. These arrays are calculated from the converged wave functions:

$$\begin{aligned}\widetilde{h}'_{\mu\nu} &= \sum_{ij} C_{i\mu}C_{j\nu}H'_{ij} = \sum_i C_{i\mu}\overline{C}^H_{i\nu} \\ \widetilde{s}_{\mu\nu} &= \sum_{ij} C_{i\mu}C_{j\nu}Q_{ij} = \sum_i C_{i\mu}\overline{C}^Q_{i\nu}\end{aligned} \tag{3.27}$$

The coefficients $\overline{C}^Q_{i\nu}$ were already needed in the calculation of atomic charges; a related orbital $\overline{C}^H_{i\nu}$ is required here and is calculated analogous to (3.12) from (3.5) and (3.7). The derivatives of the TB hopping and overlap elements themselves are obtained using a finite difference technique.

The force components from the SCC energy contribution are:

$$\begin{aligned}\boldsymbol{F}^G_l &= -\sum_{kk'}\frac{\partial E_\mathrm{G}}{\partial \gamma_{kk'}}\frac{\partial \gamma_{kk'}}{\partial \boldsymbol{R}_l} - \sum_{\mu\nu}\frac{\partial E_\mathrm{G}}{\partial s_{\mu\nu}}\frac{\partial s_{\mu\nu}}{\partial \boldsymbol{R}_l} \\ &= -\Delta q_l\sum_k \frac{\partial \gamma_{kl}}{\partial \boldsymbol{R}_l}\Delta q_k - 2\sum_{\mu\nu}\left(\frac{G_{k[\mu]}+G_{k[\nu]}}{2}\widetilde{s}_{\mu\nu} - \widetilde{g}_{\mu\nu}\right)\frac{\partial s_{\mu\nu}}{\partial \boldsymbol{R}_l}\end{aligned} \tag{3.28}$$

The first term contains the components due to the changing Madelung sums and the second term contains those due to changes in the atomic charges. There is no contribution due to $\partial E_\mathrm{G}/\partial h_{\mu\nu}$. The derivatives of the Madelung terms are obtained analytically. The array $\widetilde{g}_{\mu\nu}$ is obtained from the overlap matrix of the $\widehat{g}$ operator

$$G_{ij} = \sum_{\mu\nu} C_{i\mu}C_{j\nu}\frac{G_{k[\mu]}+G_{k[\nu]}}{2}s_{\mu\nu} \tag{3.29}$$

and its projection on the orbital pairs analogous to eq. (3.27) defined as

$$\widetilde{g}_{\mu\nu} = \sum_{ij} C_{i\mu}C_{j\nu}G_{ij} = \sum_i C_{i\mu}\overline{C}^G_{i\nu} \tag{3.30}$$

With all forces at hand, a Verlet algorithm for MD or an ionic conjugate gradient scheme can be performed.

3.5 Accuracy and performance

As a measure for performance of an iterative linear scaling scheme one will look at 3 key quantities: (1) the calculation time for a single iteration step, (2) the number of iterations required for a sufficiently converged solution and (3) the error of this

Table 3.1: Comparison of total energies and charges obtained from exact diagonalisation *(diag)*, diagonalisation with a Hamiltonian cutoff *(cutdiag)* and from the $\mathcal{O}(N)$ functional. The calculations were performed with Localisation Regions of topological radius 2 and 3, marked 'LR 2' and 'LR 3', respectively.

	Diamond	2D Graphite	3C SiC	3C SiC (scc)
N_{at}	216	96	216	216
N_{el}	864	384	864	864
E_{BS} (Hartree)				
diag	−396.339	−178.866	−337.580	−336.897
cutdiag	−396.100	−178.790	−337.537	−336.853
LR 2	−394.990	−178.044	−336.881	−336.143
LR 3	−395.792	−178.586	−337.389	−336.716
$E - E_{\text{cutdiag}}$ (meV/atom)				
diag	−30	−21	−5	−5
LR 2	140	212	83	90
LR 3	39	58	19	18
η (Hartree)				
LR 2	0.15725	−0.14738	0.12983	0.23491
LR 3	0.10616	−0.17270	0.05558	0.10963

solution. With these quantities at hand, an assessment of the *breakeven point* should be possible, i.e., the determination of the problem size at which the linear scaling scheme is at odds with a traditional $\mathcal{O}(N^3)$ scheme. There are also factors related to the initialisation procedure which influence the breakeven point. Apart from the time needed for the setup procedure of interatomic distances and topologies repeatedly required when the ionic positions are changed the overall timing also depends on the number of initial iterations needed to guide a random start wave function near a first minimum.

Starting from a good initial guess of the Lagrangian η and random wave functions the initial iteration of η and the subordinate energy minimisation require about 150...250 conjugate gradient iterations in total. Significantly less are expected to be needed after updating ionic positions due to extrapolation of previous wave function updates. Based on these values, we give as an estimate for the breakeven point of an initial energy calculation a value of 700 atoms. Important for later molecular dynamics studies is the breakeven point for extrapolated wave functions which we estimate to be about 300 atoms given that only 25 conjugate gradient steps will be needed. It must be stressed that these numbers are estimates.

3.5.1 Energy and charges

The accuracy of the solutions can be assessed from Table 3.1. We have calculated the total energies of 3 test systems: diamond, graphite and silicon carbide in the cubic (3C) polytype. We compare the total energies obtained from diagonalisation and the present non-orthogonal $\mathcal{O}(N)$ method. For the SiC model, we addition-

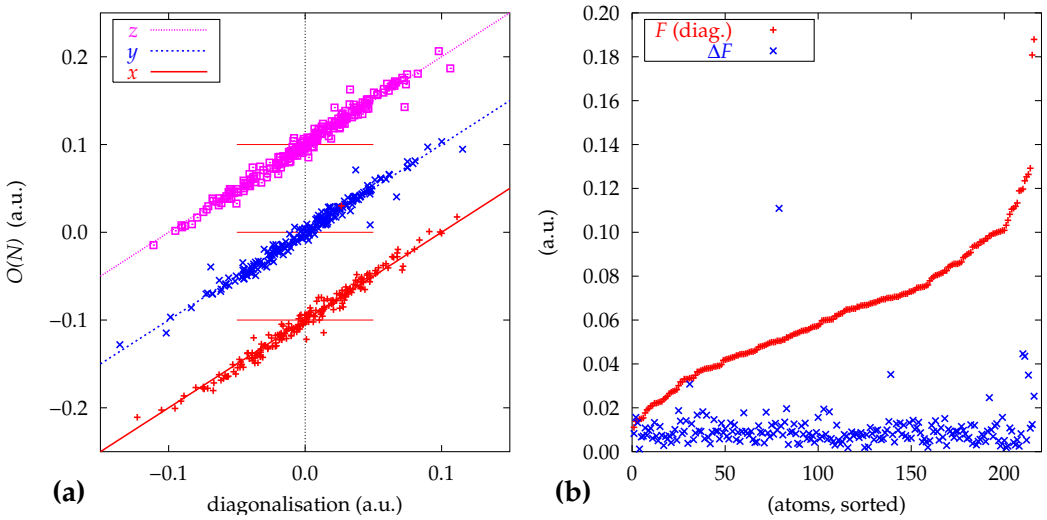

Figure 3.6: Accuracy of the $\mathcal{O}(N)$ force calculation vs. diagonalisation for a 216-atom diamond cell with an artificial hydrogen substitutional atom and all atoms randomly displaced by up to 0.2 Å. The localisation range (LR) for the $\mathcal{O}(N)$ calculation is 2. (a) Force components in x, y, and z directions (vertically separated by 0.1 a.u.). (b) Comparison of the magnitude of exact forces F and their deviations ΔF in $\mathcal{O}(N)$, sorted by F.

ally check the accuracy of the self-consistent charge corrections. The error in total energy for the localised solutions with respect to extended orbitals obtained from diagonalisation is of the order of 100 meV per atom for localisation regions of radius 2 hops and expectedly much smaller, with a value of about 30 meV, for localisation regions extending up to 3 hops. The error is highest with 233 meV total in the case of graphite. Since this system is metallic and has delocalised electronic states a higher deviation is expected. For metallic systems, the convergence is expected to be polynomial with the size of the localisation region. Given that the same number of neighbour hops was applied as in the semiconducting diamond crystal, the results are satisfactory. For both carbon systems, the influence of the cutoff Hamiltonian as obtained from diagonalisation is about 30 meV per atom due to the long range of the unconstrained basis orbitals, while in the mixed SiC system, the contribution due to the Hamiltonian cutoff alone is with 5 meV per atom negligible. In other words, the errors in diamond are larger because the DFTB-basis overlap for pure carbon are farther reaching in units of nearest-neighbour distance and the localisation region cutoff in terms of neighbour hops implies a larger error.

The self-consistent charge contributions to the total energy and the charge transfer itself agree well between diagonalisation and the localised functional. In the SiC structure the charge transfer, i.e., the overcharge of a carbon atom in electrons, is 0.630 from direct diagonalisation, while we obtain 0.657 with localisation regions of size 2 hops and 0.637 for a 3-hop model.

3.5.2 Forces

To judge the calculation of forces, we prepared a sample model of a 216 atom diamond cell, where one atom was substituted by hydrogen. This cell was subjected

Table 3.2: CPU time per electronic iteration step and memory requirements for diamond structure test systems of varying size. The last column lists the times for the calculation of the γ matrix. Up to 2nd neighbours were included for localisation regions and Slater-Koster cutoffs. All tests were performed on an HP PA7200 processor.

n_{at}	t_{BS} s	$t_{\mathrm{BS+SCC}}$ s	mem BS MB	mem γ MB	t_γ s
216	26	65	36	0.4	40
512	78	182	91	2.0	276
1024	159	373	187	8.0	1160
2048	325	765	396	32.0	5250

to a random displacement of all atoms, and then the total energy was minimised as before, with a localisation range of 2 hops for the wave function. The model so constructed represents a structure far off the equilibrium, and therefore should be a quite reasonable test case for the algorithm. The forces for this model were calculated with both localised orbitals as described in 3.4 and using traditional diagonalisation. Fig. 3.6(a) shows the comparison of these results in the form of a scatterplot for each force component on all atoms. As one would expect, the forces for carbon atoms away from the defect site are reasonably exact, such that the total deviation ΔF per atom is in general less than $0.02\,\mathrm{H}/a_B$. The deviation is independent of the force magnitude itself, see Fig. 3.6(b). For the defect ligands, the deviation value nearly doubles, and reaches $0.12\,\mathrm{H}/a_B$ for the defect atom which is in the same order of magnitude as the forces themselves.

Given that forces are derivative quantities, their accuracy is expected to be lower than that for the energy. The given example presents quite a challenge in that the electronic structure near the defect will be considerably disturbed. Obviously, the force calculation is not quite accurate enough near such distortions. It remains to be seen if this would limit practical applications. Throughout the rest of the structure, however, the forces should be sufficiently accurate and suitable for an ionic minimisation procedure.

3.5.3 Scaling

The implementation performs with linear scaling, confirmed by tests run on diamond structures with the number of atoms reaching up to 2048. Results for CPU times and memory requirements are shown in Table 3.2 and Fig. 3.7. Clearly, both time and memory requirements for the electronic minimisation scheme indeed scale linearly. When SCC corrections are switched on, the scaling is still linear, apart from quadratic admixtures in the calculation of the γ Madelung matrix once per ionic step as discussed earlier. Comparing the overall timing for the non-scc and scc calculations, one sees from Table 3.2 that an electronic iteration step which includes the scc corrections requires a factor of 2.3 of the CPU time needed for the band structure term alone. The increase is largely due to the computational cost in establishing the atomic charges and their derivatives, since they invoke the large overlap matrix between support functions. Overall, the factor is quite satisfactory. However, caution is required in comparing this at face value with the approximately five- to tenfold

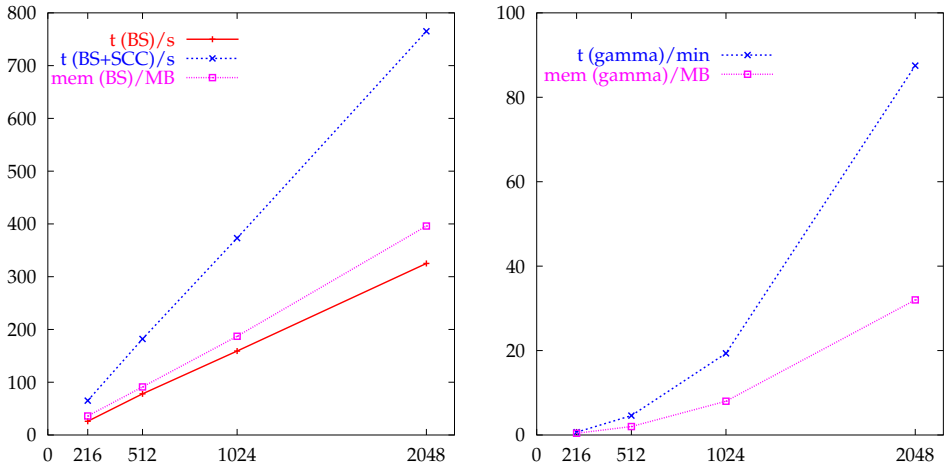

Figure 3.7: Scaling behaviour for CPU time and memory requirements for diamond structure test systems of varying size. Data from Table 3.2.

increase in time in the diagonalisation scheme. No systematic comparison has been made about whether the $\mathcal{O}(N)$ scheme including the SCC correction requires more electronic iteration steps than without. Given the iterative nature of the procedure such an estimate would be difficult at this point.

3.5.4 Assessment

As mentioned in the introduction, a great deal of work has been performed in the $\mathcal{O}(N)$ community [73, 74, 79, 80]. Every major electronic structure code was sounded using linear scaling formulations. Nonetheless, the initial enthusiasm has somewhat subsided, because most of the new mechanisms are not really robust enough to act as black-box replacements of standard programs. Most $\mathcal{O}(N)$ schemes, including the present one, are prone to be numerically unstable as the systems undergo electronic changes, particularly the opening or closing of gaps, or topological changes due to atomic reordering. A lot of work will have to be performed to overcome these weaknesses.

Two other solutions to calculate larger systems are discernible. The first relies on the growth of computing capacity. Moore's law [37] was valid for more than 35 years, having predicted an exponential growth of microchip integration density with a doubling time of just 18 months. The same applies for the clock frequency with which the processors are driven. There is all indication that the "law" will hold a few more years, and perhaps beyond, when the current silicon and copper technologies might be replaced. Such developments in computing power enable extensive growth for applications with the continued use of standard algorithms. Parallelisation takes on an increasingly important role, but requires more changes and considerable resources to implement, see, e.g., Ref. [89].

The other solution is the hybridisation of various methods in what is known as multi-scale modelling, where different length scales of the same structure are calculated with different methods at an appropriate degree of accuracy [90].

Chapter 4

Properties of Diamond

4.1 History and economics

Carbon is an exceptionally versatile chemical element. Its ability to form single, double and triple bonds leads to several allotropes of vastly different properties. For the same reason, carbon is also the basis of organic compounds.

The two most important pure forms of carbon are graphite and diamond, both of which have been known for at least two thousand years. The Greek names are $\gamma\rho\alpha\varphi\acute{\iota}\tau\eta\varsigma$ and $\alpha\delta\acute{\alpha}\mu\alpha\varsigma$, respectively, although there is an ongoing dispute about the latter. Before diamond entered the Graeco-Roman world via India, *adamas* ("the invincible") may have referred to other hard substances known at the time, probably corundum (Al_2O_3, ruby and sapphire being its gemstone varieties). The relatedness between diamond and graphite was not recognised until the late 18th century. Graphite was identified as carbon by Carl Wilhelm Scheele (1742–1786) in 1779, see [1, "pencil"]. Extending combustion experiments of Lavoisier, diamond was shown to be carbon by Smithson Tennant (1761–1815) in 1797 [91]. More recently, other allotropes were discovered first in the laboratory, and subsequently found in nature, namely, fullerenes, nanotubes, and amorphous as well as nanocrystalline diamond. A quite large variety of carbon allotropes is found in meteorites [92], many of them diamondlike [93, 94]. The first find of meteoritic "diamonds of microscopic size" dates back over a century ago [95].

On earth, natural diamond is found primarily in two rare types of volcanic igneous rock formations, known as kimberlite pipes and lamproite. Due to erosion of such primary deposits in geological time, diamond is also found in secondary and tertiary alluvial deposits. Contrary to public belief, diamond is mined not only in South Africa but on all continents save Europe and Antarctica. The world's largest producers are currently Australia and Congo (Kinshasa), albeit only 5% of their output is of gem grade. Of comparable volume, but superior quality are the mining operations of Botswana, Russia (Siberia) and South Africa, followed by Namibia, whose alluvial and marine deposits yield well over 90% in gem quality [96, 97].

In developing countries, diamond mining and trade is a major economic factor rivalling the traditional role of oil. E.g., one third of the gross domestic product (GDP) of Botswana stems from diamond mining [98, p. 392], making its economy extremely

vulnerable. During conflicts, groups controlling the relevant areas may secure their financing through diamond trade. Three situations of this type recently occurred within Africa, namely, in Sierra Leone, the Congo Republic, and Angola [99, p. 390]. UN trade sanctions where put in place, if only to little effect on diamond markets in the western world due to extensive smuggling and the lack of distinctive indicators of origin once the stones are properly cut [100, 101].

For the last decade, the (official) worldwide mining output has been around 100 million carats annually, i.e., 20 metric tonnes, of which 80% are of industrial grade. A further 400 million carats or 80 metric tonnes of *synthetic diamonds* are being produced annually [97], mostly in a high-pressure high-temperature process from graphite, at conditions of about 2000 K and 7 GPa , see [1, "synthetic diamond"]. One of the primary applications of industrial grade diamond is in abrasives and sintered tool coatings; this takes the lion's share of the annual production. Curiously, the application of diamond in tools is not a modern invention. From characteristic groove and fracture patterns in ancient quartz beads, there is convincing indirect evidence for the use of diamond-fitted drill bits in ancient India as far back as 250 BC [102].

The properties which are traditionally associated with diamond are its extreme hardness (Mohs 10) and high refractive index (2.46–2.40, blue to red [2, p. 229]). Both of these, accompanied by a high optical dispersion give diamonds its adamantine lustre and gemstone value. However, diamond has many more interesting properties. This is the major playing field of diamond grown by chemical vapour deposition (CVD), because this technology allows to coat surfaces and to create large-area wafers. In most bulk properties, CVD diamond is on par with natural diamond, although hardness and particularly strength are often reduced by factors around two [103]. In other characteristics, CVD films are potentially superior to natural diamond because their morphology and impurity concentration may be controlled to some extent as needed.

The origin of CVD diamond research dates back to 1949, when Eversole started his work on diamond synthesis, leading to growth on seed crystals in 1952, eventually patented in 1962 [104], yet after similar work has been performed in the Soviet Union by Deryagin in 1956. Since then, great effort went into developments to stabilise the growth of diamond over graphite and subsequently increase growth rate, building upon initiatives in the groups of John Angus in the U.S., Boris Spitsyn in the Soviet Union, and Yoishiro Sato et al. in Japan. The definitive account on the history of diamond CVD growth from early on was given by Angus [3, 105]. Recent developments are targeted at viable commercialisation for a broad range of applications [107].

4.2 Bulk structure and properties

The key towards understanding the extreme properties of diamond lies in its crystal structure. The crystal structure of diamond is prototypical for four-valent semiconductors. Each carbon atom is surrounded tetrahedrally by four neighbours. Out of this basic tetrapodal building block the crystal is constructed as illustrated in Fig. 4.1(a). In terms of Bravais lattices, the crystal is a face-centred cubic (fcc) lattice with a diatomic basis. The basis can be taken as just one corner atom plus the centre

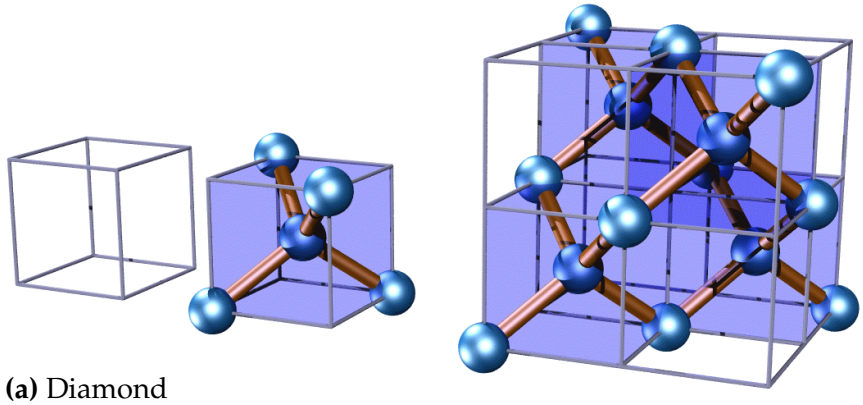

(a) Diamond

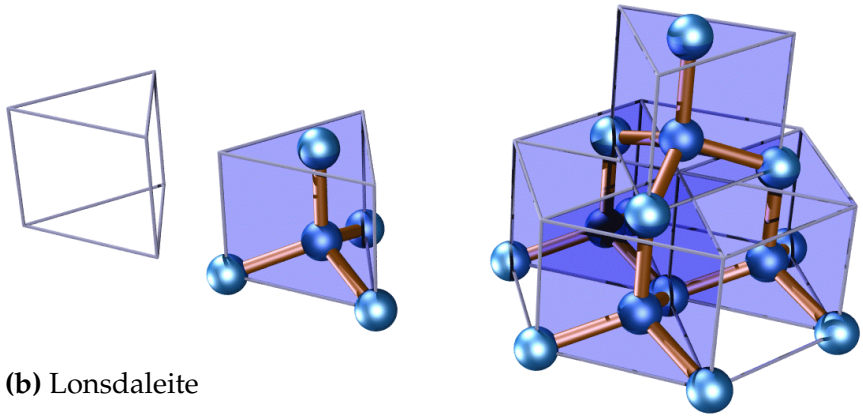

(b) Lonsdaleite

Figure 4.1: The crystal structure of diamond and Lonsdaleite ("hexagonal diamond"), built by repetition of tetrahedrally bonded blocks. (a) Nearest neighbours define four corners of a cube. Cubes are stacked to form a cubic lattice. (b) Nearest neighbours define a triangular prism. Prisms are stacked to form a hexagonal lattice.

atom of the cubic building block in Fig. 4.1(a). A rare variety of the crystal structure with the same nearest-neighbour configurations but hexagonal stacking is named lonsdaleite [Fig. 4.1(b)], after Dame Kathleen Lonsdale (1903–1971). She determined the lattice constant of individual (cubic) diamonds accurate to six significant digits (3.56665–3.56723 Å) using her novel divergent-beam X-ray technique [109]. It is interesting to note that the atomic number density resulting from the crystal structure of diamond is the highest of any known substance [3].

Diamond has the highest sound velocity of any solid and hence exhibits an exceptionally high heat conductivity,[1] about 15–20 $\mathrm{W\,cm^{-1}K^{-1}}$, which is more than four times that of copper [107, p. 62]. The reason for this virtue is a combination of three key factors. Firstly, the carbon atoms are strongly covalently bonded in a rigid lattice. Secondly, the atoms are relatively light. Thirdly, the crystal is simple enough to reduce dissipation by anharmonicity and optical phonons [110]. Similar conditions also hold for individual graphitic basal planes and carbon nanotubes. For both, anisotropic thermal conductivities with maxima exceeding diamond have been conjectured [111, and references therein]. However, as bulk material diamond is real, proven, and unsurpassed.

[1] This lends diamond stones a cold touch, and hence, the quite appropriate slang sobriquet *ice*.

This still holds for CVD diamond (despite its higher density of structural inhomogeneities like grain boundaries) and thus accounts for one of its major application as heat spreader in microelectronics. In this role, there are a number of futuristic applications like heat sink packs on the decimetre scale, where diamond helps to dissipate enormous amounts of heat produced by conventional integrated electronic devices [97]. One of the problems encountered in this context is that due to the strong covalent bonding diamond has an extremely low thermal expansion coefficient of $0.8 \times 10^{-6}\,\mathrm{K}^{-1}$ (at 300 K), which is lower than Invar, as Angus points out [3]. Since this is widely disparate from the chip carriers, mechanical stress ensues which may lead to device delamination.

The phonon spectrum of diamond gives rise to a single characteristic Raman peak [112] at $1332.5\,\mathrm{cm}^{-1}$. This peak is ubiquitously used to confirm the presence of diamond in thin films. This includes ultrananocrystalline films, where Raman scattering results corroborated the nature of the material. In general, the integrated peak area as compared to that of a broad graphitic band at about $1580\,\mathrm{cm}^{-1}$ is often interpreted as a measure of film quality.

Electronically, diamond spans the range from insulator to semiconductor, depending on the impurity density. The pure material has a large indirect bandgap of 5.49 eV, making it an insulator. It is easily *p*-type doped by boron and forms a semiconductor. The acceptor level lies 0.37 eV above the valence band [113, p. 56]. In contrast, nitrogen as a most likely *n*-type dopant forms deep levels at about 1.7 eV below the conduction band minimum [114]. Natural diamond is classified into types Ia (the most frequent and most impure), Ib, IIa and IIb (both rare and virtually pure). These classes are largely determined by the concentration and degree of agglomeration of nitrogen impurities [103, p. 51], c.f. [112]. Pure diamond is one of the best insulators. Its resistivity is above $10^{14}\,\Omega\,\mathrm{cm}$; through heavy boron doping, this may be decreased to well below $1\,\Omega\,\mathrm{cm}$ [113], making it a semimetal. It is one of the most pressing challenges to find a solution to produce shallow *n*-type doped CVD diamond, to pave the way for high-temperature high-power device applications. However, the recent advent of silicon carbide (SiC) is likely to surpass diamond in this respect.

Because of the large bandgap, pure diamond is colourless and transmissive for light in a broad range of wavelengths from infrared (IR) well into ultraviolet (UV), which accounts for the application of suitably polished CVD diamond wafers as extremely robust optical windows, e.g. in weapons targeting systems. Depending on the concentration of various dopants and defects, diamond becomes tinted. For instance, in boron doped diamond, acceptor levels above the valence band result in absorption of photons with relatively low energy, lending the material a blue appearance. Conversely, in nitrogen-doped diamond, electrons from the deep donor states may be excited into the conduction band by absorbed blue light, giving the material a yellow or red tinge. The prediction of colour, however, is a trifle more complex. Besides the dopant levels, it also depends upon selection rules and Franck-Condon-factors.

Certain diamond surfaces have a negative electron affinity (NEA) and are therefore capable of cold electron emission which makes them highly attractive for flat-panel displays [115].

Table 4.1: Elementary properties of low-index diamond surfaces. The nomenclature is the same as in Fig. 4.2; a_D denotes the cubic lattice constant (expt. 3.567 Å).

Face	Lattice	Mesh size	Atoms per cell	Dangling bond density		
				per atom	per area a_D^2	%
$\{111\}_{1db}$	hexagonal	$a_D/\sqrt{2}$	1	1	$4/\sqrt{3}$	100
$\{111\}_{3db}$	hexagonal	$a_D/\sqrt{2}$	1	3	$12/\sqrt{3}$	300
$\{110\}$	rectangular	$a_D \times a_D/\sqrt{2}$	2	1	$2\sqrt{2}$	122
$\{100\}$	square	$a_D/\sqrt{2}$	1	2	4	173

In CVD films, diamond occurs as microcrystalline or nanocrystalline phase, with grain sizes in the micrometre and nanometre range, accordingly. The grain boundaries vary widely in thickness and proportion across the various film types and play a crucial role in establishing the physical properties of the macroscopic film. Reference data on both diamond bulk and films are to be found in the excellent recent compilations within Prelas et al. [2].

4.3 Diamond surface structure

4.3.1 General properties

Most of the surface properties of diamond depend on the crystal face exposed. Each surface has its own characteristics with regards to the unreconstructed (i.e., as-cleaved) two-dimensional surface lattice, and the number of broken bonds per unit area. These characteristics are summarised for the key low-index Miller faces in Table 4.1, and their geometric relation is illustrated in Fig. 4.2. Evidently, there are two different ways to cut along a $\{111\}$ plane, either leaving one or three dangling bonds per surface atom. The resulting faces are labelled "1db" and "3db" faces, respectively. The last column in Table 4.1 establishes the relative strengths of the various surfaces as predicted by the so-called bond scission model. This model assumes that the cleavage energies are proportional to the density of bonds to be severed when the crystal is cut along a certain plane. It is long known that natural cleavage occurs along $\{111\}$ faces, which is indeed explained by the bond scission model. There are eight such faces forming an octahedron, a familiar shape of natural diamonds. The nature of cleavage was largely considered to be understood, yet the debate has recently been revived to understand the fracture process [116].

On conventional CVD diamond, the faces exposed will be those which grow *slowest*, because the faster growing faces will quickly grow themselves out of existence, their edges stacking up to the other faces. The slowest growing faces are $\{111\}$ and $\{100\}$, leading to crystallites of cubo-octahedral morphology. Their shape is usually classified in terms of a growth parameter $\alpha = \sqrt{3}v_{100}/v_{111}$, which relates the growth rates of the two indicated faces (see e.g. [117]). The crystallites will be cubic at $\alpha = 1$, cubo-octahedral for $1 < \alpha < 3$, and octahedral at $\alpha = 3$. The α-parameter depends on growth conditions like the gas composition and the substrate temperature, and can be adjusted in a controlled fashion.

The nanoscale structure of the surfaces is determined by the chemical bonding of

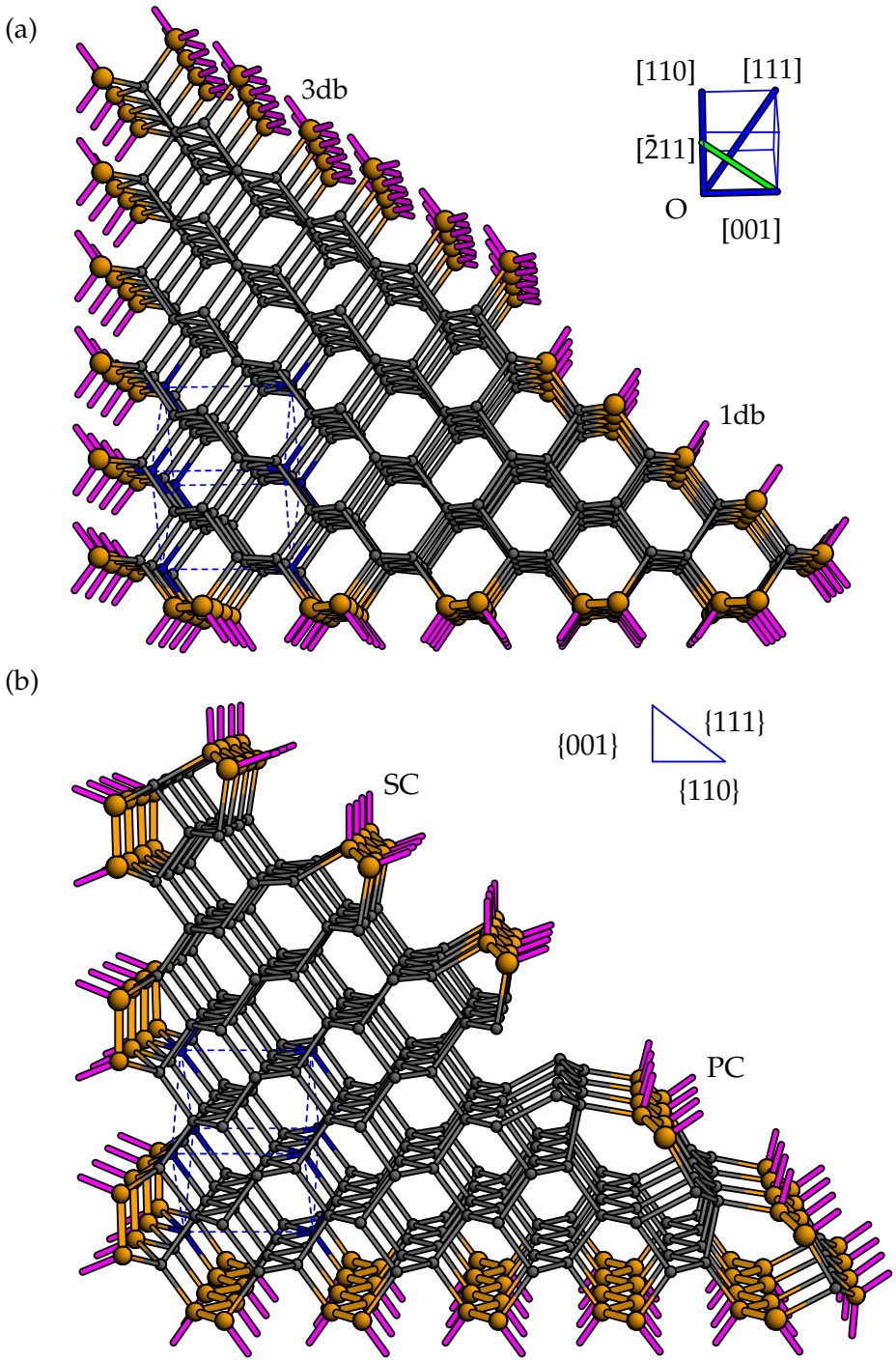

Figure 4.2: Geometry of diamond surfaces. The low-index crystallographic planes are shown in relation to each other. (a) unreconstructed (as-cleaved) surfaces, with crystallographic *directions*, and (b) reconstructed $\{111\} - (2 \times 1)$ and $\{100\} - (2 \times 1)$ surfaces (schematic); the $\{110\}$ faces do not reconstruct. The inset shows the crystallographic *planes*. The stubs on each surface atom represent dangling bonds. The labels differentiate the one- and three-dangling bond cutting planes of the $\{111\}$ faces ("1db" and "3db") and their Pandey- and Seiwatz chain ("PC" and "SC") reconstructions, respectively. The cube inscribed within the bulk section indicates a unit cell of the bulk lattice (cf. Fig. 4.1).

surface atoms. Due to missing bond partners the outer atoms of a surface are severely perturbed from their bulk configurations and will therefore find new equilibrium positions. The energy of surface atoms is reduced on the order of 1–3 eV by two related mechanisms. The first effect, called *relaxation*, is a strengthening of the bonds between the outer monolayers and the bulk, leading to a slightly decreased layer distance. The other effect is due to newly formed bonds between surface atoms or surface atoms and adsorbates and is called *reconstruction*. The driving force towards reconstruction is a saturation of dangling bonds. In general, reconstruction lowers the symmetry of the surface net. Deeper layers near the surface often also relax up to about 0.1 Å. In diamond, the influence of the surface more or less subsides beyond the fifth or sixth monolayer.

The surfaces are crystallographically characterised by a two-dimensional Bravais lattice, called *net*, with the basis vectors determined by the ideal, unreconstructed surface. Reconstructions are labelled in simplified form as $(m \times n)R\alpha$, where m and n (not necessarily integers) are the mesh sizes relative to the original mesh and α is an angle specifying a possibly rotated mesh. The $R\alpha$ notation is omitted in the absence of mesh rotation. A more elaborate nomenclature is required (but not relevant here) when the reconstructed mesh is sheared, see, e.g. [118, chapter 19].

It is difficult to obtain unambiguous atomic-scale structural information about surfaces from experiments. Commonly used techniques are:

LEED (low-energy electron diffraction). LEED data are essentially two-dimensional Laue diagrams of electron waves. In fact, the wave nature of the electron was discovered accidentally by Davisson and Germer using this technique [119]. LEED yields the crystallographic surface structure, i.e., the mesh type and width. Often, several domains are present on a microscopic scale and mix in the diffraction pattern.

HREELS (high-resolution electron-energy-loss spectroscopy). This technique measures the energy loss of electrons due to excitation of surface vibrations, see e.g. Ref. [120]. It provides indirect structural information by comparing the spectra with those known from molecules. Both HREELS and LEED require periodic surface structures and average over them.

STM (scanning-tunnelling microscopy). STM and related techniques like AFM (atomic force microscopy) locally probe the surface with a possibly atomic-scale tip and are thus able to resolve surface structures directly on atomic scales. They do not require surface periodicity and can thus distinguish domains and even identify irregular structures. Scanning techniques paved the way for major advances of surface science in the 1990s. Binnig and Rohrer invented the instrument a decade earlier [121] and were awarded part of the 1986 Nobel Prize in Physics [20].

Because atomic scale information on surfaces is difficult to obtain at any rate, theoretical studies have played an important role to complement and interpret experimental results.

4.3.2 The individual surfaces

In the following, a brief overview of the three main surfaces of diamond and their dominant reconstruction will be given. An extensive review on experimental and theoretical evidence can be found in Ref. [122]. A more detailed analysis of the $\{111\}$ and $\{100\}$ surfaces in conjunction with STM and HREELS results was presented earlier in Refs. [49, 50]. Growth processes on the $\{110\}$ face are studied in Chapter 5.

Hydrogen is often present in the feed gasses and plays an essential role in stabilising the surfaces in the conventional growth scheme. For this reason, hydrogen-terminated surfaces will be discussed alongside clean, uncovered ones. In general, hydrogen may be desorbed by heating surfaces above approx. 1000 °C. In order to prevent re-adsorption, the surfaces are usually cleaned and subsequently investigated in ultrahigh vacuum (UHV) systems.

The $\{111\}$ surfaces

The unreconstructed, $\{111\} - (1 \times 1)$ surface net is hexagonal. Of the two cutting planes, the lower-energy one (1db), shows one dangling bond normal to the surface per surface atom. The clean surface is unstable against graphitisation and delaminates at temperatures above approx. 3000 °C [123, 124, 125, 126]. Delamination occurs preferentially at twin boundaries and near step edges [127]. In contrast, when hydrogenated, the $\{111\} - (1 \times 1)$:H surface is the most stable among all other hydrogenated reconstructions and thus routinely found in LEED patterns.

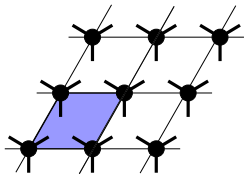

Figure 4.3: $\{111\} - (1 \times 1)$ surface net (hexagonal)

In the absence of hydrogen, the $\{111\}_{1db}$ face is most stable in a (2×1) reconstruction as observed by LEED. Numerous studies have now confirmed this reconstruction to be due to π-bonded chains as suggested by Pandey [128], illustrated in Fig. 4.2(b), labelled "PC". A bond switch between the atoms of the first and second monolayer leads to characteristic five- and seven-fold rings underlying the chains. The chains themselves are unbuckled, i.e., perfectly flat. Note that on the silicon $\{111\}$ surface these chains occur in an identical topology, yet are buckled. In fact, Pandey arrived at his suggestion for diamond by extrapolating the silicon results [129], taking into account the stronger ability of carbon to form π bonds.

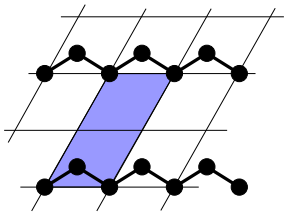

Figure 4.4: $\{111\} - (2 \times 1)$ surface net

At an additional monolayer coverage the surface corresponds to the $\{111\}_{3db}$ cutting plane and reconstructs in a (2×1) pattern into so-called Seiwatz chains [130], see Fig. 4.2(b), labelled "SC". Note that such chains occur as structural units within the Pandey chains. Other reconstructions often occur during and after growth as a result of chemisorption. For example, a $(\sqrt{3} \times \sqrt{3})R30^\circ$ reconstruction was deduced from STM data and explained theoretically as a quite strained trimer (C_3/C_3H_3) configuration [131], possibly stabilised by hydrogen. Of similar mesh

size, and thus difficult to discern in STM by its absolute length scale alone is a (2×2):CH_3 methyl superstructure. Based on energetic considerations and by relating the domains to nearby (2×1) domains in STM images some of the earlier assignments could be revised to be more likely (2×2):CH_3, as shown in Ref. [50, 117].

The {110} surface

The $\{110\}$ surface is the least studied one experimentally. The clean surface as obtained from bulk cleavage has one dangling bond per atom pointing at an angle of 35.3° away from the surface normal (i.e., 90° minus half the tetrahedral angle, $\arccos(-1/3) = 109.47°$). The atoms of the top monolayer are arranged in zigzag chains flat on the surface directed along the $[\bar{1}10]$ direction, see Fig. 4.2(a), bottom face. These chains are quite like those of the Seiwatz- and Pandey chains on the $\{111\} - (2 \times 1)$ reconstructed faces. The $[1\bar{1}0]$ chain axis and therefore, the zig-zag step width, which is $a_D/\sqrt{2} = 2.522$ Å, cf. Table 4.1, are the same in all three cases, as is obvious from Fig. 4.2(b). However, the periodicity across the chain direction is given by the cubic lattice constant a_D on the $\{110\}$ face, but is slightly larger, namely, $a_D\sqrt{3/2} \approx 1.22\, a_D$, on the $\{111\}$ face. This makes the patterns distinguishable in experiments, e.g. using LEED or STM.

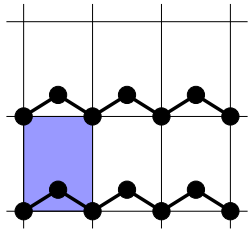

Figure 4.5: $\{110\} - (1 \times 1)$ surface net (rectangular)

The {100} surface

The unreconstructed $\{100\} - (1 \times 1)$ face presents a square net with two dangling bonds per surface atom, each one pointing 54.7° away from the surface normal (i.e., half the tetrahedral angle). The clean face is rarely seen in this configuration because the dangling bonds easily combine, leading to a (2×1) reconstruction (see below). Hydrogen saturation of both dangling bonds (i.e., a two-monolayer coverage) has been suggested [132, 133] but this leads to a strong steric repulsion between the hydrogens. A herringbone structure of the dihydrogenated units may relieve some of the stress [134]. Oxygen is variously able to singly bond to surface atoms or bridge two dangling bonds maintaining the (1×1) pattern [135].

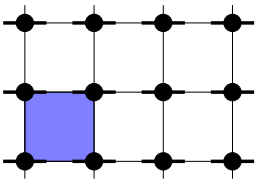

Figure 4.6: $\{100\} - (1 \times 1)$ surface net (square)

After annealing at moderate temperatures the $\{100\}$ surface reconstructs easily into (2×1) patterns by bonding between neighbouring carbon atoms. The resulting carbon dimer and dimer rows are a fingerprint feature of this surface. There is general agreement that on the clean surface the dimer bond is a weak π double bond. However, upon hydrogenation, the dimer bond transforms into a rather stretched σ-type single bond.

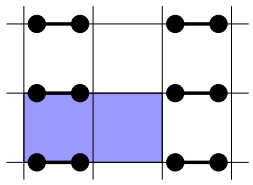

Figure 4.7: $\{100\} - (2 \times 1)$ surface net

Table 4.2: Pseudo-atom parameters used for the subsequent SCC-DFTB calculations: r_0 and r_0^ϱ – compression radii for wave function and density (see section 2.3.1 on page 21), E_s and E_p – onsite energies, E_{psat} – sum of occupied onsite energies, U – chemical hardness parameter. The onsite energies have been calculated for free atoms with the PBE exchange-correlation functional [139], and the U parameter using eq. (2.28).

Type	r_0 (a_B)	r_0^ϱ (a_B)	E_s (H)	E_p (H)	E_{psat} (H)	U (H/e^2)
H[a]	2.4	3.3	−0.238600		−0.238600	0.406483
C[b]	2.7	7.0	−0.504892	−0.194355	−1.398494	0.364302
N[c]	2.2	11.0	−0.681969	−0.260728	−2.146122	0.43
Si[d]	3.3	6.7	−0.395725	−0.150314	−1.092078	0.247609

[a] Parameter file: `hh_sieck.spl` (A. Sieck)
[b] Parameter file: `cc7.0_2.7.spl` (M. Elstner/R. Gutierrez)
[c] Parameter file: `nn-epatch.spl` (M. Elstner/M. Sternberg)
[d] Parameter file: `sisi6.7_3.30.spl` (A. Sieck)

When the surface is cut at heights differing by one monolayer, the (2×1) reconstruction occurs in two domains rotated by 90°. As with the other surfaces, such domains are difficult to distinguish by LEED, but relatively easy to resolve in STM, see the review in Ref. [117] and more recent results in Ref. [136]. Between the domains, characteristic step edges form, which are classified according to Chadi [137] as S_A, S_B, D_A, and D_B (single- and double steps). The step edges are of utmost importance during growth as adsorption sites and stopping point for diffusing species, leading to layer expansion and thus promoting layer-by-layer growth [138].

Again, on the silicon $\{100\} - (2 \times 1)$ face the same topology occurs. As was the case for the Pandey chains, the silicon dimer chains are buckled and the diamond ones flat. The reason for the different morphology is the same, namely, carbon being able to form π bonds.

4.4 Reference calculations on diamond bulk and surfaces

Numerous previous DFTB studies have been performed on diamond, but the SCC variant of the method has not been extensively tested on diamond bulk and surfaces. In this section, the DFTB results for various carbon bulk systems are presented, with the aim of obtaining reference values for total and cohesive atomic energies, and to verify the influence of the cell sizes for supercell calculations. The calculations also serve as a more detailed overview of the main surface reconstructions.

4.4.1 Atomic and diatomic energies

First, Tables 4.2 and 4.3 gives the energies for the elements which enter the subsequent calculations. The atomic energies for H and N will be used as chemical potential in the calculation of formation energies for surfaces and substitutional defects. The atomic energy for carbon is the reference point for cohesive energies.

Table 4.3: SCC-DFTB reference calculations for diatomic molecules of the total energy E_{tot}, excluding zero-point vibrational corrections, and the equilibrium bond length d.

Type	E_{tot} (H)	E_{tot} (eV/atom)	d (Å)
H_2	−0.71703	−9.7557	0.743
C_2	−3.16820	−43.1055	1.241
N_2	−4.89390	−66.5849	1.118
CN[a]	−4.01033	−54.5634	1.166

[a] Mulliken populations: $q_{\mathrm{C}} = 3.9188\,e$, $q_{\mathrm{N}} = 5.0812\,e$.

4.4.2 Bulk systems

Calculations of bulk diamond and graphite are summarised in Tables 4.4 and 4.5, respectively. For diamond, supercells in various orientations with respect to the cubic crystal directions were used, primarily in order to provide the necessary geometries for subsequent surface calculations. As a side effect, the rundown allows to judge the accuracy of the Brillouin-zone Γ-point sampling. The directions and side lengths of the primitive cells and the number of repetitions making up the supercell are given in the table in terms of the cubic lattice directions and its lattice constant a_{D}. The (111)-oriented supercell shows hexagonal symmetry along its z direction. As is customary, a conventional orthorhombic primitive cell containing two hexagonal cells was used in this case. The extent of the primitive cell along the (hexagonal) $[111]$ axis is given by three (111) double layers in ABC stacking. The (110)- and (100)-oriented cells share the $[001]$ axis, but differ by a 45° rotation about this axis, exposing either $\{110\}$ or $\{100\}$ faces on the other sides, respectively.

The equilibrium lattice constant for the used parameter files (i.e., the repulsive potential) was obtained by sampling various scaled supercells of type (110) and (111) containing 256 and 288 atoms, respectively. The result for the equilibrium diamond lattice constant is $a_{\mathrm{D}} = 3.562$ Å. The same calculations allowed an estimate of the bulk modulus via the definition:

$$B_0 = -V_0 \frac{\partial^2 E_{\mathrm{coh}}}{\partial V^2}\bigg|_{V_0} . \tag{4.1}$$

The result thus obtained by taking numerical derivatives is (541 ± 10) GPa, which is 22% above the experimental value of 442 GPa as determined by ultrasonic waves [141, 142]. A more involved fitting procedure of the total energy curve to the Murnaghan equation of state [143, 144] yielded the same value while a non-SCC DFTB parameter set gives 487 GPa (10% above the experimental value) [145].

The total energy is converged for cells with $N_{\mathrm{at}} \geq 216$, corresponding to supercell sizes above approx. 10 Å in either extent. This supercell size is about twice the effective range of the Slater-Koster integrals for carbon. This is not only well-known behaviour for group-IV semiconductors but also a required criterion for the *nearest-box approximation* generally applied for molecular dynamics simulations here. The cohesive (or binding) energy per atom is 9.278 eV. This is slightly higher than in several other theoretical works [146], but lies well within the interval of variation of about 1 eV by which even the more accurate methods differ.

For graphite, the same supercell type as for (111) diamond was used, but with different stacking of the (now flat) graphene layers. Since the interaction between

Table 4.4: Reference energies of diamond bulk systems calculated with DFTB in the Γ-point approximation at the equilibrium lattice constant $a_D = 3.562$ Å. Atom parameters as in Table 4.2. The cohesive energy E_{coh} is defined as the total energy per atom minus the atomic energy E_{psat} in Table 4.2; (spin polarisation, 1.125 eV/atom [46, sec. 4.3], is *not* included).

Cell type	primitive cells			N_{at}	E_{at} (H)	E_{coh} (eV)
	n_x	n_y	n_z			
	$[1\bar{1}0]$	$[11\bar{2}]$	$[111]$[a]			
	$a_D/\sqrt{2}$	$a_D\sqrt{3/2}$	$a_D/\sqrt{3}$			
(111)	3	2	3	72	−1.74173	−9.340
	3	2	6	144	−1.74230	−9.355
	4	3	6	288	−1.74304	−9.375
	5	3	6	360	−1.74315	−9.378
	[110]	$[1\bar{1}0]$	[001]			
	$a_D/\sqrt{2}$	$a_D/\sqrt{2}$	a_D			
(110)	4	4	2	128	−1.74268	−9.366
	4	4	4	256	−1.74292	−9.372
	[100]	[010]	[001]			
	a_D	a_D	a_D			
(100)	2	2	2	64	−1.74178	−9.341
	3	3	3	216	−1.74310	−9.377

[a] {111} double layer unit.

Table 4.5: Reference energies of graphite calculated with DFTB in the Γ-point approximation at the equilibrium hexagonal lattice constant of $a_G = 2.473$ Å, i.e., at bond length $a_G/\sqrt{3} = 1.428$ Å. Atom parameters as in Table 4.2. The cohesive energy E_{coh} is defined as the total energy per atom minus the atomic energy E_{psat} in Table 4.2.

Cell type	Primitive cells			Layer sep.	N_{at}	E_{at} (H)	E_{coh} (eV)
	n_x	n_y	n_z	$d_{equil.}$ (Å)			
	$[1\bar{1}00]$	$[11\bar{2}0]$	[0001][a]				
	a_G	$a_G\sqrt{3}$	d				
single sheet	4	2	1		32	−1.73928	−9.273
single sheet	5	3	1		60	−1.74010	−9.295
AB stacking	5	3	4	∞	240	−1.74009	−9.295
AB+disp.[b]	5	3	4	3.1	240	−1.74475	−9.422
AA+disp.[b]	5	3	4	3.2	240	−1.74460	−9.418

[a] single sheet units
[b] Ref. [147].

graphene sheets is small at best, the calculation was started with single sheets. The minimum reliable lateral size of a supercell for a single graphene sheet is again approx. 10 Å, as for bulk diamond. The equilibrium lattice constant for graphite was determined by sampling as $a_G = 2.473$ Å.

A drawback of the DFTB method as used is that it does not correctly take into account the van der Waals interaction between individual graphene sheets. In DFTB, the interaction between two such sheets is very weakly repulsive, as is evident

from Table 4.5, column E_{at}, the atomic energy for a single sheet (60 atoms) is lower than for hexagonal graphite (4 sheets, 240 atoms). Furthermore, the cohesive energy for carbon atoms in graphite is 9.295 eV, or about 80 meV above diamond. Zero-point vibrational energies are not included; they would contribute (Ref. [146]) $E_{vib}(\text{diamond}) = 0.1809\,\text{eV/atom}$ and $E_{vib}(\text{graphite}) = 0.1659\,\text{eV/atom}$. Experimentally [3], graphite is more stable than diamond by approx. 30 meV. The recently suggested inclusion of London-type dispersion interactions [147] appears to improve this behaviour qualitatively, as the preliminary calculations in the last lines of Table 4.5 indicate. The dispersion interaction lowers the cohesive energy per atom by 120 meV, making graphite more stable than diamond by approx. 40 meV/atom. The dispersion interaction correctly reproduces the hexagonal AB stacking to be more stable than rhombohedral AA stacking, and roughly estimates the correct layer distance (3.1 Å, vs. 3.37 Å from experiment). Note that the corrections have been included only for these reference calculations, but not in other parts of this work.

4.4.3 Surfaces

With the bulk calculations secured, the subject of surfaces is finally at hand. The surface models discussed here are generated from the bulk supercells presented in the previous section by extending their periodic boundary in the z direction to a sufficiently large value, here, 80 Å. This distance ensures that no direct interaction takes place between adjacent surfaces thus exposed. As is customary in this type of simulation, the dangling bonds on the new "bottom" faces were saturated with hydrogen; the impact of this practice is minimal as we will see.

To furnish a comparison of the DFTB performance with *ab initio* methods, a consistent set of first-principle calculations covering all the relevant bulk and surfaces needed to be selected. The results published in Refs. [133, 148, 149, 150] (using the Vienna *ab initio* simulation package or VASP) provide such a set, and themselves contain extensive comparisons with other *ab initio* methods and semi-empirical ones, including previous non-SCC DFTB results.

In Table 4.6 total energy data are collected for the low- index surfaces and their main reconstructions, both clean and hydrogenated. The details of this table are discussed in the following sections.

DFTB results for the {111} surfaces

A detailed discussion of the geometries of the particularly rich set of reconstructions on the $\{111\}$ face is beyond the scope of the present work. Four surfaces were chosen, since they represent typical cases: (a) the clean (1×1) face, resembling the bulk cleavage situation, (b) the hydrogenated (1×1) face representing the most stable surface among the hydrogenated ones, (c) the clean Pandey chain as most stable clean surface, and finally, (d) the hydrogenated Pandey chain, for consistency. The geometries of these surfaces are given in Table 4.7. For comparison with the Pandey chains, Table 4.6 also contains the energetics of the Seiwatz chains, while a discussion of their geometry has been omitted since it is rather similar to the Pandey chain.

Table 4.6: Reference energies of relaxed diamond surfaces in two-dimensional slab geometry calculated with SCC-DFTB in the **Γ**-point approximation at the bulk equilibrium lattice constant a_D. Cell geometry as in Table 4.4. E_{surf} is the surface energy per site, defined as $E_{surf} = (E_{tot} - N_C E_C - N_H E_H)/N_{site}$ using the atomic energy for bulk diamond and the hydrogen atomic energy in H_2, Table 4.3. ΔE_{rec} is the reconstruction energy per site.

Surface	Cells $x \times y \times z$	N_C	N_H	E_{tot} (H)	E_{surf} (eV)	ΔE_{rec} (eV)	E_{surf}[a] (eV)	ΔE_{rec}[a] (eV)
{111} *surfaces, relaxed, saturated at bottom by hydrogen*								
unreconstructed, clean and hydrogenated								
(1×1)	$5 \times 3 \times 6$[b]	360	30	−635.9754	2.098		2.151	
(1×1):H	$5 \times 3 \times 6$	360	60	−649.0324	0.005		−2.826	
Pandey chain, clean and hydrogenated								
(2×1)−PC	$5 \times 3 \times 6$	360	30	−636.5737	1.555	−0.54	1.356	−0.80
(2×1)−PC:H	$5 \times 3 \times 6$	360	60	−648.1864	0.772	0.77	−2.132	0.69
Seiwatz chain, clean and hydrogenated								
(2×1)−SC	$3 \times 2 \times 6$	132	12	−233.0172	2.873	0.77	2.689	0.54
(2×1)−SC:H	$3 \times 2 \times 6$	132	24	−238.3894	0.445	0.44	−2.403	0.42
{110} *surfaces, relaxed, saturated at bottom by hydrogen*								
(1×1)	$5 \times 3 \times 3$	180	30	−322.5128	1.743		1.66	
(1×1):H	$5 \times 3 \times 3$	180	60	−335.1901	0.021		−2.68	
{100} *surfaces, relaxed, saturated at bottom by two pseudo-hydrogen per carbon*								
(1×1):2H′	$4 \times 4 \times 4$	256	64	−469.3359	−0.087[c]		3.63	
(2×1)	$4 \times 4 \times 4$	256	32	−456.4161	2.288		2.12	
(2×1):H	$4 \times 4 \times 4$	256	32	−463.2214	0.469		−2.42	

[a] From Refs. [148, 149, 150]; Hydrogen accounted for at its atomic energy, $E_H = 13.004$ eV.
[b] The numbering refers to the same cell size as the (2×1) reconstruction, i.e., a rectangular primitive cell containing 2 hexagonal unit cells, cf. Table 4.4. The slab thickness along $z = \{111\}$ is given in units of *double layers*.
[c] Pseudo-dihydrogenated on both top and bottom surface.

First, one sees that the geometry of the hydrogen-saturated (1×1):H face is remarkably bulklike. Laterally, all atoms are on their hexagonal positions. The outer carbon monolayer merely relaxes slightly inwards by 0.014 Å. The relaxations of the other ten monolayers in the 12-monolayer slabs are less than 0.002 Å away from their ideal separations. Equally remarkable is the surface energy for this model, given in Table 4.6.

Subtracting from the total energy of the surface models the diamond bulk energy (using the model of matching size in Table 4.4) as well as the appropriate multiple of the energy of a hydrogen atom in a reservoir of H_2 molecules (Table 4.3), one obtains a surface energy of just 5 meV per (111):H site. Both the absence of relaxation and the near-vanishing surface energy clearly establish that hydrogen-passivation on one side of a $\{111\}$ slab of this type has virtually no influence on the geometry and energetics for reconstructions on the other side.

Now broadening the view to the Pandey- and Seiwatz chain reconstructions one can clearly deduce from their energetics (Table 4.6) that in the absence of hydrogen the diamond (111) face is most stable in the (2×1) Pandey chain (PC) reconstruction

	DFTB	Ref. [148]	DFTB	Ref. [148]
a_D	3.531	3.562		
d_0	1.529	1.542		
	(1×1)		(1×1):H	
d_{H1}			1.12	1.12
d_{12}	1.49	1.46[b]	1.53	1.52
d_{34}	1.54	1.52[b]	1.54	1.53
Δz_{12}	0.34	0.26	0.50	
Δz_{23}	1.64	1.67	1.54	1.54
Δz_{34}	0.49	0.48	0.51	
Δz_{45}	1.55	1.55	1.54	1.53
	(2×1)PC		(2×1)PC:H	
d_{Ha}			1.12	1.11
d_{ab}[a]	1.44	1.43	1.56	1.55
d_{ac}	1.54	1.53	1.58	1.57
d_{bd}	1.54	1.53	1.58	1.57
d_{cd}	1.55	1.54	1.59	1.58
d_{df}	1.67	1.63	1.59	1.59
d_{ce}	1.62	1.60	1.56	1.55
d_{fh}	1.53	1.52	1.53	1.53
d_{eh}	1.52	1.51	1.53	1.52
d_{eg}	1.54	1.53	1.54	1.53
d_{fg}	1.57	1.57	1.57	1.56
d_{gi}	1.60	1.60	1.60	1.59
d_{hj}	1.50	1.49	1.50	1.48
ϑ_1	121.7		107.7	
ϑ_2	108.3		104.2	
Δz_1	0.01	0.01	0.01	0.01
Δz_2	0.00	0.01	0.01	0.01
Δz_3	0.04	0.03	0.04	0.04
Δz_4	0.17	0.17	0.18	0.18
Δz_5	0.07	0.06	0.07	0.07
Δz_6	0.02	0.02	0.02	0.02

[a] undimerised, $5\times3\times6$ primitive cells
[b] calculated from available data

Table 4.7: Calculated geometry of diamond $\{111\}$ surfaces. d_0 is the equilibrium bulk bond length, d_{ab} etc., are the bond lengths between atoms labelled as in the inset figure; Δz_{ij} are the interlayer separations, and Δz_i is the intralayer buckling for monolayer i. ϑ_i is the intrachain bond angle within layer i. The units are Å and degrees.

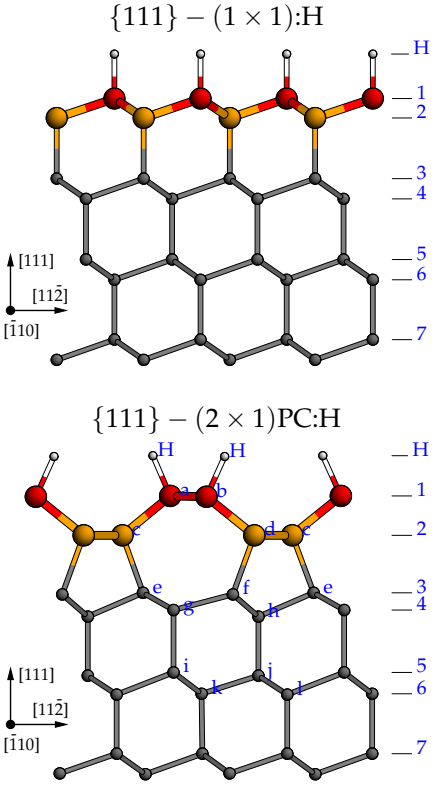

as predicted by Pandey. The surface energy is 1.6 eV per site. The surface energies of the unreconstructed surface and the Seiwatz chain are decidedly higher, at 2.1 eV and 2.9 eV, respectively.

The situation is very different for the hydrogen-covered surfaces. In this case, the unreconstructed $\{111\}-(1\times1)$:H surface is the most stable one, with an extremely low surface energy of 5 meV per site, as noted above, followed by the hydrogenated SC and PC chains with 0.4 eV and 0.8 eV per site, respectively. This means that hydrogenation will induce de-reconstruction of the Pandey chains as is indeed observed [122].

The comparison of the surface energies with the *ab initio* results, given in the last columns of Table 4.6, is highly satisfactory. The energies of the respective reconstructions agree with those obtained from DFTB to within about 0.2 eV per site. Un-

fortunately, in the cited works, the energy of *isolated* hydrogen atoms rather than bonded ones was used to renormalise energies of systems with unequal numbers of atoms. For this reason, the energies for hydrogenated and unhydrogenated surfaces are not directly comparable; nonetheless, those for the same numbers of atoms but different reconstructions are.

The four typical surfaces discussed above were chosen for a statistical comparison of geometries. Because of disparate equilibrium bond lengths in DFTB and VASP, the geometry parameters of VASP, i.e., bond lengths and monolayer separations, must be scaled proportionately to the same bulk bond length, to reach a common footing. This is equivalent to expressing all reconstructed geometry parameters in terms of the equilibrium bond length of the respective method.

With the exception of the clean surface, the root-mean-square (rms) deviation of the bond lengths and layer separations for the uppermost layers, as given in Table 4.7, is below 0.01 Å, after scaling to the DFTB bondlength. The largest discrepancy, 0.08 Å or +30 %, occurs in the buckling of the clean $\{111\} - (1 \times 1)$ face, see Δz_{12} in Table 4.7. Given that this face is unstable at high temperatures, the equilibrium geometry at zero temperature is bound to be a sensitive indicator of accuracy. At any rate, the DFTB geometries are in general astoundingly accurate.

Various methods disagree on whether the zigzag chains of the clean Pandey chain reconstruction are dimerised, i.e., show a Peierls distortion with alternate bond lengths. Ref. [148] reports a tendency for dimerisation depending on $\boldsymbol{k}$-point sampling. The same tendency occurs in DFTB under the $\boldsymbol{\Gamma}$-point approximation. At 4 primitive cells along the $[1\bar{1}0]$ (chain) direction, the bond lengths d_{11} along the chain are 1.39 Å and 1.50 Å, or ±3.8 % in terms of their average. At 5 primitive cells along the chain direction, no dimerisation is found, as given in the table. Unequivocal experimental evidence has yet to be brought forward [151], while theoretically, a reliable prediction of this phenomenon requires many-particle theories.

DFTB results for the {110} surfaces

Table 4.8 compares the geometries of the clean and hydrogenated {110} surfaces, calculated *ab initio* [150] and with DFTB.

The hydrogenated surface shows hardly any relaxation and is therefore equally suitable for hydrogen passivation as the {111} face. This is supported by the low surface energy of just 21 meV per site, see Table 4.6. Both the {111} and {110} surface energies are of course close to the uncertainty of the DFTB method, and are subject to the somewhat debatable normalisation for hydrogen as the total energy per atom in H_2. With the normalisation being the same, however, the meaning of the values is that (a) the surface energy per site on the hydrogenated {111} and {110} diamond surfaces are essentially equal and (b) hydrogen saturation is possible on either face without significant relaxation effects in energy and geometry.

On the clean surface the relaxations are more pronounced than on the hydrogenated one, but still rather small. The upper carbon monolayer moves inward by $\Delta z = -0.15$ Å, and the next layer outward by $\Delta z = 0.02$ Å. The chains in the top layer are slightly straightened by a relaxation of 0.09 Å towards the chain axis, resulting in a bond angle of 121.7° and a bond length of 1.44 Å. For the set of bondlengths

	DFTB	Ref. [150]	DFTB	Ref. [150]
a_D	3.566	3.531		
d_0	1.544	1.529		
	(1×1)		(1×1):H	
d_{H1}			1.117	1.106
d_{11}	1.444	1.419	1.526	1.508
d_{12}	1.491	1.467	1.534	1.520
d_{22}	1.505	1.490	1.542	1.526
d_{23}	1.586	1.576	1.545	1.533
d_{33}	1.541	1.526	1.545	1.530
ϑ_1	121.7	123.3	111.4	111.8
ϑ_2	113.7	113.8	109.7	109.8
ϑ_{H1z}			33.6	33.5
Δz_{bulk}	1.26	1.25	1.26	1.25
Δz_{12}	1.09	1.11	1.24	1.23
Δz_{23}	1.29	1.28	1.26	1.25
Δy_1	±0.09	±0.10	±0.02	±0.02
Δy_2	±0.03	±0.03	±0.00	±0.00

Table 4.8: Calculated geometry of diamond {110} surfaces. Nomenclature as in the previous Table 4.7. In addition, Δy_i is the chain straightening relaxation along $y = [001]$, i.e., transversal to chains. The units are Å and degrees.

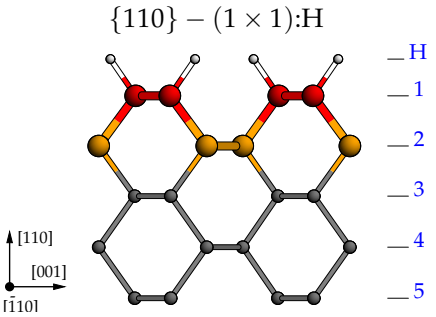

labelled d_{ij}, the rms deviations after matching the lattice constant are 0.008 Å and 0.002 Å, for the clean and hydrogenated surface, respectively, again an astoundingly satisfactory agreement.

While there is general consensus on the zigzag chains of the {110} surface being slightly straightened, there has been some controversy in the literature about a possible dimerisation or buckling [132, 152]. Both of these modifications maintain a (1×1) surface net, which is identical to the unrelaxed surface. Maier et al. [153] were able to conclude from LEED the prevalence of symmetric chains on both the clean and hydrogenated surface by considering extinction rules, i.e., the two-dimensional structure factor. UHV STM experiments [154] as well as *ab initio* studies[150] also indicate a symmetric, undimerised, flat (1×1) surface, which is just the most stable morphology in DFTB.

DFTB results for the {100} surfaces

The {100} surface presents a simple and typical (2×1) reconstruction. The DFTB results on the geometry and a comparison to *ab initio* values are given in Table 4.9. The most critical measure is the length of the characteristic surface dimer and, again, whether it buckles or not. The DFTB result are well in line with the recent *ab initio* data. On the clean surface, the dimer is rather short and similar to a double bond in C_2H_4 (1.33 Å), while on the hydrogenated face it is elongated beyond the single-bond analogue in C_2H_6 (1.50 Å). The dimers are symmetric and unbuckled, as in most other theoretical and experimental studies of this surface [117, 133, 136].

The surface dimer causes a pinchlike strain near the surface which leads to a rather strong buckling of the third and even fourth monolayer. The subdimer atoms along the [110] chain direction of these layers are lower than the sub-gap atoms in the parallel row by 0.25 Å and 0.15 Å, respectively. There is hardly any buckling on the next monolayers, but their intralayer second-neighbour distances (measured parallel to

	DFTB	Ref. [133]	DFTB	Ref. [133]
a_D	3.562	3.531		
d_0	1.544	1.529		
	(2×1)		(2×1):H	
d_{Ha}			1.114	1.10
d_{aa}	1.398	1.37	1.604	1.61
d_{ab}	1.517	1.50	1.544	1.53
d_{bc}	1.571	1.57	1.533	1.52
d_{bd}	1.569	1.55	1.574	1.56
d_{ce}	1.514	1.50	1.520	1.50
d_{df}	1.574	1.56	1.565	1.55
d_{eg}	1.523		1.527	
d_{fg}	1.570		1.562	
d_{gh}	1.542		1.542	
Δy_5	±0.05		±0.03	
Δy_6	±0.03		±0.03	
Δz_{bulk}	0.891	0.88	0.891	0.88
Δz_{12}	0.704	0.67	0.814	0.80
Δz_3	0.249	0.26	0.185	0.19
Δz_4	0.145	0.16	0.108	0.11
			(1×1):H′	
$d_{H'a}$			1.086	
d_{ab}			1.519	
d_{bc}			1.547	
d_{cd}			1.541	
Δy_i			±0.00	
Δz_{12}			0.849	
Δz_{23}			0.899	

Table 4.9: Calculated geometry of diamond {100} surfaces. The nomenclature is the same as in the previous tables, 4.7 and 4.8. Δy_i is the lateral displacement along $y = [\bar{1}10]$. The length unit is Å.

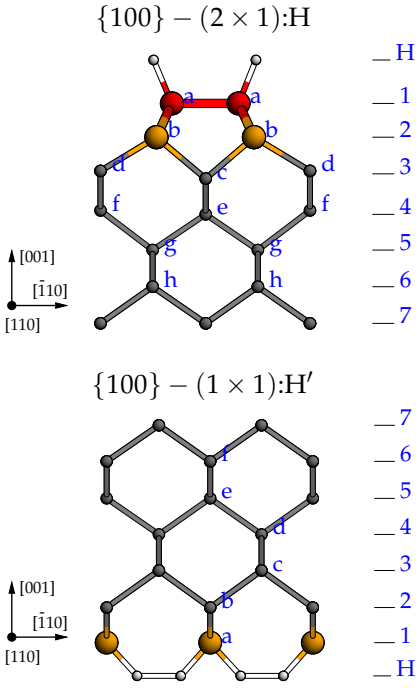

the surface dimer) are still somewhat affected by the strain field of the surface.

The as-cleaved {100} face is difficult to passivate by hydrogen in the same spirit as the {111} and {110} faces. High hydrogen coverage of the {100} face has been the subject of several studies [133, 134], but the goal here is the saturation of both dangling bonds per surface atom with minimal strain. A simple placement of H atoms at a C–H distance of 1.03 Å would result in an H–H separation of 0.83 Å, and thus cause significant repulsion [Fig. 4.2 on page 56]. Fortunately, in DFTB it is possible to circumvent the problem. One usually defines a pseudohydrogen species with its homoatomic interactions switched off while leaving all heteroatomic interactions the same as for regular hydrogen. The resulting geometry, given in Table 4.9, is essentially bulklike from the second monolayer inwards, with very small vertical relaxations. This is clear indication on the viability of this saturation concept.

4.4.4 Summary

This chapter collected various data on the atomic structure of diamond surfaces. By a systematic survey of bulk and surfaces using SCC-DFTB the method under the given parameter set was confirmed to be quite accurate (to within about 0.2 eV/site) and thus sufficient to describe the formation energies of the various reconstructions

Table 4.10: Summary of stable reconstructions on diamond surfaces as calculated using SCC-DFTB; cf. Tables 4.1 on page 55 and 4.6 on page 64.

Face	clean surface			hydrogenated surface	
	structure	E_{surf} (eV)	E_{surf} (%)	structure	E_{surf} (eV)
$\{111\}_{1\text{db}}$	(2×1)−PC	1.555	100	(1×1):H	0.005
$\{111\}_{3\text{db}}$	(2×1)−SC	2.873	185	(2×1)−SC:H	0.445
$\{110\}$	(1×1)	1.743	112	(1×1):H	0.021
$\{100\}$	(2×1)	2.288	147	(2×1):H	0.469

as compared to *ab initio* data [133, 148, 149, 150]. Furthermore, the geometry description is, with rms deviations in the 0.02 Å range, fabulously accurate. Some weaknesses exist in the description of metallic surfaces such as the zigzag chains on the $\{111\}-(2\times1)$ and $\{110\}-(1\times1)$ surfaces, which is partly due to problems in the one-electron description and partly due to numerical problems with scc convergence. Furthermore, the parameter set used has the slight blemish of overestimating the bulk modulus by about 20%.

To close the circle to the bond scission model Table 4.10 summarises the most stable diamond surface reconstructions and their formation energies. Even though the bond scission model does not account for reconstructions it does predict the correct energetic ordering. However, since reconstructions in general reduce the number of dangling bonds, especially on the $\{111\}_{3\text{db}}$ surface where only one bond remains after reconstruction, the high-energy values estimated by the simpler model are significantly off the mark.

The clean surfaces show considerable geometrical reconstructions with appreciable reconstruction energies around 2 eV. In contrast, the hydrogenated surfaces show smaller reconstructions and have reconstruction energies below 1 eV. Therefore, hydrogen saturation is suitable for surface passivation, especially for the $\{111\}$ and $\{110\}$ surfaces. Hydrogen saturation also induces a de-reconstruction on the $\{111\}_{1\text{db}}$ surface.

Chapter 5

Growth of (110) Diamond Using Pure Dicarbon

5.1 Introduction

The growth of ultrananocrystalline diamond (UNCD) films from C_2 precursors produced by C_{60} fragmentation in hydrogen-poor plasmas [4, 155, 156, 157] has recently attracted attention because of the high growth rates and resulting good mechanical and electronic properties of the films. The physical properties of these films, which are mainly determined by their microstructure, must be tuned for each of these applications. Conventional diamond films as grown from H/CH_3 mixtures are characterised by crystallites in the micrometer size range. In several recent experiments [158, 159, 160, 161] it was confirmed that the addition of argon to the plasma allows continuous control over the crystallite size. Most importantly, at argon concentrations in a narrow window around 95%, the resulting films are ultrananocrystalline with a typical crystallite size of just 3–10 nm. Fig. 5.1 illustrates the dramatic change in morphology as a function of the argon percentage in the feed gasses. The transition is accompanied by a marked increase in the concentration of C_2 near the surface during growth. The presence of C_2 and its likely contribution to the growth process have been confirmed experimentally through characteristic intense Swan-band radiation in both microwave plasma chemical vapour deposition [158, 160] (MPCVD) and hot-filament chemical vapour deposition [161] (HFCVD). The resulting UNCD films exhibit a smooth surface and a uniform morphology throughout the film, which has a thicknesses of at least 20 μm. The films are found to be hard, have low friction, and are surprisingly wear resistant [155, 162, 163]. The small size of the crystallites implies that a relatively high percentage (up to 10%) of all atoms are located at grain boundaries, where they are π bonded [164, 165] and contribute to electrical conductivity. The UNCD films thus exhibit a combination of useful properties typical for diamond films supplemented by electrical conductivity and electron emissivity [166], which makes them very attractive for device applications.

There is evidence that diamond growth proceeds mainly on the (110) face [167]. Previous studies [168, 169] explored initial growth stages with dicarbon on the hydrogen-terminated (110) face without hydrogen abstraction by way of insertion

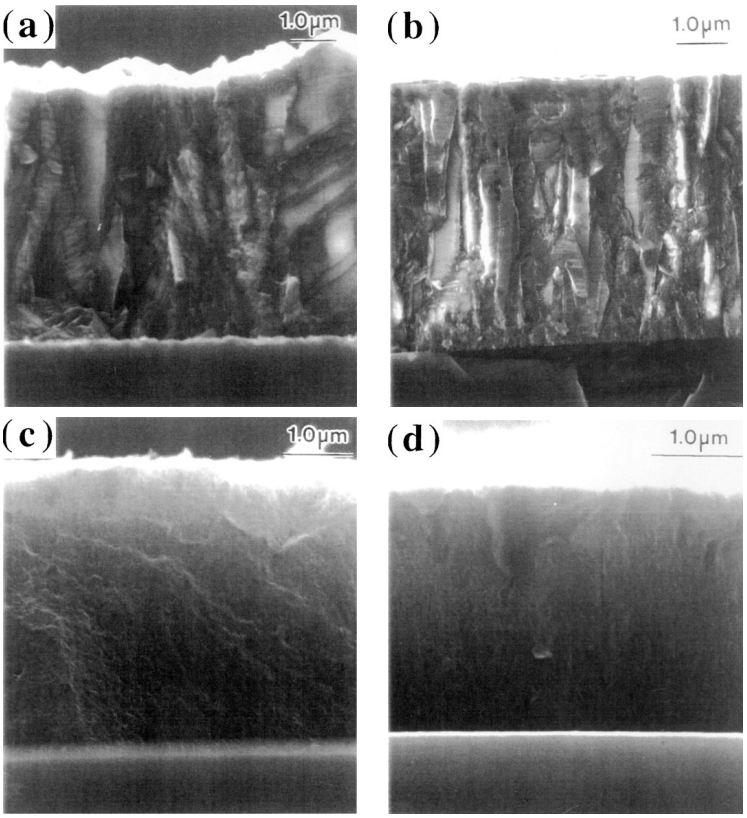

(%)	Ar	H_2	CH_4
(a)	2	97	1
(b)	80	19	1
(c)	90	9	1
(d)	97	2	1

Figure 5.1: Cross-section SEM images of as-grown UNCD films prepared from microwave plasmas with varying volume percentages of feed gasses, as given in the adjacent table (reprinted from Ref.[158] with permission from Am. Inst. Phys.).

of C_2 into C–H bonds on the surface. In the present work, we consider deposition steps onto the clean diamond (110) surface *without* hydrogen participation. We neglect hydrogen because firstly, its concentration in the feed gasses is much lower than in the conventional process and secondly, growth generally proceeds on surface sites which have become reactive only after hydrogen abstraction.

Starting out from a clean surface we investigate the local atomic configuration arising from the adsorption of a C_2 molecule. Subsequently, more C_2 molecules are deposited in the vicinity of a previous adsorbate cluster. By comparing the total energy of these structures, we identify preferred growth stages as those arising from C_{2n} clusters in the form of zigzag chains running along the $[\bar{1}10]$ direction parallel to the surface.

We also perform simulations of the diffusion of C_2 molecules on the surface in the vicinity of existing adsorbate clusters using a constrained minimisation technique [170, 171, 172]. The barrier heights and pathways indicate that the growth from gaseous dicarbon proceeds either by direct adsorption onto clean sites or after migration above existing C_{2n} chains.

The simulation approach is briefly outlined in Sec. 5.2. The initial adsorption steps for diamond growth are studied in Sec. 5.3, followed by an evaluation of diffusion

barriers for C_2 on diamond (110) in Sec. 5.4. We then analyse some molecular dynamics trajectories in Sec. 5.5.

5.2 Simulation setup

The surfaces are simulated using a two-dimensional slab geometry with varying thickness. The bottom layer is saturated by a fixed monolayer of pseudo hydrogen atoms which do not mutually interact. The lateral extent of the cell varies from 3×3 unit cells up to 8×3 unit cells, where the bigger extent is along the chain direction. This direction is assigned as the x axis. For all atomic structure calculations, we used the Γ-point approximation to sample the Brillouin zone, which amounts to a $\boldsymbol{k}$-point sampling with as many points as real-space unit cells. We let the atoms relax in a conjugate gradient scheme.

The diffusion and adsorption runs are done using a constrained conjugate gradient method. The forces during the conjugate gradient minimisation are modified by the method described by Ciccotti et al. and by Ryckaert [170, 171, 172]. The centre of mass of the C_2 molecule is moved in a given direction with steps of 0.1 Å. Because the constraint is to the centre of mass movement, the C_2 may rotate or dissociate freely.

For initial studies we used six bulk monolayers of carbon. We find that only negligible relaxations take place in the lower two layers and therefore we use only four carbon monolayers for the remaining calculations. The applicability of this size of supercell was tested by comparing the minimum energy geometries of a C_4 adsorbate on the (110) surface with supercells consisting of four and six monolayers, respectively. The comparison between fully relaxed structures calculated with both numbers of monolayers yields very small differences in the atomic positions of about 0.015 Å in both the lateral and vertical positions of all corresponding atoms, including those of the adsorbate.

5.3 Adsorption and energetics of small carbon clusters on (110) diamond

The energetically most favourable cluster configurations after repeated C_2 additions are summarised in Fig. 5.2 up to C_8 on (110). In the following, a detailed description of the individual deposition steps and the resulting surface cluster geometries will be given.

5.3.1 Initial C_2 deposition

In order to sample the energy landscape above the clean (110) diamond surface for C_2 adsorption we place a C_2 molecule in a vertical orientation near the surface on a hexagonlike set of points above the atoms and bond centres of the two topmost monolayers. By symmetry, only seven positions remain unique. The lower atom

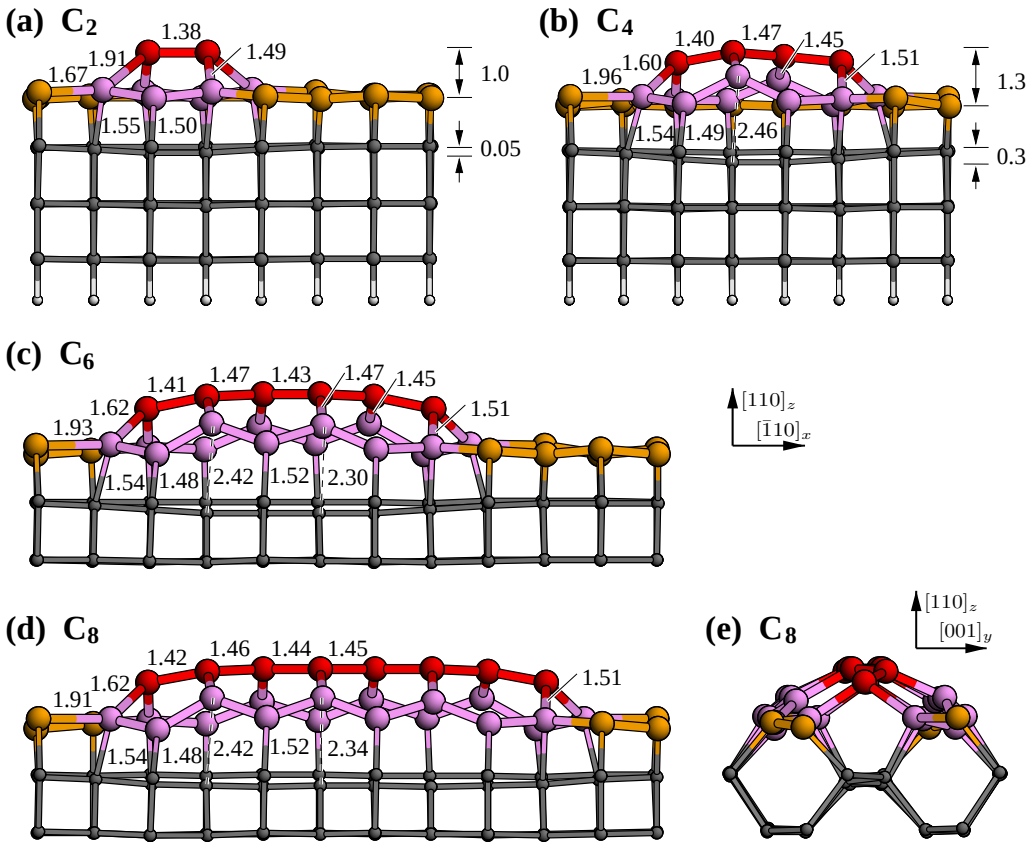

Figure 5.2: Overview of relaxed structures from subsequent depositions of C_2 molecules onto a clean diamond (110) surface. (a) C_2, (b) C_4, (c) C_6, (d) C_8, all along the $y = [001]$ direction, and (e) C_8, along the $x = [\bar{1}10]$ direction. The numbers given are distances in Å. Atoms of the adsorbate and the surface layer are shown larger. Red (dark) atoms indicate the adsorbate cluster, and magenta (medium grey) atoms its first and ring-forming second neighbours within the surface layer. Small spheres at the bottom indicate hydrogen saturation. For (c)–(e), only partial models are shown.

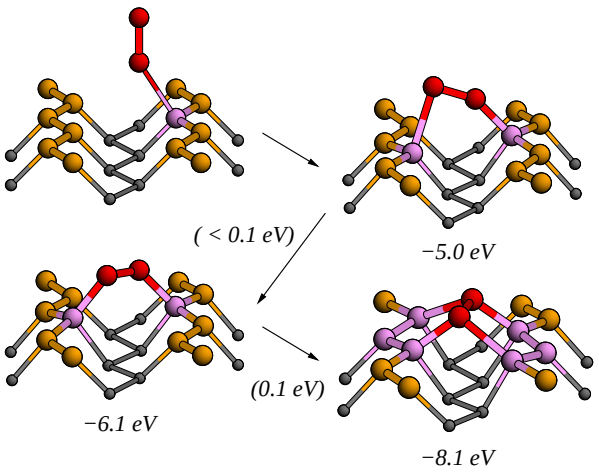

Figure 5.3: Initial steps for deposition of a C_2 molecule onto a clean diamond (110) surface. The energies are given relative to a clean surface and a distant C_2. Energies in parentheses indicate barriers. Atom designation is the same as in Fig. 5.2.

Table 5.1: Energy barriers (E_{barr}) and adsorption energies (E_{ads}) of C_2 (and C) at the initial and final stages of growth, for varying target sites. The "top" position means that the initial position of the C_2 is above a C_{2n} cluster; "end" refers to an initial C_2 position above the edge along the $[\bar{1}10]$ direction of the C_{2n} cluster; "same" and "other" express whether the added C_2 is above the same or the adjacent (110) trough as the existing C_{2n} cluster on the surface. Negative indices indicate missing C atoms in an otherwise continuous chain or on the (110) surface.

Row	Initial configuration	Final configuration	Figure	E_{barr} (eV)	E_{ads} (eV)	E_{ads} (eV), (Ref. [169])
1.	C_2 + (110)	(110):C_2	Figs. 5.2(a), 5.3	0.1	-8.1^a	−7.8
2.	C_2 + (110):C_2 top	(110):C_4	Figs. 5.2(b), 5.5	0.1	-10.3^a	−8.8
3.	C_2 + (110):C_2 same	(110):C_2,C_2 same	Fig. 5.4(a)	0.2	−7.2	
4.	C_2 + (110):C_2 other	(110):C_2,C_2 other	Fig. 5.4(b)	0.0	−8.3	−7.8
5.	C_2 + (110):C_4 end	(110):C_6	Fig. 5.2(c)	0.1	-9.6^a	
6.	C_2 + (110):C_4 top	(110):C_4,C_2	–	0.7	−6.5	
7.	C_2 + (110):C_6 end	(110):C_8	Fig. 5.2(d)	0.5	-8.8^a	
8.	C_2 + (110):C_6 top	(110):C_6,C_2	Fig. 5.6(b)	0.0	−2.0	
9.	C_2 + (110):C_6 top	(110):C_8 defect	Fig. 5.6(c)	1.8	−4.9	
10.	C_2 + (110):C_6 other	(110):C_6,C_2 other	–	0.0	−7.8	
11.	C_2 + (110):(2×1):C_{-3}	(110):(2×1):C_{-1}	Fig. 5.7(b)	0.6	−6.3	
12.	C_2 + (110):(2×1):C_{-2}	(110):(2×1)	Fig. 5.7(d)	0.3	-10.2^a	
13.	C_2 + (110):(2×1)	(110):(2×1):C_2	Fig. 5.8	0.0	−7.2	
14.	C_2 + (110):C_{-3}	(110):C_{-1}	–	0.5	−6.9	
15.	C_2 + (110):C_{-2}	(110)	–	0.4	−8.1	
16.	C_2 + (110):C_{-1}	(110):C	–	0.0^b/2.6	-6.8^b/−8.3	
17.	C + (110):C_{-1}	(110)	–	0.0	−10.4	

[a] C_{2n} chain growth and coalescence processes
[b] Metastable state

of the molecule is placed about 2 Å away from the nearest surface atom. A conjugate gradient relaxation from each of the lateral starting positions shows that the molecule is either reflected from or adsorbed onto the surface. The reflections occur for starting positions directly above the atoms and bonds of the top monolayer. From all of the starting positions not directly above a top-layer chain the C_2 molecule is bonded and forms a bridge above the "trough" between two adjacent top-layer chains. The deposition proceeds in two stages (see Fig. 5.3).

Initially, the C_2 sticks with one end to the nearest surface atom with an inclination of about 45° to the surface normal. There is a very low energy barrier of order 0.1 eV towards the final adsorption stage in which the molecule bonds symmetrically in an orientation corresponding to the diamond lattice. At this final stage, both adsorbate atoms are 1.0 Å above the top monolayer and are threefold coordinated with a bond length of 1.38 Å between them. Each adsorbate atom forms two bonds towards the surface, one bond corresponding to the diamond lattice with a length of 1.49 Å, the other being a stretched bond of 1.91 Å towards the adjacent atom in the same surface chain [see Fig. 5.2(a)]. The result is the formation of two fivefold rings with a common bond formed by the adsorbed molecule. There is a slight lateral pinch contraction of the surface monolayer. All its atoms remain bonded to the subsurface, which is indented below the adsorbate by about 0.05 Å.

The energetics of all depositions discussed in this chapter are summarised in Table 5.1. For the first deposition, the binding energies of the C_2 molecule to the clean (110) surface are fairly high, as can be seen in the fifth column of Table 5.1. The energy gain is mainly the result of forming four bonds to the surface, which yields about 2 eV for each bond; this is plausible considering its similarity to the atomic binding energy of 2.3 eV/bond as obtained by the DFTB method for bulk diamond. Breaking the initial triple bond within the C_2 molecule and the stretch of surface bonds near the adsorbate offsets the result to give the adsorption energy of 8.1 eV, listed in the table.

5.3.2 Addition of C_2

As a next step, we studied the effect of adding another C_2 molecule near an existing C_2 adsorbate. Obviously, the deposition onto a site more than one surface lattice spacing away from the initial adsorbate results in two isolated clusters of similar configuration as discussed above, unless a topological mismatch prevents the completion of the ring formation for a nearby site, as shown in Fig. 5.4(a). In this case, the strain field introduced by the second adsorbate results in a bond switch for one of the backbonds, with an accordingly high adsorption energy of -7.2 eV. For deposition onto a site of the neighbouring trough, the geometry and energy are essentially the same as for the isolated case [Fig. 5.4(b)]. We note that in this case the low barriers found in the initial adsorption process are no longer present, probably due to the small local strain field induced. This effect supports the idea of a rapid spread of such C_2 adsorption sites across the surface.

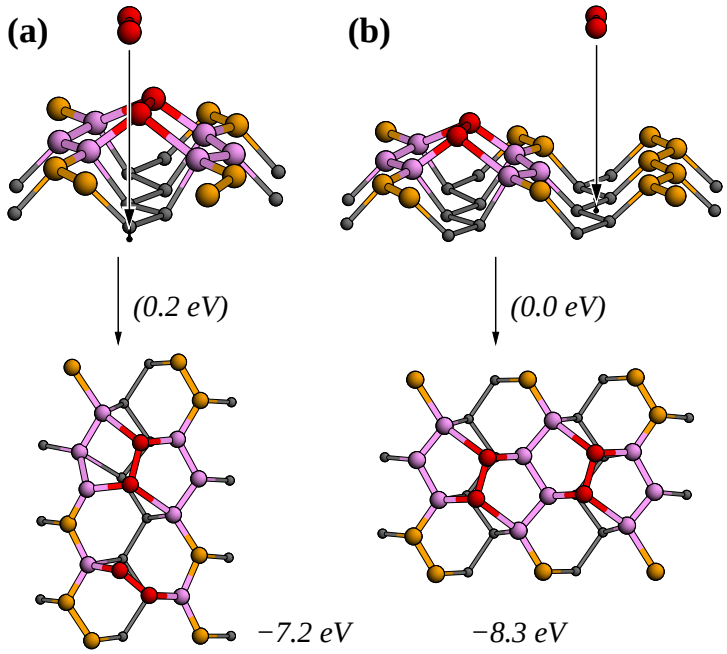

Figure 5.4: Continued deposition of a C_2 molecule onto a diamond (110) surface on sites *next to* an existing C_2 adsorbate. The targeted neighbouring site is (a) along the $x = [\bar{1}10]$ direction, and (b) along the $y = [001]$ direction. The total energies are given relative to initially separated components. Energies in brackets indicate barriers. Atom designation is the same as in Fig. 5.2. Additional small markers indicate the target location.

5.3.3 C_4 clusters

The highest gain in energy for the second C_2 deposition is obtained at a site directly above the first C_2 molecule [see Figs. 5.2(b) and 5.5]. The second molecule bonds at the neighbouring diamond lattice site along the $[\bar{1}10]$ valley, in a diamondlike configuration next to the first one, and forms a four-atom-long zigzag chain which amounts to a seed for the next monolayer. At the ends of the new chain, fivefold rings are formed similar to the ones in the C_2 case. The ridge of the adsorbate is a z-shaped symmetric chain of three bonds with lengths of 1.40 Å at the ends and 1.47 Å in the centre. The central two atoms are raised 1.3 Å above the top monolayer, which corresponds to a slightly outward relaxation with respect to the ideal lattice sites. The end atoms are 0.3 Å closer to the surface. The centre bond is the common side of two adjacent sixfold rings connecting the new chain to the surface monolayer. Topologically, the rings supporting the C_4 adsorbate above the surface form a pyracylene structure, which is the basic structural element of a C_{60} fullerene. A local pinch contraction of the surface monolayer occurs as in the previous case. However, the outer bonds of the adsorbate are here, at 1.6 Å, closer in length to actual bonds, at the expense of the transition to the uncovered parts of the surface, for which the bonds are now stretched to a distance of 1.9–2.0 Å. Furthermore, we observe the breaking of backbonds in the middle of the aggregate, resulting in a cluster of sp^2-like coordinated atoms arranged in a domelike configuration. The similarity

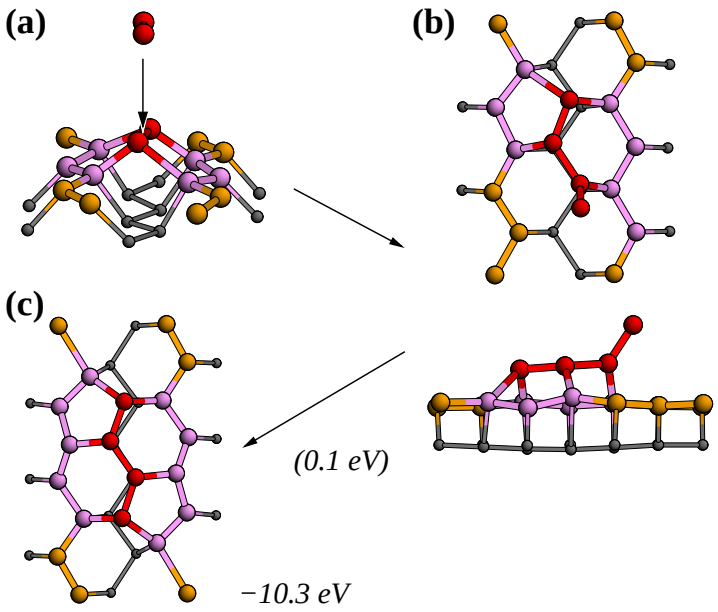

Figure 5.5: Continued deposition of a C_2 molecule onto a diamond (110) surface on *top of* an existing C_2 adsorbate, with the transition state shown from the top and side. The resulting adsorbate cluster is topologically similar to a C_{60} fragment. The panels show (a) the initial, (b) the transition, and (c) the final state. The total energies are given relative to initially separated components. Atom designation is the same as in Fig. 5.2.

to such a highly stable configuration as a fullerene explains the fact that this C_4 cluster represents the highest energy gain for an approaching C_2 molecule among the structures considered in Table 5.1.

5.3.4 C_6 and C_8 clusters

The next C_2 adsorption to the C_4 pyracylenelike adsorbate results in a C_6 adsorbate, shown in Fig. 5.2(c), with an adsorption energy of 9.6 eV. Further C_2 adsorption yields an adsorption energy of 8.8 eV and a surface C_8 cluster, shown in Fig. 5.2(d). Thus, the energy gain is at least 8 eV for the repeated C_2 surface chain addition as shown up to C_8 on the surface. We expect the adsorption gain to level off at about 8.5 eV for longer chains.

The C_6 adsorbate has four sixfold rings in the middle and a fivefold ring at each end. The C_8 adsorbate is essentially identical to it, but has of course two more sixfold rings along its length. As in the case of the C_4 adsorbate, the underlying substrate atoms are raised above the surface and flattened to sp^2-like coordination together with the adsorbed atoms.

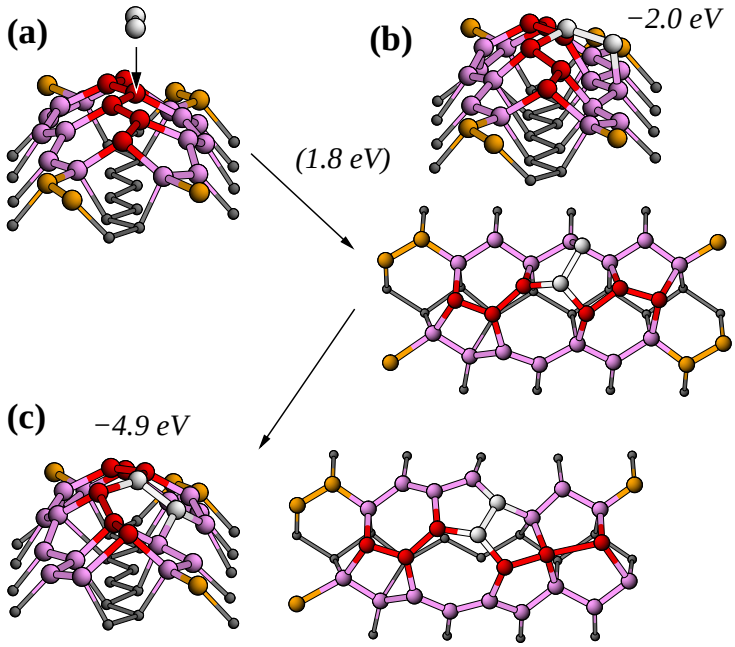

Figure 5.6: Continued deposition of a C_2 molecule onto a diamond (110) surface over a C_6 adsorbate with high insertion energy. The panels show (a) the initial, (b) the transition, and (c) the final state. The total energies are given relative to initially separated components. Atom designation is the same as in Fig. 5.2, with the added C_2 molecule shown in white.

5.3.5 Adsorption barriers

The energy barriers for C_2 adsorption (Table 5.1, fourth column) are either zero or very low. The highest energy barrier in the case of C_2 addition at the end of C_8 is probably a finite size effect.

The initial C_2 addition at a diamond site in a "valley" on the surface makes the bonds shorter in the neighbouring "valley." This makes the adsorption of an additional C_2 easier at the neighbouring "valley" at a diamond site, as can be seen by comparing the energies in the third and fourth rows in Table 5.1.

5.3.6 Surface defect formation

There is a metastable energy minimum when adsorbing a C_2 molecule on the top of C_4 or C_6 adsorbates (rows 6 and 8 in Table 5.1). In the metastable state (C_2 + C_{2n}) one of the C_2 atoms is singly bonded to the surface C_{2n} complex [see Fig. 5.6(b)]. The bonded C_2 is only 2.0 eV lower in energy than free C_2. We believe this metastable minimum configuration plays a key role in the growth of (110) diamond. It enables the diffusion of the C_2 molecule to the end of an existing growing C_{2n} complex in the diamond configuration. If the C_2 molecule is forced deeper onto a C_6, there is another metastable minimum energy structure consisting of one seven-membered ring, one six-membered ring and six five-membered rings (row 9 in Table 5.1). The

energy gain from the gaseous C_2 to this non-diamond-growth favouring configuration is 4.9 eV and the energy barrier towards the final metastable minimum is 1.8 eV. We believe that similar metastable defect structures form when a C_2 adsorbs on C_{2n} with too high kinetic energy, approximately $E_K > 3$–5 eV, taking into account kinetic contributions to the energy barriers.

5.3.7 Surface vacancy filling

When the growth proceeds further, different C_{2n} clusters along the same (110) surface trough will eventually meet and coalesce. Given that growth proceeds by C_2 addition, the critical stage is reached just before coalescence, when there will be a gap between two cluster ends corresponding to either three or two missing atoms. Assuming the clusters are seeded at random sites, both cases have equal probability but quite different energetics for subsequent C_2 additions.

In either case we see the approaching C_2 first in a metastable bridging configuration from a chain end to a bare surface site, and directly between the two chain ends, for the three- and two-site-wide gap, respectively [see Figs. 5.7(a) and 5.7(c)]. Both added atoms remain just twofold coordinated. After overcoming barriers of 0.6 eV and 0.3 eV, respectively, the adsorbate extends the existing C_{2n} chain by another atom pair [see Figs. 5.7(b) and 5.7(d)].

For the original three-atom gap, a single-atom vacancy remains next to a still just twofold coordinated atom. Accordingly, the gain in adsorption energy is rather low at 6.3 eV. However, the remaining single-atom gap remains reactive, and may be filled at a later stage.

The two-atom gap yields a much higher adsorption energy of 10.2 eV, comparable to the high gains found in the initial adsorption stages. The final stable configuration is a continuous chain with broken backbonds for atoms on either side of the top ridge. This structure is a bent graphene sheet with a bending radius of about 3 Å. Before discussing its properties in the next section, we briefly sketch the other variants for surface vacancy filling.

For the final stage of surface coalescence, we considered a nearly complete surface monolayer, with up to three consecutive atoms along the $[\bar{1}10]$ direction removed. The filling of these surface vacancies results in energy gains between 6.9 and 10.4 eV, as listed in the last rows of Table 5.1. The filling of the last single-atom vacancy can take place either by a single C atom adsorption at the vacancy, with an energy gain of 10.4 eV without a barrier, or by a C_2 addition process, which has a rather high barrier from a metastable minimum at a gain of 6.8 eV to its completion at 8.4 eV. Furthermore, it leaves a singly bonded C atom on an otherwise perfect (110) surface. The energy required to desorb the extra C atom is of order 8 eV.

5.3.8 Graphitisation and rebonding

As shown in the preceding sections, the growth by the C_2 chain addition mechanism will eventually lead to coalescing chains, with broken backbonds on either side. In order to investigate the consequences of the broken backbonds for the sur-

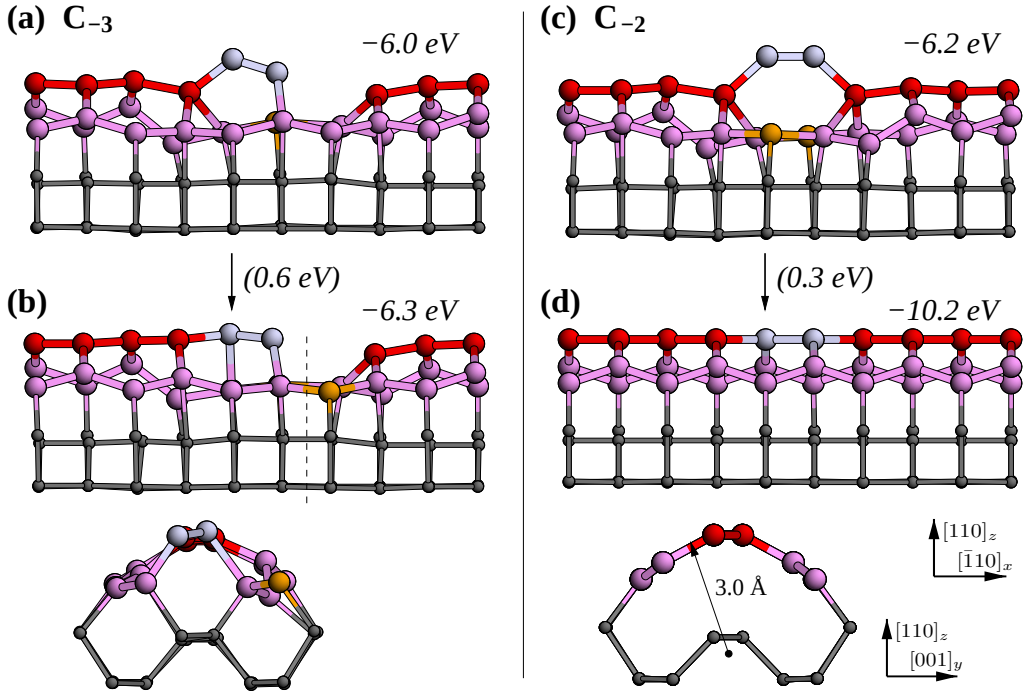

Figure 5.7: Final stages of $[\bar{1}10]$ chain growth and coalescence on a diamond (110) surface: (a) and (b) for a three-site vacancy, (c) and (d) for a two-site vacancy. Panels (a) and (c) show the metastable adsorption phases, and panels (b) and (d) the relaxed minimum configuration. Atom designation is the same as in Fig. 5.2, with the added C_2 molecule shown in white. The total energies are given relative to initially separated substrate and added C_2. Energies in parentheses indicate barriers. The dashed line in (b) indicates a cut used for the alternative view along $[\bar{1}10]$ in this panel. The arrow in (d) indicates an empirical bending radius for the graphene sheet.

face stability during growth we have generated and relaxed a model in which every other trough along $[\bar{1}10]$ was covered with a continuous chain, resulting in a C(110):(2×1) reconstruction, shown in Fig. 5.8(a). The relaxed structure shows multiple bent graphene sheets along $[\bar{1}10]$. The bending orientation is that of a carbon nanotube of the (n, n) type, known as the armchair tube [173, 174]. The bending radius of the sheets is about 3 Å, which corresponds to a (4,4) tube, illustrated in Fig. 5.8(c). Nanotubes as small as this are energetically in competition with flat graphene sheets. However, tubes with diameters as small as 5 Å have been observed recently [175].

The structural similarity of the bent graphene sheet to a single-wall carbon nanotube allows us to deduce the electronic structure of the bent sheet. The common feature between the bent sheets and the armchair tubes is an atomic zigzag chain of carbon atoms running parallel to the bending axis. Atoms contributing to these chains are sp^{2+x} hybridised, with $x = 0$ for flat graphene and $0 < x \ll 1$ for nanotubes. Along either chain, the overlap of carbon p orbitals normal to the sheet and tube wall, respectively, results in an extended π-bonded system which forms a one-dimensional band. This band has a negligible gap because we find here that Peierls distortion

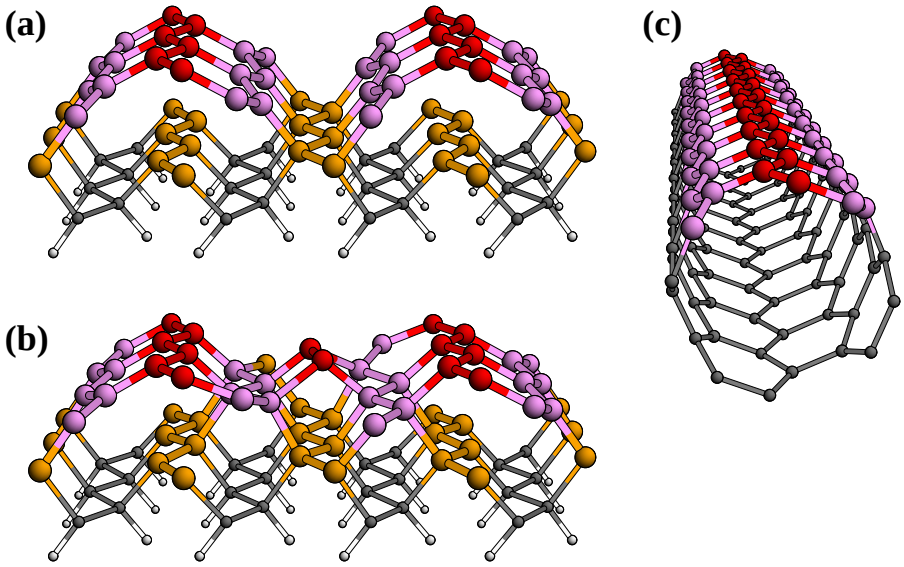

Figure 5.8: (a) Graphitisation on a 50% covered diamond (110) surface in (2×1) reconstruction, and (b) induced rebonding after deposition of C_2. Dark, grey and white atoms indicate atoms in the top three monolayers, which are also shown larger than the remaining atoms. The bottom monolayer is the hydrogen termination. (c) For comparison, a (4,4) single-wall carbon nanotube with similar structure and atom designation as (a).

does not occur, quite similar to the situation in armchair nanotubes [174]. Therefore, the atomic and electronic structure will be susceptible to distortions which break the symmetry.

The question of stability of the bent sheets and therefore the diamond surface itself during growth naturally arises. It is known that graphitisation on clean diamond surfaces, namely, on (111) and near (111) twin boundaries, leads to delamination [123, 125, 176]. We find for the present configuration that it is stable and does not debond. Furthermore, continued adsorption of C_2 in the valley between two arches is possible without a barrier and, more importantly, it causes the sp^2-like atoms near the adsorbate to return to an sp^3 configuration and rebond in the diamond structure, as is illustrated in Fig. 5.8(b).

Considering the electronic structure of the sheet, we can deduce the reason for the rebonding. Clearly, an approaching dimer will lead to a disturbance of the π-electron system near the graphene sheet. Furthermore, at the terminus of the graphene sheets near the surface, the π-electron system is imperfect to begin with because sp^2-hybridised atoms of the sheets are bonded to sp^3-hybridised, fourfold coordinated atoms at the diamond surface. Since ideal sp^2- and sp^3-hybridised carbon atoms are energetically close, as the cohesive energies of graphite and diamond indicate, the rebonded sp^3-hybridised configuration will be lower in energy than the disturbed sp^2 system near the C_2 molecule.

We thus reach the important conclusion that, in the C_2 growth regime established here, intermediate graphitisation may occur, but the diamond growth process is stabilised against extended graphitisation and delamination.

Table 5.2: The diffusion barriers E_{barr} and the change in total energy along the diffusion path. The low energy barriers (rows 4 and 5) are associated with the diffusion of a vertically aligned C_2 on top of a C_{2n} cluster.

Path	E_{barr} (eV)	$(E_{\text{final}} - E_{\text{init}})$ (eV)
C_2 along valley	3.8	0.0
C_2 to other valley	3.3	0.0
C_2 to C_4 along $\rightarrow C_6$	3.7	-1.8
C_2 to end of $C_6 \rightarrow C_8$	$1.0^a/0.6^b$	-3.7
C_2 to side of $C_6 \rightarrow C_8$	$1.0^a/0.6^c$	-3.1

[a] Near centre of C_6.
[b] Near end of C_{2n}.
[c] From metastable state to final energy minimum.

5.4 Surface diffusion of C_2

In order to estimate the influence of surface diffusion of C_2 on the growth mechanism, we investigated some diffusion paths, as summarised in Table 5.2. The associated diffusion barriers along the various C_2-related diffusion paths are shown in the second column of this table, and the gain in energy in the last column.

Generally, on the clean diamond (110) surface, the diffusion barriers are rather high, and exceed 3 eV (Table 5.2, rows 1–3). This is easily understood from the strong covalent bond that is formed between a C_2 adsorbed species and the surface once the molecule reaches the surface. The only exceptions to such high barriers are for sites above existing adsorbates, where the binding energy for further adsorbed species is low to begin with. C_2 has the lowest diffusion barriers when it starts diffusion on top of an existing C_{2n} complex. In this case, the barrier for diffusion along the adsorbate ridge is of the order of 1 eV. The C_2 remains nearly vertically oriented, with one of its atoms bonded to one or two surface atoms throughout the diffusion path. The energy barriers are decreasing when the chain end is approached. The last energy barrier towards completing a chain addition step is only 0.6 eV.

We note that the energy gain attainable for a C_2 molecule by diffusion to the end of an existing C_{2n} adsorbate is considerable [see Table 5.2, last column]. These gains, when added to the adsorption energies found for the "top" deposition sites, as listed in Table 5.1, naturally result in the same total adsorption energies as those for the "end" sites. We have thus found two different growth channels, converging to the same growth mechanism. One is adsorption-dominated growth on nearly clean surfaces with deposition directly into diamond lattice sites, and the other is diffusion driven on surfaces densely covered with adsorption clusters.

In the diffusion studies, we found that when the C_2 is directed in either major diffusion direction, along the chain direction of C_{2n} or perpendicular to it, it passes metastable minima before reaching the lowest energy configurations at the chain ends. Along the parallel diffusion path, the last metastable minimum consists of a C_2 fragment singly bonded to the surface, similar to the configuration shown in Fig. 5.5(b). For the perpendicular direction away from the chain axis towards

a neighbouring surface valley, the metastable minimum is such that the C_2 atoms complete a fivefold ring, with each one being singly bonded to the surface.

While both intermediate and final diffusion barriers are incidentally the same for diffusion parallel and orthogonal to the C_{2n} chain direction, the ultimate energy *gain* is higher by 0.6 eV for the growth-favouring parallel diffusion; this indicates high adsorption rates in either case, with a preference towards crystalline growth. However, the introduction of defects is quite easily possible under this regime, which helps to explain the rather small grain size found in the final material.

5.5 Molecular dynamics depositions

Inspired by the adsorption and diffusion results discussed above we simulated the deposition of C_2 on top of a C_6 complex on the surface directly using molecular dynamics (MD), though within a rather short time span of just 0.1–0.5 ps. The time step in the MD simulations was 10 a.u., i.e., 0.24 fs, and the surface atoms (but not the deposited C_2) were coupled to a heat bath at 1000 K by scaling their velocities with a probability of 0.1 per time step. All the atoms except the terminating hydrogen atoms on the bottom of the surface slab were allowed to follow the Newtonian equations of motion. The goal of these runs was to investigate a diamond growth reaction as follows:

$$C_2^{\text{gas}} + C_{2n}^{\text{surf}} \rightarrow C_{2n+2}^{\text{surf}} \,. \tag{5.1}$$

In a first set of experiments, each molecule was initially aligned orthogonal to the surface and shot with a kinetic energy of 2–9 eV along the direction of the $[\bar{1}10]$ surface chains at an angle of 80° to the surface normal vector. The motivation of this particular choice was that the molecule may get adsorbed at the lowest energy position at the end of a C_{2n} cluster, as identified in the diffusion studies. The molecules with up to 7 eV kinetic energy resulted in a C_2 fragment on top of a C_{2n} cluster, similar to the structure in Fig. 5.5(b). At 9 eV kinetic energy the molecule was deflected from the C_{2n} cluster but was subsequently adsorbed as a lone C_2 on a neighbouring clean surface site. While the deflection at higher impact energy seems counterintuitive at first sight, it must be recalled that the incident angle is high, so that the nature of the process is rather one of a steady dissipation of kinetic energy from the approaching C_2 into the substrate until the molecule is slowed down enough to be deposited.

In a second set of runs, a C_2 was aligned parallel to the surface with an initial kinetic energy of 0.1–2 eV and a starting position on top of a C_6 cluster. This leads again to the C_2 fragment being singly bonded to the C_6 surface cluster, a configuration from which diffusion to either end is possible, as established before. There is a small region above the edge of a C_{2n} $(n = 2, 3)$ cluster, from where a C_2, if given an initial velocity towards the surface, can bond to the metastable minimum which precedes the diamond position, shown in Fig. 5.6. However, in the molecular dynamics simulations the barrier towards growth completion is too high on our timescale, and we obtained solely the metastable minimum.

Chapter 6

Structure and Impurities in Ultrananocrystalline Diamond Grain Boundaries

6.1 Introduction

The preceding chapter presented a model for the growth of diamond surfaces by dicarbon in the absence of hydrogen. Now, the question of the nature of grain boundaries in the interior of UNCD films comes into focus.

Ultrananocrystalline diamond (UNCD) films are characterised by crystallites with an average size of just 3–10 nm, c.f. [159]. While submicron grain sizes have been observed in conventional diamond films[1] the average grain size is an order of magnitude above the one for UNCD films. This leads to qualitative differences and justifies their separate classification. Most importantly, the small grain size invariably leads to a significantly higher fraction of atoms at or near grain boundaries. In UNCD films, this fraction is estimated to be as high as 10% [159], derived from simple grain surface to volume ratio considerations. Many of the physical properties of the films show a strong dependence on this ratio, on the concentration of impurities and on the crystallite size in general, all of which can be influenced during growth in a controlled fashion. This opens an opportunity to design materials for specific applications such as tribology and electronic devices.

There have been a number of studies for microcrystalline diamond grain boundaries [177, 178, 179], that have reported on the structures of twins, stacking faults and tilt boundaries. Most of these defects have relatively low formation energies and largely maintain tetrahedral bonding within the interface layer. They are also quite ordered, evidenced by relatively small unit cells or the repetition of closely repeated structural units [178, 179]. In contrast, crystallites in UNCD films are randomly oriented because of a much higher nucleation rate precluding the growth of larger grains.[2]

[1] So-called nanodiamonds are also produced for abrasives applications by high-pressure high-temperature synthesis. These are not relevant here.

[2] Nucleation rate, growth rate, and crystallite size are connected by the following phenomenologi-

The focus in this study will be on high-energy high-angle (100) twist grain boundaries. Such twist grain boundaries are of interest for two reasons: (a) they involve one of the growth termination faces and are thus likely to occur, and (b) they are representative of generic grain boundaries in diamond, since the interface plane results in two broken bonds per atom, as would be the case for most randomly oriented planes in the diamond crystal (see Fig. 4.2 on page 56), save for vicinal planes.

The structure of high-energy high-angle (100) twist grain boundaries in diamond and silicon was previously addressed by Keblinski et al. [164] using Tersoff interatomic potentials in extensive Monte-Carlo simulations. It was found that (100) grain boundaries are more stable against decohesion than (110) and (111) grain boundaries. A particularly interesting observation was that up to 80% of the $\Sigma 29$ grain boundary carbon atoms were threefold coordinated. The $(100)\Sigma 29$ twist grain boundary of diamond was also studied by Cleri et al. [181] using molecular dynamics within a tight-binding model, allowing to discuss the electronic structure of the grain boundaries. This study indicated that only about 40% of the grain boundary atoms are threefold coordinated and that the electronic band structure has a broad spectrum of gap states due to dangling bonds and double bonds. It was shown that the states are localised, but can participate in hopping conduction. Finally, a calculation on the density-functional level was performed by Zapol et al. [182] on a stacking fault which models a diamond grain boundary with pure sp^2 bonding across the interface. The electronic structure of this model is characterised by the presence of π-states in the forbidden gap. Those states are localised on the interfacial atoms. All these theoretical studies, while disagreeing on some aspects of the coordination statistics, unanimously agree on the fact that the width of the grain boundaries in UNCD is extremely small, close to 0.2 nm, as is indeed confirmed experimentally by transmission electron microscopy data [159].

In comparing the diamond results with the analogous grain boundaries for silicon, the latter were found to be slightly thicker (relative to the lattice constant) and show more extensive interfacial disorder. The difference is attributed to silicon being restricted to sp^3-type local bonding, whereas carbon is flexible between sp^2 and sp^3-type bonding, resulting in a higher coordination disorder at lower structural disorder [164, 181].

The effect of impurities such as nitrogen, silicon, and hydrogen on the properties of UNCD is of great interest. Impurities can be accidentally or intentionally introduced into diamond during the growth process. On the one hand, small amounts of hydrogen and nitrogen are unavoidably present in plasmas. On the other hand, substrate materials such as silicon contribute impurities by diffusion processes. Sometimes, nitrogen is added to control electrical properties. These impurities have already been well studied in bulk CVD and natural diamonds, as reviewed by Mainwood [112]. As compared to impurities in bulk diamond, impurities in the disordered grain boundaries can have a different concentration, geometry, and electronic struc-

cal equation (cf. [159]):

$$\text{Nucleation rate } [\mathrm{s^{-1}\,cm^{-2}}] = \frac{\text{Growth rate } [\mathrm{cm\,s^{-1}}]}{\text{Crystallite volume } [\mathrm{cm^3}]}\,.$$

Both UNCD and conventional growth rates are of the order of $1\,\mu$m/h. UNCD crystallite sizes are around 10 nm, and nucleation rates are of the order of $10^{10}\,\mathrm{cm^{-2}\,s^{-1}}$.

ture and may drastically change the mechanical and electrical properties of UNCD. The distribution of impurities between grains and grain boundaries within UNCD has not yet been determined unequivocally in experiments. The main goal of the present study is to provide information on the geometry and electronic structure of impurities in high-energy disordered diamond grain boundaries using the DFTB method.

Before proceeding any further, however, a brief introduction to the relevant grain boundary nomenclature is in order. Beginning with section 6.2, the results on chemical bonding, structure, and electronic density of states of three selected twist (100) grain boundaries are presented and discussed, followed by results on bonding, substitution energies, geometries, and energy levels of N, Si, and H impurities.

6.1.1 Grain boundary primer

Classification

Grain boundaries are a class of materials interfaces defined as the region showing appreciable structural perturbation between otherwise more or less perfect crystallites of the *same* material. Grain boundaries can thus be considered extended planar defects. The crystallography of grain boundaries is derived from the considerably more complicated case of general crystalline interfaces, which was comprehensively described by Wolf [183].

In general, there are eight degrees of freedom (DOF) for an interface formed between two semi-infinite crystals. Five of them are classified as macroscopic or rotational DOF describing the direction of the interfacial plane in each semicrystal and a mutual twist angle. The other three DOF are microscopic or translational ones which describe residual atomic-scale translations between the crystal lattices. Of these, an interface-normal translation is particularly important since it accounts for a thermodynamically relevant volume change of the interface region due to stress relaxation. All degrees of freedom, except for that of the volume change are subject to symmetry operations of the crystals. Ordinarily, this leads to a relatively small irreducible phase space for these DOF. If the directions of the interface planes are identical, the interface is termed *symmetrical* and the number of macroscopic DOF reduces from five to three.

Several subtly overlapping nomenclatures are in use for the description of crystalline interfaces, most of them concentrating on the macroscopic DOF by describing the interface in terms of *twist* and *tilt angles* and the Miller indices of the interface planes. Grain boundaries in the narrow sense of homophase interfaces are traditionally described in terms of a *coincident site lattice (CSL)*, however. The CSL scheme assumes a superlattice common to the two semicrystals, prior to a possible translation. For this reason, the scheme is restricted to *commensurate* interfaces, i.e., interfaces possessing a planar unit cell. The CSL notation for a grain boundary contains the Miller indices of the two interface planes and the twist angle ϑ. A twist angle of 180° leads to a pure tilt between the semicrystals, except for special cases where this operation is a symmetry element of the semicrystal. A suitably adapted nomenclature is used in the pure tilt situation, naming just tilt axis and angle. The

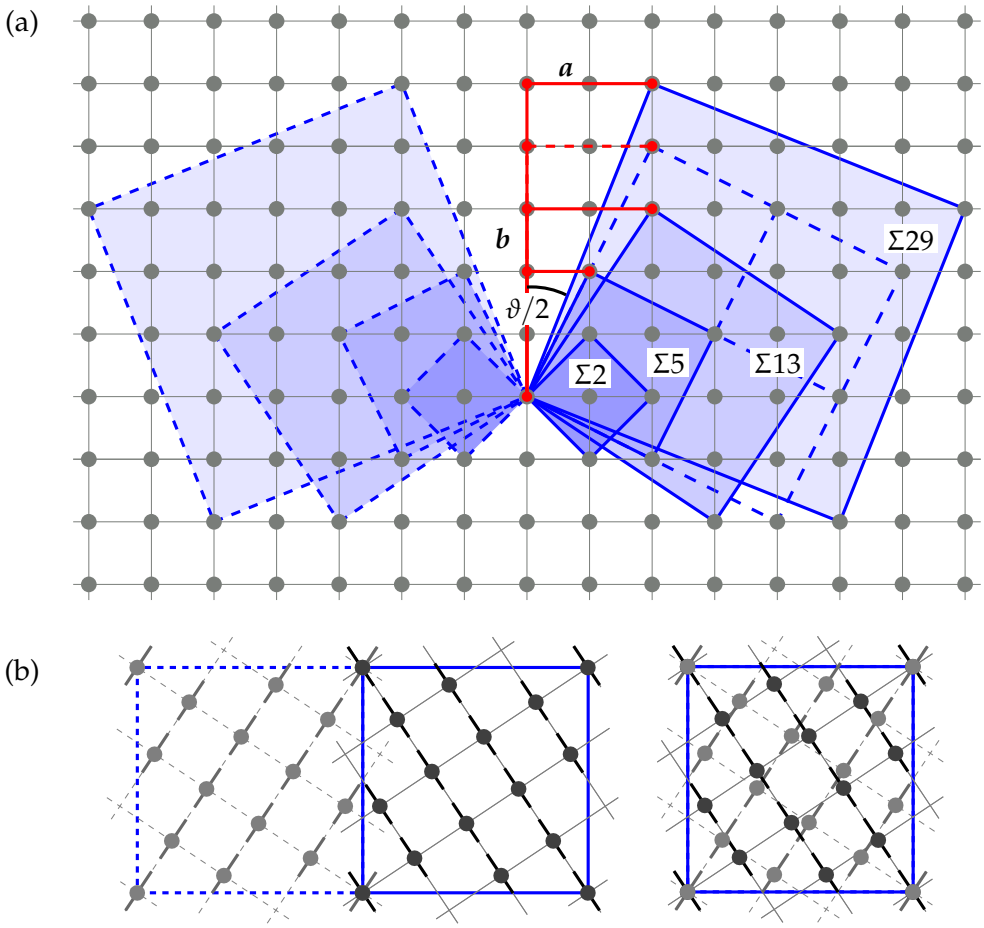

Figure 6.1: Crystallographic relation for twist grain boundaries on a square Bravais lattice (see text). (a) Various supercells before rotation. (b) Σ13 cells after conjugate rotation and overlay. The added thick short lines indicate the direction of bonds on a diamond (100) interface plane.

twist or tilt angle is commonly augmented or even replaced by the inverse volume density of CSL sites, denoted Σ.

Since most calculations performed on interfaces apply periodic boundary conditions in at least the lateral directions, they *require* commensurability to generate a simulation cell and therefore the CSL concept is a convenient way to select and describe supercells. Limitations in computing power restrict the selection of tractable supercells to those with relatively small Σ.

Twist (100) grain boundaries

The grain boundaries of interest here are of the (100) twist type. The diamond (100) face exhibits a square grid of atomic sites. Fig. 6.1 illustrates the CSL formation for this case. Any pair of lattice vectors $\boldsymbol{g} = \boldsymbol{b} \pm \boldsymbol{a}$ leads to conjugate square superlattices with a unit cell area $\Sigma = a^2 + b^2$ and a mutual twist angle ϑ. For uniqueness it shall be required that a and b are incommensurate. The twist angle is trivially obtained

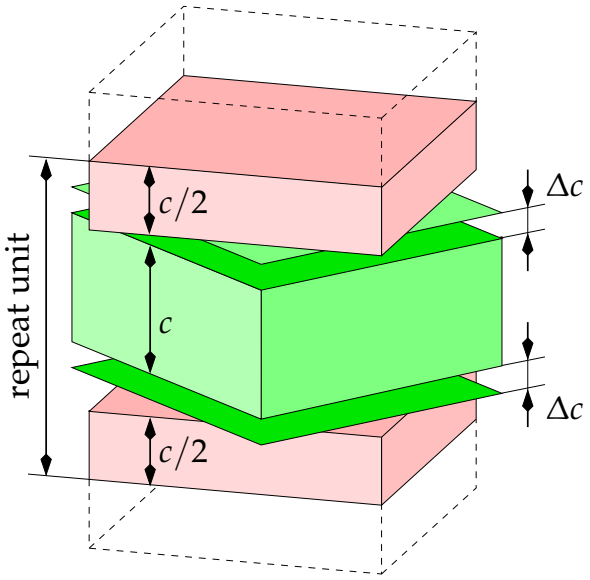

Figure 6.2: Setup of a grain boundary simulation cell with the middle layer twisted and additional interfacial separation Δc inserted. The periodic unit in the vertical direction is $z = 2(c + \Delta c)$.

from

$$\tan\frac{\vartheta}{2} = \frac{a}{b}\,, \tag{6.1}$$

and the supercell size in terms of the diamond lattice constant is (cf. Table 4.1 on page 55):

$$d = a_{\mathrm{D}}\sqrt{\Sigma/2}\,. \tag{6.2}$$

The CSL lattice for the twist grain boundary is formed by matching the two conjugate superlattices on top of each other, as shown in Fig. 6.1(b). Note that the broken bonds from the diamond lattice introduce non-equivalent directions on the original lattice and consequently reduce the symmetry of the CSL. For the same reason, the case $\vartheta = 90^\circ$ ($\Sigma 2$) is more properly described as a *stacking fault*. This case has been studied in detail by Zapol et al. [182].

The CSL scheme leads to a certain lateral periodic cell for a given surface. To achieve periodicity in the third dimension, the twist operation must be restricted to a finite slab rather than extending through the two semicrystals. This generates two related grain boundaries per periodic cell as illustrated in Fig. 6.2. Effectively, a three-dimensional periodic model of the crystal with planar repeating grain boundaries is constructed. An alternative setup would be to use hydrogen passivation as discussed in Chapter 4. The disadvantage of such a setup is that it would add a separate species and introduce alien electronic states.

It should be stressed at this point that due to relatively large unit cells for the grain boundaries studied here, the actual coincidence of atomic sites is rather unimportant, as are minute in-plane translations [164]. The reason for using the CSL description is that only certain twist angles yield two-dimensional periodic boundary conditions with sufficiently small unit cells, both of which are prerequisite to supercell electronic structure calculations.

Table 6.1: Structure and energetics of twist grain boundary supercells from density functional tight binding calculations. a and b are the components of the generating surface cell vector [see Fig. 6.1(a)], ϑ is the twist angle, d the lateral size of the supercell, N_C is the number of carbon atoms in the periodic cell used for the calculations, $\Delta V = \Delta c/a_D$ is the increase in volume of the grain boundary layer per unit area as a fraction of the lattice constant, and $\mathcal{E}_{GB}$ is the grain boundary energy discussed on page 96.

Grain boundary	Geometry parameters						$\mathcal{E}_{GB}$	
	a	b	ϑ (deg.)	d (Å)	N_C	ΔV (%)	(J/m^2)	(eV/atom)
$\Sigma5(2\times2)$	2	4	53.1	11.28	320	14	7.80	1.55
$\Sigma13$	2	3	67.4	9.09	208	14	7.91	1.57
$\Sigma29$	2	5	43.6	13.58	464	10	7.96	1.58

6.1.2 Grain boundary supercell setup

We have selected three grain boundaries for our inquiries: Σ5, Σ13, and Σ29. Their geometry parameters are listed in Table 6.1. The Σ5 unit cell had to be doubled in both lateral directions to make the cell viable for minimum-image conventions and to allow more freedom for bond reorientations. As is evident from the table and Fig. 6.1(a), the three selected cells are fairly representative for general high-angle twist grain boundaries.

For all models, we have chosen 16 monolayers per supercell, resulting in a separation of about 7.5 Å between the two grain boundaries in the cell. The interface structures of selected models constructed with 24 monolayers essentially agreed with those from the models with 16 monolayers, which were therefore used for all subsequent calculations. We recall that the $O(N^3)$ scaling of the standard DFTB formalism would have incurred a more than threefold increase in calculation time.

An additional separation Δc in the interface-normal direction was applied in order to account for a volume increase in the grain boundary region. The value was optimised by discrete sampling with a step size for Δc of 2% of the lattice constant. For this setup procedure and all analyses which follow, a thermal equilibration of the initial structures was performed at 1500 K for 0.5 ps. Subsequently, simulated annealing was performed at gradually lower temperatures and the final structure was optimised by a conjugate gradient method. It was verified that an increase in equilibration temperature up to 5000 K does not qualitatively change the results (see Table 6.2 on page 93). In particular, the GB cohesion energy remains practically the same and statistical distributions of structural and bonding parameters are similar.

The same procedure was used in the simulations of the Σ13 twist (100) grain boundaries with impurities. Substitutional Si or N atoms or interstitial H atoms were placed in the GB followed by equilibration, annealing and relaxation of the resulting structure.

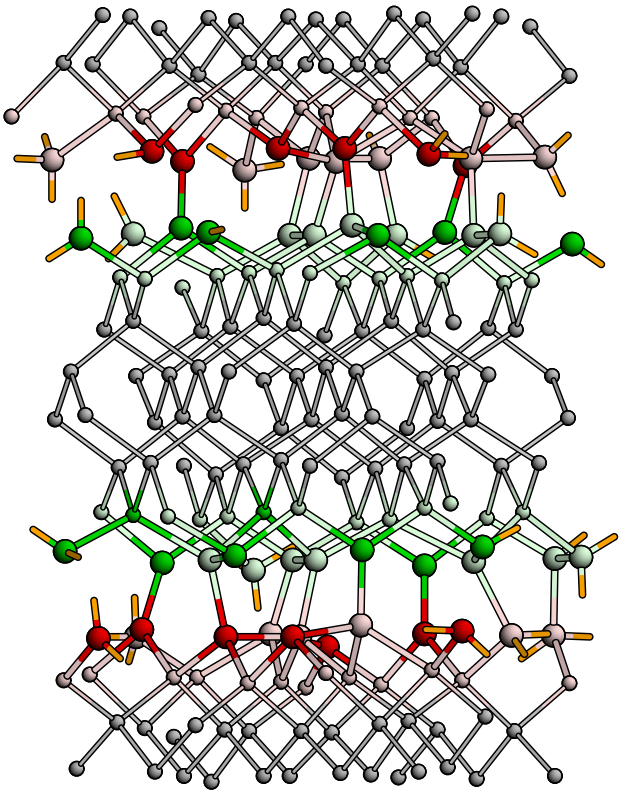

Figure 6.3: Side view of the periodic cell for a relaxed diamond Σ13 grain boundary. Two grain boundaries are shown, oriented as in Fig. 6.2. Dark shading indicates threefold coordinated atoms and light shading fourfold coordination. Atoms in the first monolayers of the interfaces are shown as larger spheres. Bonds extending across the cell boundary are shown as half bonds (interface layer only).

6.2 Twist (100) grain boundaries without impurities

6.2.1 Structure and bonding

As detailed in the preceding section, DFTB molecular dynamics calculations and simulated annealing were done on Σ5, Σ13, Σ29 twist (100) grain boundaries in diamond. The final minimum-energy structure for Σ13 is shown in Fig. 6.3. The next figure, Fig. 6.4 on the next page, gives an overview of all three selected grain boundary structures.

First, we notice that the structural disorder in all of the grain boundaries considered is confined to two atomic monolayers constituting the interface while the rest of the diamond crystal remains ordered. Since carbon can form both single and double bonds, energy minimisation is achieved by rehybridisation rather than significant atomic displacements. Therefore, a major component of disorder in the grain boundary is manifested by the different bond-order of the carbon atoms. Our results are consistent with TEM studies which give a grain boundary width of the order of 0.3 nm in the UNCD without impurities [158].

Calculated coordination and bond length distributions are given in Table 6.2. Threefold-coordinated atoms (denoted by *C3p* and *C3np* in Table 6.2; *p* = planar and *np* = nonplanar) constitute from 23% to 35% of atoms in the two grain boundary planes. About one half, denoted *C3p*, of the three-coordinated atoms have bond angles close to 120° with their neighbours, forming π-bonds, and the other half,

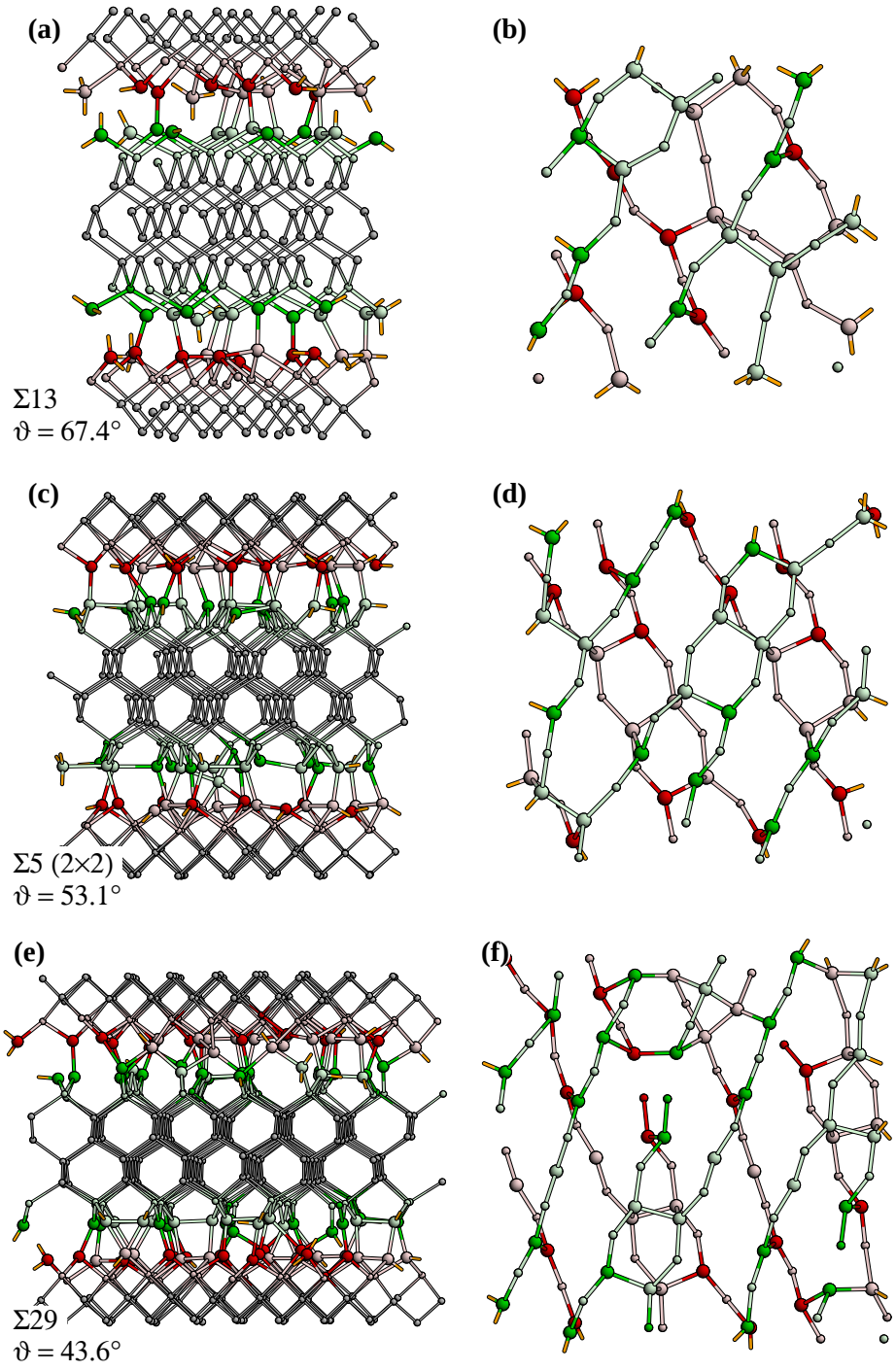

Figure 6.4: Comparison of relaxed periodic cells of grain boundaries: (a,b) Σ13, (c,d) Σ5(2×2), and (e,f) Σ29. The left panels show a side view containing two grain boundaries, and the right panels a top-view of the four interface layers for the upper grain boundary in each periodic cell. Atom appearance is the same as in Fig. 6.3.

Table 6.2: Coordination distribution and average bondlengths for carbon atoms in two grain boundary planes. *C3p*: threefold planar coordinated carbon, *C3np*: threefold nonplanar coordinated carbon, *C4*: fourfold coordinated carbon, and *C3/4*: fourfold coordinated carbon with the fourth bond longer than 1.84 Å (but less than 1.96 Å). T is the annealing temperature.

Grain boundary	T (K)	Coordination (%)				Average bond distance (Å)			
		C3p	*C3np*	*C3/4*	*C4*	*C3p-C3p*	*C3p-C4*	*C4-C3np*	*C4-C4*
$\Sigma5(2\times2)$	1500	11.3	23.8	16.2	48.8	1.40	1.53	1.54	1.56
$\Sigma29$	1500	19.8	9.5	22.4	31.0	1.38	1.51	1.52	1.56
$\Sigma13$	1500	23.1	7.7	15.4	53.8	1.43	1.51	1.51	1.57
$\Sigma13$	3000	19.2	7.4	19.2	53.8	1.42	1.50	1.53	1.57
$\Sigma13$	5000	11.5	11.5	28.8	48.1	1.41	1.51	1.58	1.57

denoted *C3np*, have a tetrahedral arrangement of their three bonds, leading to a geometry configuration which is typical for a carbon atom with a dangling bond. The results in Table 6.2 indicate that the fraction of threefold coordinated carbons does not change drastically for the three twist angles studied, although the ratio of *C3p* to *C3np* changes. Fourfold-coordinated carbons, *C4*, constitute about 50% of atoms in the grain boundaries. This is in good agreement with 40% of threefold-coordinated carbons in the $\Sigma29$ grain boundaries reported in previous tight-binding [181] studies. A larger fraction of 80% reported in an earlier atomistic [164] study is likely to originate from the known tendency of the Tersoff potential to overbind radicals, and thus stabilise threefold coordinated carbons. The remaining atoms in our case, denoted *C3/4*, have a tetrahedral arrangement of bonds, but the fourth bond is stretched beyond 1.84 Å. The radial distribution function $J(r)$ shown in Fig. 6.5 features these bonds next to the first maximum. Spin-unrestricted B3LYP density functional calculations on a C_2H_6 molecule with the C–C bond stretched up to 2.1 Å indicate that the electrons prefer energetically to remain paired and, therefore, there will be no dangling bonds formed at these interatomic distances. The presence of such bonds was not reported in previous calculations of carbon grain boundaries, but similar weak carbon bonds were reported before in rapidly quenched amorphous tetrahedral carbon [184].

Estimates from UV Raman spectra indicate that the concentration of sp^2 carbon in the UNCD films is about 5%. If one assumes a model where all of the sp^2 carbon from the Raman estimates is located in the grain boundaries and none in the grains, the resulting sp^2 percentage in the grain boundaries is consistent with the one found here in the simulations.

Although UNCD and tetrahedral amorphous carbons have predominantly tetrahedral bonding, there are two important differences between these materials. First, the ordered diamond structure is still the dominant phase in UNCD (more than 90%) and the fractions reported above are related to disordered grain boundaries only, i.e., 30% of threefold-coordinated carbons in the grain boundary translates into less than 3% in the material. Conversely, structures reported for amorphous carbon give an overall fraction of threefold-coordinated atoms (often summarily called sp^2) typically around 15–30%. Second, force-unbiased structural relaxation in the grain boundaries of UNCD is more difficult than in amorphous carbon because the former

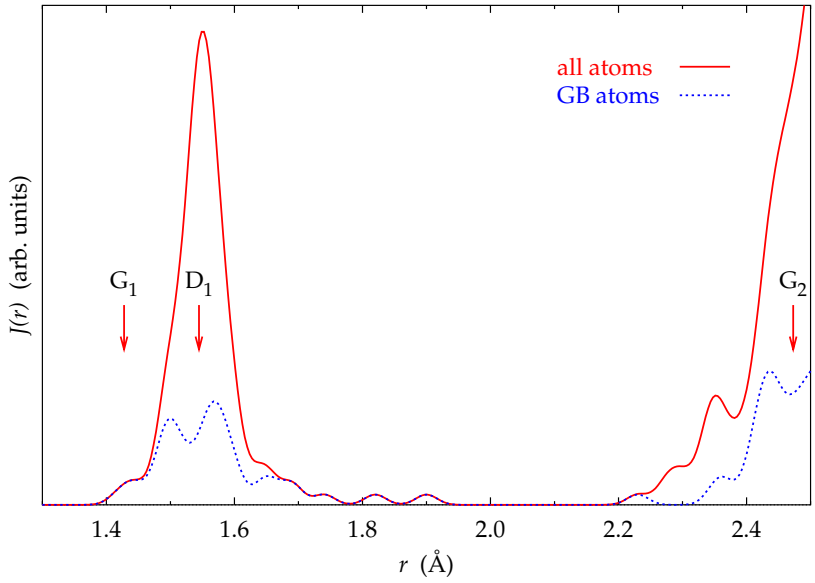

Figure 6.5: Radial distribution function $J(r)$ for a Σ13 grain boundary and a partial contribution to $J(r)$ of the first interface layers. For reference, nearest and next nearest neighbour distances of diamond and graphite are indicated by arrows labelled D and G, respectively.

has constraints on the geometry imposed by the presence of extremely rigid grains having diamond structure. About 20% of the atoms in the grain boundaries have one of their bonds weakened and stretched, which might be the consequence of the geometry constraints.

Across the interface, most of the bonds are single bonds between fourfold coordinated carbons and bonds involving a strongly deformed four-coordinated carbon and a three-coordinated carbon. A small number of double bonds are formed between sp^2-like carbons (*C3p*). The structures of the interfacial planes for the Σ13 model are shown in Fig. 6.6. It is evident that in addition to bonds formed across the interface, there are some bonds between interface atoms belonging to the same (100) plane. These bonds between pairs of four (three)-coordinated carbons are similar to surface dimers formed on a monohydrided (free) diamond (100) surface (see Chapter 4). The rest of the in-plane bonds are between three-coordinated and four-coordinated carbons, the latter having a bond across the interface. The number of in-plane dimers appears to be somewhat higher in our studies, especially for the Σ5 model [Fig. 6.4(d)], than found in the previous atomistic and tight-binding simulations for general high-angle grain boundaries; only at lower angles ($\approx 10°$) do in-plane dimers occur on the (100) faces in these simulations and are then more properly described as dislocations [164, 181]. The fact that we used a twofold enlarged $\Sigma 5(2 \times 2)$ supercell may explain the disparity. Obviously, the formation of surface dimers within a single Σ5 mesh is incommensurate with the odd number of atoms. While the same assertion holds for the other grain boundaries we simulated, it has lesser impact there because of the larger meshes, see Fig. 6.1 on page 88.

An analysis of bond length distributions in the Σ13 grain boundary (cf. Table 6.2) shows that the average bond length between two sp^2 atoms (*C3p*) is about 1.40 Å

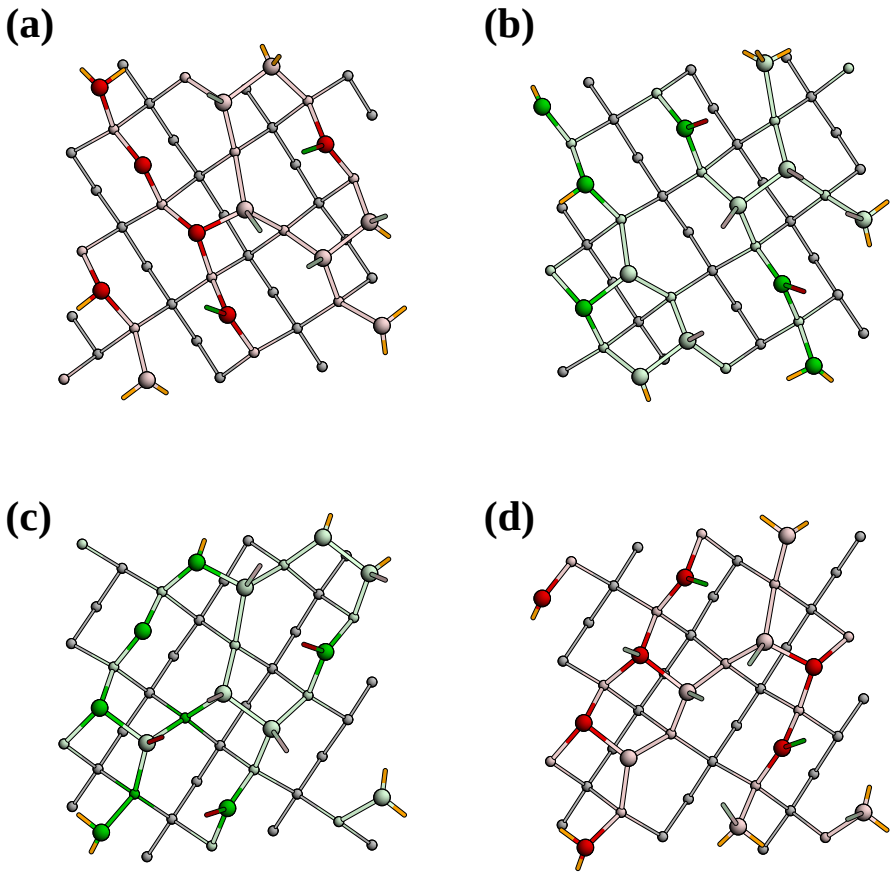

Figure 6.6: Overview of the individual interface planes for both grain boundaries in the diamond Σ13 grain boundary cell shown in Fig. 6.3. (a)-(d) are the top and bottom faces of the first and the top and bottom faces of the second grain boundary interface, respectively. Atom appearance is the same as in Fig. 6.3.

(double bond) and the average bond length between sp^2 and sp^3 ($C4$) atoms is 1.51 Å. The latter bonds are slightly shorter than single bonds, which on average have a length of 1.54 Å. It was found previously by Cleri et al. [181] for the case of the Σ29 twist grain boundary that π-bonds across the grain boundary are distorted by a dihedral torsion around the interfacial C–C bond arising from the twist angle of the grain boundary. This distortion is stronger in the case of Σ13, which has a twist angle of 67.4°, vs. 43.6° for Σ29. Larger twist angles weaken the π-bonds across the interface and lead to a larger number of in-plane dimers, i.e., bonds between carbon atoms belonging to the same interface plane. In the study of the π-bonded stacking fault [182], where all C–C interfacial bonds are double bonds, a strong repulsion between carbon atoms forming these bonds was identified to be due to the geometry restrictions imposed by the diamond lattice spacings. Because of this repulsion, the formation of some in-plane dimers will lead to an energetically more favourable geometry.

6.2.2 Energetics

The grain boundary energy per atom is defined as

$$\mathcal{E}_{GB} = (E_{cell} - \mathcal{E}_{diam} N_{cell})/N_{GB} \tag{6.3}$$

Here, E_{cell} is the total energy for the entire grain boundary periodic cell, $\mathcal{E}_{diam}$ the diamond bulk cohesive energy per atom [Tab. 4.4 on page 62], N_{cell} is the number of atoms in the grain boundary periodic cell and N_{GB} the number of grain boundary atoms involved (in both grain boundary layers). To convert to the more general quantity of energy per area, denoted E_{GB}, the value per atom must be taken *twice*, apart from the normalisation for the area of a $(100) - (1 \times 1)$ mesh.[3]

The grain boundary energies thus calculated were already included in Table 6.1 on page 90. The grain boundary energies are very similar for the three grain boundaries considered here. This indicates that the misorientation angle for high angle grain boundaries is not crucial in determining its energy, as is well known from other high-angle grain boundaries, both twist (e.g., Wang et al. [185]) and tilt (Shenderova et at. [178, 179]). Therefore, any of the angles can be taken as a representative for a disordered grain boundary. Our grain boundary energy of about $7.9\,J/m^2$ can be compared to about $6\,J/m^2$ obtained by Wang et al. [185] for a $\Sigma 5$ diamond grain boundary using energy minimisation and to $6.15\,J/m^2$ obtained by Keblinski et al. [164] for a high-temperature relaxed $\Sigma 29$ grain boundary. Both studies used Tersoff potentials. Energy values obtained with Tersoff potentials are known to be somewhat lower than tight binding results [185]. At any rate, the formation energies for diamond are much higher than those for silicon on twist [164] and tilt [178, 179] GB.

The calculated energy of about $1.6\,eV/atom$ is higher than typical energies of low-angle and special grain boundaries; nevertheless it is much lower than the surface energy of $2.3\,eV/atom$ of a $(100) - (2 \times 1)$ reconstructed surface [Table 4.6 on page 64]. Therefore, the high angle grain boundaries are relatively stable.

The grain boundary energy is the result of energy competition among different local configurations in the interface; the major competing configurations are two distorted single bonds and one double bond. If we imagine that any pair of atoms across the interface is connected by a double bond instead of two single bonds in the bulk, the resulting loss in energy per atom will be twice the energy of a single bond ($E_{coh}/4 = 2.34\,eV$ in the present calculations, Tab. 4.4) less the energy of the double bond which is $4/3$ times stronger. The result is $E_{coh}/6 = 1.56\,eV$ which matches quite well the calculated grain boundary energies. Because of the large misorientation between the two planes in the interface, two single bonds will come out strongly distorted or, if the distortion is too strong, they will compete with a more stable and flexible double bond configuration. Some of the distorted tetrahedral arrangements that we have commonly seen in the resulting structures are similar to surface carbons on the monohydrided (100) surface, i.e., one of the initially broken bonds belongs to a dimer formed in the interface plane whereas the other one is directed across the interface.

[3] The energy conversion for the diamond (100) face is: $1\,eV/atom = 2 \times 2.518\,J/m^2$, cf. Table 4.1 and Appendix A.

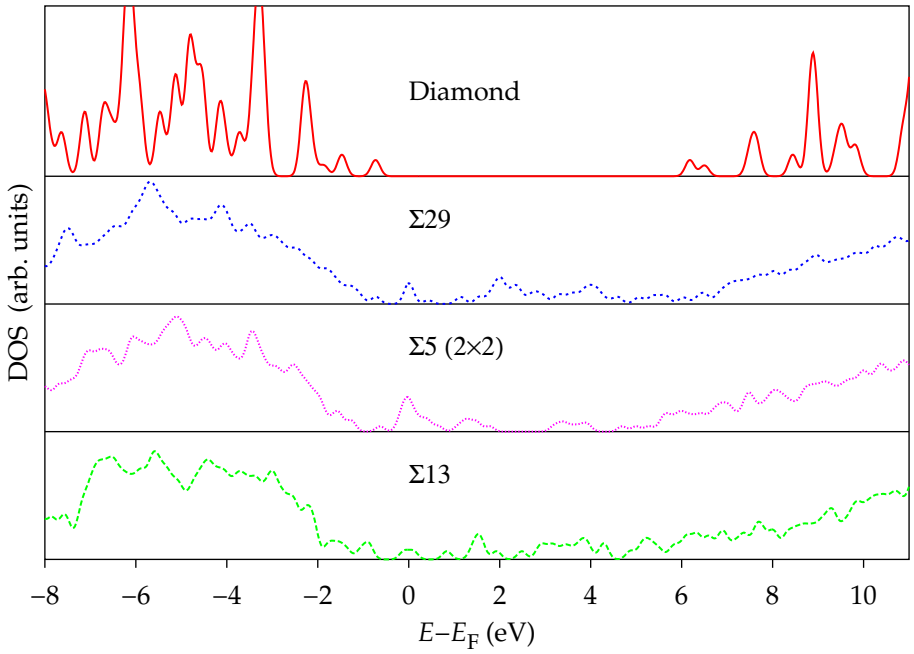

Figure 6.7: Electronic density of states for diamond, Σ13, Σ5(2×2) and Σ29 grain boundaries. Each plot is normalised by the number of atoms in the periodic cell. Energies are given relative to the Fermi energy. Note that the fraction of grain boundary atoms is higher in the calculation compared to experimental structures giving density of states peaks associated with the grain boundary atoms higher than expected weight.

6.2.3 Energy levels

It is well known that one-electron Kohn-Sham energies within LDA produce forbidden gaps which are too narrow (known as overbinding). On the other hand, use of our DFTB approach has the opposite effect mainly due to the use of a minimal basis set. Thus, the LDA underestimation of the gap width is partially compensated in our calculations. Therefore, the results reported here should be considered semi-quantitative. For example, the gap in diamond calculated using our DFTB method is 6.4 eV compared to the experimental value of 5.45 eV.

When topological disorder is introduced and is mostly confined to the two interface planes in the grain boundary region, the electronic structure changes profoundly. A number of electronic states appear in the band gap, which are π and π^* states on sp^2 carbon atoms as well as σ^* states associated with dangling bonds and distorted tetrahedral arrangement of four-coordinated carbons. The identification of states by their hybridisation (sp^2, sp^{2+x} and sp^3) is based here on the arrangement of neighbours relative to the carbon atom rather than a rigorous analysis of the corresponding orbitals. For instance, if an atom has four neighbours, the orbitals of this atom are assumed to be sp^3 hybridised. In certain situations, the hybridisation might not be clearly sp^2 or sp^3 because of distortions of bonds and angles induced by geometry restrictions. Nevertheless, we retain the common hybridisation terminology for the sake of discussion.

The density of states plots for Σ5(2×2), Σ13, Σ29 and diamond are given in Fig. 6.7.

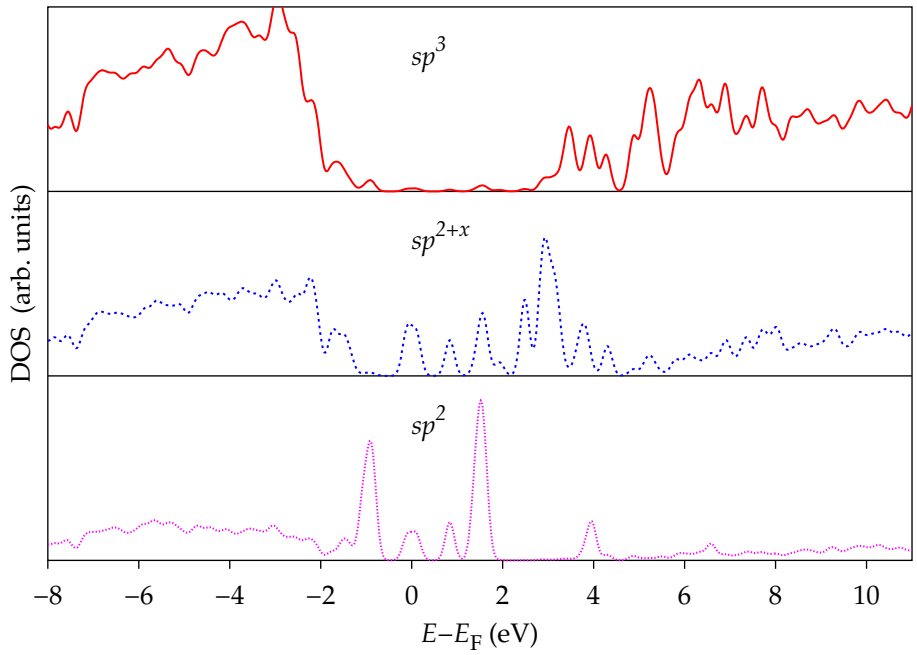

Figure 6.8: Local density of states for a diamond Σ13 twist grain boundary. Contributions from planar (sp^2) and nonplanar (sp^{2+x}) three-coordinated atoms and four-coordinated atoms (sp^3) in the grain boundary region are shown. Contributions from bulk atoms are omitted.

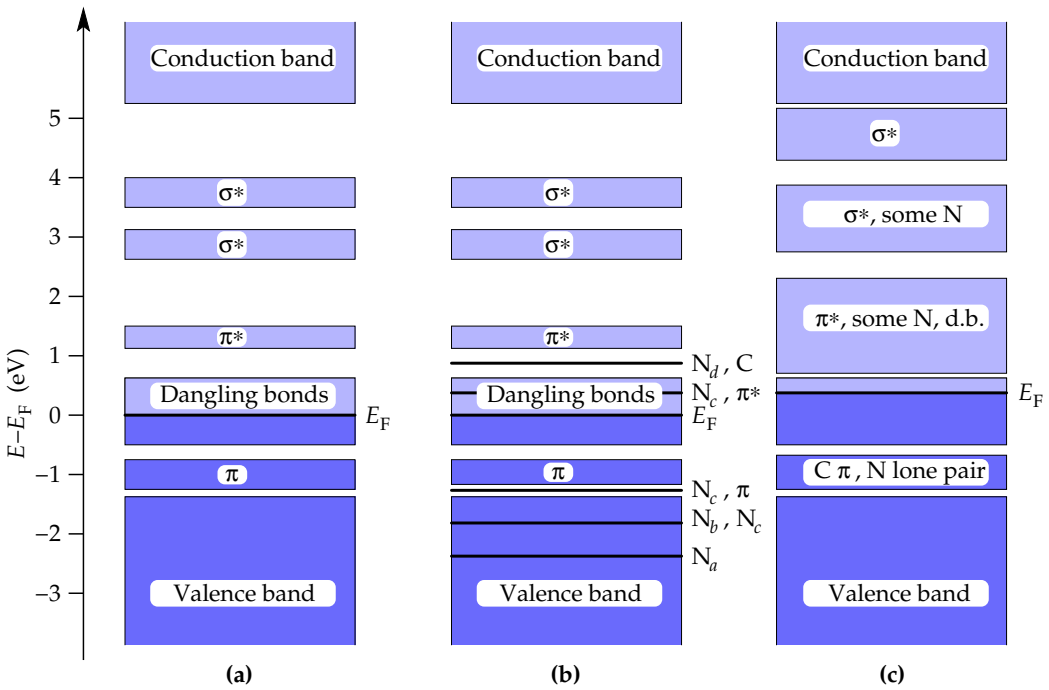

Figure 6.9: Schematic band structure for a diamond Σ13 grain boundary: (a) without nitrogen impurities, (b) with one nitrogen per cell, and (c) with sixteen nitrogens per cell. Subscripts on nitrogen levels correspond to different substitution sites (see text).

Several features in the band gap can be distinguished: (a) tails near the valence and conduction band edges, (b) a peak at the Fermi level (E_F) and (c) broad features from 0.7 eV to 2.5 eV and from 3 eV to 4.5 eV. To distinguish contributions of orbitals on sp^2 (*C3p*), sp^{2+x} (*C3np* and *C3/4*) and sp^3 (*C4*) carbons, we have calculated the local density of states for each of these types of atoms. The local densities of states for these different contributions are shown in Fig. 6.8 for Σ13. A scheme of the different energy levels is shown in Fig. 6.9. The states below $E_F - 1.4$ eV are delocalised and are in the diamond valence band. Threefold coordinated atoms with planar bond configurations (sp^2, *C3p*) produce π states from 1.2 eV to 0.8 eV below the Fermi level and π^* states from 1.2 eV to 1.5 eV above the Fermi level. These π and π^* levels are illustrated in Fig. 6.9(a). For comparison, electronic structure calculations of a diamond (100) surface, which agree with experimental photoemission data, produce π and π^* surface states in the ranges -1 to 0 eV and 2 to 4 eV, respectively [133]. The states near the Fermi level (-0.5 eV to 0.6 eV) are identified predominantly with threefold coordinated atoms in the nonplanar configuration (*C3np*, sp^{2+x}). These atoms have only fourfold-coordinated neighbours and thus are associated with dangling bonds. The orbitals of the *C3/4* atoms give rise to the σ^* peak from 2.65 eV to 3.1 eV above the Fermi level in Fig. 6.8. The four-coordinated atoms in the grain boundary layers as well as in the adjacent layers contribute to the σ^* feature at 3.5 eV to 4 eV. The states above 5.3 eV are delocalised at the bulk-like atoms and are in the diamond conduction band. As a result, the valence band and conduction band mobility edges are 6.7 eV apart, somewhat similar to the 7.9 eV reported in a previous tight-binding study [181]. The separation between the Fermi level and the bulk-like conduction band is 5.3 eV, which is 1.1 eV lower than the calculated diamond band gap. However, some of the states in the gap might be quite delocalised and could form a new band similar to an impurity band with its own mobility edges. In a future publication we will present a more detailed analysis of the amount of delocalisation of the wave function in the grain boundaries.

6.3 Nitrogen substitutional impurities

6.3.1 Structure and bonding

For the study of nitrogen impurities, carbon atoms at various sites in the interface layer of the annealed grain boundary were substituted by nitrogen and the annealing procedure was fully repeated to find the optimised position of the nitrogen atom. The choice of the substitutional site in the disordered structure is not unique because local disorder creates a number of chemically diverse carbon atom arrangements. The sites themselves are no longer strictly determined by the translational symmetry of the system, since carbon atoms in the interface layers are significantly displaced from their initial positions in the coincident site lattice geometry. The positions of the grain boundary carbon atoms are determined by energy minimisation of the structure and any of the positions can be considered for impurity substitution in the simulations.

Four different initial positions for a single nitrogen atom substitution in the grain boundary were considered: *C3np*, *C3p*, *C4* in the grain boundary layer and *C4* in

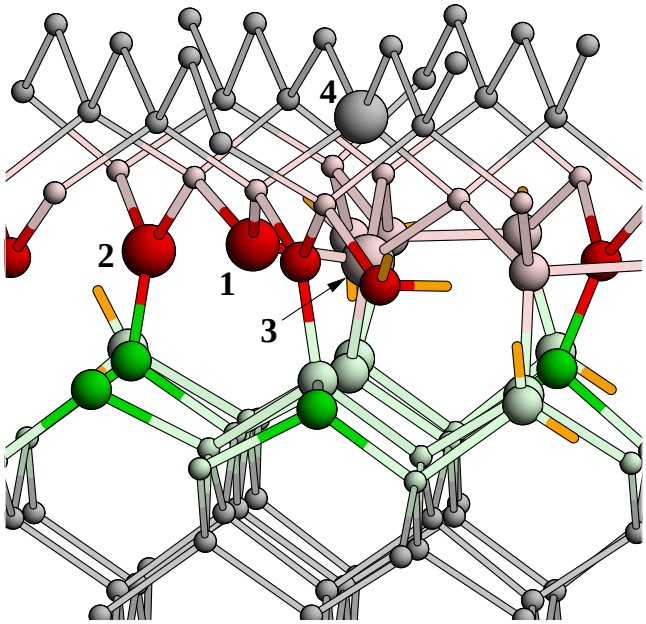

Figure 6.10: Substitution sites selected in a Σ13 grain boundary. The sites are: **1.** *C3np* [threefold non-planar], **2.** *C3p* [threefold planar], **3.** *C4* [fourfold] within the grain boundary, and **4.** *C4* [fourfold] in the second layer.

Table 6.3: Coordination distribution for nitrogen and carbon atoms in two grain boundary planes of Σ13. n_N is the number of nitrogen atoms per cell, T the initial annealing temperature, and E is the nitrogen substitution energy (see text). The notation for carbon atoms is the same as in Table 6.2. *C2* is twofold coordinated carbon, and *C3/4* is included in *C3np*.

n_N	T (K)	Initial N	C-coordination (%)				N-coordination (%)			E (eV)
		position	*C2*	*C3p*	*C3np*	*C4*	*N2*	*N3p*	*N3np*	
1	1500	*C3np*	0	23.1	21.2	53.8	0	0	1.9	−0.6
1	1500	*C3p*	0	19.2	28.8	50.0	0	1.9	0	0.7
1	1500	*C4*	0	23.1	25.0	50.0	1.9	0	0	1.7
1	1500	2nd layer	0	25.0	23.1	50.0	0	0	1.9	2.6
16	1500	Random	3.8	9.6	19.2	32.7	13.5	9.6	7.7	
16	5000	Random	5.8	11.5	36.5	15.4	13.5	9.6	7.7	

the second layer, as shown in Figure 6.10.

A summary of the nitrogen and carbon coordinations is given in Table 6.3. The most stable nitrogen position is a three-coordinated site with nonplanar arrangement of the bonds identified originally as a carbon with a dangling bond. This site changes its geometry only slightly after the substitution. The local structure of the optimised nitrogen geometry is shown in Fig. 6.11(a). The nitrogen atom is located 0.57 Å out of the plane of its three neighbours. The small changes in the geometry upon relaxation are an expected result considering that the nonplanar threefold coordinated nitrogen configuration is favoured for substitutional nitrogen in diamond bulk [186, 187, 188]. It will be shown later that the nitrogen saturates the original dangling bond and forms a lone pair instead. As opposed to the bulk case, no bond breaking is required. In the bulk, substitutional nitrogen moves from a T_d position along the [111] direction away from a nearest neighbour to a threefold coordinated position of C_{3v} symmetry.

Annealed and relaxed local structures for the other three positions are shown in

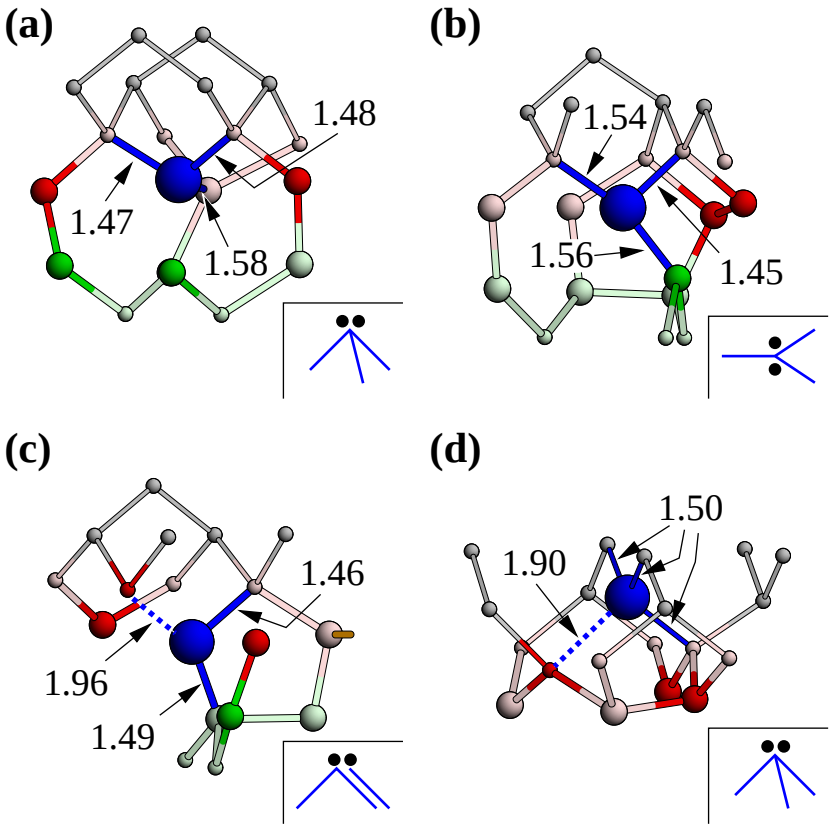

Figure 6.11: Relaxed local structure around a substitutional nitrogen atom at various sites in a Σ13 grain boundary. The panels correspond to the substitution sites shown in Fig. 6.10, i.e. (a) *C3np*, (b) *C3p*, (c) *C4* in grain boundary, and (d) *C4* in second layer. The molecular analogies of nitrogen bonding are shown schematically in the insets. Bondlengths in Å.

Fig. 6.11(b-d). Substitution in the planar threefold-coordinated site (*C3p*, sp^2 carbon), shown in Fig. 6.11(b), results in a slightly puckered nitrogen configuration with the nitrogen atom located 0.27 Å out of the plane. Thus, it is similar to the resulting geometry of substitution into a *C3np* site discussed above. However, its carbon bond partner across the interface moves from a previously planar configuration into a considerably more pyramidal one. In the final structure, this carbon atom has moved to 0.42 Å out of plane, compared to 0.12 Å originally. The bond to the nitrogen lengthens from 1.42 Å to 1.56 Å. Both processes indicate a change of the bonding character from a double bond to a single bond and a new dangling bond on the carbon atom. The next substitution site for nitrogen substitution, a fourfold-coordinated site (*C4*) in the grain boundary layer becomes twofold coordinated upon relaxation and the third nearest neighbour is 1.96 Å away. Finally, the configuration of nitrogen upon substitution in the second layer, shown in Fig. 6.11(d), is nonplanar threefold coordinated and the fourth neighbour is 1.90 Å away, quite similar to that in the bulk diamond. Generally, the carbon-nitrogen bond lengths are in the range 1.45 Å–1.56 Å. The distortions of bonds are caused by the geometrical constraints due to the surrounding carbon lattice. These restrictions are weaker for nitrogen in the grain boundary compared to the diamond bulk because of the local disorder. Therefore, it is easier to accommodate nitrogen in the grain boundary.

6.3.2 Energetics

The nitrogen defect formation energies were calculated as the work to bring a nitrogen atom from an N_2 reservoir to the system minus the work to remove a carbon atom from the system to a diamond bulk reservoir:

$$E = E^{\mathrm{N}}_{\mathrm{cell}} - \left(E_{\mathrm{cell}} - \mathcal{E}_{\mathrm{diam}} + \frac{1}{2} E_{\mathrm{N}_2} \right) , \tag{6.4}$$

where $E^{\mathrm{N}}_{\mathrm{cell}}$ (E_{cell}) is a total energy of the grain boundary periodic cell with (without) substituted nitrogen, $\mathcal{E}_{\mathrm{diam}}$ the diamond total energy per atom, and E_{N_2} the total energy of the nitrogen dimer.

The calculated formation energy of a substitutional defect in the grain boundary for the most stable configuration is -0.64 eV compared to 4.9 eV in the diamond single crystal (see Table 6.3). The formation energies for other nitrogen substitutions are slightly higher: the planar three-coordinated site energy is 0.7 eV, the four-coordinated carbon site energy is 1.7 eV and the energy of the site in the grain boundary second layer is 2.6 eV. All of the grain boundary sites are preferred over the diamond bulk site for nitrogen substitution. Since the substitution energy in the bulk of the grain should be close to that in a diamond crystal, under equilibrium conditions the nitrogen concentration in the grain boundary will be many orders of magnitude higher than in the grains. Typical growth conditions are usually far from equilibrium; however, in view of the large energy difference it is likely that nitrogen will be concentrated in the grain boundaries.

It was found experimentally that the nitrogen concentration saturates in the UNCD at 0.2% with increasing nitrogen content in the plasma [189]. This concentration is much higher than in microcrystalline diamond and lower than the nitrogen saturation limit in amorphous carbon. The saturation of the UNCD nitrogen concentration is consistent with the calculated lower formation energy for nitrogen defects in the grain boundary compared to the bulk because if nitrogen were incorporated into the grains during the growth, the saturation limit would be much higher. Furthermore, if some sites in the grain boundaries are more favourable for nitrogen incorporation, their limited number would further limit nitrogen concentration in the UNCD.

6.3.3 Energy levels

Nitrogen in bulk diamond

The electronic structure of nitrogen defects in diamond has been the subject of many theoretical and experimental studies. Single substitutional nitrogen in diamond (the P1 centre) gives rise to a well-known carbon dangling bond state in the diamond band gap and a nitrogen state below the valence band maximum (VBM). Our DFTB calculations on diamond find the dangling bond state at 3.0 eV above the valence band top compared to 3.8 eV from experiment [114] (1.7 eV below the diamond conduction band minimum). This state is localised mostly on the threefold-coordinated carbon atom which is 2.04 Å away from the nitrogen, which also has about 25% participation. The atomic charge distribution of this state is illustrated in Fig. 6.12(a). A

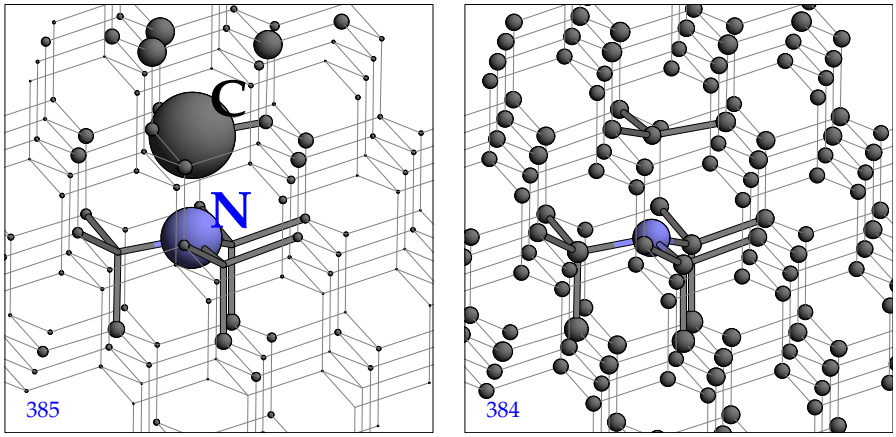

(a) $E_{\mathrm{VBM}} + 2.96\,\mathrm{eV} = E_F$ (b) $E_{\mathrm{VBM}} + 0.11\,\mathrm{eV}$

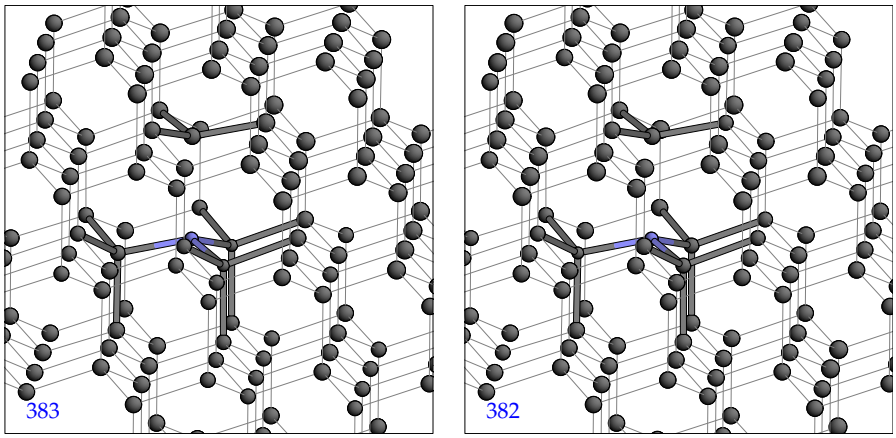

(c) E_{VBM} (degenerate) (d) E_{VBM} (degenerate)

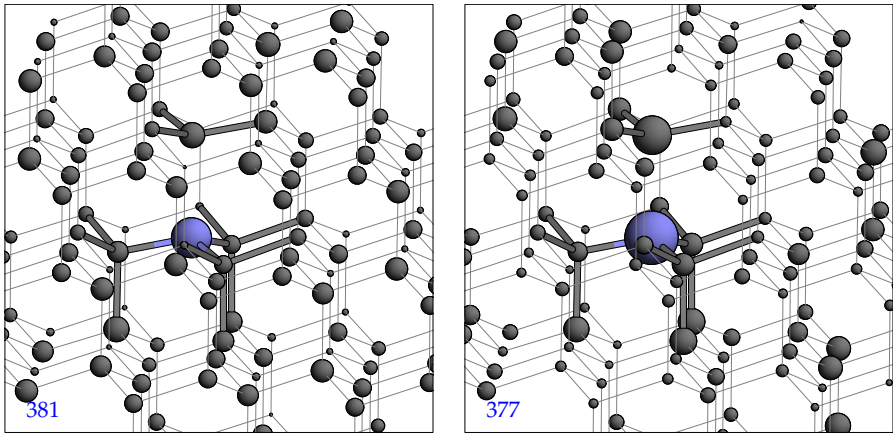

(e) $E_{\mathrm{VBM}} - 0.62\,\mathrm{eV}$ (f) $E_{\mathrm{VBM}} - 1.36\,\mathrm{eV}$

Figure 6.12: Localisation of electronic states around a substitutional nitrogen atom in diamond (P1 centre), as calculated in SCC-DFTB and discussed in the text. Mulliken population per state, q_a^i from eq. (2.35), are visualised as sphere volume. All states are normalised. A (110) type supercell with 192 atoms was used. The panels show the charge distribution for states near the valence band maximum which have a significant N participation. The inset labels denote state numbers.

similar antibonding combination of the carbon dangling bond and nitrogen orbitals was found at 1.9 eV below the conduction band by Kajihara et al. [190] in their Car-Parinello study. The nitrogen state which Kajihara et al. reported to be at 0.15 eV above the valence band top was ascribed to the nitrogen lone pair with an admixture of valence band states. In our study, we find a similar state near the top of the valence band [Fig. 6.12(b)]. However, a closer look reveals that there is a bonding combination of the lone pair with the orbitals of the unique carbon neighbour (as verified by a molecular orbital analysis of a cluster model) which is strongly hybridised with other delocalised carbon states near the VBM, as can be seen clearly in the figure from the nearly equal charges associated with all atoms. As a result, we observed a number of states [Fig. 6.12(b-f)] with appreciable nitrogen participation near the top of the valence band. A resonance which has the largest nitrogen contribution was found at 1.4 eV below the VBM and this state will be referred to as a lone pair.

Nitrogen in diamond grain boundaries

The DFTB calculations of this study indicate that some nitrogen substitutions in the Σ13 grain boundary give rise to electronic states similar to those for nitrogen defects in diamond. However, the positions and occupancies of the levels in the case of GB substitutions are more diverse and in some cases have no analogy with the bulk substitution. The states for different nitrogen sites are shown schematically in Fig. 6.9(b). Substitution into the three-coordinated sites in the grain boundary (sites *a* and *b*) gives a nitrogen lone pair state about 1.5 to 2 eV below the Fermi level. If nitrogen is substituted into a fourfold coordinated site (site *c*), the nitrogen orbitals give contributions to the carbon π states at -1 eV and to the π^* states at 0.5 eV relative to the Fermi level, in addition to the nitrogen lone pair. Finally, the substitution site in the second layer (site *d*) gives rise to an unoccupied level at about 0.8 eV above the Fermi level, which has strong carbon participation. In this case, the Mulliken charge on the nitrogen is reduced by about 0.4 e. This charge is transferred to the state at the Fermi level associated with a carbon dangling bond, forming a carbon lone pair. Whereas there is no evidence of shallow donor levels near the σ^* conduction band, the σ^* carbon dangling bond levels which are above the Fermi level will donate electrons to the states at the Fermi level. This will lead to the increase of the electron density at the Fermi level. The Fermi level will shift towards the conduction band and this could result in the increase in *n*-type conductivity in ultrananocrystalline diamond.

To investigate the possible shift of the Fermi level due to nitrogen substitution as well as the interaction of nitrogen impurities, we performed a calculation with a higher concentration of nitrogen in the grain boundaries. Thirty percent of the grain boundary carbons were substituted by nitrogen resulting in an overall nitrogen concentration of about eight atomic percent. After annealing and relaxation, the nitrogen distribution in the grain boundaries with respect to configuration is about 50% sp^1, i.e., nitrogen with two bonds to carbons (*N2*), and the rest nearly equally divided between sp^2 (*N3p*) and sp^{2+x} (*N3np*) geometries. The sp^1 configuration appears only at the increased nitrogen concentration and it is similar in bonding to the nitrogen in a pyridine molecule. However, no aromatic rings or pyridine rings were

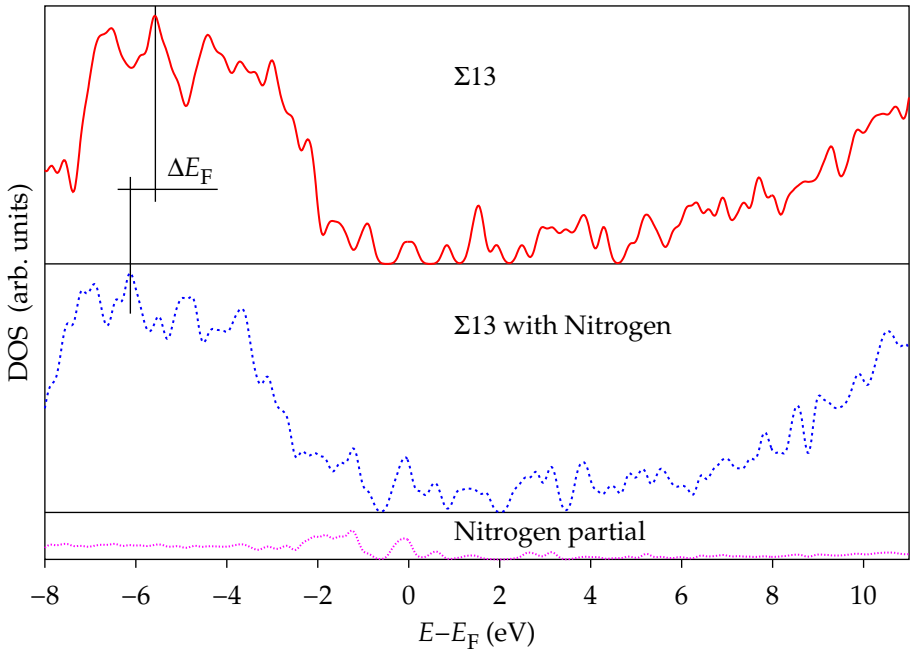

Figure 6.13: Densities of states for a diamond Σ13 grain boundary without and with 30% nitrogen impurities. The local density of states for nitrogen atoms is given in lower panel.

found in the resulting structure. Nitrogen atoms are found to avoid each other in the grain boundaries, which was also found in amorphous carbon nitride studies using non-SCC-DFTB [191, 192].

The electronic states associated with nitrogen are most prominent just above the top of the valence band, near the Fermi level and in the σ^* carbon dangling bond region around 3 eV above the Fermi level. This is illustrated schematically in Fig. 6.9(c), as well as in the density of states plot in Fig. 6.13. The Fermi energy is shifted towards the conduction band by about 0.4 eV. The states near the top of the valence band originate from nitrogen lone pair electrons and they are significantly mixed with carbon π states. Due to the finite size of the periodic cell in our model, it is difficult to determine the mobility edge since these states are not strongly localised. There is some admixture of nitrogen states in the carbon dangling bond states at the Fermi level and at 3 eV above. The latter states are quite similar to the states which appear due to the interaction between a carbon dangling bond and nitrogen in diamond bulk, where the electron is localised on the carbon with some nitrogen participation. Since the orbitals at 3 eV are no longer the highest occupied ones as in the case of nitrogen defects in bulk diamond, the electrons are transferred to the lowest unoccupied states right above the Fermi level, which explains its shift relative to the nitrogen-free case. The highest occupied state was found to be associated with a threefold coordinated carbon atom which has a Mulliken charge of -0.6 e, i.e., a carbon lone pair. The tail of the conduction band has been significantly extended, primarily due to distortions of tetrahedral bond geometries that in this case involve not only the immediate grain boundary atomic layer but the second atomic layer as well. The states in the band gap are visibly more delocalised in the presence of impurities in the grain boundaries.

We propose that the conduction in UNCD occurs via grain boundaries based on the results of our calculations. The conclusion that nitrogen is predominantly in the grain boundaries makes it highly unlikely that the UNCD conductivity is due to nitrogen doping in the grains. The DFTB calculations of nitrogen substitution show that new electronic states associated with carbon and nitrogen in the grain boundaries are introduced into the diamond fundamental gap. The carbon dangling bond states hybridised with nitrogen lone pairs are above the Fermi level and donate electrons to the carbon defect states near the Fermi level causing it to shift upward, towards the delocalised π^* carbon band. Thus, it is reasonable to imagine that variable range hopping or other thermally activated conduction mechanisms can occur in the grain boundaries and result in enhanced electron transport. Note that this mechanism does not require a true doping nitrogen state (fourfold-coordinated nitrogen or threefold-coordinated nitrogen with a double bond). Furthermore, an increase in nitrogen concentration could lead to a semimetallic behaviour because of the increase in the connectivity of sp^2 bonded carbon, higher delocalisation of the π^* electronic states and broadening of the π^* band. A similar conduction mechanism was discussed by Veerasamy et al. [193] based on their experimental results on tetrahedral amorphous carbon.

6.4 Silicon substitutional impurities

Silicon impurities were generated using the same substitution procedure as for nitrogen. The optimised structure of a grain boundary with a substituted silicon atom is shown in Fig. 6.14. Silicon substitution into a grain boundary site always results in the Si atom being four-coordinated independent of the initial configuration. The carbon – silicon bond lengths are typically 1.78 Å to 2.01 Å. The bond angles are distorted from tetrahedral angles, with values between 84° and 110°. The formation energies of the substitutional Si are -0.85 eV to 1.45 eV compared to bulk reservoirs as a reference. The energy required to insert Si into the grain boundary is much lower than the 4.45 eV required to insert it into the diamond crystal. A grain boundary has a much lower local density than the ordered diamond structure and, therefore, it is easier to accommodate a larger silicon atom. The number of four-coordinated carbon atoms in the vicinity of Si increases. In the timescale of a simulation (about 1 ps) neither silicon nor nitrogen atoms move between different sites. In our calculations, we have not found electronic levels due to silicon in the diamond band gap. Therefore, we believe that Si will not influence the electrical and electronic properties of UNCD.

6.5 Hydrogen addition

Hydrogen incorporation into UNCD was simulated by *adding* four hydrogen atoms per grain boundary unit cell at random positions in the interface of the annealed structure. As in the previous simulations, the annealing procedure was repeated. In the final structure, all hydrogens are bonded to carbon atoms, which, as a result, become four-coordinated. The average carbon hydrogen bond length is about

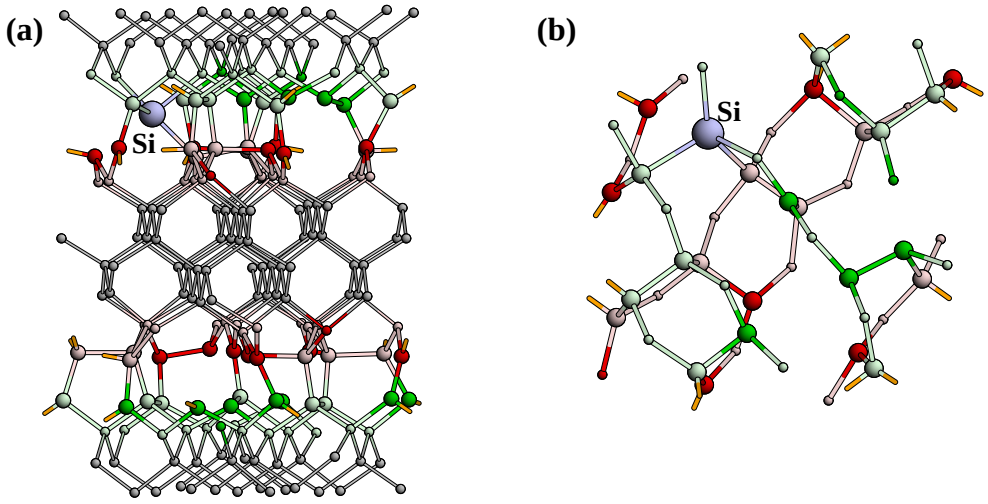

Figure 6.14: Side view (a) and top view (b) of the four interface layers of the periodic cell for an optimised diamond Σ13 grain boundary with a silicon impurity.

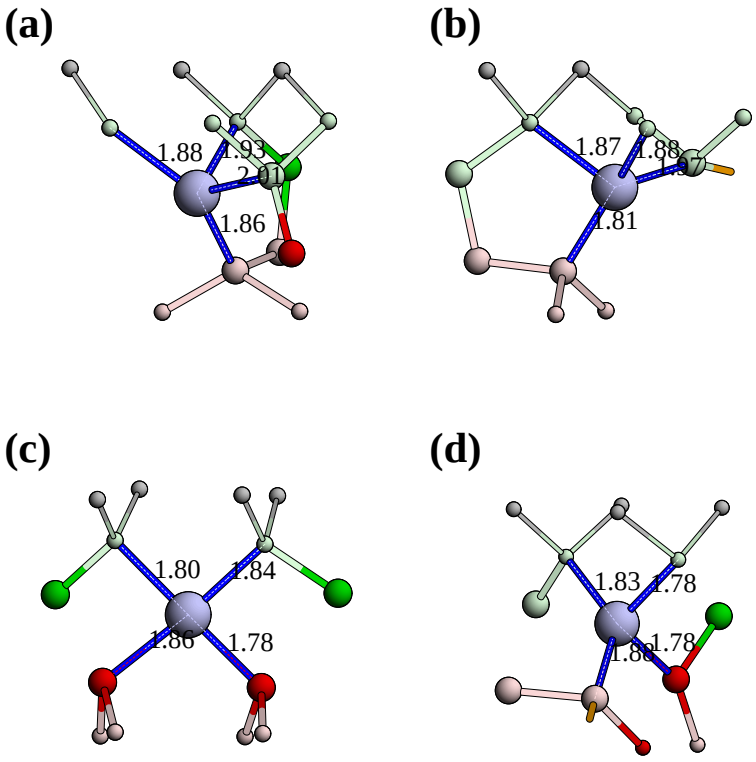

Figure 6.15: Relaxed local structure around a substitutional silicon atom at various sites in a Σ13 grain boundary, analogous to Fig. 6.11.

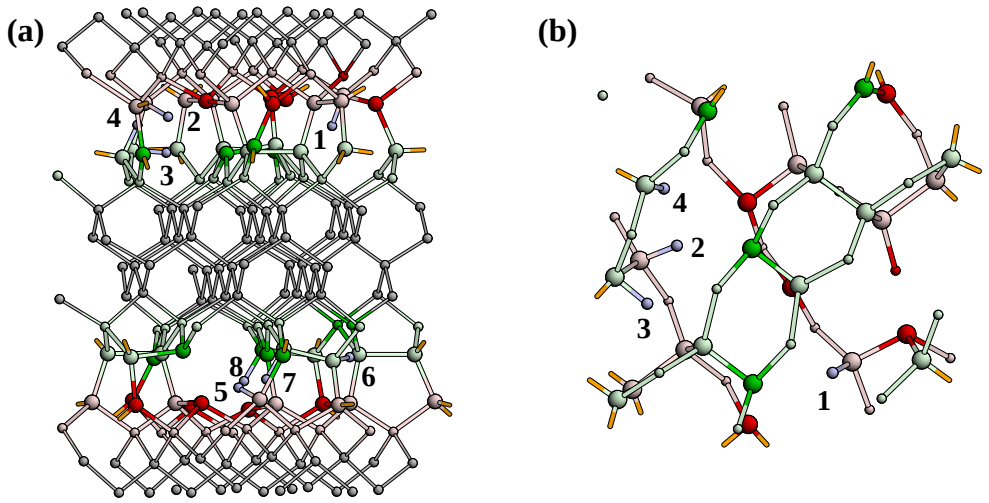

Figure 6.16: Relaxed structure of a Σ13 grain boundary with added hydrogen. (a) side view of the periodic cell showing four added hydrogens in each of the two grain boundaries, and (b) top view of one grain boundary. The numbers enumerate the added hydrogen atoms.

1.10 Å. The average hydrogen binding energy is 3.5 eV. The number of carbon atoms with a dangling bond (*C3np*) decreased from 21% to 4%. Thus, hydrogens saturate dangling bonds of three-coordinated carbons, as expected. The hydrogen concentration in UNCD films is smaller than the concentration of carbon atoms in the grain boundaries because the films are grown under hydrogen-poor conditions and also the overall fraction of atoms in the grain boundaries is high. We have not found any EPR active hydrogen-related defects since the hydrogen concentration in our calculations is lower than the density of the dangling bonds. Such defects, labelled H1 and H2 centres, are known in microcrystalline CVD diamond [194, 195]. Since the total amount of hydrogen used in the calculation was lower than the number of dangling bonds in the initial structure, some dangling bonds are still present. The main change in the electronic structure is the reduction of the density of states near the Fermi level. This finding is consistent with the fact that hydrogen is known to passivate surfaces, grain boundaries and other lattice imperfections in CVD diamond. Small shifts of other carbon levels and a broadening of the peak at about 4 eV above the Fermi level were found.

A particular observation from the molecular dynamics on the mobility of hydrogen within the grain boundaries supports the passivation conclusion. At the beginning of the simulation (at about 1200 K) the hydrogens were found to move among different carbon sites within the grain boundary plane, whereas at lower temperatures (about 1000 K) their (thermal) motion is restricted to the vicinity of their carbon bond partner. A similar migration pattern was observed in a tight-binding study of hydrogen in diamond [196] where real hydrogen diffusion was observed above 1700 K and jumps between equivalent sites around the same C–C bond were observed at 1200 K. Our observation of a lower temperature of the diffusion onset might indicate that grain boundaries have lower barriers for diffusion compared to the bulk diamond. It was found experimentally that hydrogen plasma treatment suppresses the electrochemical activity of the UNCD films [197]. This is consistent with the

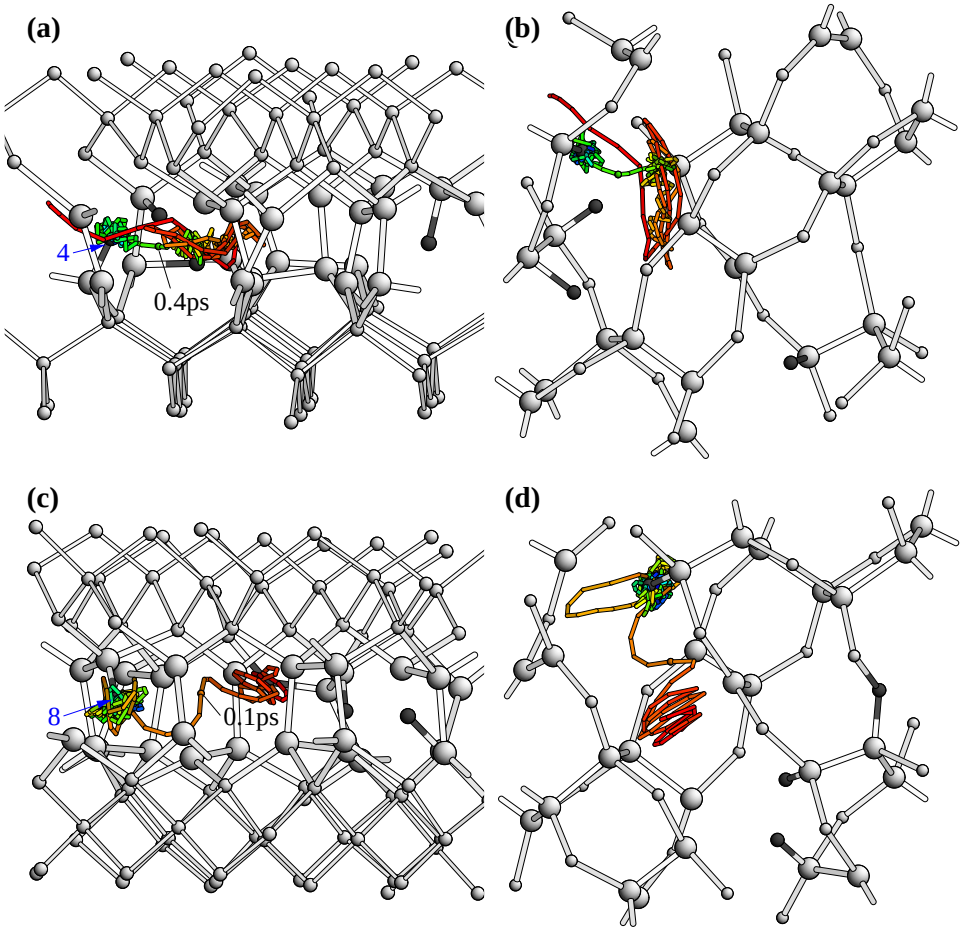

Figure 6.17: Molecular dynamics path of two selected hydrogen atoms during the initial annealing phase (0.5 ps at 1200 K, and 0.4 ps at 1000 K). The MD time step is 1 fs, but one path segment covers three steps. Characteristic transition times for site hops are indicated. The colour of the path indicates elapsed time, progressing from red to blue over the course of 0.9 ps. For clarity, the customary atom colouring has been subdued. (a) and (b) show atom 4 of Fig. 6.16, and (c) and (d) atom 8. The selected atoms belong to different interfaces.

calculated saturation of the dangling bonds by hydrogen and the corresponding decrease of the sp^2/sp^3 ratio of the grain boundaries.

6.6 Summary

This concludes the study of high-energy twist-angle (100) grain boundaries in diamond. In summary, the grain boundaries were confirmed to be atomically narrow, spanning only the two immediate interface monolayers. About 40%–50% of all atoms in the interface at the grain boundaries are threefold coordinated. The amount of three-coordinated carbons is very similar for all of the twist angles studied. The formation energies for the $\Sigma 5$, $\Sigma 13$ and $\Sigma 29$ (100) twist grain boundaries are also about the same, namely, 1.6 eV per interface atom.

The electronic structures of clean GB's are quite similar, being characterised by a smaller band gap than in bulk diamond and the presence of electronic levels at and above the Fermi level. Those gap states are localised on grain boundary atoms.

The incorporation of nitrogen impurities into the grain boundary is easier than into bulk diamond. The nitrogen substitution energy for the GB is lower than for bulk diamond by 2.6 eV to 5.6 eV. Nitrogen increases the amount of three-coordinated carbon atoms in the grain boundary. A shift in the Fermi energy toward the conduction band of about 0.4 eV at larger nitrogen concentrations was observed. We propose that GB conduction involving carbon π-states in the GB is responsible for the high electrical conductivities in these films.

Silicon substitution into the grain boundary is more favourable by 3.0 eV to 5.3 eV than into the bulk and always results in a four-coordinated Si atom in the grain boundary. Finally, hydrogen saturates dangling bonds of carbon atoms in the grain boundary and an average hydrogen binding energy of 3.5 eV. Similar to clean surfaces, hydrogen removes electronic states associated with dangling bonds from the band gap and so lowers the film conductivity.

Chapter 7

Summary and Conclusions

The main contributions of this work are a methodological development of the density-functional based tight-binding method and the application of the standard SCC DFTB method to calculate the growth and structure of ultrananocrystalline diamond films.

The theoretical background on density functional theory was reviewed in Chapter 1. This was followed by a closer look on the DFTB method in Chapter 2, where the variational background was reviewed. The developments over the years of the DFTB implementations up to the SCC formulation were also reviewed and juxtaposed.

In Chapter 3, a linear-scaling implementation of the DFTB total energy calculation including charge self-consistency was presented. Specific problems solved in comparison with existing schemes were of quantitative and qualitative nature. Firstly, the interaction ranges between support functions in $\mathcal{O}(N)$-DFTB are much bigger than in usual tight binding $\mathcal{O}(N)$ schemes. In the present implementation, the longer ranging TB interaction pushes the breakeven point with diagonalisation rather far out. Stability problems were addressed by the adaptation of existing root finders to a nonlinear optimisation problem. Secondly, the present method handles heteroatomic systems with a species dependent number of LCAO basis functions. Finally, bond charges were introduced due to the overlapping basis functions. The bond charges and, trivially, onsite charges enter the calculation of atomic charges as well as energy and gradient corrections due to charge self-consistency contributions, approximately doubling the time for a wave function minimisation. The implementation was verified with several numerical examples to satisfactorily reproduce energies and forces and to scale linearly for the major energy and force contributions, apart from the quantum Coulomb problem, which plays a subordinate role. The scheme presented is potentially suitable for both condensed matter and molecular systems containing multiple species and naturally couples to molecular dynamics simulations. Nonetheless, practical applications will require significantly extended effort.

Chapter 4 offered a review on more general aspects on diamond, followed by experimental data for bulk and surfaces, and closes with DFTB calculations on these systems. The calculations serve as benchmarks corroborating the reliability of the

Γ-point- and nearest-box approximations in DFTB. Given their fundamental importance these issues have of course been studied before, but a systematic review has not been performed within SCC DFTB. The primary goal of the chapter was to establish reference data for bulk and surface energies. A comparison to relevant *ab initio* results is quite satisfactory, yielding deviations of about ± 0.2 eV/site for energies and 0.02 Å rms deviations for the geometry, relative to the respective equilibrium lattice constants. However, the bulk modulus is overestimated by about 20%.

In Chapter 5, growth steps on a (110) diamond surface were modelled by simulating successive depositions of C_2 molecules onto the surface. The initial C_2 adsorption onto a clean (110) diamond surface proceeds with small barriers (0.1–0.2 eV) into the diamond lattice site. The growth mechanism and energetics of this insertion are similar to those on hydrogenated surfaces, as suggested previously [169]. Subsequent C_2 additions on and around the initial adsorbate preferably lead to C_{2n} chains forming along the $[\bar{1}10]$ direction on the surface. The adsorption energies, as listed in Table 5.1, are in the range of 7–10 eV per C_2 molecule at adsorption sites which lead to chain growth, and slightly smaller, 5–7 eV, for sites leading to defected growth. Some backbonds at the C_{2n} chains are broken, leading to a graphenelike morphology, if 50% coverage is reached for the added monolayer. However, the surface remains stable at this point. If the C_2 deposition continues, it induces healing of the broken backbonds due to re-formation of sp^3 bonds at the terminus of the graphene sheets.

Some metastable C_2 defects were also found to occur during growth, which may be responsible for starting new nucleation sites, a tendency that would explain the rather small grain size in the experimental studies which motivated this work. Low energy growth may be possible, if the approaching molecule has a kinetic energy within a window of 3–5 eV in order to overcome barriers and avoid defect formation. Direct adsorption into a diamond lattice position is possible only at the end of a C_{2n} cluster or onto a clean site of the surface. Upon coalescence of different C_{2n} chains, the remaining vacancies can be filled by the same growth species, although with slightly higher barriers (0.3–0.6 eV) than in the initial stages.

Finally, surface diffusion studies were carried out. Because the C_2 adsorptions normally result in tightly bonded adsorbate structures, interisland diffusion of C_2 molecules is rather unlikely. However, an intraisland diffusion path exists, where an added C_2 molecule diffuses on top of a C_{2n} chain until it reaches its end and is incorporated there. This diffusion behaviour supports the C_2 addition model that was evident from the deposition energetics. An implication of this fact is that an enhancement of surface diffusion rates would result in an increase in growth rate, by virtue of diffusion of migrating C_2 species to and eventual incorporation into growth sites.

Chapter 6 reported on density-functional based tight-binding molecular dynamics calculations of high-energy twist-angle (100) grain boundaries in diamond. Grain boundaries with and without impurities were investigated. In agreement with previous atomistic and tight-binding simulations, all grain boundaries were confirmed to be atomically narrow, spanning only the two immediate interface monolayers.

Within the grain boundaries about 40%–50% of all atoms in the interface are threefold coordinated. The fraction of three-coordinated carbons does not depend on the

twist angles. Formation energies of $\Sigma 5$, $\Sigma 13$ and $\Sigma 29$ (100) twist grain boundaries are also about the same, namely, 1.6 eV per interface atom, or $7.9\,\mathrm{J/m^2}$. The electronic structures are quite similar. It is characterised by a smaller band gap than in bulk diamond and the presence of electronic levels at and above the Fermi level that are localised on the grain boundary atoms.

Further, the incorporation of nitrogen impurities into the grain boundary is easier than into bulk diamond. The nitrogen substitution energy for the GB is lower than for bulk diamond by 2.6 eV to 5.6 eV. Nitrogen increases the amount of three-coordinated carbon atoms in the grain boundary. A shift in the Fermi energy toward the conduction band of about 0.4 eV at larger nitrogen concentrations was observed. A grain boundary conduction mechanism involving carbon π-states in the GB is suggested to be responsible for the high electrical conductivities in these films.

Silicon substitution into the grain boundary is more favourable by 3.0 eV to 5.3 eV than into the bulk and always results in a four-coordinated Si atom in the grain boundary. Hydrogen saturates dangling bonds of carbon atoms in the grain boundary and the average hydrogen binding energy is 3.5 eV. Hydrogen removes electronic states associated with dangling bonds from the band gap and so lowers the film conductivity.

A look ahead

The issue of conductivity in the UNCD material is one of the major forces which drives materials research in this area. Recent evidence underpins the pivotal role of nitrogen during growth and for the conductivity mechanism. These issues could only be scratched here. Work is under way towards a closer look of the role of nitrogen during growth [198].

The actual conduction mechanisms could only be addressed indirectly here. A further development will attempt to investigate them employing tools from the field of disordered electronic systems [199, 200].

Appendix A

Atomic Units Reference

In molecular dynamics simulations one deals with physical quantities on atomic scales. Under such circumstances, the use of units from the *Système International d'Unités* (SI), which are defined in terms of macroscopic quantities, would lead to unwieldy numerical values.[1] Appropriate decimal fractions of SI units, e.g., the *nanometre*, or non-SI units like the *electron volt* (which is officially accepted), or the *angstrom* (which is merely tolerated), serve much better to present results in digestible numbers. However, these units do not fulfil the practical demand that numerical calculations be decoupled from specific values of fundamental constants [12]. In order to achieve this, one divides the governing equations by reference quantities formed from fundamental constants. In non-relativistic quantum theory, these reference quantities form the body of *atomic units*[2] (a.u.). Bohr's model of the hydrogen atom provides the atomic units relevant for dynamical simulations:

Length: a_B (also a_0), the radius of the first Bohr orbit,

Time: τ_B, the inverse of the (circular) frequency of this orbit,

Mass: m_e, the mass of an electron,

Energy: E_h, the Coulomb energy of two elementary charges at distance a_B.

The last quantity is called *Hartree* energy. Historically, the value of the ionisation energy for the hydrogen ground state has been named a *Rydberg*, and differs from the Coulomb energy in Bohr's model by the kinetic energy of revolution, which is half of the former's magnitude, such that 1 Ry = 0.5 H. The abbreviation 'a.u.' is used as common designation for either one of these units. To avoid confusion, the unit Ry should be discouraged.

The tables in this section give the recommended values of constants (Tab. A.1), derived atomic units (Tab. A.2), and energy conversion factors (Tabs. A.3 and A.4). A compact version of these tables is also available on the web [201].

[1] The trend in national standards laboratories of actually *realising* SI units by quantum objects does not remedy this incongruity in the least.

[2] Basic quantities like length, time and energy may be formed from a set of fundamental constants either including or excluding the speed of light. Those variants in which the speed of light does enter are called *natural units*. They play a role mainly in cosmology.

Table A.1: List of selected fundamental constants of physics and chemistry based on the CODATA recommended values of the 1998 adjustment [202]. For brevity, the accuracy has been reduced in general to 7 significant digits and uncertainty data has been omitted. The values as shown are unaffected by uncertainty, except for k (± 2 in the last digit). Full data, including uncertainties, are to be found in Ref. [202] and on the web [203].

Quantity	Symbol	Numerical value	Unit	Note
speed of light in vacuum	c	299 792 458	m/s	(per definition)
magnetic constant	μ_0	$4\pi \times 10^{-7}$	V s/A m	(per definition)
electric constant, $1/\mu_0 c^2$	ε_0	$8.854\,188 \times 10^{-12}$	A s/V m	
Planck constant	h	$6.626\,069 \times 10^{-34}$	J s	$4.135\,667 \times 10^{-15}$ eV s
$h/2\pi$	$\hbar$	$1.054\,572 \times 10^{-34}$	J s	$6.582\,119 \times 10^{-16}$ eV s
elementary charge	e	$1.602\,176 \times 10^{-19}$	A s	
Boltzmann constant	k	$1.380\,650 \times 10^{-23}$	J/K	$8.617\,342 \times 10^{-5}$ eV/K
Avogadro constant	N_A	$6.022\,142 \times 10^{23}$	mol^{-1}	
atomic mass unit	u	$1.660\,539 \times 10^{-27}$	kg	1 822.888 m_e
electron mass	m_e	$9.109\,382 \times 10^{-31}$	kg	510.999 keV/c^2
proton mass	m_p	$1.672\,622 \times 10^{-27}$	kg	938.272 MeV/c^2
neutron mass	m_n	$1.674\,927 \times 10^{-27}$	kg	939.565 MeV/c^2
fine structure constant	α	$7.297\,353 \times 10^{-3}$		1/137.036 00
Rydberg constant	R_∞	10 973 731.6	m^{-1}	(13.6057 eV)/hc

Table A.2: Values of some atomic units in SI and non-SI units. Source, accuracy and uncertainty as in the previous table.

Quantity	Symbol	Numerical value	Unit	Note
Bohr radius (bohr)	a_B	$0.529\,177 \times 10^{-10}$	m	0.529 177 Å
Hartree energy (hartree, H)	E_h	$4.359\,744 \times 10^{-18}$	J	27.2114 eV
a.u. of time, τ_B	$\hbar/E_h$	$2.418\,884 \times 10^{-17}$	s	0.024 189 fs

In Bohr's model, the radial force $F_{\mathrm{rad}} = m_e r\omega^2$ for an electron circling around a proton arises from their Coulomb attraction $F_{\mathrm{el}} = e^2/4\pi\varepsilon_0 r^2$. Further, the angular momentum $l = m_e r^2\omega = n\hbar$ is quantised. From these postulates, one easily obtains the radius a_n, the angular frequency ω_n and the total (Coulomb plus kinetic) energy E_n of the nth Bohr orbit as:

$$\begin{aligned} a_n &= \frac{4\pi\varepsilon_0 n^2\hbar^2}{m_e e^2} = \frac{n^2\alpha}{4\pi R_\infty}; \quad a_B = a_1 \\ \omega_n &= \frac{n\hbar}{m_e a_n^2} = \frac{4\pi R_\infty c}{n^3}; \quad \tau_B = \frac{1}{\omega_1} \\ E_n &= \frac{1}{2}\frac{e^2}{4\pi\varepsilon_0 a_n} = \frac{R_\infty hc}{n^2}; \quad E_h = 2E_1 \end{aligned} \tag{A.1}$$

Historically, these units have been derived spectroscopically from the Rydberg constant $R_\infty = m_e e^4/8h^3\varepsilon_0^2 c = \alpha^2 m_e c/2h$ and the Sommerfeld fine structure constant $\alpha = e^2/4\pi\varepsilon_0\hbar c$, as shown.

Table A.3: Conversion between units of energy and values of energy equivalents derived from the relations $E = hc/\lambda = h\nu = kT$. Source, accuracy and uncertainty as in Tab. A.1. 'H' is the Hartree unit. The non-SI unit 'kcal/mol' is obsolete but included here for reference. Frequently consulted values are highlighted in **bold**.

	J	eV	H	kcal/mol*
1 J	1	$6.241\,51\times10^{18}$	$2.293\,71\times10^{17}$	$1.438\,36\times10^{20}$
1 eV	$\mathbf{1.602\,18\times10^{-19}}$	1	$3.674\,93\times10^{-2}$	**23.0451**
1 H	$4.359\,75\times10^{-18}$	**27.2114**	1	627.090
1 kcal/mol*	$6.952\,34\times10^{-21}$	$4.339\,31\times10^{-2}$	$1.594\,67\times10^{-3}$	1
(1 cm^{-1})hc	$1.986\,45\times10^{-23}$	$1.239\,84\times10^{-4}$	$4.556\,34\times10^{-6}$	$2.857\,23\times10^{-3}$
(1 Hz)h	$6.626\,07\times10^{-34}$	$4.135\,67\times10^{-15}$	$1.519\,83\times10^{-16}$	$9.530\,70\times10^{-14}$
(1 K)k	$1.380\,65\times10^{-23}$	$8.617\,34\times10^{-5}$	$3.166\,82\times10^{-6}$	$1.985\,88\times10^{-3}$

* $1\,cal_{IT} = 4.1868\,J$ (International Table calorie, exact)

continued ...

(continued)

	cm^{-1}	Hz	K
1 J	$5.034\,12\times10^{22}$	$1.509\,190\times10^{33}$	$7.242\,96\times10^{22}$
1 eV	**8 065.54**	$2.417\,989\times10^{14}$	$1.160\,45\times10^{4}$
1 H	$2.194\,75\times10^{5}$	$6.579\,684\times10^{15}$	$3.157\,75\times10^{5}$
1 kcal/mol[1]	349.989	$1.049\,241\times10^{13}$	503.556
(1 cm^{-1})hc	1	$2.997\,925\times10^{10}$	1.438 78
(1 Hz)h	$3.335\,64\times10^{-11}$	1	$4.799\,24\times10^{-11}$
(1 K)k	$6.950\,36\times10^{-1}$	$2.083\,664\times10^{10}$	1

Table A.4: Energy equivalents for electromagnetic radiation of selected wave lengths for visible light, and selected energies for infrared (IR) and ultraviolet (UV) [1, "Colour"].

Energy E (eV)	Wave number $\lambda^{-1}(cm^{-1})$	Wave length λ (nm)	Colour (typical)
1.00	8 066	1240	IR
1.77	14 286	700	Red (limit)
1.91	15 385	650	Red
2.07	16 667	600	Orange
2.25	18 182	550	Green
2.48	20 000	500	Cyan
2.76	22 222	450	Blue
3.10	25 000	400	Violet (limit)
5.00	40 328	248	UV

Appendix B

Approximations for Exchange and Correlation Energies

Practical applications of the DFT apparatus hinge on suitable approximations of the exchange-correlation functional $E_{xc}[n(\boldsymbol{r})]$. It should be recognised that the contribution of E_{xc} to the total energy (1.11) is by design a rather small, albeit significant one. Without it, chemical bonds would be much weaker [204].

To study the electron interaction effects, Harris and Jones suggested in 1974 [205] a fictitious many-particle Hamiltonian $\widehat{H}_\lambda$ as interpolation between non-interacting and fully interacting electrons. The Coulomb-interaction is scaled by a coupling parameter $0 \leq \lambda \leq 1$ as $\lambda/|\boldsymbol{r}_i - \boldsymbol{r}_j|$, with $\lambda = 0$ representing the non-interacting system and $\lambda = 1$ the physical system. An additional potential $V_\lambda(\boldsymbol{r})$ is introduced such that the corresponding density $n_\lambda(\boldsymbol{r})$ always equals the physical density, $n(\boldsymbol{r})$:

$$n_\lambda(\boldsymbol{r}) \equiv n_{\lambda=1}(\boldsymbol{r}) = n(\boldsymbol{r})\,. \tag{B.1}$$

The exchange-correlation energy is the result of the interaction of an electron with its *xc hole* around it. The xc hole describes the reduction of the average density $n(\boldsymbol{r}')$ due to the presence of an electron at $\boldsymbol{r}$:

$$n_{xc}(\boldsymbol{r}, \boldsymbol{r}'; \lambda) = g(\boldsymbol{r}, \boldsymbol{r}'; \lambda) - n(\boldsymbol{r}')\,, \tag{B.2}$$

where $g(\boldsymbol{r}, \boldsymbol{r}'; \lambda)$ is the pair correlation function for the system with interaction parameter λ, i.e., the conditional density at $\boldsymbol{r}'$ given that one electron is at $\boldsymbol{r}$. Consequently, the xc hole is normalised:

$$\int n_{xc}(\boldsymbol{r}, \boldsymbol{r}'; \lambda)\, \mathrm{d}\boldsymbol{r} = -1\,. \tag{B.3}$$

Several authors [205, 206, 207] have found an *exact* description for E_{xc} in the form of the Coulomb interaction:

$$E_{xc}[n(\boldsymbol{r})] = \frac{1}{2} \iint \mathrm{d}\boldsymbol{r}\, \mathrm{d}\boldsymbol{r}'\, \frac{n(\boldsymbol{r})\bar{n}_{xc}(\boldsymbol{r}, \boldsymbol{r}')}{|\boldsymbol{r} - \boldsymbol{r}'|}\,, \tag{B.4}$$

where $\bar{n}_{xc}$ is a *λ-averaged* xc hole,

$$\bar{n}_{xc}(\boldsymbol{r},\boldsymbol{r}') = \int_0^1 \mathrm{d}\lambda\; n_{xc}(\boldsymbol{r},\boldsymbol{r}';\lambda)\,. \tag{B.5}$$

Kohn pointed out in 1996 [208] that a many-electron system is "near-sighted", i.e., correlation effects have a microscopically limited range, typically of the order of the Fermi wavelength $\lambda_F = [3\pi^2 n(\boldsymbol{r})]^{-1/3}$. This fact *a posteriori* justifies many attempts at series expansions and parametrisations for eq. (B.4), e.g. [25, 27, 207, 209, 210].

The simplest and unexpectedly accurate expansion is the *Local Density Approximation* (LDA):

$$E_{xc}^{\mathrm{LDA}}[n(\boldsymbol{r})] = \int \varepsilon_{xc}(n(\boldsymbol{r}))n(\boldsymbol{r})\;\mathrm{d}\boldsymbol{r}\,. \tag{B.6}$$

where $\varepsilon_{xc}(n)$ is the exchange-correlation energy per electron in a *uniform* electron gas of density $n(\boldsymbol{r}) = \text{const}$. The energy $\varepsilon_{xc}(n)$ is a function of only the local density value, and no longer a functional of the global density distribution. $\varepsilon_{xc}(n)$ may be split into an exchange and a correlation contribution:

$$\varepsilon_{xc}(n(\boldsymbol{r})) = \varepsilon_x(n(\boldsymbol{r})) + \varepsilon_c(n(\boldsymbol{r}))\,. \tag{B.7}$$

The exchange part follows directly from Hartree-Fock theory for the homogeneous electron gas as follows (in atomic units):

$$\varepsilon_x(n(\boldsymbol{r})) = -\frac{3}{4}\left(\frac{3}{\pi}n(\boldsymbol{r})\right)^{1/3} \tag{B.8}$$

For the effective potential (1.20) we have, by eq. (1.22) from (B.6):

$$V_x(\boldsymbol{r}) = \varepsilon_x(n(\boldsymbol{r})) + n(\boldsymbol{r})\left.\frac{\mathrm{d}\varepsilon_x(n(\boldsymbol{r}))}{\mathrm{d}n(\boldsymbol{r})}\right|_{\boldsymbol{r}} = -\left(\frac{3}{\pi}n(\boldsymbol{r})\right)^{1/3}\,. \tag{B.9}$$

The correlation part is much more involved and is only available numerically from many-body calculations of the homogeneous electron gas as energy residue after all known contributions have been subtracted. Very accurate interpolation expressions (up to 0.1%) have been given early by Hedin and Lundqvist [211] and later, interpolating quantum Monte-Carlo simulations of Ceperley and Alder [212], by Perdew and Zunger [209]. These expressions are conveniently summarised in a recent introductory review [34]. To illustrate a simple case, the Hedin-Lundqvist expression reads for metallic densities [41]:

$$V_{xc}^{\mathrm{HL}}(\boldsymbol{r}) = \left\{1 + 0.0368\left(\frac{3}{4\pi n(\boldsymbol{r})}\right)^{1/3}\ln\left[1 + 21\left(\frac{4\pi}{3}n(\boldsymbol{r})\right)^{1/3}\right]\right\}V_x(\boldsymbol{r})\,. \tag{B.10}$$

LDA is only the first step in the expansion of E_{xc}. This is followed by parametrisations which retain the spin degrees of freedom as independent variables throughout the theory. This *Local Spin Density Approximation* (LSDA[1]) reads:

$$E_{xc}^{\mathrm{LSDA}}[n_\uparrow(\boldsymbol{r}), n_\downarrow(\boldsymbol{r})] = \int \varepsilon_{xc}(n_\uparrow(\boldsymbol{r}), n_\downarrow(\boldsymbol{r}))n(\boldsymbol{r})\;\mathrm{d}\boldsymbol{r}\,. \tag{B.11}$$

[1] also abbreviated as LSD

LSDA is only slightly more complicated than LDA and shows marked improvements or is even essential when the systems considered contain unpaired spins [34].

Despite its gross simplification, L(S)DA works remarkably well. While ionisation energies of atoms, dissociation energies for molecules and cohesive energies for solids are reproduced with errors in the 1 eV range, geometry parameters like bond lengths are described particularly well. This is even more surprising given the fact that the electron density in those systems does not at all represent a slowly varying function, as would be deemed necessary. For a long time, there had been no stringent explanation for the success of this approach, which was the reason for its reluctant appreciation by the quantum chemistry community. Only recently, Burke et al. [213, 214] pointed out that LSDA fulfils several conditions for the xc hole, among them the sum rule (B.3) and certain gradient conditions. Furthermore, as is evident from eq. (B.4), E_{xc} only depends on the spherical average of the xc hole $\bar{n}_{xc}$, which is well-approximated in LSDA.

Taking into account gradient information, and thus leaving the domain of strictly local functions, leads to *Generalised Gradient Approximations* (GGA). Commonly accepted GGA's are spin-dependent and employ a function f of the spin densities coupled with the magnitude of their gradients,

$$E_{xc}^{\mathrm{GGA}} = \int f\left(n_\uparrow(\boldsymbol{r}), n_\downarrow(\boldsymbol{r}), |\nabla n_\uparrow(\boldsymbol{r})|, |\nabla n_\downarrow(\boldsymbol{r})|\right)\ \mathrm{d}\boldsymbol{r}\,. \tag{B.12}$$

Early parametrisations of GGA's have been rather disappointing. Recent improvements in their functional form, up to essentially parameter-free expressions by Perdew, Burke and Ernzerhof [139] (known as PBE, or "GGA made simple"), have led to considerable improvements in the description of total energies. The remaining errors are about twice as high as those obtained from the best wave function methods. The relative simplicity of GGA's have made them an accepted companion to wave function methods in quantum chemistry for systems in which their size prohibits accurate calculations of the Hartree-Fock type.

It must be noted that neither LSDA nor GGA is applicable in systems with separated components which typically interact via van der Waals forces. For instance, the seemingly simple problem of the inter-layer interaction of graphite is not well described by either of these methods. Likewise, some details of the adsorption of aromatic molecules on graphite are difficult to model satisfactorily. In most practical cases, however, minor empirical or first-principle [58] corrections suffice to remedy such shortcomings.

Bibliography

Universal Resource Locators (URL): Where available, the titles of articles, books as well as journal names are active hyperlinks in the electronic version of this work. [1]

Page backreferences: To facilitate locating the context of citations, numbers at the very end of an entry indicate the page or pages on which the entry is cited.

[1] *The New Encyclopædia Britannica* (Encyclopædia Britannica, Inc., Chicago, 1989), 15th ed., later online at britannica.com. 1, 51, 52, 117

[2] M. A. Prelas, G. Popovici, and L. K. Bigelow, eds., *Handbook of Industrial Diamonds and Diamond Films* (Marcel Dekker, New York/Basel/Hong Kong, 1997). 1, 52, 55, 126, 127

[3] J. C. Angus and C. C. Hayman, *Low-pressure, metastable growth of diamond and "diamondlike" phases*, Science **241**, 913 (1988). 2, 52, 53, 54, 63

[4] D. M. Gruen, S. Liu, J. L. Alan R. Krauss, and X. Pan, *Fullerenes as precursors for diamond film growth without hydrogen or oxygen additions*, Appl. Phys. Lett. **64**, 1502 (1994). 2, 71

[5] R. O. Jones and O. Gunnarsson, *The density functional formalism, its application and prospects*, Rev. Mod. Phys. **61**, 689 (1989). 5, 6

[6] R. M. Dreizler and E. K. U. Gross, *Density Functional Theory* (Springer, Berlin and Heidelberg, 1990). 5, 7

[7] E. K. U. Gross and R. M. Dreizler, eds., *Density Functional Theory*, vol. 337 of *NATO ASI Series. Series B: Physics*, NATO Advanced Study Institute (Plenum Press, New York and London, 1994). 5, 121

[8] W. Kohn, *Overview of Density Functional Theory*, in [7], pp. 3–10. 5

[9] W. Kohn, *Nobel lecture: Electronic structure of matter—wave functions and density functionals*, Rev. Mod. Phys. **71**, 1253 (1999). 5

[10] W. J. Hehre, L. Radom, P. v. R. Schleyer, and J. A. Pople, *Ab Initio Molecular Orbital Theory* (John Wiley & Sons, New York, 1985). 5

[1] All conventional bibliographic details are printed. Hyperlinks to external resources were added since they are by now solidly established in scientific publishing and can be of tremendous help in accessing a resource. Still, the print version of this work forgoes URLs (except for a few explicit web references) for reasons of appearance, economy of space, and the foreseeable volatility of some links.

In general, journal titles will point to a journal's home page. Given that feasible article links exist, a separate URL points to individual articles by their title. Not all publishers provide a stable linking scheme to journals, let alone to individual articles. A few years on, some of the links will no longer function. The author asks for lenience when such dangling links are encountered. The mature ones will continue to work for the benefit of the reader.

[11] E. Schrödinger, *Quantisierung als Eigenwertproblem (Erste Mitteilung)*, Ann. Phys. (Leipzig) (IV) **79**, 361 (1926). 5

[12] D. R. Hartree, *The Wave Mechanics of an Atom with a Non-Coulomb Central Field. Part I. Theory and Methods*, Proc. Cambr. Phil. Soc. **24**, 89 (1928), parts II and III in same vol., pp. 111 and 426. 6, 115

[13] V. Fock, *Näherungsmethode zur Lösung des quantenmechanischen Mehrkörperproblems*, Z. f. Physik **61**, 126 (1930). 6

[14] C. C. J. Roothaan, *New developments in molecular orbital theory*, Rev. Mod. Phys. **23**, 69 (1951). 6

[15] P. Hohenberg and W. Kohn, *Inhomogeneous electron gas*, Phys. Rev. **136**, B864 (1964). 6, 8

[16] L. H. Thomas, *The calculation of atomic fields*, Proc. Cambridge Philos. Soc. **23**, 542 (1927). 6

[17] E. Fermi, *Un metodo statistico per la determinazione di alcune proprietà dell'atomo*, Rend. Lincei **6**, 602 (1927), cf. [18]. 6

[18] E. Fermi, *Eine statistische Methode zur Bestimmung einiger Eigenschaften des Atoms und ihre Anwendung auf die Theorie des periodischen Systems der Elemente*, Z. f. Physik **48**, 73 (1928). 122

[19] E. H. Lieb, *Thomas-Fermi and related theories of atoms and molecules*, Rev. Mod. Phys. **53**, 603 (1981), errata: *ibid.* **54**, 311 (1982). 6

[20] *The Official Web Site of The Nobel Foundation* (2001), URL `http://www.nobel.se/`. 7, 57

[21] A. S. Davydov, *Quantum mechanics*, International Series in Natural Philosophy (Pergamon Press, Oxford, 1976), 2nd ed. 7

[22] W. Kohn, in *Highlights of condensed-matter theory*, edited by F. Bassani, F. Fumi, and M. P. Tosi (1985), vol. LXXXIX of *Proceedings of the International School of Physics "Enrico Fermi"*, p. 4. 7

[23] M. Levy, *Electron densities in search of Hamiltonians*, Phys. Rev. A **26**, 1200 (1982). 7, 8

[24] E. H. Lieb, *Density functionals for Coulomb systems*, Int. J. Quantum Chem. **24**, 243 (1983). 7, 8

[25] U. von Barth and L. Hedin, *A local exchange-correlation potential for the spin polarized case: I*, J. Phys. C **5**, 1629 (1972). 7, 119

[26] H. Eschrig and W. E. Pickett, *Density functional theory of magnetic systems revisited*, Solid State Comm. **118**, 123 (2001). 7

[27] W. Kohn and L. J. Sham, *Self-consistent equations including exchange and correlation effects*, Phys. Rev. **140**, A1133 (1965). 9, 119

[28] J. F. Janak, *Proof that $\partial E/\partial n_i = \epsilon_i$ in density-functional theory*, Phys. Rev. B **18**, 7165 (1978). 9, 13, 26

[29] F. Gygi, *Electronic-structure calculations in adaptive coordinates*, Phys. Rev. B **48**, 11692 (1993). 11

[30] D. R. Hamann, *Generalized-gradient functionals in adaptive curvilinear coordinates*, Phys. Rev. B **54**, 1568 (1996). 11

[31] E. Tsuchida and M. Tsukada, *Adaptive finite-element method for electronic-structure calculations*, Phys. Rev. B **54**, 7602 (1996). 11

[32] J. Bernholc, E. Briggs, C. Bungaro, M. Buongiorno Nardelli, J.-L. Fattebert, K. Rapcewicz, C. Roland, W. Schmidt, and Q. Zhao, *Large-scale applications of real-space multigrid methods to surfaces, nanotubes, and quantum transport*, phys. stat. sol. (b) **217**, 685 (2000). 11

[33] J. Chelikowsky, Y. Saad, S. Öğüt, I. Vasiliev, and A. Stathopoulos, *Electronic structure methods for predicting the properties of materials: Grids in space*, phys. stat. sol. (b) **217**, 173 (2000). 11

[34] J. P. Perdew and S. Kurth, *Density functionals for non-relativistic Coulomb systems*, in *Density Functionals: Theory and Applications*, edited by D. Joubert (Springer, Berlin, 1998), vol. 500 of *Lecture notes in physics*, pp. 8–59. 13, 119, 120

[35] C. O. Almbladh and U. von Barth, *Exact results for the charge and spin densities, exchange-correlation potentials, and density-functional eigenvalues*, Phys. Rev. B **31**, 3231 (1985). 13

[36] M. C. Payne, M. P. Teter, and D. C. Allan, *Iterative minimization techniques for ab initio total-energy calculations: molecular dynamics and conjugate gradients*, Rev. Mod. Phys. **64**, 1045 (1992). 14, 28

[37] G. E. Moore, *Cramming more components onto integrated circuits*, Electronics **38**, 114 (1965). 15, 50

[38] D. Brenner, *The Art and Science of an Analytic Potential*, phys. stat. sol. (b) **217**, 23 (2000). 15

[39] W. Harrison, *Electronic Structure and the Properties of Solids* (W. H. Freeman and Company, San Francisco, USA, 1980). 15, 22

[40] Th. Frauenheim, G. Seifert, M. Elstner, Z. Hajnal, G. Jungnickel, D. Porezag, S. Suhai, and R. Scholz, *A self-consistent charge density-functional based tight-binding method for predictive materials simulations in physics, chemistry and biology*, phys. stat. sol. (b) **217**, 41 (2000), special issue with reviews on materials modelling. 16, 20, 23, 24, 29

[41] H. Eschrig, *Optimized LCAO Method and the Electronic Structure of Extended Systems*, Research Reports in Physics (Springer-Verlag and Akademie-Verlag, Berlin, 1989). 16, 119

[42] W. Bieger, G. Seifert, H. Eschrig, and G. Großmann, *Berechnung von Grundzustandseigenschaften kleiner Moleküle mit Hilfe eines LCAO-X_α Verfahrens*, Z. Phys. Chem. **266**, 751 (1985). 16

[43] G. Seifert, H. Eschrig, and W. Bieger, *Eine approximative Variante des LCAO-X_α Verfahrens*, Z. Phys. Chem. **267**, 529 (1986). 16, 20, 21, 22, 23

[44] Th. Frauenheim, P. Blaudeck, U. Stephan, and G. Jungnickel, *Atomic structure and physical properties of amorphous carbon and its hydrogenated analogs*, Phys. Rev. B **48**, 4823 (1993). 16

[45] D. Porezag, Th. Frauenheim, Th. Köhler, G. Seifert, and R. Kaschner, *Construction of tight-binding-like potentials on the basis of density-functional theory: Application to carbon*, Phys. Rev. B **51**, 12947 (1995). 16, 20

[46] D. Porezag, *Development of ab-initio and approximate density functional methods and their application to complex fullerene systems*, Dissertation, Fakultät für Naturwissenschaften, Technischen Universität Chemnitz-Zwickau (1997). 16, 17, 20, 21, 22, 27, 29, 30, 62

[47] Th. Köhler, Th. Frauenheim, and G. Jungnickel, *Stability, chemical bonding, and vibrational properties of amorphous carbon at different mass densities*, Phys. Rev. B **52**, 11837 (1995). 17

[48] K. Jackson, M. R. Pederson, D. Porezag, Z. Hajnal, and Th. Frauenheim, *Density-functional-based predictions of Raman and IR spectra for small Si clusters*, Phys. Rev. B **55**, 2549 (1997). 17

[49] Th. Köhler, M. Sternberg, D. Porezag, and Th. Frauenheim, *Surface properties of diamond (111):* $1 \times 1, 2 \times 1$ *and* 2×2 *reconstructions*, phys. stat. sol. (a) **154**, 69 (1996). 17, 58

[50] M. Sternberg, Th. Frauenheim, W. Zimmermann-Edling, and H.-G. Busmann, *STM images from diamond surfaces: Steps towards comparisions of experiment and theory*, Surf. Sci. **370**, 232 (1997). 17, 58, 59

[51] U. Stephan and D. A. Drabold, *Order-N projection method for first-principles computations of electronic quantities and Wannier functions*, Phys. Rev. B **57**, 6391 (1998). 17, 35

[52] U. Stephan, D. A. Drabold, and R. M. Martin, *Improved accuracy and acceleration of variational order-N electronic-structure computations by projection techniques*, Phys. Rev. B **58**, 13472 (1998). 17, 35

[53] U. Stephan, *Comparison of the convergence properties of linear-scaling electronic-structure schemes for nonorthogonal bases*, Phys. Rev. B **62**, 16412 (2000). 17, 35

[54] M. Sternberg, G. Galli, and Th. Frauenheim, *NOON - a non-orthogonal localised orbital order-N method*, Comp. Phys. Comm. **118**, 200 (1999). 17, 135

[55] T. Niehaus, *Entwicklung approximativer Methoden in der zeitabhängigen Dichtefunktionaltheorie*, Dissertation, Fachbereich Physik, Universität Gesamthochschule Paderborn (2001). 17

[56] Th. Niehaus, S. Suhai, F. Della Sala, P. Lugli, M. Elstner, G. Seifert, and Th. Frauenheim, *Tight-binding approach to time-dependent density-functional response theory*, Phys. Rev. B **63**, 085108 (9) (2001). 17

[57] Ch. Köhler, G. Seifert, U. Gerstmann, M. Elstner, H. Overhof, and Th. Frauenheim, *Approximate density-functional calculations of spin densities in large molecular systems and complex solids*, Phys. Chem. Chem. Phys. (2001), in print. 17

[58] J. Harris, *Simplified method for calculating the energy of weakly interacting fragments*, Phys. Rev. B **31**, 1770 (1985). 18, 120

[59] W. M. C. Foulkes and R. Haydock, *Tight-building models and density-functional theory*, Phys. Rev. B **39**, 12520 (1989). 18, 19, 24

[60] M. Elstner, *Weiterentwicklung quantenmechanischer Rechenverfahren für organische Moleküle und Polymere*, Dissertation, Fachbereich Physik, Universität Gesamthochschule Paderborn (1998), in german. 20, 21, 22, 23, 25, 29

[61] M. Elstner, D. Porezag, G. Jungnickel, J. Elsner, M. Haugk, Th. Frauenheim, S. Suhai, and G. Seifert, *Self-consistent-charge density-functional tight-binding method for simulations of complex materials properties*, Phys. Rev. B **58**, 7260 (1998). 20, 29

[62] C. Köhler and G. Seifert (2001), private communication. 21, 23

[63] J. C. Slater and G. F. Koster, *Simplified LCAO method for the periodic potential problem*, Phys. Rev. **94**, 1498 (1954). 22

[64] A. Sieck, *Structure and physical properties of silicon clusters and of vacancy clusters in bulk silicon*, Dissertation, Fachbereich Physik, Universität Gesamthochschule Paderborn (2000). 23

[65] J. A. Pople, D. P. Santry, and G. A. Segal, *Approximate self-consistent molecular orbital theory. I. Invariant procedures*, J. Chem. Phys. **43**, S129 (1965). 26

[66] M. Scholz and H.-J. Köhler, *Quantenchemische Näherungsverfahren und ihre Anwendung in der organischen Chemie*, vol. 3 of *Quantenchemie–Ein Lehrgang* (Deutscher Verlag der Wissenschaften, Berlin, 1981). 26, 28

[67] K. Ohno, *Some remarks on the Pariser-Parr-Pople method*, Theoret. chim. Acta (Berlin) **2**, 219 (1964). 26

[68] G. Klopman, *A semiempirical treatment of molecular structures. II. Molecular terms and application to diatomic molecules*, J. Amer. Chem. Soc. **86**, 4550 (1964). 26

[69] J. A. Pople and D. L. Beveridge, *Approximate Molecular Orbital Theory*, McGraw-Hill Series in advanced Chemistry (McGraw Hill, New York, 1970). 27

[70] P. P. Ewald, *Die Berechnung optischer und elektrostatischer Gitterpotentiale*, Ann. Phys. (Leipzig) **64**, 253 (1921). 28

[71] J. M. Ziman, *Principles of the Theory of Solids* (University Press, Cambridge, England, 1965), 1st ed. 28

[72] W. H. Press, S. A. Teukolsky, W. T. Vetterling, and B. P. Flannery, *Numerical Recipes* (University Press, Cambridge, England, 1992), 2nd ed., URL `http://www.nr.com/`. 29, 39, 44

[73] G. Galli, *Linear scaling methods for electronic structure calculations and quantum molecular dynamics simulations*, Current Opinion Sol. State & Mater. Sci. **1**, 864 (1996). 31, 50

[74] G. Galli, *Large-scale electronic structure calculations using linear scaling methods*, phys. stat. sol. (b) **217**, 231 (2000). 31, 50

[75] E. Hernández, M. J. Gillan, and C. M. Goringe, *Linear-scaling density-functional-theory technique: The density-matrix approach*, Phys. Rev. B **53**, 7147 (1996). 31, 33

[76] D. R. Bowler, I. J. Bush, and M. J. Gillan, *Practical methods for ab initio calculations on thousands of atoms*, Int. J. Quantum Chem. **77**, 831 (2000). 31

[77] W. Hierse and E. B. Stechel, *Order-N methods in self-consistent density-functional calculations*, Phys. Rev. B **50**, 17811 (1994). 31

[78] E. B. Stechel, A. R. Williams, and P. J. Feibelman, *N-scaling algorithm for density-functional calculations of metals and insulators*, Phys. Rev. B **49**, 10088 (1994). 31

[79] P. Ordejón, *Order-N tight-binding methods for electronic-structure and molecular dynamics*, Comput. Mater. Sci. **12**, 157 (1998), special issue on tight binding. 31, 50

[80] S. Goedecker, *Linear scaling electronic structure methods*, Rev. Mod. Phys. **71**, 1085 (1999). 31, 50

[81] G. Galli and M. Parinello, *Large scale electronic structure calculations*, Phys. Rev. Lett. **69**, 3547 (1992). 32

[82] J. Kim, F. Mauri, and G. Galli, *Total-energy global optimizations using nonorthogonal localized orbitals*, Phys. Rev. B **52**, 1640 (1995). 32, 33

[83] A. Canning, G. Galli, F. Mauri, A. de Vita, and R. Car, *O(N) tight-binding molecular dynamics on massively parallel computers: an orbital decomposition approach*, Comp. Phys. Comm. **94**, 89 (1996). 32, 34, 37

[84] F. Mauri and G. Galli, *Electronic-structure calculations and molecular-dynamics simulations with linear system-size scaling*, Phys. Rev. B **50**, 4316 (1994). 33

[85] M. C. Strain, G. E. Scuseria, and M. J. Frisch, *Achieving linear scaling for the electronic quantum Coulomb problem*, Science **271**, 51 (1996). 33

[86] P. Ordejón, E. Artacho, and J. M. Soler, *Self-consistent order-N density-functional calculations for very large systems*, Phys. Rev. B **53**, 10441 (1996). 33

[87] M. P. Allen and D. J. Tildesley, *Computer Simulations of Liquids* (Oxford Science Publishers, Oxford, England, 1987). 34

[88] M. Sternberg, W. R. L. Lambrecht, and Th. Frauenheim, *Molecular-dynamics study of diamond/silicon (001) interfaces with and without graphitic interface layers*, Phys. Rev. B **56**, 1568 (1997). 43

[89] M. R. Pederson, D. Porezag, J. Kortus, and D. Patton, *Strategies for massively parallel local-orbital-based electronic structure methods*, phys. stat. sol. (b) **217**, 197 (2000). 50

[90] R. Rudd and J. Broughton, *Concurrent coupling of length scales in solid state systems*, phys. stat. sol. (b) **217**, 251 (2000). 50

[91] M. E. Weeks, *The discovery of the elements. I. Elements known to the ancient world*, J. Chem. Educ. **9**, 4 (1932). 51

[92] A. G. Whittaker, E. J. Watts, R. S. Lewisu, and E. Anders, *Carbynes: Carriers of primordial noble gases in meteorites*, Science **209**, 1512 (1980). 51

[93] S. S. Russell, C. T. Pillinger, J. W. Arden, M. R. Lee, and U. Ott, *A new type of meteoritic diamond in the enstatite chondrite Abee*, Science **256**, 206 (1992). 51

[94] P. G. Brown, A. R. Hildebrand, M. E. Zolensky, M. Grady, R. N. Clayton, T. K. Mayeda, E. Tagliaferri, R. Spalding, N. D. MacRae, E. L. Hoffman, et al., *The fall, recovery, orbit, and composition of the Tagish Lake meteorite: A new type of carbonaceous chondrite*, Science **290**, 320 (2000). 51

[95] G. F. Kunz, *Diamonds in meteorites*, Science (Old Series) **11**, 118 (1888). 51

[96] H. O. A. Meyer and M. Seal, *Natural diamond*, in [2], chap. 10, pp. 481–583. 51

[97] American Museum of Natural History, *The Nature of Diamonds*, web site (1998), URL `http://www.amnh.org/exhibitions/diamonds/`. 51, 52, 54

[98] *Britannica Book of the Year 2000 – Events of 1999* (Encyclopædia Britannica, Inc., Chicago, 2000). 51

[99] *Britannica Book of the Year 2001 – Events of 2000* (Encyclopædia Britannica, Inc., Chicago, 2001). 52

[100] *Losing their sparkle*, The Economist (2000), 1 Jun. 52

[101] *Fuelling Africa's wars*, The Economist (2001), 11 Jan. 52

[102] L. Gorelick and A. J. Gwinnett, *Diamonds from India to Rome and beyond*, Amer. J. Archaeol. **92**, 547 (1988). 52

[103] P. J. Gielisse, *Surface properties of diamond*, in [2], chap. 3, pp. 49–88. 52, 54

[104] W. G. Eversole, *Synthesis of diamond*, U.S. Patent Nos. 3,030,187 and 3,030,188 (1962). 52

[105] J. C. Angus, *A short history of diamond synthesis*, in [106], pp. 1–8. 52

[106] A. Paoletti and A. Tucciarone, eds., *The Physics of Diamond*, vol. CXXXV of *Proceedings of the International School of Physics "Enrico Fermi"*, Società Italiana di Fisica (IOS Press, Amsterdam, 1997), ISBN 90 5199 352 8. 127

[107] S. Shikata, *The Road to commercialization of vapor-phase-grown diamond*, in [108], pp. 61–64. 52, 53

[108] D. M. Gruen and I. Buckely-Golder, *Diamond Films: Recent Developments*, MRS Bull. **23** (1998). 127

[109] K. Lonsdale, *Divergent-beam X-ray photography of crystals*, Philos. Trans. Roy. Soc. London Ser. A **240**, 219 (1947). 53

[110] G. P. Srivastava, *Theory of thermal conductivity in nonmetals*, MRS Bull. **26**, 445 (2001). 53

[111] J. S. Goela, N. E. Brese, M. A. Pickering, and J. E. Graebner, *Chemical-vapor-deposited materials for high thermal conductivity applications*, MRS Bull. **26**, 458 (2001). 53

[112] A. Mainwood, *Point defects in natural and synthetic diamond: What they can tell us about CVD diamond*, phys. stat. sol. (a) **172**, 25 (1999). 54, 86

[113] G. M. Swain, A. B. Anderson, and J. C. Angus, *Applications of diamond thin films in electrochemistry*, in [108], pp. 56–60. 54

[114] R. G. Farrer, *On the substitutional nitrogen donor in diamond*, Solid State Comm. **7**, 685 (1969). 54, 102

[115] G. R. Brandes, *Diamond vacuum electronics*, in [2], chap. 31, pp. 1103–1128. 54

[116] R. H. Telling, C. J. Pickard, M. C. Payne, and J. E. Field, *Theoretical strength and cleavage of diamond*, Phys. Rev. Lett. **84**, 5160 (2000). 55

[117] H.-G. Busmann and I. V. Hertel, *Vapour grown polycrystalline diamond films: Microscopic, mesoscopic and atomic surface structures*, Carbon **36**, 391 (1998). 55, 59, 60, 67

[118] C. Kittel, *Introduction to Solid State Physics* (John Wiley & Sons, New York, 1986), sixth ed. 57

[119] C. Davisson and L. H. Germer, *Diffraction of electrons by a crystal of nickel*, Phys. Rev. **30**, 705 (1927). 57

[120] T. Aizawa, T. Ando, M. Kamo, and Y. Sato, *High-resolution electron-energy-loss spectroscopic study of epitaxially grown diamond (111) and (100) surfaces*, Phys. Rev. B **48**, 18348 (1993). 57

[121] G. Binnig and H. Rohrer, *Scanning tunneling microscopy-from birth to adolescence*, Rev. Mod. Phys. **59**, 615 (1987), nobel lecture. 57

[122] M. P. D'Evelyn, *Surface properties of diamond*, in [2], chap. 4, pp. 89–146. 58, 65

[123] G. Jungnickel, C. D. Latham, M. I. Heggie, and Th. Frauenheim, *On the graphitization of diamond surfaces: the importance of twins*, Diamond & Rel. Materials **5**, 102 (1996). 58, 82

[124] G. Jungnickel, D. Porezag, Th. Frauenheim, M. I. Heggie, W. R. L. Lambrecht, B. Segall, and J. C. Angus, *Graphitization effects on diamond surfaces and the diamond/graphite interface*, phys. stat. sol. (a) **154**, 109 (1996). 58

[125] V. L. Kuznetsov, I. L. Zilberberg, Y. V. Butenko, A. L. Chuvilin, and B. Segall, *Theoretical study of the formation of closed curved graphite-like structures during annealing of diamond surface.*, J. Appl. Phys. **86**, 863 (1999). 58, 82

[126] C. Z. Wang, K. M. Ho, M. D. Shirk, and P. A. Molian, *Laser-induced graphitization on a diamond (111) surface*, Phys. Rev. Lett. **85**, 4092 (2000). 58

[127] G. Kern and J. Hafner, *Ab initio molecular-dynamics studies of the graphitization of flat and stepped diamond (111) surfaces*, Phys. Rev. B **58**, 13167 (1998). 58

[128] K. C. Pandey, *New dimerized-chain model for the reconstruction of the diamond* $(111) - (2 \times 1)$ *surface*, Phys. Rev. B **25**, 4338 (1982). 58

[129] K. C. Pandey, *New* π*-bonded chain model for Si*$(111) - (2 \times 1)$ *surface*, Phys. Rev. Lett. **47**, 1913 (1981). 58

[130] R. Seiwatz, *Possible structures for clean, annealed surfaces of germanium and silicon*, Surf. Sci. **2**, 473 (1964). 58

[131] H.-G. Busmann, W. Zimmermann-Edling, S. Lauer, H. Hertel, Th. Frauenheim, P. Blaudeck, and D. Porezag, *Observation of* $(\sqrt{3} \times \sqrt{3})R30^\circ$ *diamond (111) on vapour-grown polycrystalline films*, Surf. Sci. **295**, 340 (1993). 58

[132] B. N. Davidson and W. E. Pickett, *Tight-binding study of hydrogen on the C(111), C(100), and C(110) diamond surfaces*, Phys. Rev. B **49**, 11253 (1994). 59, 67

[133] J. Furthmüller, J. Hafner, and G. Kresse, *Dimer reconstruction and electronic surface states on clean and hydrogenated diamond (100) surfaces*, Phys. Rev. B **53**, 7334 (1996). 59, 63, 67, 68, 69, 99

[134] M. D. Winn, M. Rassinger, and J. Hafner, *Atomic and electronic structure of the diamond (100) surface: Reconstructions and rearrangements at high hydrogen coverage*, Phys. Rev. B **55**, 5364 (1997). 59, 68

[135] S. Skokov, B. Weiner, and M. Frenklach, *Molecular-dynamics study of oxygenated (100) diamond surfaces*, Phys. Rev. B **49**, 11374 (1994). 59

[136] R. E. Stallcup II and J. M. Perez, *Scanning tunneling microscopy studies of temperature-dependent etching of diamond (100) by atomic hydrogen*, Phys. Rev. Lett. **86**, 3368 (2001). 60, 67

[137] D. L. Chadi, *Stabilities of single-layer and bilayer steps on Si(001) surfaces*, Phys. Rev. Lett. **59**, 1691 (1987). 60

[138] S. Skokov, B. Weiner, M. Frenklach, Th. Frauenheim, and M. Sternberg, *Dimer-row pattern formation in diamond (100) growth*, Phys. Rev. B **52**, 5426 (1995). 60

[139] J. P. Perdew, K. Burke, and M. Ernzerhof, *Generalized gradient approximation made simple*, Phys. Rev. Lett. **77**, 3865 (1996), erratum: [140]. 60, 120

[140] J. P. Perdew, K. Burke, and M. Ernzerhof, *Erratum: Generalized gradient approximation made simple*, Phys. Rev. Lett. **78**, 1396 (1997). 128

[141] H. J. McSkimin and W. L. Bond, *Elastic moduli of diamond*, Phys. Rev. **105**, 116 (1957). 61

[142] M. H. Grimsditch and A. K. Ramdas, *Brillouin scattering in diamond*, Phys. Rev. B **11**, 3139 (1975). 61

[143] F. D. Murnaghan, *Finite deformations of an elastic solid*, Amer. J. Math. **59**, 235 (1937). 61

[144] F. D. Murnaghan, *The compressibility of media under extreme pressures*, Proc. Nat. Acad. Sci. USA **30**, 244 (1944). 61

[145] A. Blumenau (2001), private communication. 61

[146] J. Furthmüller, J. Hafner, and G. Kresse, *Ab initio calculation of the structural and electronic properties of carbon and boron nitride using ultrasoft pseudopotentials*, Phys. Rev. B **50**, 15606 (1994). 61, 63

[147] M. Elstner, P. Hobza, Th. Frauenheim, S. Suhai, and E. Kaxiras, *Hydrogen bonding and stacking interactions of nucleic acid base pairs: A density-functional-theory based treatment*, J. Chem. Phys. **114**, 5149 (2001). 62, 63

[148] G. Kern, J. Hafner, and G. Kresse, *Atomic and electronic structure of diamond (111) surfaces. I. Reconstruction and hydrogen-induced de-reconstruction of the one dangling-bond surface*, Surf. Sci. **366**, 445 (1996). 63, 64, 65, 66, 69

[149] G. Kern, J. Hafner, and G. Kresse, *Atomic and electronic structure of diamond (111) surfaces. II.* (2×1) *and* $(\sqrt{3} \times \sqrt{3})$ *reconstructions of the clean and hydrogen-covered three dangling-bond surfaces*, Surf. Sci. **366**, 464 (1996). 63, 64, 69

[150] G. Kern and J. Hafner, *Ab initio calculations of the atomic and electronic structure of clean and hydrogenated diamond (110) surfaces*, Phys. Rev. B **56**, 4203 (1997). 63, 64, 66, 67, 69

[151] R. Graupner, M. Hollering, A. Ziegler, J. Ristein, , L. Ley, and A. Stampfl, *Dispersions of surface states on diamond (100) and (111)*, Phys. Rev. B **55**, 10841 (1997). 66

[152] D. R. Alfonso, D. A. Drabold, and S. E. Ulloa, *Structural, electronic, and vibrational properties of diamond (100), (111), and (110) surfaces from ab initio calculations*, Phys. Rev. B **51**, 14669 (1995). 67

[153] F. Maier, R. Graupner, M. Hollering, L. Hammer, J. Ristein, and L. Ley, *The hydrogenated and bare diamond (110) surface: a combined LEED-, XPS-, and ARPES study*, Surf. Sci. **443**, 177 (1999). 67

[154] S. C. Lim, R. E. Stallcup II, I. Akwani, and J. M. Perez, *Structural and electronic properties of negative electron affinity epitaxial diamond (110) films studied using atomic resolution UHV STM*, in *Materials Issues in Vacuum Microelectronics*, edited by W. Zhu, L. Pan, T. Felter, and C. Holland (Materials Research Society, Pittsburgh, 1998), vol. 509 of *MRS Symposia Proceedings*, p. 165. 67

[155] C. Zuiker, A. R. Krauss, D. M. Gruen, X. Pan, J. C. Li, R. Csencsits, A. Erdemir, C. Bindal, and G. Fenske, *Physical and tribological properties of diamond films grown in argon-carbon plasmas*, Thin Solid Films **270**, 154 (1995). 71

[156] H.-G. Busmann, U. Brauneck, and H.-W. David, *Fullerenes as the parent molecule for the deposition of tetrahedral carbon*, in *Fullerenes and Carbon based Materials*, edited by P. Delhaes and H. Kuzmany (Elsevier Science SA, Lausanne, 1998), vol. 68 of *Europ. Mater. Res. Soc. Symp. Proc.*, pp. 529–533, also published as [157]. 71

[157] H.-G. Busmann, U. Brauneck, and H.-W. David, *Fullerenes as the parent molecule for the deposition of tetrahedral carbon*, Carbon **36**, 529 (1998). 71, 129

[158] D. Zhou, D. M. Gruen, L.-C. Qin, T. G. McCauley, and A. R. Krauss, *Control of diamond film microstructure by Ar additions to CH_4/H_2 microwave plasmas*, J. Appl. Phys. **84**, 1981 (1998). 71, 72, 91

[159] D. M. Gruen, *Nanocrystalline diamond films*, Annu. Rev. Mater. Sci. **29**, 211 (1999). 71, 85, 86

[160] A. N. Goyette, Y. Matsuda, L. W. Anderson, and J. E. Lawler, *C_2 column densities in $H_2/Ar/CH_4$ microwave plasmas*, J. Vac. Sci. & Tech. A **16**, 337 (1998). 71

[161] T. Lin, G. Y. Yu, A. T. S. Wee, Z. X. Shenu, and K. P. Loh, *Compositional mapping of the argon-methane-hydrogen system for polycrystalline to nanocrystalline diamond film growth in a hot-filament chemical vapor deposition system*, Appl. Phys. Lett. **77**, 2692 (2000). 71

[162] A. Erdemir, M. Halter, G. R. Fenske, C. Zuiker, R. Csencsits, A. R. Krauss, and D. M. Gruen, *Friction and wear mechanisms of smooth diamond films during sliding in air and dry nitrogen*, Tribology Trans. **40**, 667 (1997). 71

[163] A. Erdemir, C. Bindal, G. R. Fenske, C. Zuiker, R. Csencsits, A. R. Krauss, and D. M. Gruen, *Tribological characterization of smooth diamond films grown in Ar-C_{60} and Ar-CH_4 plasmas*, Diamond Films Technol. **6**, 31 (1996). 71

[164] P. Keblinski, D. Wolf, S. R. Phillpot, and H. Gleiter, *Role of bonding and coordination in the atomic structure and energy of diamond and silicon grain boundaries*, J. Mater. Res. **13**, 2077 (1998). 71, 86, 89, 93, 94, 96

[165] M. Sternberg, P. Zapol, Th. Frauenheim, D. M. Gruen, and L. A. Curtiss, *Molecular Dynamics simulation of impurities in nanocrystalline diamond grain boundaries*, in *Amorphous and Nanostructured Carbon*, edited by J. Robertson, J. Sullivan, O. Zhou, T. Allen, and B. Coll (Materials Research Society, Pittsburgh, 2000), vol. 593 of *MRS Symposia Proceedings*, pp. 483–487. 71

[166] D. Zhou, A. R. Krauss, T. D. Corrigan, T. G. McCauley, R. P. H. Chang, and D. M. Gruen, *Microstructure and field emission of nanocrystalline diamond prepared from C_{60} precursors*, J. Electrochem. Soc. **144**, L224 (1997). 71

[167] C. J. Chu, R. H. Hauge, J. L. Margrave, and M. P. D'Evelyn, *Growth kinetics of (100), (110), and (111) homoepitaxial diamond films*, Appl. Phys. Lett. **61**, 1393 (1992). 71

[168] D. A. Horner, L. A. Curtiss, and D. M. Gruen, *A theoretical study of the energetics of insertion of dicarbon (C_2) and vinylidene into methane C–H bonds*, Chem. Phys. Lett. **233**, 243 (1995). 71

[169] P. C. Redfern, D. A. Horner, L. A. Curtiss, and D. M. Gruen, *Theoretical studies of growth of diamond (110) from dicarbon*, J. Phys. Chem. **100**, 11654 (1996). 71, 75, 112

[170] G. Ciccotti, M. Ferrario, and J.-P. Ryckaert, *Molecular dynamics of rigid systems in cartesian coordinates. a general formulation*, Mol. Phys. **47**, 1253 (1982). 72, 73

[171] J.-P. Ryckaert, *Special geometrical constraints in the molecular dynamics of chain molecules*, Mol. Phys. **55**, 549 (1985). 72, 73

[172] J. M. Thijssen, *Computational Physics* (University Press, Cambridge, 1999), pp. 218–220. 72, 73

[173] R. Saito, M. Fujita, G. Dresselhaus, and M. S. Dresselhaus, *Electronic structure of chiral graphene tubules*, Appl. Phys. Lett. **60**, 2204 (1992). 81

[174] J. W. Mintmire, B. I. Dunlap, and C. T. White, *Are fullerene tubules metallic?*, Phys. Rev. Lett. **68**, 631 (1992). 81, 82

[175] L.-M. Peng, Z. L. Zhang, Z. Q. Xue, Q. D. Wu, Z. N. Gu, and D. G. Pettifor, *Stability of carbon nanotubes: How small can they be?*, Phys. Rev. Lett. **85**, 3249 (2000). 81

[176] G. Jungnickel, D. Porezag, Th. Frauenheim, W. R. L. Lambrecht, B. Segall, and J. C. Angus, *Diamond (111) surface: Graphitization or reconstruction?*, in *Mechanical Behavior of Diamond and Other Forms of Carbon*, edited by M. D. Drory, M. S. Donley, D. Bogy, and J. E. Field (Materials Research Society, Pittsburgh, 1995), vol. 383 of *MRS Symposia Proceedings*, p. 349. 82

[177] J. Narayan and A. S. Nandedkar, *Atomic structure and energy of grain boundaries in silicon, germanium and diamond*, Phil. Mag. B **63**, 1181 (1991). 85

[178] O. A. Shenderova and D. W. Brenner, *Atomistic simulations of structures and mechanical properties of ⟨011⟩ tilt grain boundaries and their triple junctions in diamond*, Phys. Rev. B **60**, 7053 (1999). 85, 96

[179] O. A. Shenderova, D. W. Brenner, and L. H. Yang, *Atomistic simulations of structures and mechanical properties of polycrystalline diamond: Symmetrical ⟨001⟩ tilt grain boundaries*, Phys. Rev. B **60**, 7043 (1999), erratum: [180]. 85, 96, 131

[180] O. A. Shenderova, D. W. Brenner, and L. H. Yang, *Erratum: Atomistic simulations of structures and mechanical properties of polycrystalline diamond: Symmetrical ⟨001⟩ tilt grain boundaries*, Phys. Rev. B **62**, 3565 (2000), cf. [179]. 131

[181] F. Cleri, P. Keblinski, L. Colombo, D. Wolf, and S. R. Phillpot, *On the electrical activity of sp^2-bonded grain boundaries in nanocrystalline diamond*, Europhys. Lett. **46**, 671 (1999). 86, 93, 94, 95, 99

[182] D. M. Gruen, P. C. Redfern, D. A. Horner, P. Zapol, and L. A. Curtiss, *Theoretical studies on nanocrystalline diamond: Nucleation by Dicarbon and electronic structure of planar defects*, J. Phys. Chem. B **103**, 5459 (1999). 86, 89, 95

[183] D. Wolf, *Atomic-level geometry of crystalline interfaces*, in *Materials Interfaces: atomic-level structure and properties*, edited by D. Wolf and S. Yip (Chapman & Hall, London, 1992), chap. 1, pp. 1–57, 1st ed., ISBN 0-412-41270-5. 87

[184] P. C. Kelires, *Structural properties and energetics of amorphous forms of carbon*, Phys. Rev. B **47**, 1829 (1993). 93

[185] Z. Q. Wang, S. A. Dregia, and D. Stroud, *Energy-minimization studies of twist grain boundaries in diamond*, Phys. Rev. B **49**, 8206 (1994). 96

[186] R. J. Cook and D. H. Whiffen, *Electron nuclear double resonance study of a nitrogen centre in diamond*, Proc. Roy. Soc. London A **295**, 99 (1966). 100

[187] C. A. J. Ammerlaan, *Electron paramagnetic resonance studies of native defects in diamond*, in *Defects and Radiation Effects in Semiconductors*, edited by R. R. Hasiguti (IOP, Bristol and London, 1981), vol. 59 of *Inst. Phys. Conf. Ser.*, pp. 81–94. 100

[188] A. Cox, M. E. Newton, and J. M. Baker, *^{13}C, ^{14}N and ^{15}N ENDOR measurements on the single substitutional nitrogen centre (P1) in diamond*, J. Phys. Cond. Matter **6**, 551 (1994). 100

[189] S. Bhattacharyya, O. Auciello, J. Birrell, J. A. Carlisle, L. A. Curtiss, A. N. Goyette, D. M. Gruen, A. R. Krauss, J. Schlueter, A. Sumant, et al., *Synthesis and characterization of highly-conducting nitrogen-doped ultrananocrystalline diamond films*, Appl. Phys. Lett. **79**, 1441 (2001). 102

[190] S. A. Kajihara, A. Antonelli, J. Bernholc, and R. Car, *Nitrogen and potential n-type dopants in diamond*, Phys. Rev. Lett. **66**, 2010 (1991). 104

[191] F. Weich, J. Widany, and Th. Frauenheim, *Paracyanogenlike structures in high-density amorphous carbon nitride*, Phys. Rev. Lett. **78**, 3326 (1997). 105

[192] Th. Köhler, G. Jungnickel, and Th. Frauenheim, *Molecular-dynamics study of nitrogen impurities in tetrahedral amorphous carbon*, Phys. Rev. B **60**, 10864 (1999). 105

[193] V. S. Veerasamy, J. Yuan, G. A. J. Amaratunga, W. I. Milne, K. W. R. Gilkes, M. Weiler, and L. M. Brown, *Nitrogen doping of highly tetrahedral amorphous carbon*, Phys. Rev. B **48**, 17954 (1993). 106

[194] X. Zhou, G. D. Watkins, K. M. McNamara Rutledge, R. P. Messmer, and S. Chawla, *Hydrogen-related defects in polycrystalline CVD diamond*, Phys. Rev. B **54**, 7881 (1996). 108

[195] D. F. Talbot-Ponsonby, M. E. Newton, J. M. Baker, G. A. Scarsbrook, R. S. Sussmann, A. J. Whitehead, and S. Pfenninger, *Multifrequency EPR, ^{1}H ENDOR, and saturation recovery of paramagnetic defects in diamond films grown by chemical vapor deposition*, Phys. Rev. B **57**, 2264 (1998). 108

[196] D. Saada, J. Adler, and R. Kalish, *Lowest-energy site for hydrogen in diamond*, Phys. Rev. B **61**, 10711 (2000). 108

[197] Q. Chen, D. M. Gruen, A. R. Krauss, T. D. Corrigan, M. Witek, and G. M. Swain, *The structure and electrochemical behavior of nitrogen-containing nanocrystalline diamond films deposited from $CH_4/N_2/Ar$ mixtures*, J. Electrochem. Soc. **148**, E44 (2001). 108

[198] M. Sternberg, P. Zapol, Th. Frauenheim, J. Carlisle, D. M. Gruen, and L. A. Curtiss, *Density functional based tight binding study of C_2 and CN deposition on (100) diamond surface*, in *Nanotubes, Fullerenes, Nanostructured and Disordered Carbon*, edited by T. A. Friedmann, D. B. Geohegan, D. E. Luzzi, J. Robertson, and R. S. Ruoff (Materials Research Society, Pittsburgh, 2001), vol. 675 of *MRS Symposia Proceedings*, pp. W12.11.1–5. 113, 135

[199] F. Wegner, *Inverse participation ratio in $2 + \varepsilon$ dimensions*, Z. f. Physik B **36**, 209 (1980). 113

[200] P. A. Lee and T. V. Ramakrishnan, *Disordered electronic systems*, Rev. Mod. Phys. **57**, 287 (1985). 113

[201] M. Sternberg, *Numbers and Units for Molecular Dynamists*, web page (1998–2001), URL `http://www.phys.upb.de/topic/units/`. 115

[202] P. J. Mohr and B. N. Taylor, *CODATA recommended values of the fundamental physical constants: 1998*, Rev. Mod. Phys. **72**, 351 (2000). 116

[203] National Institute of Standards and Technology, *The NIST Reference on Constants, Units, and Uncertainty*, web site (2001), URL `http://physics.nist.gov/cuu/`. 116

[204] S. Kurth and J. P. Perdew, *Role of the exchange correlation energy: Nature's glue*, Int. J. Quantum Chem. **77**, 814 (2000). 118

[205] J. Harris and R. O. Jones, *The surface energy of a bounded electron gas*, J. Phys. F **4**, 1170 (1974). 118

[206] D. C. Langreth and J. P. Perdew, *The exchange-correlation energy of a metallic surface*, Solid State Comm. **17**, 1425 (1975). 118

[207] O. Gunnarsson and B. I. Lundqvist, *Exchange and correlation in atoms, molecules, and solids by the spin-density formalism*, Phys. Rev. B **13**, 4274 (1976). 118, 119

[208] W. Kohn, *Density functional and density matrix method scaling linearly with the number of atoms*, Phys. Rev. Lett. **76**, 3168 (1996). 119

[209] J. P. Perdew and A. Zunger, *Self-interaction correction to density-functional approximations for many-electron systems*, Phys. Rev. B **23**, 5048 (1981). 119

[210] A. D. Becke, *Density-functional thermochemistry. IV. A new dynamical correlation functional and implications for exact-exchange mixing*, J. Chem. Phys. **104**, 1040 (1996). 119

[211] L. Hedin and B. I. Lundqvist, *Explicit local exchange-correlation potentials*, J. Phys. C **4**, 2064 (1971). 119

[212] D. M. Ceperly and B. J. Alder, *Ground state of the electron gas by a stochastic method*, Phys. Rev. Lett. **45**, 566 (1980). 119

[213] K. Burke, J. P. Perdew, and M. Ernzerhof, *Why the generalized gradient approximation works and how to go beyond it*, Int. J. Quantum Chem. **61**, 287 (1997). 120

[214] K. Burke, J. P. Perdew, and M. Ernzerhof, *Why semilocal functionals work: Accuracy of the on-top pair density and importance of system averaging*, J. Chem. Phys. **109**, 3760 (1998). 120

[215] M. Sternberg, M. Kaukonen, R. M. Nieminen, and Th. Frauenheim, *Growth of (110) diamond using pure dicarbon*, Phys. Rev. B **63**, 165414 (9) (2001). 135

[216] M. Sternberg, P. Zapol, L. A. Curtiss, D. M. Gruen, and Th. Frauenheim, *Tight-Binding molecular dynamics modeling of impurity atom-grain boundary interaction in diamond*, in *Symp. A: Multiscale Phenomena in Materials–Experiments and Modeling* (Boston, MA, 1999), Materials Research Society Fall Meeting, Poster award. 135

[217] P. Zapol, M. Sternberg, Th. Frauenheim, D. M. Gruen, and L. A. Curtiss, *Electronic structure studies of nanocrystalline diamond grain boundaries*, in *Diamond Materials VI.*, edited by J. L. Davidson, W. D. Brown, A. Gicquel, B. V. Spitsyn, and J. C. Angus (Electrochemical Society, Pennington, NJ, USA, 2000), vol. PV 99-32 of *ECS Proceedings*, pp. 185–190. 135

[218] P. Zapol, M. Sternberg, L. A. Curtiss, Th. Frauenheim, and D. M. Gruen, *Tight-binding molecular dynamics simulation of impurities in ultrananocrystalline diamond grain boundaries*, Phys. Rev. B **65** (2002), in print. 135

[219] D. E. Knuth, *TEX and Metafont–New Directions in Typesetting* (The American Mathematical Society and Digital Press, Stanford, 1979). 137

[220] C. Babbage, *Passages from the Life of a Philosopher* (Longman, Green, Longman, Roberts, & Green, London, 1864). 137

Acknowledgements

It's is not, it isn't ain't, and it's it's, not its, if you mean it is. If you don't, it's its. Then too, it's hers. It isn't her's. It isn't our's either. It's ours, and likewise yours and theirs.

– Oxford University Press, Edpress News

This place is customarily reserved for notes of a more private nature. They are essential and will duly follow below. First, however, professional acknowledgements are in order. I would like to thank all persons involved in the preparation of this manuscript.

The material presented in Chapter 3 has been published as Ref. [54]. I am most grateful to Giulia Galli for her interest, welcoming support, and guidance in the preparation of this material. I thank the Institut Romand de Recherche Numérique en Physique des Matériaux (IRRMA) for enabling several visits to Lausanne, not in the least allowing me to pick up a bit of French from the locals.

The work presented in Chapter 5 has been published in Ref. [215] and has been carried out with the support of Helsinki University of Technology and The Center for Scientific Computing in Finland. I thank my colleague Markus Kaukonen from the HUT Laboratory of Physics for the chance to bring in my experience on diamond surfaces and apply DFTB to the problem of growth and his significant contributions to the barrier calculations for the adsorption and diffusion studies. I also thank Prof. Risto Nieminen and Markus for welcoming and supporting me in Helsinki and the discussions we had there. While in Helsinki, among quite a few more things on Finish culture, I learned to appreciate modern art in the then newly opened *Kiasma*. I am also grateful to Dieter Gruen and Gotthard Seifert for many fruitful discussions concerning the transient role of the graphene sheets. Gotthard always answered my theory questions thoroughly and with patience.

Last, but not least, Chapter 6 is the result of a very stimulating and ongoing collaboration with my colleague Peter Zapol and the groups of Larry Curtiss and Dieter Gruen at the Chemistry Division of Argonne National Laboratory. I am indebted to these distinguished individuals for calling me aboard their undertaking in the exciting field of ultrananocrystalline diamond. Material in this chapter has been presented in various meetings [198, 216, 217] and will presently appear as publication [218].

Most of the activity over the years would have been impossible without the financial

support from the Deutsche Forschungsgemeinschaft. Specifically, the roots of my interest in diamond go back to being part of the tri-national D-A-CH collaboration 1991–2000 on Superhard Materials established by the DFG and its sister organisations in Austria (A) and Switzerland (CH).

Finally, these collaborations would not have come into being without the instigation and support by my thesis advisor Prof. Thomas Frauenheim. He helped push forward the use of the methodology into the areas here presented and provided the prerequisite machinery and contacts. I am grateful to Thomas for setting me on this track and allowing me to pursue own interests in the field of computing, even if they consumed considerable resources occasionally.

I would like to express gratitude to Walter Lambrecht and John Angus of Case Western Reserve University who allowed me to share in their theoretical and practical experience in the very early stages of this undertaking. It is by the suggestion of John that Fig. 4.1 on page 53 came into being some years ago (quite a few, actually!) I also wish to thank Walter and his family for their warm welcome and re-kindling in me an appreciation for the silver screen.

Much of the methodological work was performed while the group was located in Chemnitz. I thank Prof. Schreiber and all my former colleagues there for providing a good working atmosphere during that time and beyond.

The final stages of this work were performed in Paderborn. I thank my office neighbour Uwe Gerstmann not only for the admirable *tangram* he performed with our furniture and so organising the space but also for enduring my presence over the years and being a fountain of insight extending far beyond the field of defects in semiconductors. Prof. Overhof was always responsive when I approached him about physical and meta-physical issues, for which I express my gratitude. H.-J. Wagner left a lasting impression on me by tactfully pointing out quite a number of literature resources which helped to refine not only the bibliography in this work but also my personal library and interests about the far distant past. Our secretary, Astrid Canisius quickly and efficiently took the reigns of office into her hands once she joined us. I highly appreciate her help in expertly relieving the pain in organising official matters. I also express my gratitude to Christof and Thomas Köhler for their critical reading of the manuscript, helping to dissolve some obscure verbal constructs of mine. I would also like to thank Zoltán Hajnal specifically for relieving me of some of the responsibilities in maintaining our machine pool and being vigilant of its running.

My thanks to all those whom I forgot to mention but influenced the work nonetheless by being around and enlightening the atmosphere.

Ein besonders herzlicher Dank gilt meinen Eltern, die trotz der Entfernung immer für mich da waren und mir Verständnis und Unterstützung entgegenbrachten.

Colophon

> *TEX is potentially the most significant invention in typesetting in this century. It introduces a standard language for computer typography, and in terms of importance could rank near the introduction of the Gutenberg press.*
>
> *– Gordon Bell, in [219]*

This work was prepared using the free LaTeX and pdfLaTeX typesetting system on a machine considered modern at the time of writing—a laptop with a Pentium III processor running the Linux operating system. The main text is typeset in the Palatino font family accompanied by matching mathematical fonts provided with the mathpple package. Extensive cross-referencing was facilitated by the package hyperref. The bibliography was prepared using BibTeX with the REVTeX4 citation style provided by the American Physical Society and modified here to show article titles and include hyperlinks to local and external resources.

Data plots were prepared with a recent version of Gnuplot (v3.7.1). Atomic structure images were produced using RasMol (v2.6.4) by Roger Sayle, which I have extended to provide perspective views. Auxiliary images were generated using the vector graphics program XFig. The scripting facilities offered by all these programs helped towards maintaining a consistent style.

The text has been edited with the vim text editor and has been version-controlled using CVS.

Because of my past experience and a fondness of mine for that particular accent British spelling is used throughout. It is hoped that this gets little in the way of readers who are accustomed otherwise.

The quote in the introduction is due to Charles Babbage, known chiefly as pioneer of information technology in association with Lady Ada Lovelace. His rather witty autobiography [220] attests that he was well versed in other fields as well, among them economics and street musicians.